Universidade de Aveiro
Ano 2016
Departamento de Engenharia de Materiais e Cerâmica

Alichandra Maria Gonçalves Castro

Design of multifunctional mesoporous thin films for electronic applications

Concepção de filmes finos mesoporosos multifuncionais para aplicações electrónicas

Universidade de Aveiro
Ano 2016
Departamento de Engenharia de Materiais e Cerâmica

Alichandra Maria Gonçalves Castro

Design of multifunctional mesoporous thin films for electronic applications

Concepção de filmes finos multifuncionais para aplicações electrónicas

Tese apresentada à Universidade de Aveiro para cumprimento dos requisitos necessários à obtenção do grau de Doutor em Ciência e Engenharia dos Materiais, realizada sob a orientação científica da Doutora Paula Celeste da Silva Ferreira, Investigadora Principal do CICECO-Instituto de Materiais de Aveiro, Departamento de Engenharia de Materiais e Cerâmica da Universidade de Aveiro, Professora Doutora Paula Maria Vilarinho, Professora Associada do Departamento de Engenharia de Materiais e Cerâmica da Universidade de Aveiro e Professor Doutor Clément Sanchez, Professor Catedrático da Université Pierre et Marie Curie, Paris, França.

Este trabalho foi desenvolvido no âmbito do projeto CICECO-Aveiro Institute of Materials POCI-01-0145-FEDER-007679 (Refª. FCT UID/CTM/50011/2013) e do projeto FCOMP-01-0124-FEDER-009356 (PTDC/CTM/098130/2008), financiados por fundos nacionais através da FCT/MEC e quando aplicável cofinanciado pelo FEDER, no âmbito do Acordo de Parceria PT2020.
FCT e POPH/FSE são agradecidas pela bolsa de doutoramento de SFRH/BD/67121/2009.
As acções COST MP0904 e IC1208 financiaram as missões a Dublin e a Madrid.

o júri

Presidente

José Carlos da Silva Neves
Professor Catedrático, Universidade de Aveiro

Prof. Doutor Albano Augusto Cavaleiro Rodrigues de Carvalho
Professor Catedrático, Faculdade de Ciências e Tecnologia, Universidade de Coimbra

Prof. Doutora Maria Margarida Godinho
Professora Catedrática, Faculdade de Ciências, Universidade de Lisboa

Prof. Doutor Christopher Rhys Bowen
Professor, University of Bath, Reino Unido

Prof. Doutor Luís António Ferreira Martins Dias Carlos
Professor Catedrático, Universidade de Aveiro

Prof. Doutora Verónica Cortés de Zea Bermudez
Professora Catedrática, Escola da Vida e do Ambiente, Universidade de Trás-os-Montes e Alto Douro

Prof. Doutora Paula Maria Lousada Silveirinha Vilarinho
Professora Associada, Universidade de Aveiro (co-orientadora)

Doutora Paula Celeste da Silva Ferreira
Investigadora Principal, Universidade de Aveiro (orientadora)

Acknowledgements

Firstly I would like to thank my supervisors, Dr. Paula Ferreira, Prof. Paula Vilarinho and Clément Sanchez for the guidance, personal support and constant motivation in this work.

I want to acknowledge in particular Dr Paula Ferreira for all discussions, patient, support and mainly for her friendship. During this long and hard “battle” she was always motivated to continue and never give up. Many thanks for all… my scientific mother.

I would like to deeply acknowledge:

- Christel Laberty-Robert and Jadra Mosa from LCMCP, UPMC Collège de France for the cobalt deposition through electrochemical deposition;
- Denise Denning and Dr. Brian Rodriguez from the Nanoscale Function group of Conway Institute of Biomolecular and Biomedical Research for assistance and discussion related with the Scanning Probe Microscopy measurements;
- Prof. José de Frutos from Universidad Politécnica de Madrid, Escuela Técnica Superior de Ingenieros de Telecomunicaciones, for all his help in the dielectric measurements;
- Dr Rui Borges, Dr Mário Rodrigues, Prof. Liliana Ferreira and Prof Margarida Godinho from the Physics Department of the Faculty of Science of the University of Lisbon for the magnetic measurements and all discussion;
- Prof Albertina Cabañas from the Departamento de Química-Física I, Universidad Complutense de Madrid for the nickel deposition through the Supercritical Fluid Deposition;
- Prof Elvira Fortunato from CENIMAT - Centre for Materials Research for the Focused Ion Beam analyses;
- Prof Liliana Mitoseriu and Leontin Padurariu from Department of Physics, Alexandru Ion Cuza University, Iasi for all modelling results by Finite Element Model.

I am grateful to Eng. Marta Ferro, Dr. Rosário Soares, Eng. Maria João Bastos and Eng. Célia Miranda from University of Aveiro for all help, patient and discussion about SEM, XRD and TGA/DTA respectively. I am thankful also to MSc Celeste Azevedo and Eng. Ana Caço for all help on TGA/DTA and TG/DSC analysis

I am thankful to my laboratory colleagues for the good moments that we have passed together, namely Mirtha, Cláudia, Carla, Stella, Adelaide, Violeta and Manuel.

Finally, I am would like to thank the most important persons in my life, my mom, my father, my nephews and obviously, my boyfriend who kept with me during this long and hard way!

palavras-chave

Filmes finos nanoporosos, estruturas porosas nanoestruturadas, *evaporation-induced self-assembly*, soluções sol-gel com copolímeros em bloco anfifílicos, microelectrónica, ferroeléctricos, ferromagnéticos e filmes finos multiferroícos.

resumo

Os materiais multiferróicos possuem simultaneamente pelo menos duas das três propriedades ferróicas: *i)* ferroelectricidade; *ii)* ferromagnetismo; e / ou *iii)* ferroelasticidade. Estes materiais têm despertado considerável interesse na indústria microeletrónica devido ao seu potencial para serem usados em dispositivos de armazenamento de informação com elevada capacidade e eficiência energética. A constante procura pela redução do tamanho e aumento da funcionalidade dos dispositivos, imposta pela Lei de Moore, exige materiais ferróicos, na forma de filmes finos e multifuncionalidade. Contudo, à medida que a espessura dos filmes diminui, as propriedades ferróicas ficam comprometidas em virtude de constrangimentos provocados pelo substrato ou outros efeitos. Neste contexto, esta tese estuda a possibilidade de utilizar a porosidade em filmes funcionais para criar sistemas compósitos multifuncionais. Assim, desenvolveram-se estratégias para a preparação de filmes de ferroeléctricos, ferromagnéticos e multiferroícos com porosidade uniforme e ordenada. O efeito dessa porosidade foi avaliado nas propriedades físicas locais e macroscópicas. Foram estudados óxidos multimetálicos com estrutura de perovisquite ou de espinela por serem promissores para aplicação em sensores; atuadores; condensadores; memórias; etc. Escolheu-se uma metodologia química em que os filmes são depositados por técnica de mergulho em soluções sol-gel contendo um copolímero em bloco que se organiza espontaneamente conjuntamente com os precursores durante o processo de evaporação. $PbTiO_3$ foi a composição inicialmente escolhida para entender o efeito da nanoporosidade nas propriedades eléctricas locais por ser o material piezoeléctrico protótipo que possui o mais alto coeficiente piezoeléctrico conhecido. Assim, foram preparados filmes nanoporosos e densos de $PbTiO_3$ com espessura de cerca de 100 nm e diâmetro de poro na ordem dos 50 nm. A presença da nanoporosidade contribui para a cristalização precoce da fase cristalina por aumento local da temperatura durante a decomposição do copolímero e / ou por funcionarem como núcleos de cristalização. Consequentemente, os fimes porosos exibem melhores coeficientes piezoeléctricos e baixo campo coercivo, sendo mais fácil inverter a direção da polarização por efeito do campo elétrico. Sendo a porosidade um meio para atingir propriedades melhoradas, esta pode funcionar como uma ferramenta para ajustar as propriedades ferroeléctricas à aplicação desejada. Todos os resultados de PFM foram previstos através de modelação teórica usando o modelo de elementos finitos.

Foi também investigada a preparação de filmes porosos de titanado de bário enquanto protótipo de um ferroeléctrico sem chumbo.

Neste contexto, foi avaliado o efeito de vários parâmetros, tais como: *i)* o aquecimento da solução de precursores; *ii)* adição de precursores inorgânicos / solventes orgânicos; e *iii)* envelhecimento da solução inicial, na estrutura final dos filmes.Verificou-se que o uso de uma solução fresca de precursores sem qualquer ciclo de aquecimento contribuía para uma melhor organização dos filmes porosos de $BaTiO_3$. Verificou-se também que o tamanho dos blocos num copolímero à base de poliestireno e poli(óxido de etileno) era preponderante para a ordem e microestrutura cristalina dos filmes finais. Copolímeros em bloco com cadeias de bloco mais longas são preferíveis para obter uma estrutura ordenada e aparentemente desempenham um papel na cristalização precoce da fase ferroeléctrica tetragonal, contribuindo para uma melhoria da resposta piezoeléctrica. Em analogia com o $PbTiO_3$, os resultados indicam que nos filmes nanoporosos de $BaTiO_3$, a cristalização ocorre a temperaturas mais baixas do que nos filmes densos. Utilizou-se a deposição electroquímica para inserir nanopartículas metálicas de cobalto dentro dos poros dos filmes de $BaTiO_3$. O carácter multiferróico dos filmes foi constatado através da avaliação nanoscópica das propriedades elétricas e pela medida das propriedades magnéticas macroscópicas à temperatura ambiente. Verificaram-se as dificuldades de conseguir um preenchimento uniforme dos poros e de otimizar a interface entre as duas fases ferróicas. Assim com vista a tentar ultrapassar estas dificuldades, prepararam-se filmes mais finos e em que a porosidade estivesse devidamente organizada, com poros perpendiculares à superfície. Conceberam-se filmes nanotexturados ordenados de óxidos multimetálicos com propriedades ferroelétricas, ferromagnéticas e multiferróicas com espessuras e texturas de dimensão inferior a 100 nm. As composições escolhidas foram $PbTiO_3$, $CoFe_2O_4$ e $BiFeO_3$. Os filmes finos porosos nanotexturados $PbTiO_3$ apresentaram a fase cristalográfica tetragonal mesmo em espessuras de filme de 22 nm. Os filmes finos de $CoFe_2O_4$ apresentaram uma orientação preferencial no plano e elevadas magnetizações de saturação. Deduziu-se que os filmes teriam uma impureza ferromagnética compatível com uma liga metálica rica em platina. A presença desta impureza não só melhora o desempenho magnético dos filmes mas também fornece uma forte evidência para a potencial aplicabilidade dos filmes de $CoFe_2O_4$ como catalisadores para a oxidação de hidrocarbonetos através do mecanismo de Mars-Van-Krevelen. Foram também preparados filmes finos porosos nanotexturados de $BiFeO_3$, com 66 nm de espessura e tamanho médio de diâmetro de 100 nm. Verificou-se o caráter multiferróico destes filmes e mais uma vez a melhoria clara das propriedades eléctricas locais induzida pela porosidade. A estrutura porosa também tem um efeito positivo nas propriedades magnéticas no plano, mostrando uma componente ferromagnética 50% maior que a medida em filmes densos.

Verificou-se também que porosidade dos filmes de $BiFeO_3$ pode ter interesse para aplicações fotocatalíticas, conjugando reduzido valor do hiato óptico direto (2.58 eV) com relativamente elevada área porosa (ca. 57 %). Para testar a aplicabilidade dos filmes nanotexturados na construção de um filme multiferróico compósito, uma matriz porosas ferroelétricos ($BaTiO_3$) foi funcionalizada por preenchimento dos poros com nanopartículas ferromagnéticas de níquel. A estratégia de funcionalização dos poros foi a deposição por arrastamento com CO_2 supercrítico, seguida de redução da espécie metálica a 250 ºC ativada por etanol. Pequenas nanopartículas de níquel com cerca de 21 nm foram depositadas dentro dos poros da matriz porosa, tendo-se verificado as propriedades estruturais e magnéticas do compósito.

Esta tese, provou a adequação desta metodologia química de baixo custo na concepção de materiais multifuncionais, criando novas perspectivas para a indústria da microeletrónica na sua abordagem contínua de redução de tamanho e custo, enquanto aumenta a complexidade de funcionamento.

Keywords

Nanoporous thin films, nanopatterned porous structures, evaporation-induced self-assembly (EISA), sol-gel solution with amphiphilic block-copolymers, microelectronics, ferroelectric, ferromagnetic and multiferroic oxide thin films.

Abstract

Multiferroic materials, exhibiting simultaneously at least two of the three ferroic properties: *i)* ferroelectricity; *ii)* ferromagnetism; and *iii)* ferroelasticity, have attracted considerable interest from the microelectronics industry. Due to their potential, these materials can be used in information storage applications with significantly high energetic efficiencies and elevated capacities. During the last decades and owing the increasing need for miniaturization of electronic devices, the ferroic materials, mainly in the format of thin films, have been extensively studied both theoretically and experimentally. However, as the film thickness decreases the ferroics properties progressively decreases due to the in-plane strain relaxation constrained by the substrate or others intrinsic and extrinsic effects. Within this context, here we exploit the role of nanoporosity on local and macroscopic properties of ferroelectrics, ferromagnetic and multiferroics thin films. Although, porosity is normally considered as a defect (or secondary phase) having usually a detrimental effect on the electrical macroscopic response; it can also be regarded as an asset, in terms of: *i)* density (light weight) and *ii)* capacity to host other functionality/ies. Oxides with perovskite and spinel structures are promising materials because they possess extraordinarily useful properties namely to be used as piezoelectrics sensors, as ferroelectric actuators, capacitors and memories, in high-strength dielectrics, for ferromagnetics or even multiferroics. Among the bottom-up approaches, the sol-gel method and evaporation-induced self-assembly methodology are the most suitable, low-cost and easy preparation method to prepare nanoporous and nanopatterned thin films of different compositions.

$PbTiO_3$ is the chosen composition to understand the role of the nanoporosity on the local electric properties. Thus, nanoporous and dense ferroelectric $PbTiO_3$ thin films with 100 nm and ~ 50 nm pore size formed using a block polymer as a structure-directing agent are prepared. The presence of nanoporosity markedly affects the microstructure, crystallization and ferroelectric film properties. The crystallization of tetragonal phase is enhanced in nanoporous films. It seems that the decomposition of the block-copolymer in porous films triggers the crystallization of the perovskite phase at low temperatures via the local increase of temperature. Moreover, pores may work as initiators of the crystallization. Consequently, nanoporous films with improved tetragonality exhibit enhanced piezoelectric coefficients, switchable polarization and low local coercivity. In fact, the porosity induces instability in the dipole-dipole interactions and consequently the reverse polarization can be favoured for low bias values. By providing a means of achieving enhanced properties, nanoporosity may work as a tool to tune electric properties to the desired ferroelectric application. All the PFM results were supported by theoretical modelling using Finite Element Model.

To have a more complete picture of the role of the nanoporosity on the crystallization and electric properties, the procedure is applied to prepare a nanoporous lead-free material, $BaTiO_3$. However, this expantion was not trivial whereas the crystallization temperature of the tetragonal phase necessary for the ferroelectric properties is much higher than the decomposition temperature of the block-copolymer used as template. From this, several parameters such as: heating the solution, addition of inorganic precursors / organic solvent and aging time of solution are studied in order to understand the effect of these on the micellization process and consequently in the final porous $BaTiO_3$ films. Based on the results of this study, for this specific multimetallic oxide system it is preferable to use a very fresh solution, without any heating cycles. In addition, block-copolymers based on polystyrene and poly(ethylene oxide) with different block sizes are used to investigate their influence on the order and crystalline microstructure of the final films. Blocks-copolymers with longer block chains are preferable to get an ordered structure and apparently play a role on the earliest crystallization of the tetragonal ferroelectric perovskite phase, contributing to an enhancement of the piezoelectric response. Similarly to $PbTiO_3$, our results indicate that in nanoporous $BaTiO_3$ films the crystallization occurs as well before in dense films. Moreover, besides providing a means of achieving enhanced properties, nanoporosity may work as a tool to tune electric properties to the desired ferroelectric application.

$BaTiO_3$ nanoporous films are tested as a kind of “golf course” full of holes to accommodate ferromagnetic particles. In this way, electrochemical deposition is used to insert the cobalt metal nanoparticles into the pores of $BaTiO_3$ films. Films containing cobalt particles within the pores are obtained and piezoelectric and ferromagnetic properties are evaluated. For many applications would be a challenge to prepare ferroelectric thin films with lateral sizes well below 100 nm. Furthermore, the design of nanofeatures, uniformed in size and shape at a reasonable large-range order, i.e. “nanopatterning”, would extend their utility for electronic devices and integrated circuits, which require that each pixel feature can be individually addressable. Additionally, nanopatterned porous ferroelectric thin films may be interesting to develop vertical composite structures with perfect strain coupling at the interface. Thus, and using the chemical self-assembly method, different functional nanopatterned porous thin films: $PbTiO_3$, $BiFeO_3$ and $CoFe_2O_4$ are designed. Nanopatterned $PbTiO_3$ thin films display the tetragonal ferroelectric crystallographic phase even when the films are as thin as 22 nm. $CoFe_2O_4$ thin films present a preferential in-plane orientation. High saturation magnetizations (close or even higher than in bulk $CoFe_2O_4$) are determined in all films, pointing to the presence of a ferromagnetic impurity compatible with a platinum-rich metal alloy.

The presence of this impurity not only enhances the magnetic performance but also provides evidence for the catalytic activity of these $CoFe_2O_4$ films for hydrocarbon oxidation through a Mars-Van-Krevelen mechanism.
For the $BiFeO_3$ composition, crystalline nanopatterned $BiFeO_3$ layers with 66 nm of thickness and average pore diameter of 100 nm at 600 ºC are obtained. The large vertical porosity markedly enhances the local electric and macroscopic magnetic properties when compared with the dense counterparts. The porous structure also has a positive effect on the parallel magnetic characteristics of the system, displaying a 50% larger ferromagnetic component and enhanced remanent magnetization when compared to the dense thin films counterpart. The porosity is also important for the photocatalytic applications conjugating the smallest direct band gap (2.58 eV) and extended porous area (ca. 57 %).
The nanopatterned thin films allow the exploitation of a new concept to prepare multiferroic nanocomposite thin films. The multiferroic films based on in two chemical-based bottom-up steps, including: *i)* the formation of a porous ferroic matrix and *ii)* the accomodation of nanoparticles from another ferroic phase within the pores. Hexagonal-arranged pores with diameter of ca. 95 nm, running perpendicularly to the substrate are filled with nickel nanoparticles using the supercritical fluid deposition technique from reduction of hydrated nickel nitrate in a supercritical CO_2-ethanol mixture at 250 ºC. Small nickel nanoparticles with ca. 20 nm are deposited inside the pores of the porous matrix. Structural and magnetic properties proved the coexistence of both phases.

The chemical based methodology offers thus an excellent control of the physical and chemical properties of nanostructured materials such as: stoichiometry, thickness, size, array and porous distribution. Moreover the self-assembly of block-copolymers provides a versatile platform to prepare functional nanostructured materials, namely mesostructured oxide thin films, due to their capability to form large pores and thick walls, apart from being industrially available and hazard-free. Additionally, the chemical-assembly method can allow the direct nanopatterning of large substrate areas with a functional oxide at a cost-effective price, in the absence of expensive equipment or etching processes (which typically affect negatively the ferroic properties).Besides, the functional properties of the porous films by themselves, the porous films are extremely promising to achieve multiferroic composites.

List of publications

From the work performed so far, four scientific original articles were published, and another was recently submitted for publication, in international journals:

1. P. Ferreira, A. Castro, P. M. Vilarinho, M. -G. Willinger, J. Mosa, C. Laberty, C. Sanchez, **Electron Microscopy Study of Porous and Co Functionalized $BaTiO_3$ Thin Films**, Microsc. Microanal., 2012, 18, 115;
2. Alichandra Castro, Paula Ferreira, Brian Rodriguez, Paula Vilarinho, **The role of nanoporosity on local piezo and ferroelectric properties of lead titanate thin films**, Journal Materials Chemistry C, 2015, 3, 1035;
3. Alichandra Castro, Paula Ferreira, Brian Rodriguez, Paula Vilarinho, **Porosity… Advantage or Disadvantage?;** Microscopy and Microanalysis, 2015, 21, 17;
4. Alichandra Castro, Paula Ferreira, Paula M. Vilarinho, ***Block-copolymer-assisted nanopatterning of porous lead titanate thin films for advanced electronics***; The Journal of Physical Chemistry C, 2016,120, 10961;
5. Alichandra Castro, Paula Ferreira, Stella Skiadopoulou, Paula M. Vilarinho, Liliana P. Ferreira, Margarida Godinho, Brian J. Rodriguez, ***Thin film porous ferroic nanostructures: Strategies and characterization***; Nanoscale Ferroelectrics and Multiferroics: Key Processes and Characterization Issues, and Nanoscale Effects, 1st Edition. Edited by Miguel Algueró, J. Marty Gregg, and Liliana Mitoseriu. John Wiley & Sons, Ltd. 2016;
6. Alichandra Castro, Manuel A. Martins, Liliana P. Ferreira, Margarida Godinho, Paula M. Vilarinho, Paula Ferreira, **Low-cost functional bismuth ferrite nanopatterned porous thin films**; *submitted*.

Three other works are being prepared for publication:

1. Alichandra Castro, Leontin Padurariu, Paula Ferreira, Brian Rodriguez, Liliana Mitoseriu, Paula Vilarinho, **Modelling the role of nanoporosity on the switching properties of ferroelectric thin films and experimental verification**; in preparation;
2. Alichandra Castro, Brian Rodriguez, Liliana P. Ferreira, Margarida Godinho, Paula Ferreira, Paula M. Vilarinho, **Nanopatterned porous cobalt ferrite thin films for magnetic and catalytic applications**; in preparation;

3. Alichandra Castro, Jacobo Morère, Albertina Cabañas, Liliana P. Ferreira, Margarida Godinho, Paula Ferreira, Paula M. Vilarinho, **Chemical designed multiferroic nanocomposite films: a Proof of Concept**; in preparation.

Contents

List of figures

List of tables

List of symbols

P_S	Spontaneous Polarization
T_C	Curie temperature
E_d	Depolarizing Field
E_C	Electric Coercive Field
P r	Remanent Polarization
E	Electric Field
ε_r	Relative Dielectric Permittivity
ε_0	Dielectric Permittivity of the Vacuum (8.85×10^{-12} F/m)
Z	Cantilever displacement
hkl	Miller Indexes
$(d_{33})_{eff}$	Piezoelectric coefficient
Vac	ac Voltage
Vdc	dc Voltage, bias
I_m	Imprint
V^+	Positive coercive bias
V^-	Negative coercive bias
R_m	Switchable polarization
$(R_S)^+$	Positive saturated piezoresponse
$(R_S)^-$	Negative saturated piezoresponse
T_N	Néel temperature
θ	Curie-Weiss temperature
H	Magnetic field
H_C	Magnetic coercivity
B	Flux density
B_S	Saturation magnetic induction
B_r	Residual magnetic induction
S_{Pt}	Fraction accessible substrate surface
d_p	Pore diameter
α	Absorption coefficient
$h\nu$	Incident photon energy

ITRS	Road Map for Semiconductor Industry
NV-FeRAMs	Non-Volatile Ferroelectric Random Access Memories
FeRAMs	Ferroelectric Random Access Memories
MRAMs	Magnetic Random Access Memories
DRAM	Dynamic Random Access Memory
CMOS	Commentary Metal Oxide Semiconductor
MERAM	Magnetoelectric RAM
IC	Integrated Circuit
0D	Zero Dimensional
1D	One Dimensional
2D	Two Dimensional
3D	Three Dimension
Amm2	Orthorhombic phase
R3m	Rhombohedral phase
DLS	Dynamic Light Scattering
XRD	X-Ray Diffraction
HRTEM	High-resolution transmission electron microscopy
TEM	Transmission Electron Microscopy
EELS	Electron Energy Loss Spectroscopy
SAD	Selected-Area-Diffraction
EDS	Energy Dispersive X-Ray Spectroscopy
SEM	Scanning Electron Microscopy
SPM	Scanning Probe Microscopy
AFM	Atomic Force Microscopy
RMS	Root Mean Square
PFM	Piezoelectric Force Microscopy
VPFM	Vertical Piezoelectric Force Microscopy
LPFM	Lateral Piezoelectric Force Microscopy
SS-PFM	Switching Spectroscopy Piezoelectric Force Microscopy
PFS	Piezoresponse Force Spectroscopy
FIB	Focused Ion Beam
EB	Electron Beam
EBDW	Electron Beam Direct Writing
Ac	Alternating Current
Dc	Direct Current
TGA	Thermogravimetric Analysis
DTA	Differential Thermal Analysis
DSC	Differential scanning calorimetry

SQUID	Superconducting Quantum Interference Device
ZFC	Zero Field Cooled
FC	Field Cooled
CSD	Chemical Solution Deposition
CVD	Chemical Vapor Deposition
MOCVD	Metalorganic Chemical Vapor Deposition
PVD	Physical Vapor Deposition
EISA	Evaporation-Induced Self-Assembly
LCT	Liquid Crystal Templating-based method
CSA	Cooperative Self-Assembly-based method
CMC	Critical Micellar Concentration
PS-*b*-PEO	Polystyrene-*b*-poly(ethylene oxide)
MW_{PS}	Polystyrene Molecular Weight
MW_{PEO}	Poly(ethylene oxide) Molecular Weight
MW_{PB}	Polybutadiene Molecular Weight
IUPAC	International Union of Pure and Applied Chemistry

CHAPTER 1

Context, state of the art, motivation and objectives

Index

1.1 Context

Nowadays Microelectronics Industry is one the best representations of the fast development of technology with continuous search for improved performance based on low-cost processing technologies. This trend was first predicted by Gordon Moore, in 1965,[1] stating the doubling of the number of transistors per integrated circuit every two years. This scaling down tendency is entitled “Moore’s Law” and is followed by all microelectronic companies to enable the integration of complex circuits on a single semiconductor substrate reducing the manufacturing costs per function and increase production as shown in the Figure 1.1.

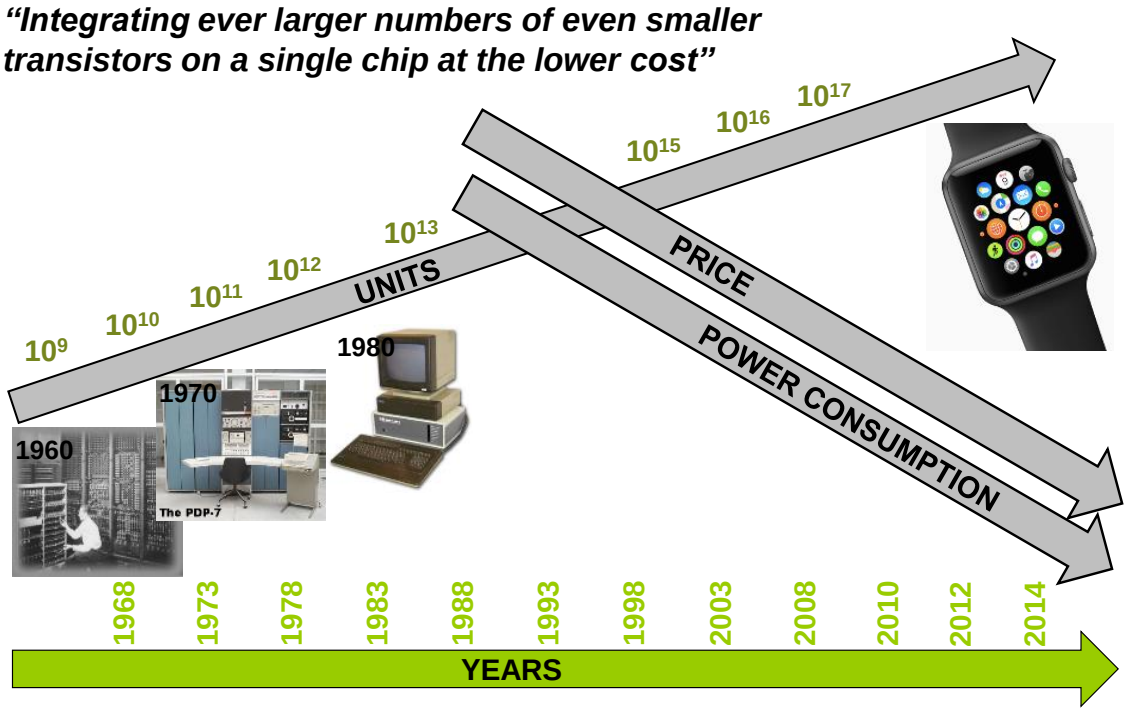

Figure 1.1: Moore's law – scaling down trend.

Several approaches have been involved, including microassembly techniques for individual components, thin film structures and semiconductor integrated circuits. Figure 1.2, shows technology node and transistor feature size as function of the year evolution for the Semiconductor Industry.

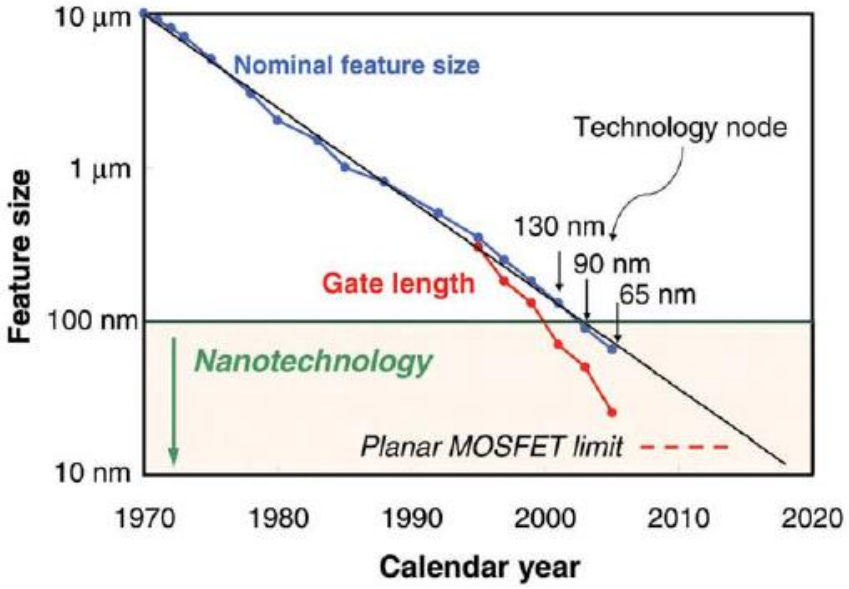

Figure 1.2: Logic technology node and transistor gate length versus calendar year. Note mainstream silicon technology is nanotechnology [adapted from reference 2].

It is important to observe from this Figure that the traditional top-down microelectronics have not only become nanoelectronics but the device dimensions are now comparable to those being explored in the new field of bottom-up nanotechnology and molecular electronics. For example, for the 0.13 µm technology node, the industry incorporated ~ 70 nm gate length transistors on average.[2] However, due to thermal and technological management constrains, the "scaling" of the device size is approaching the limit.[3] Since 2007 the Road Map for the Semiconductor Industry (ITRS) pointed a new trend, designated as "More than Moore" which precisely addresses functional diversification. Besides the size, devices should incorporate more and new functionalities, which provide additional value to the end customer. The physical device dimensions of the gate length in a transistor are expected to cross down the 10 nm threshold.

Figure 1.3 shows many possible solutions to find a promising solution that will be able to replace Silicon Semiconductor Industry. One of the most explored solution for this problem consist in to radically alter the configuration and substitute this classical two dimension (2D) memory cell structure by a completely new one based on a three dimension (3D) structure cell design.[3]

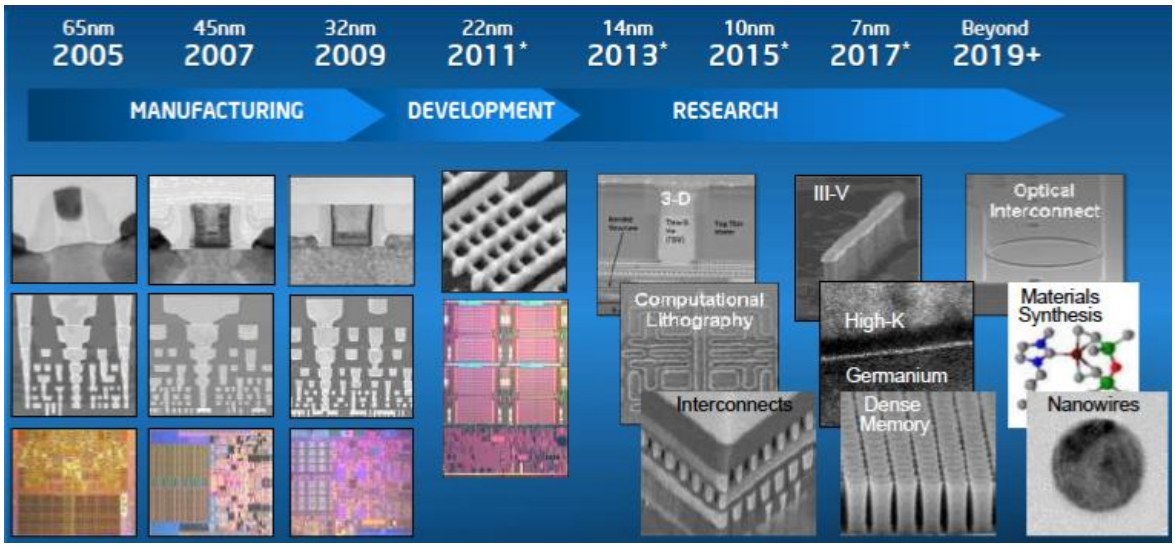

Figure 1.3: Research of many possible solutions to find a promising solution that will be able to replace silicon semiconductor industry [adapted from 4].

Although this approach is interesting, another current promising solution for an increased functionality consists in the use of multiferroics (MF) based materials

systems. Indeed, MF materials can be a promising strategy to incorporate more and new functionalities to devices, since this class of materials presents the coexistence of at least two ferroic orders: ferroelectric (FE), ferromagnetic (FM), or ferroelastic in a unique material, Figure 1.4.

In the FM materials, upon the phase transition with symmetry breaking from a paramagnetic to a FM phase a spontaneous magnetization is created. In this case, T_C is known as the Curie temperature. Ferromagnetism is the physical phenomenon widely known in permanent magnets. Applications such as electromagnets and hard disk drives are based on this phenomenon. Similarly, for FEs below the transition temperature spontaneous dipole moments are created along one of the axis of the unit cell that as a whole may generate important polarization values without an applied field, justifying some of the most important electrical properties of FEs. Examples of applications are FE random access memories, actuators, sensors and transducers.

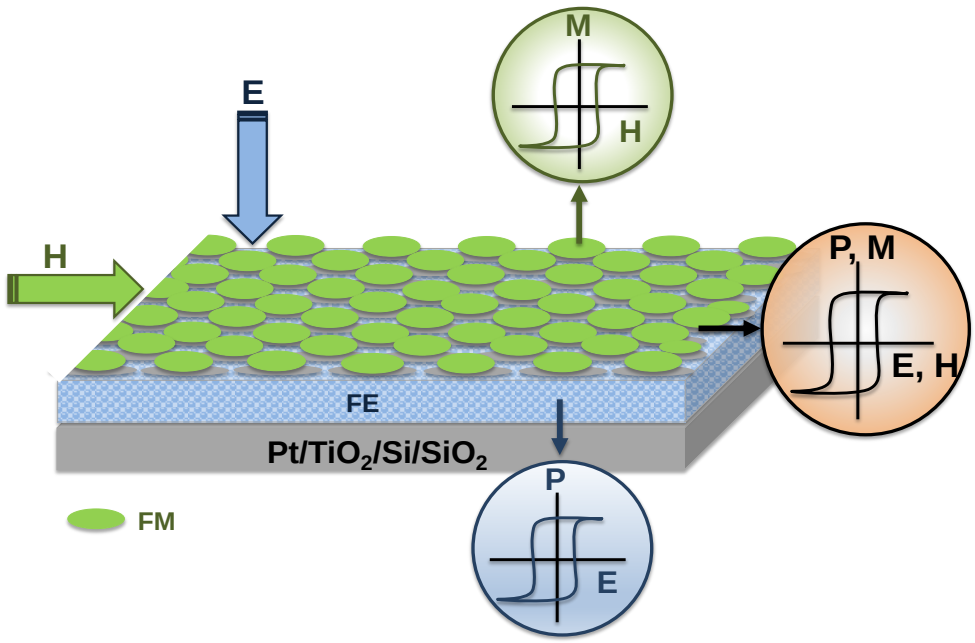

Figure 1.4: MFs materials showing coexistence of FM and FE ordering.

In the form of thin films, MFs can be used in devices based on magnetoelectric coupling, such as spintronic devices, tunnel magneto resistance sensors and spin valves with electric field tunable functions.[5] Besides that, these materials can also offer the possibility of fabricating a new type of storage devices combining the best qualities of FE random access memories (FeRAMs) and magnetic random access memories

(MRAMs), as fast low-power electric write operation, and non-destructive magnetic read operation.[6,7] However, currently, MF materials coupling FE and FM orders have only potential applications in multi-state data storage if the ferroic orders switch independently, or in electric-field controlled spintronics if the magnetoelectric coupling is strong.[8,9]

The development of MF materials and devices is in part a consequence of the development of high-quality FE thin films. Depending on the application, the thickness of the FE films plays also an important role. For example, for tunnel junction devices the required thickness is <10 nm.[10] It is well known that upon reduction of the physical dimension of the FE thin films, the change in the physical properties associated with size reduction become extremely difficult to characterize and understand.[11] In the last decade, the FE properties have been explored for many nanosized materials, proving that ferroelectricity can be present in ultra-thin films, and the spontaneous polarization can be sustained in a material till few tens of nanometers.[11,12]

Generally, two classes of MFs are considered: single-phase MFs and nanocomposite MFs.[13,14] Single-component MFs, also called intrinsic MFs, are characterized by the coexistence of ferroelectricity and magnetism in a single crystallographic phase. Within the nanocomposite MFs, three main architectures of nanocomposite MFs have been studied, Figure 1.5.

The nanoparticulate MFs are formed by dispersion of FM nanoparticles in a FE matrix (0-3 geometry). Horizontal multilayered thin film composites consist of alternating layers of FE and magnetic phases and are named 2-2 type. Usually both 0-3 and 2-2 composites exhibit a weak magnetoelectric effect due to large in-plane constrains from the substrate. The vertical heterostructured (1-3 type) composite consist of vertical structures of one of the ferroic phases embedded vertically within the other phase.

Currently, the main problem of single-phase MFs lies on the magnitude of the MF response usually with an insufficiently high magnetoelectric coupling for applications.[13,14] For this reason at this time the MF community believes that in order to obtain an applicable MF it is important to engineer multiphase composites.

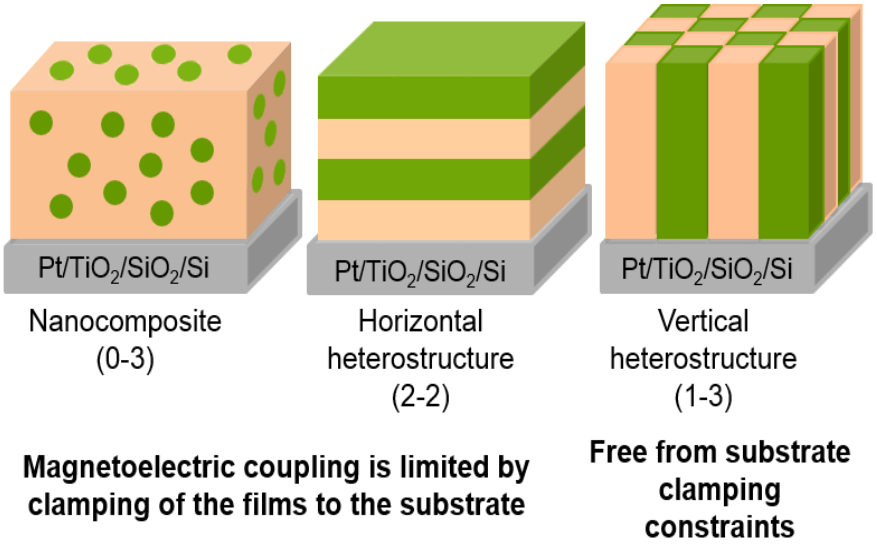

Figure 1.5: Schematic illustration of three kinds of magnetoelectric composite nanostructures: particulate nanocomposite (0-3) films with magnetic particles (0) embedded in a FE film matrix (3); horizontal heterostructure (2-2) with alternating FE (2) and magnetic (2) layers and vertical heterostructure (1-3) with one-phase nanopillars (1) embedded in a matrix of another phase (3). The Pt(111)/TiO_2/SiO_2/Si(100) is the used substrate (Pt - platinum, TiO_2 - titanium oxide, SiO_2 - silica and Si - silicon).

Vertical heterostructured composites seems to be the most promising heterostructure since this heterostructure presents low substrate-imposed mechanical clamping and large interfacial surface area which allows achieving, theoretically, strong magnetoelectric coupling. Recent reports describe magnetoelectric thin films as being at an infant stage and emphasize the need to explore vertical nanostructures with long-range order and insuring a precise control of each ferroic phase composition, atomic arrangements and interfaces.[10,15,16,17,18] It is crucial to achieve magnetoelectric films presenting room-temperature coupling at a low-cost allowing their mass-production and application in a wide variety of applications.

1.1.1 Contents of the Thesis

This Thesis is divided in eight chapters. The present chapter (Chapter 1) presents the context, a detailed introduction about FE, FM and MF materials as well as their application in electronic devices. In addition, this chapter includes a literature review on the FE, FM and magnetoelectric behaviour at the nanoscale and in nanostructures.

Chapter 2 describes the experimental details carried out along the work, including the characterization techniques and used conditions. Specific experimental conditions are detailed in Chapters 3 to 7 for each composite and nanostructure. The results and respective discussion are presented in chapters 3 to 7.

Chapter 3 reports the role of the porosity on the microstructure development and phase evolution of lead titanate porous thin films. It also establishes a relation between nanoporosity (pores with diameter of ~ 50 nm) and the electrical properties at the nanoscale. A theoretical study on the effect of porosity based on Finite Element Model (FEM) will be presented.

Chapter 4 is dedicated to the study the micelles of block-copolymer in a solution of $BaTiO_3$ as well as the effect of different parameters such as: solution heating, addition of inorganic precursors / organic solvent and solution aging time on the micellization process. The influence of the block-copolymer block dimensions on the microstructure; phase crystallization, piezoelectric and FE properties will be also discussed.

Chapter 5 is focused on the preparation of chemical designed MF nanocomposite films using $BaTiO_3$ nanoporous thin films as porous matrix for the functionalization (in this Thesis the functionalization step not involves covalent bonds) with cobalt FM nanoparticles through eletrochemical deposition.

Chapter 6 describes the preparation of the nanopatterned porous thin films (thin films with very well-ordered porous array and with pore diameter below 100 nm) of different compositions, $PbTiO_3$, $BiFeO_3$ and $CoFe_2O_4$. The structural characterization as well as the physical properties (electrical and magnetic) are reported depending on the composition in study.

Chapter 7 presents a proof of concept of a potential way to functionalize $BaTiO_3$ nanopatterned porous thin films with magnetic nanoparticles. The results of some structural and magnetic characterization are described.

General conclusions are presented in Chapter 8.

1.2 State of the art

The intent of this section is to provide a background on the current knowledge of the most relevant topics such as: FE, FM and MF materials, top-down and bottom-up synthesis approaches and porous / nanostructured ferroic materials. The basic concepts and definitions of ferroelectricity, piezoelectricity, ferromagnestim and MF coupling are introduced, as well as a brief review about the size effects on ferroic behaviour. Details on the two main synthesis approaches, top- down and bottom up, used for the fabrication of nanostructured materials, are also included. Significant relevance will be given to the preparation of nanoporous ferroics thin films by evaporation-induced self-assembly (EISA). The section ends with a summary of the presented concepts, showing our contribution on the preparation and characterization of nanoporous ferroics thin films, which can be used in electronics applications due to their functional properties.

1.2.1 Ferroic materials

Ferroic materials reflect the ability of a material to perform a certain function under a determined stimulus and are usually related to materials whose "function" is associated with their electric, magnetic, and / or optical properties. This group of materials include dielectrics, ferroelastics, pyroelectrics, piezoelectrics, FEs, FE relaxors, incipient FEs, semiconductors, ionic conductors, superconductors, electro-optics, magnetic and MF materials. Ferroic materials can be applied in medical diagnostics as ultrasonic imaging, aerospace as accelerometers and micro-positioners, automotive as solid state piezoelectric fuel injectors, and chemical and process control, which requires the use of thermal, strain and force sensors. The employment of functional materials in such applications is due to their unique properties, such as spontaneous polarization, piezoelectricity, superconductivity and magnetoresistance. All these properties are directly dependent on the preparation process, chemical composition and crystallographic structure.[19] Typically functional materials possess spinel (denoted A_2BX_4) or perovskite (designed ABX_3) structures. Figure 1.6 exemplifies compositions and functionalities of different perovskites.[20]

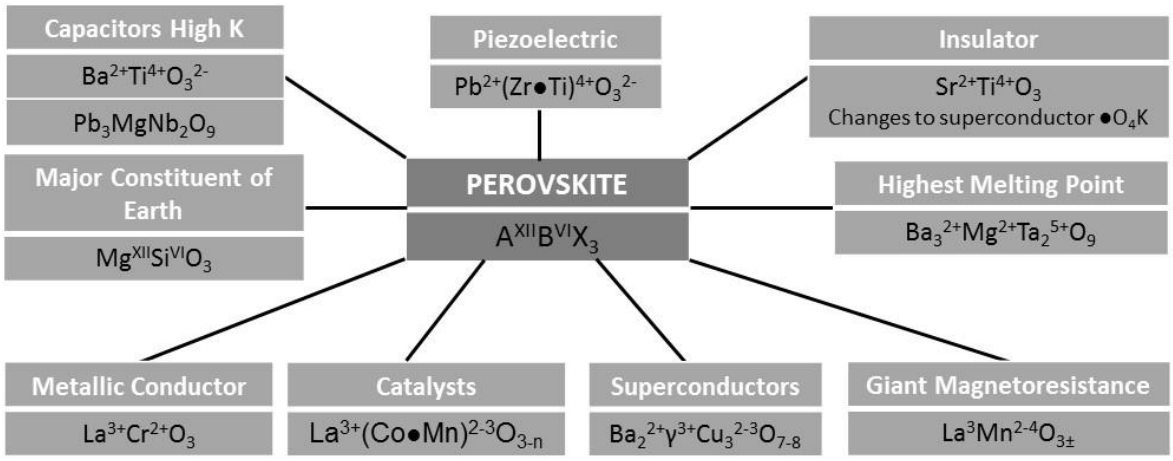

Figure 1.6: Perovskite – the ultimate multifunctional structure [adapted from reference 20].

1.2.2 FE materials: Perovskite structure and phase transistion

FE materials are nonlinear dielectrics that have permanent dipoles, which interact with each other giving up to a net polarization in the absence of an applied electric field. The FE term comes from the analogy with ferromagnetism, however actually FEs rarely contain iron. For a material to be FE, its structure should be non-centrosymmetric. This is the structural requirement for the ferroelectricity. There are a total of 32 different symmetry point groups, 21 of which do not possess a center of symmetry, as shown in Figure 1.7.[21]

Within the non-centrosymmetric groups we can find materials presenting piezoelectric, pyroelectric and FE properties. These materials can crystallize under different structures as corner sharing oxygen octahedral or perovksite structure (ABO_3); bronze tungsten ($A_2B_2O_6$); pyrochlore ($A_2B_2O_7$) and bismuth-layer ($Bi_4Ti_3O_{12}$). The perovksite is the most important group due to its particular properties having a wide impact in several applications, mainly in microelectronic devices.[19,21]

Perovskite is the name for a structural family besides being the name for a particular mineral with the composition, $CaTiO_3$. The ideal perovskite has a very simple arrangement of ions and is defined as ABO_3 structure, where A and B represent a cationic element or a mixture of two or more elements, Figure 1.8. This ABO_3 structure is a cubic structure with space group *Pm*3m, where the A atoms are located at the corners and the B atoms at the center of the cube. The O is placed at the centers of the

twelve cube edges, giving corner-shared strings of AO_6 octahedra, which extend infinitely in three dimensions.

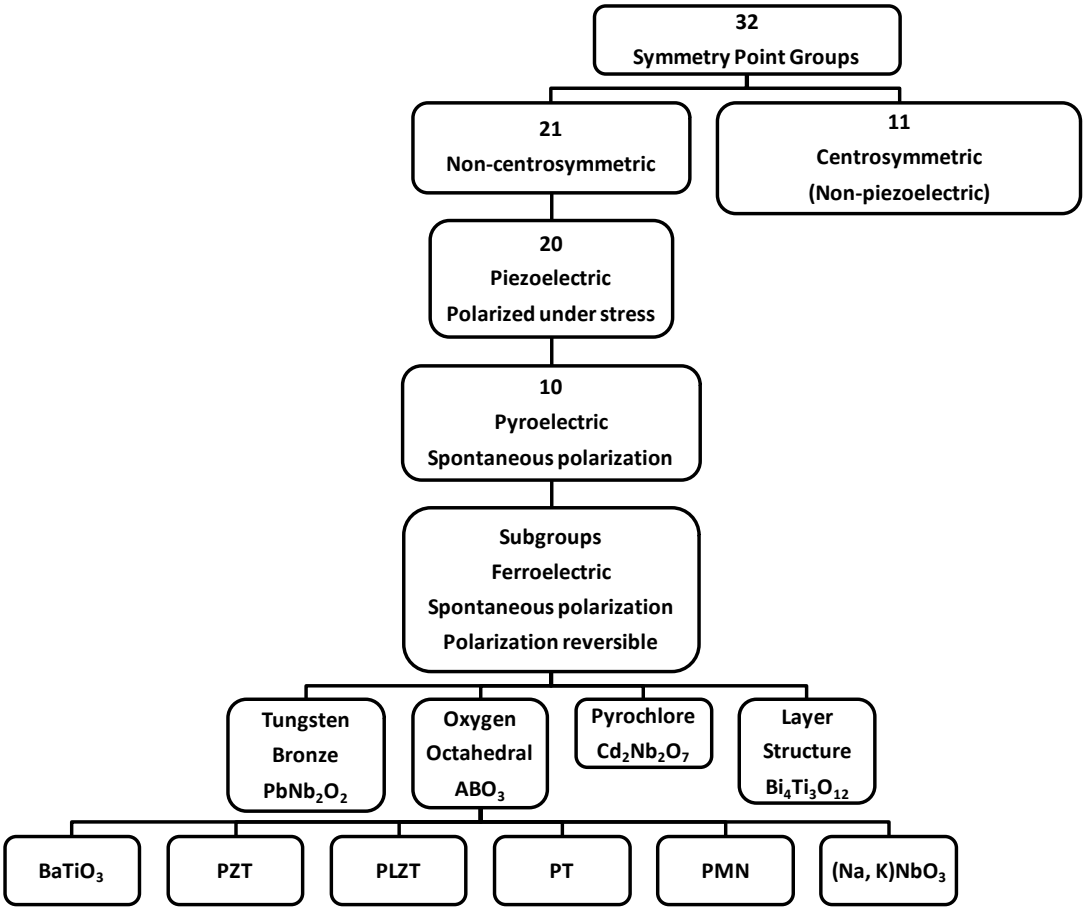

Figure 1.7: Interrelationship of piezoelectrics and subgroups on the basis of symmetry [adapted from reference 12].

The AO_6 octahedra are perfect with 90 ° angles and six equal A-O bonds. Each B atom is surrounded by twelve equidistant O atom.[20] As the O atom has a lower-symmetry coordination environment, each O atom is adjacent to 2B atoms and 4A atoms. However, the A and B cations can change the position staying the B atom in the corners of the cube and A atom in the center. The O atoms are always located at the midpoint of each edge, Figure 1.8.[12]

In 1945,[22,23] FE properties were identified in the $BaTiO_3$ perovskite structure characterized by the appearance of spontaneous polarization (P_S) when cooling below the Curie temperature (T_C) and by the switching of P_S when reversing the electric field.

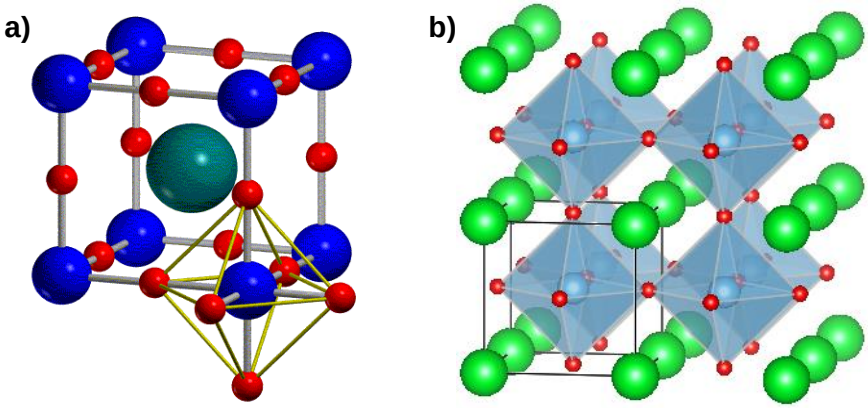

Figure 1.8: Perovskite (ABO_3) structure: a) corner-shared octahedra b). assemble of 8 unit cells [adapted from reference 24].

At high temperatures, $BaTiO_3$ structure is a paraelectric centrosymmetric cubic structure, (*Pm3m*), Figure 1.9. Below T_C, at 130 ºC, the displacement of the titanium ions located at the center of the unit cell occurs with transformation of the cubic centrosymmetric into FE tetragonal structure (P4mm), which is non-centrosymmetric. This phase remains stable until 0 ºC, where a second transformation into FE orthorhombic phase (*Amm*2) takes place. The last transition occurs at -90 ºC, forming a rhombohedral phase (*R*3*m*). Each transition corresponds thus to a structural distortion, which is accompanied by small atomic displacements of the Ti ions relative to the oxygen octahedron network, Figure 1.9.[12,25]

However, it is important to point out that the $BaTiO_3$ was not the first FE material to be found. Rochelle salt with a more complex structure ($NaKC_4H_4O_6.4H_2O$) was the first material in which FE properties were reported back in 1920.[24] Rochelle salt possess the orthorhombic structure in the paraelectric phases and monoclinic structure in the FE phase. Nevertheless, as shown later by Valasek,[24] Rochelle salt exhibits instability against dehydration, structural complexity, poor mechanical properties, low Curie temperature and weak ferroelectricity which impeded any significant applications.[25]

After $BaTiO_3$, many other FE materials with a perovskite type structure, including lead zirconate titanate ($PbZr_{1-x}Ti_xO_3$, PZT); $BaTiO_3$ solid solution as $Ba_{(1-x)}Sr_xTiO_3$ and alkali based niobates as $KNbO_3$ were developed and used for several applications. The lead based perovskites have up to now some of the highest

piezoelectric coefficients and relative high FE transition temperature, presenting excellent piezoelectricity at room temperature.[19]

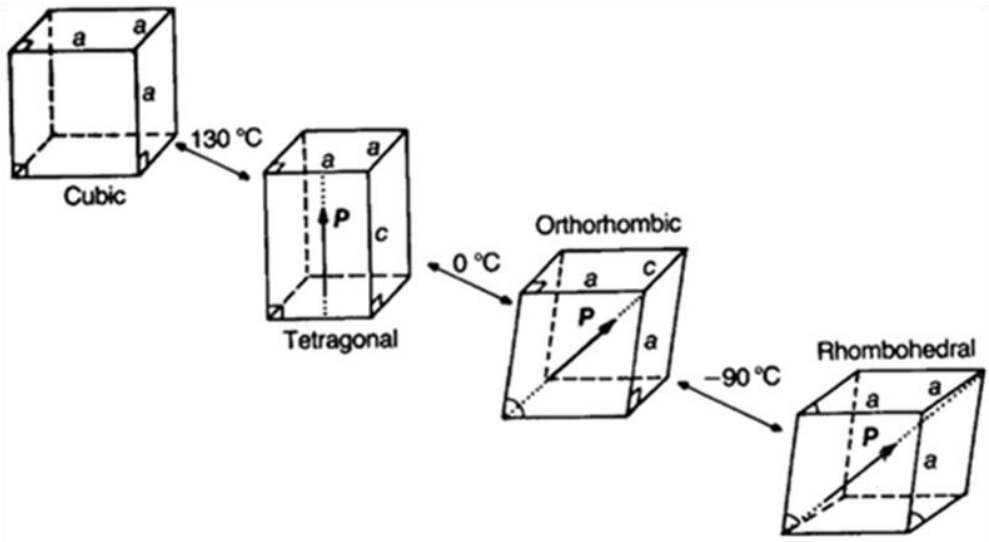

Figure 1.9: Structural properties of single-crystal $BaTiO_3$: unit-cell distortions of the polymorphs [adapted from reference 26].

The physical properties of perovskites are extremely diverse depending on the composition, structure and cationic ordering. These materials can be metallic or insulating and exhibit many different types of structural and ferroic orders.[12]

Basically, as it is shown in the Figure 1.7, FE materials are a special category of pyroelectrics (materials with spontaneous polarization due to only the non-centrosymmetric structure) in which the direction of P_S can be switched by the application of an electric field of magnitude lower than the dielectric breakdown of the material, exhibiting thus piezoelectricity, high non-linear optical activity, and non-linear dielectric behavior.[12,27] One of the main features of FE materials is thus P_S which is the consequence of spontaneous dipole moment created in the FE crystal by small displacements of the ions off their centrosymmetric position in the unit cell. The value of the P_S can vary over several orders of magnitude depending on the material as shown in the Figure 1.10.[28]

Another fingerprint of most of the FE materials is a dielectric anomaly at T_C, due to a distortion in the crystalline lattice as the phase structure changes. This distortion provokes an anomalous behavior in the thermodynamic properties, including dielectric, elastic, optical, and thermal constants. A maximum in the dielectric permitivity is often

observed at the T_C, where the transition between centrosymmetric to non-centrisymmetric is observed.[29]

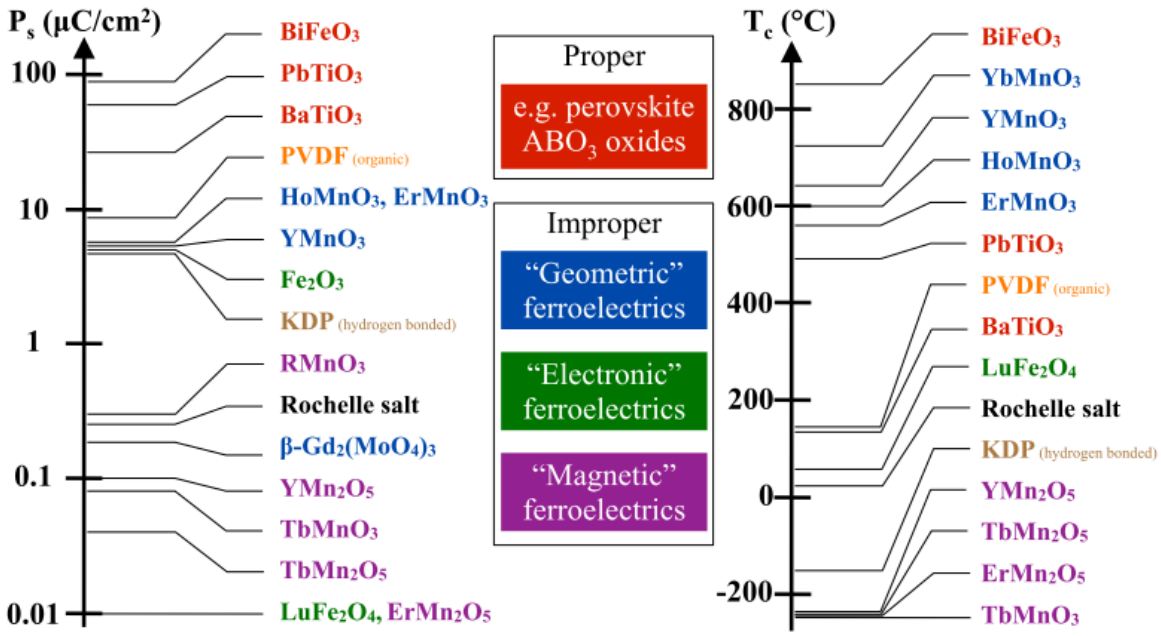

Figure 1.10: FEs include a wide range of compounds, with a multitude of structures and compositions, both organic and inorganic. Their defining and technologically relevant properties –P_S and T_C – cover a wide range of values [adapted from reference 28].

Figure 1.11 shows the variation of relative permittivity with the temperature for $BaTiO_3$. In most of FE materials, the temperature dependence of the dielectric permittivity above T_C can be described by the Curie-Weiss law:

$$\varepsilon_r = \varepsilon_0 \frac{(1+C)}{(T-\theta)} \qquad \textbf{Eq.1.1}$$

where, ε_r is the dielectric permittivity of the materials, ε_0 is the dielectric permittivity of vacuum, C is the Curie-Weiss constant, T is the temperature and θ is the Curie-Weiss temperature, which is in general smaller than T_C. For first order transitions $\theta < T_C$, while for second order phase transitions $\theta = T_C$.

As mentioned before and shown in Figure 1.7, all FEs are pyroelectric and piezoelectric but a piezoelectric or a pyroelectric is not inevitably a FE.[19] The piezoelectric materials are materials that become electrically polarized when subjected to a mechanical force.

The piezoelectric effect was firstly observed by Jacques and Pierre Curie in 1880 in crystals such as quartz, tourmaline and Rochelle salt. These crystals when subjected to a mechanical force became electrically polarized and the degree of polarization was proportional to the applied stress.

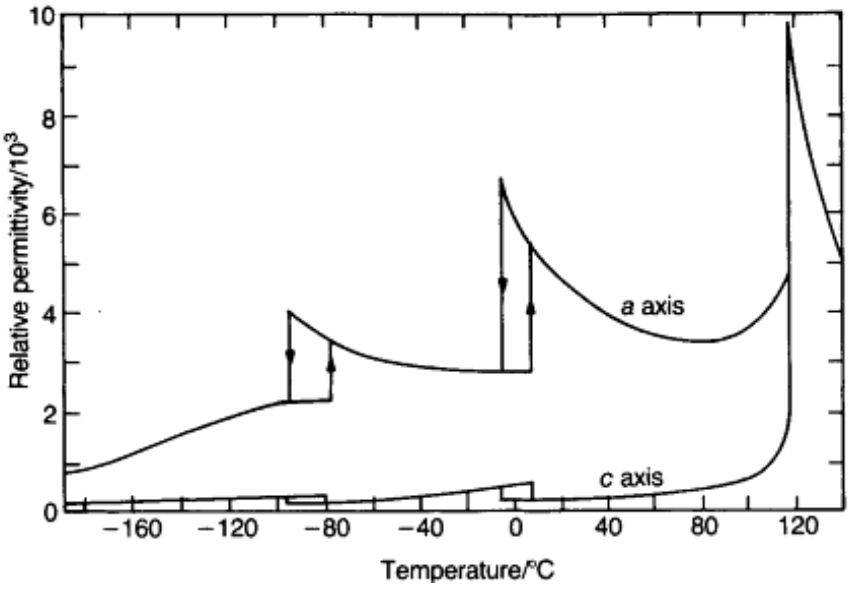

Figure 1.11: Relative dielectric permittivities measured along *a* and *c* axis as a function of temperature for $BaTiO_3$ [adapted from reference 26].

In addition, piezoelectric materials also show the inverse effect; i.e. a geometric strain is produced by the application of an electric field. Thus, the name "piezoelectric" derived from the combination of the two words: piezo and electric, where the prefix piezo comes from the Greek word meaning press. As a result, the piezoelectricity is the generation of electricity that results from a mechanical force, or vice versa.

1.2.2.1 Ferroelectricity

In the following FE structures, which are characterized by an expansion of the original cubic lattice in the direction of P_S and a contraction in the perpendicular direction, as shown in Figure 1.9, the polar axis is aligned respectively along [100], [110] and [111] directions corresponding to the direction of the atomic displacements with respect to their position in the cubic reference structure.[21,28] In $BaTiO_3$ phase transitions from cubic to tetragonal to orthorhombic to rhombohedral are observed with the low temperature polarization along the [111] direction while in $PbTiO_3$ the phase

transition to a tetragonal phase occurs below 490 ºC, with the polarization along the [001] direction.[30] According to Cohen and Krakauer[30] the presence of ferroelectricity in $BaTiO_3$ and $PbTiO_3$ perovskite structure is due to the Ti 3d-O 2p hybridization, which is fundamental for stabilizing the FE distortion. In $BaTiO_3$, the Ba-O interaction is largely ionic in nature while in $PbTiO_3$, there is hybridization between the Pb 6s and O 2p electrons which leads to a large Pb polarizability and a strain that stabilizes the tetragonal phase over the rhombohedral one. The small B cation should always be able to decrease its energy by shifting along one of the [111] directions.[30]

For the case of a tetragonal configuration, for example, there are two equivalent antiparallel polarization states along the polar *c*-axis, Figure 1.12.

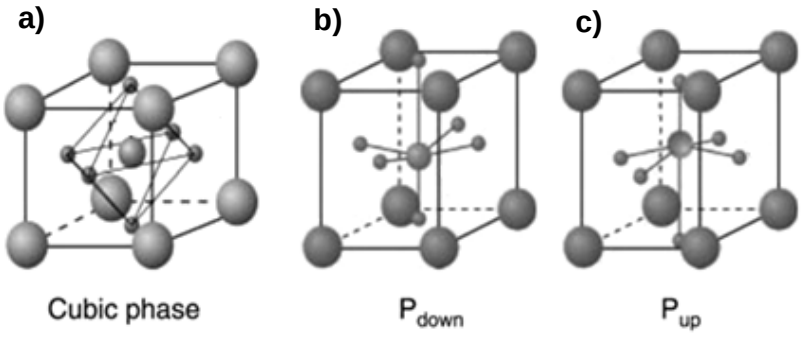

Figure 1.12: Crystal structure of the perovskite FE material: a) high-temperature, paraelectric, cubic phase; b) and c) room-temperature, FE, tetragonal phases showing down and up polarization variants, respectively [adapted from reference 31].

The relationship between the polarization and the applied field is described by an hysteresis loop, which shows the non-linear behavior of these materials.[19,21,28] The hysteresis loop is similar to the one exhibited by the FM materials, whereas FE materials have also domains and show a hysteretic response, polarization and electric displacement when the electric field is applied.[12,25,31] An hysteresis loop for a FE material is depicted in Figure 1.13; a low electric field provokes a linear and reversible increase of the polarization as the field increases. The further increase of the polarization is non-linear and several points are of relevant importance to take into account: P_S and remanent polarization (P_r), coercive field (E_C), and the general shape of the loop. The polarization is considered saturated when all of the dipole moments are aligned in the direction of the applied field, and a further increase in the applied voltage

will not increase further the polarization. At this polarization value, the linear extrapolation of the curve back to the polarization axis (zero field (E=0)) is equivalent to Ps.

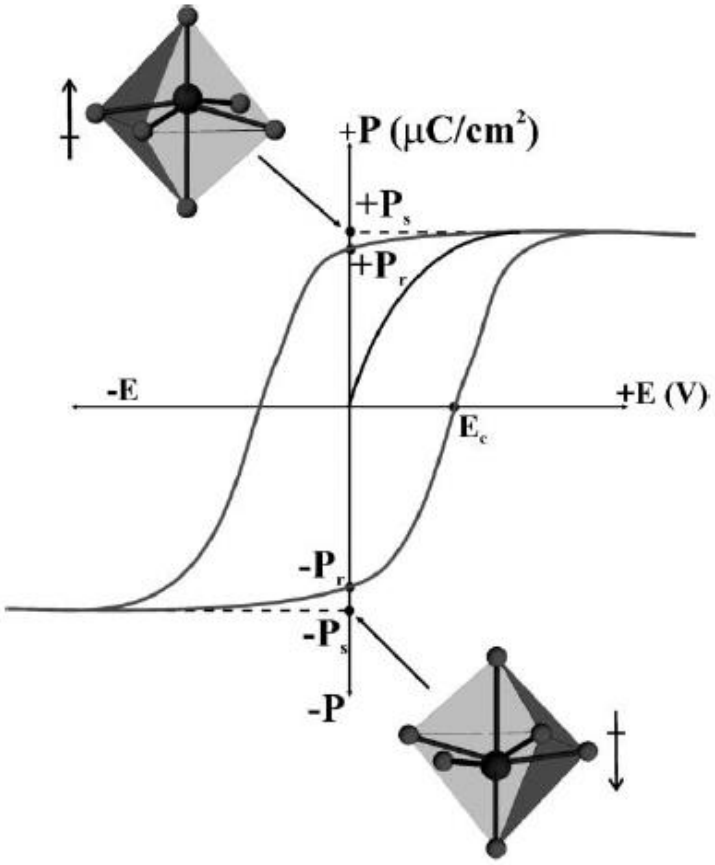

Figure 1.13: FE hysteresis loop - Polarization (P) as function of the applied voltage (E). Ps and Pr are spontaneous polarization and remanent polarization, respectively. E_C corresponding to the coercive field [adapted from reference 29].

As the applied voltage is reduced from its maximum positive value to zero, some dipole moments remain aligned, and a Pr is observed. To cancel this value, a field in the opposite direction and of magnitude, and designated as coercive field, E_C should be applied. At this field required to reduce the polarization to zero all the domains are randomly oriented. As the applied voltage crosses the range from its maximum positive to negative values, P_S and P_r, will be observed (one in positive direction and other in negative direction) as shown in Figure 1.13. The phenomena involved in the design of the complete hysteresis loop is designated by switching.[29] This mechanism typically starts by the nucleation and growth of inverted domains with an external electric field

inducing the domain-wall motion. Consequently the domain volumes suffer a modification as well as the total polarization, whereas structurally all the dipole moments are switched from the positive to the negative direction and the area contained within the loop is related to the energy required to cause the polarization to switch direction. This energy as well as the E_C are dependent on the composition of the material as well as on grain size and consequently on the crystallization degree. The temperature is another parameter that can affect the format of the hysteresis loop. As temperature decreases, the loops become broaden and E_C increases corresponding to a larger energy required for domain reorientation. On the contrary, as temperature increases the E_C also decreases until T_C is achieved, with disappearance of the hysteresis loop. The material becomes paraelectric. Linear dielectrics do not show hysteresis loop in the presence of an external electric field.

In addition to the hysteresis loop, the polarization switching by an external electric field leads to a strain-electric field hysteresis as shown in Figure 1.14. The shape of this loop resembles a butterfly and it is often referred as butterfly loop. At low electric fields, only a linear strain versus electric field relationship is obtained due to the converse piezoelectric effect. The slope of the curve near to the zero electric field represents the piezoelectric modulus (d_{33} for the longitudinal strain). As the field increases the strain is no longer linear with the field due to domain switching.[21]

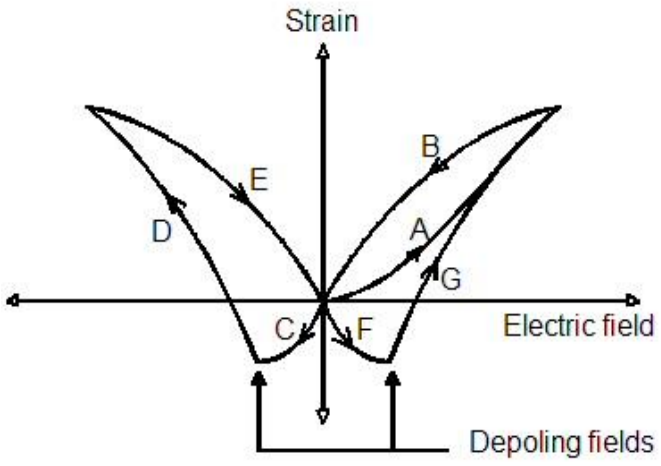

Figure 1.14: FE hysteresis loop - strain as function of the applied voltage [adapted from reference 32].

1.2.2.2 FE domains

The domains in FE materials occur in order to minimize the electrostatic energy related to the polarization interaction with the depolarizing field, Figure 1.15. The depolarizing field is an immediate consequence of the onset of P_S, which lead to the appearance of an apparent surface charge density and consequently to a depolarizing field (E_D). Thus, within a domain all the dipoles are aligned in the same direction, differing from the direction of the adjacent domain. These adjacent domains are separated by interfaces called domain walls with normally width on the order of one lattice parameter (~ 10 - 100 Å depending of temperature and crystal purity).

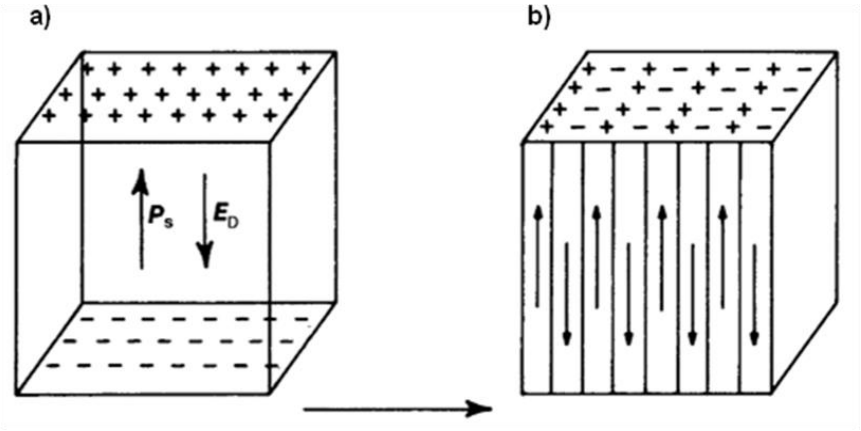

Figure 1.15: a) Surface charge associated with spontaneous polarization and b) formation of 180 º domains to minimize electrostatic energy [adapted from reference 32].

The division into domains only occurs while the reduction in magnetostatic energy is greater than the energy required to form the domain wall. The energy associated to a domain wall is proportional to its area.[32]

Inside the domain wall the dipole/strain orientation changes gradually from one domain orientation to another, Figure 1.16. These domain walls are thus transition regions in which the direction of polarization changes. As a result of that, the surface consists of a pattern of areas (domains) with polarization in opposite and parallel orientation, which can be transformed into a single domain by applying a field parallel to one of the polar direction. This process is called poling.

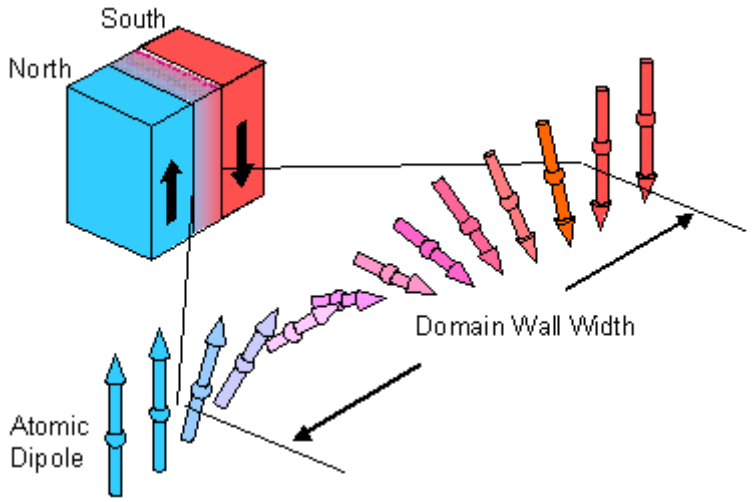

Figure 1.16: Schematic representation of a 180 º domain wall. The domain walls are transition regions in which the direction of polarization changes [adapted from reference 33].

In an ideal FE crystal, P_S can be distributed equally among several crystallographic directions of the centrosymmetric structure. However, for a FE material with a tetragonal structure, the polarization can be only oriented along two equally perpendicular crystallographic directions, giving rise to two types of domain walls, 180º or 90º walls. This is only possible for materials that do not have a strong uniaxial anisotropy, and the neighbouring domains do not have to be at 180 º to each other. The 180º walls separate adjacent domains with antiparallel oriented polarization (up and down polarization), and the 90º walls separate domains with equally perpendicular oriented polarization. The 90° walls are both FE and ferroelastic domain walls, whereas these separate regions with different orientation of the polarization and strain. The net polarization depends on the difference in volumes of the two domain orientations. If the volumes are equal, the material will not exhibit a net polarization. On other words, if the dipoles are all oriented in an antiparallel way, up and down directions, the total polar moment is zero. However, these antipolar materials can convert to a FE state when subjected to a sufficiently high electric field (poling process).[19] The motion of the domains misoriented by 180 ° are more easily switched than 90 ° domain walls since no lattice physical deformation is required. In opposite to the 180 º walls the 90 º walls can only be induced by the ferroelastic effect and / or applying a compressive stress along the polar axis without an accompanying electric field. An example of 90 º walls appearance is when the $BaTiO_3$ and / or $PbTiO_3$ structure is cooled through the T_C, in

which the individual crystallites are subjected to large mechanical stresses. The defects and internal strains within the crystallites hinder the movement of domain walls.

1.2.2.3 Ferroelectricity at the nanoscale: size effects

Nowadays with the current demand for ultrahigh density FE data storage applications, scaling the dimension of FEs down to the nanometer scale is the trend. It is well known that upon reduction of the physical dimension of the FE materials, the change in physical properties associated with size reduction becomes extremely difficult to characterize and to understand due to a complicated interplay between structures, surface properties, strain effects from substrates, domain nucleation and wall motions.[34] The ferroelectricity becomes thus unstable due to the intrinsic and extrinsic effects. The intrinsic effects include depolarization effects resulting from imperfect screening of divergences in the polarization, for screening either by domain formation or by interfacial compensation charge, the absence of long-range cooperative interactions and elastic constraints.[28] Nonstoichiometry, domain structure, free carriers, impurities defects, planar defects, crystal quality as well as interface phenomena are included in the extrinsic effects group. All these effects can modify and impair the FE properties. Electromechanical effects can shift the FE phase transition temperatures by tens or even hundreds of Celsius degrees, and rescale various properties which make FEs so useful.[35] From this point of view and whereas the problem of critical size is very complex, several theoretical *ab initio* studies[36,37,38,39] and based on Landau theory were developed,[40,41] specially the Devonshire-Ginzburg-Landau-type phenomenological theory. During several years, Devonshire-Ginzburg-Landau theory was successfully employed to describe many features of ferroelectricity as well as its phase transitions on a macroscopic scale. However, as the structures scaled down to the length-scales of FE coupling, the extension of the assumption theories is not trivial. An extrapolation length introduction it is always necessary and consequently the critical size below which ferroelectricity is suppressed (in small particles and thin films)[42] was predicted to be much larger than the values recently observed (few tens of nanometers).

Some results,[28,30] namely on $PbTiO_3$ films and superlattices showed that the ferroelectricity can still exist in FE films with the thickness equal to several unit cells revealing thus, that the critical size can be much smaller than previously thought. In

fact, these results reveal that ferroelectricity persists in superlattices containing only one-unit-cell-thick layer of FE embedded in much thicker non-FE.

Critical thickness for $PbTiO_3$ films using a microscopic effective Hamiltonian method was obtained from first-principles calculations.[39] The authors observed that in tetragonal films with thickness as low as three unit cells (1.2 nm) and a perpendicular polarized FE ground state significant enhancement of the polarization at the surface can be obtained and consequently the ferroelectricity persists.

Fong *et al*.[43] in 2004 reported a synchrotron X-ray study of $PbTiO_3$ as a function of temperature and film thickness for films as thin as a single unit cell. At room temperature and for film thicknesses down to three unit cells (1.2 nm), the ferroelectric phase is stable impling that no thickness limit is imposed on pratical devices by an intrinsic FE size effect. In 2006, using Raman spectroscopy, Fong *et al*.[44] determined the T_C of ultrathin *c*-axis epitaxial $PbTiO_3$ by changes in the dynamics of lattice vibrations occurred during the phase transition. The decreasing of T_C was relatively small, even for the thin films with a thickness of 1.2 nm. The absence of 180 ° stripe domains suggested that the depolarizing field is compensated by free charges at both interfaces. This result was confirmed by *ab initio* calculations that demonstrated the presence of polar ground states in the presence of ionic adsorbates. The contribution of the electrostatic energy in thin films associated with depolarization fields can be reduced by the formation of 180 ° domains, leading to the retention of ferroelectricity in films with thickness below three unit cells (1.2 nm). For thin films with the same composition, it was predicted that the *c* lattice parameter and, consequently, the tetragonality (*c/a*) decreases substantially below the crystal size of 20 nm.[45] Lichtensteiger *et al*.[45] established through an effective Hamiltonian approach that the decrease of *c/a* is related with a progressive reduction of the polarization due to an imperfect screening of the depolarizing field. Although their polarization is significantly reduced, epitaxial grown thin films with 2.4 nm of thickness (about 6 unit cells) still remain FE at room temperature.[45] Indeed some results show that the FE critical size values for $PbTiO_3$ vary considerable and are directly dependent on the preparation methodology.[11,46]

Regarding $BaTiO_3$ [37] in 2003 Junquera and Gosez using first-principle simulations estimated that the critical thickness of $BaTiO_3$ thin films is around 5 nm. In

this model the interface between $BaTiO_3$ thin films and the metallic electrodes $SrRuO_3$ was taken in to account. The authors observed that the FE properties are lost below 2.4 nm due to the depolarization electrostatic field. The theoretical prediction was experimentally proved in 2005 by Kim *et al.*[47] in $SrRuO_3$/BT/$SrRuO_3$ heterostructures on $SrTiO_3$ substrates prepared by pulsed laser deposition.

In 2009, Tenne *et al.*[48] demonstrated the effect of film thickness on the T_C in $BaTiO_3$ films as thin as 1.6 nm by UV Raman spectroscopy. The authors showed that interplay between strain and film thickness (1.6 to 10 nm) allows T_C tuning from 70 to about 925 K. T_C as high as 925 K was observed in 10 nm films, which is over 500 K above the bulk $BaTiO_3$ value. These results were supported by synchrotron X-ray scattering, which indicate the presence of 180 º domains below T_C, and thermodynamic phase-field model calculations of T_C as a function of thickness.

More recently, synchrotron X-ray diffraction and high-resolution scanning transmission electron microscopy revealed the presence of crystalline domains with the long axis of the tetragonal structure oriented perpendicular to the substrate in 8 – 40 nm thick $BaTiO_3$ films with metal-FE-semiconductor structures. Using piezoelectric force microscopy, polar domains were reversibly switched with a phase change of 180 º and saturated hysteresis loops were observed.[49]

As mentioned before, the depolarization field is one of the most important problem that appears when the thickness film is below a certain value and can be partially screened by free charges. The depolarization field increases as the sample thickness is reduced and eventually it can suppress the ferroelectricity. At very small thicknesses, the physical properties are dominated by strong depolarization fields, and the thermal fluctuations and static defects play a relatively small role.[50] In the absence of free charges, a FE film can minimize its energy while preserving its polar state through: a) the formation of domains with opposite polarization; b) the rotation of the polarization into the plane of the FE thin film; and c) by formation of the heterostructures such as FE-paraelectric superlattices, in which non-FE layers may be polarized to preserve the uniform polarization state and eliminate the depolarization fields. In addition, as most of the FE materials are insulators and become single domain when the size is reduced, there is the need to include the contribution of metallic electrodes to extract only the contribution of the depolarization field. In this approach,

the thin film works as a FE capacitor in short circuit. The presence of surface molecules and the nature of the bonding at the interface can be other ways to control and retain the ferroelectricity when the sample size is reduced.[11,46]

However, sometimes thin films below a certain thickness do not display ferroelectricity due to the intrinsic / extrinsic size effects but rather due to difficulties in their preparation such as: a) appropriate substrate choice; b) presence of dead layers; c) grain boundaries and d) structural defects (oxygen vacancies which have strong influences on FE properties). Feuersanger *et al.*[51,52] reported that in stoichiometric $BaTiO_3$ films prepared by electron-beam evaporation the FE phase becomes unstable for film thicknesses below about 0.1 μm. Later using similar measurements, Slack and Burfoot[53] showed FE switching behavior in thin films prepared by flash-evaporated $BaTiO_3$ films with around 40 nm.

1.2.2.4 Applications

The knowledge of the relationships between composition, structure, processing and properties allows the cost-effective production of FE materials with enhanced performance for a certain application. In thin film form, FEs have been used for several years in rf devices and in non-volatile memories (one of the most important applications up to date).[35] Indeed, from their development in the late sixties, beginning of seventies, FE thin films have demonstrated to be promising candidates for microelectromechanical sensors. However, the practical difficulties in processing and integrate FE materials delayed their application in memory devices until 1980s. Most of these difficulties were related with the lack of reliability, fatigue of the switching cycles, imprint (the shift of the hysteresis loop along the origin axis due to self-polarization), high operation voltages and leakage currents. In mid 80s, with the advances in processing complex FE oxides and the discovery of high temperature superconductor oxides, the interest in FE memories was reborn. In 1987, the first FE memory integrated with silicon complementary metal-oxide semiconductor (CMOS) was prepared. This memory consisted of two transistors and two capacitors (2T - 2C) with the storage capacity of 512 b to 16 kb. The first FeRAM with capacity of 256 b using one capacitor - one transistor (1T - 1C) was prepared only in 1994. Since then, many efforts have been dedicated to reduce the size of the FE memory cell as well as designing new

architectures. Circuit/device technologies have been developed in such way that currently the high-speed, low-voltage operation and low-power consumption turning the non-volatile memories competitive not only with other non-volatile memories but also with the current volatile dynamic random access memory (DRAM). These later memories are used in a variety of personal and industrial applications, such as: smart cards, low power consumption devices, printers, digital cameras, digital audio, video games, mobile phones, portable computers, among others.[54] In a simple way, the working principle of FeRAM memories consists in the switching of the polarization of a polar material as FE by applying an external electric field larger than the coercive field. As the P_S is the fingerprint of FEs materials, this is used to store data in FeRAM in format "0" if the dipoles point up and "1" if the dipoles point down (binary number for digital computing) and whereas no external field is required to keep these states once reached, the memory device is called as non-volatile i.e. when the power is switched off the information is kept saved. Normally this kind of memories requires FE thin films (90 - 200 nm) due to their low coercive field and can be switched from one P_S state to other with the application of ~ 3 to 5 V.[21,55,56]

A FeRAM memory cell contains one FE capacitor and one access transistor. The information is stored in the FE capacitor and the transistor addresses the desired cell, Figure 1.17.[54]

The most known FeRAMs are Fujitsu 8-kb, 32 Mb FeRAM from Samsung both prepared with PZT and 4 Mb FeRAM made with strontium bismuth tantalate (SBT) by Matsushita.[57] $BiFeO_3$, one of the natural single-phase MF materials, is used in FeRAMs by Fujitsu. Nowadays, FE films are also used in a number of commercial, widespread products. These applications include microwave electronic components, infrared detectors, and microdevices with pyroelectric and piezoelectric microsensors / actuators.[58] According to the International Technology Roadmap for Semiconductors (ITRS), non-volatile memories miniaturization is still requiring development.[59] In order to miniaturize and enhance the properties of the memories, several efforts have been made to improve the preparation techniques as well as the microstructure. This will be described in the section 1.2.5 of this Chapter.

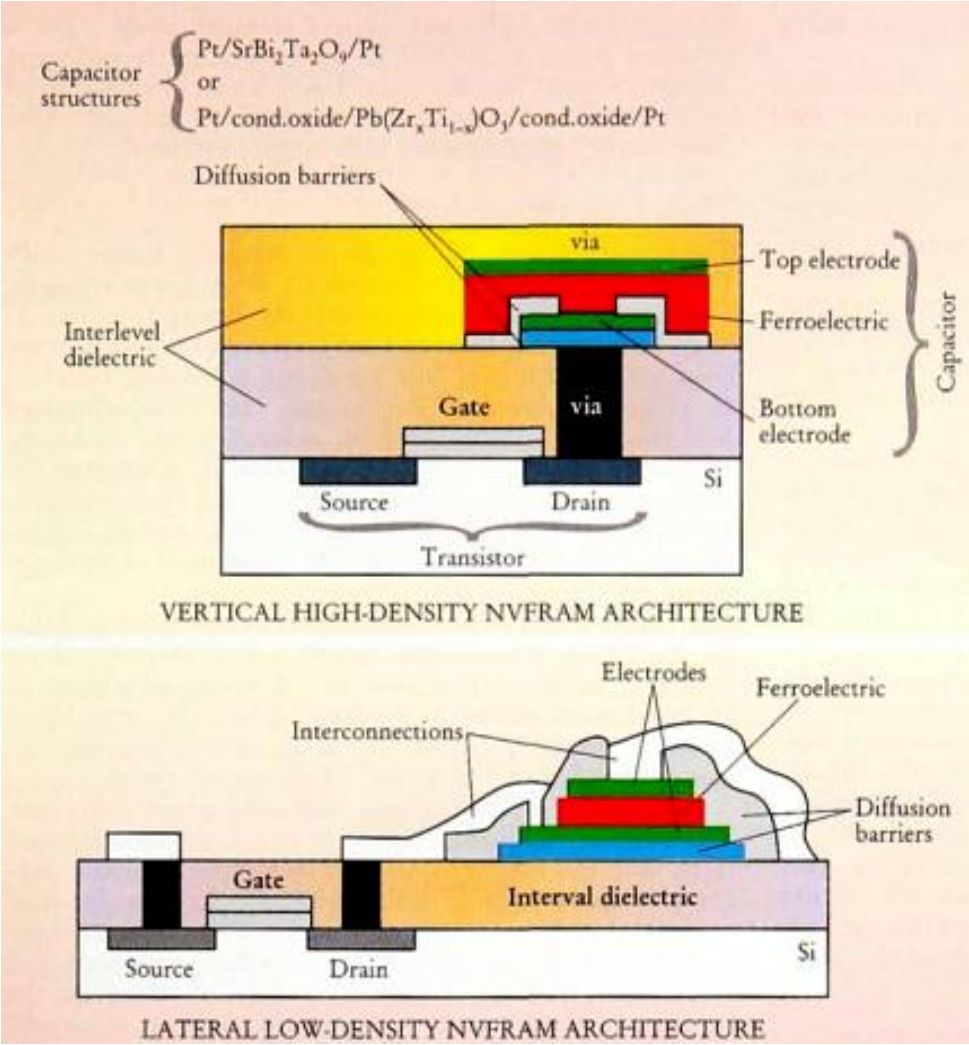

Figure1.17: Schematic diagram of two kinds of non-volatile FE random-access memory (FeRAM) architecture. The high-density architecture on top is designed for use as computer memory. The low-density architecture on bottom is for smart cards and other applications of embedded memories, such as microprocessor controllers [adapted from reference 54].

1.2.3 FM materials: spinel structure

As mentioned before, the spinel structure is another of the most known functional ferroic structures. It is characteristic of some FM materials. Similarly to FE materials, FMs suffer a phase transition from a phase in which the macroscopic magnetic moment is not present to a phase characterized by spontaneous magnetization even in the absence of an applied magnetic field. The spontaneous magnetization means that FM materials tend to concentrate magnetic flux density. Usually, the as-prepared

ferromagnets do not show macroscopic magnetization due to the presence of domains of magnetization oriented in different directions. The subsequent alignment and reorientation of the domains upon the application of a magnetic field, H, results in a hysteresis of the magnetization and flux density, B. Thus, in the presence of external magnetic field, the spontaneous magnetization of a ferromagnet can be switched through hysteric behavior (Figure 1.18). Very often there is a coupling between polarization and the shape of the unit cell. Consequently, as the FM polarization decreases with increasing temperature up to a critical Tc, the phase transition to a high-symmetry unpolarized phase takes place and the corresponding polarization order parameter is vanished. However, below Tc, the macroscopic polarization can also be vanished if the homogeneously polarized state breaks into domains (regions with oppositely oriented polarization within the sample).[25,28] Thus, according to the response to the external magnetic field, the material can be classified into: FM, paramagnetic, anti-FM and ferrimagnetic, Figure 1.19.

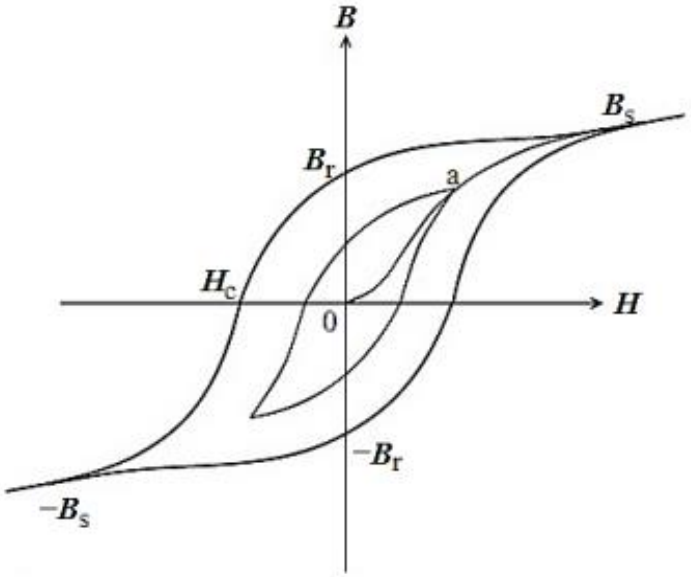

Figure 1.18: Hysteresis loop of a FM (outer curve, large saturation and residual magnetic induction, B_S and B_r, respectively) and a ferrimagnetic material (inner curve, low saturation and residual magnetic induction, B_S and B_r, respectively) [adapted from reference 60].

In FM materials, the electron spins are aligned parallel to each other at absolute zero. When the electron spins of the atoms are aligned randomly, the material is

paramagnetic, Figure 1.19. These materials, in the presence of an external applied magnetic field form induced magnetic fields in the direction of the applied magnetic field. The anti-FM behavior corresponds to an antiparallel alignment of equal moments. Antiferromagnets do not find wide application in magnetic technologies because they do not have a net overall magnetization. The term "weak ferromagnetism" is normally used to describe antiferromagnets with a small canting of the spins away from antiparallel alignment.[61] The ferrimagnetic behavior corresponds to the materials with antiparallel moments with different magnitudes, i.e. some of the dipole moments are larger than others and the material has a net overall magnetic moment.[25] So, a ferrimagnetic material exhibits also a hysteric response when an external magnetic field is applied.

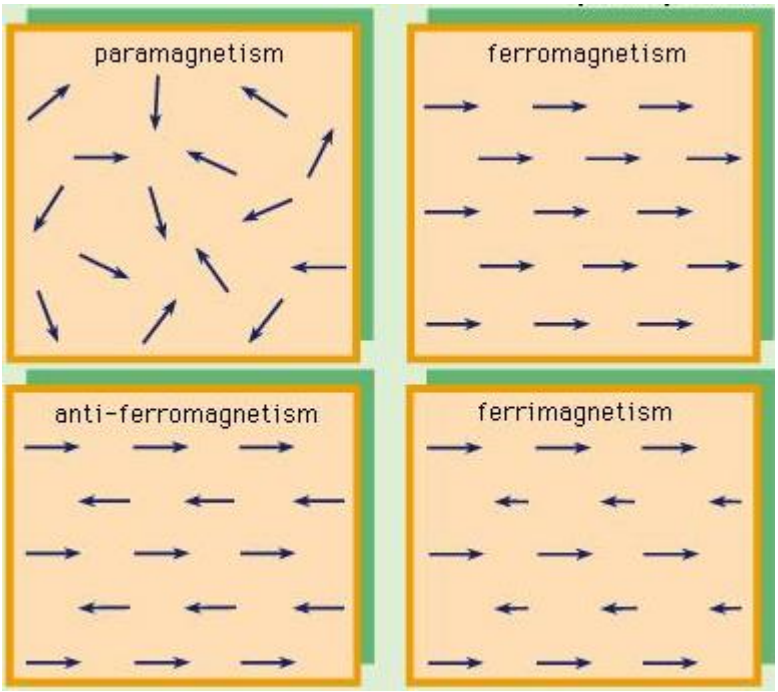

Figure 1.19: Description of the ordering of spins in paramagnetism, ferromagnetism, anti-ferromagnetism and ferrimagnetism. In FM materials, the electron spins are aligned parallel to each other at absolute zero. In opposite way, the anti-FM materials present an antiparallel alignment of equal moments. A ferrimagnetic material present antiparallel moments with different magnitudes exihibiting a hysteric response when an external magnetic field is applied [adapted from reference 62].

The switching process starts by a non-magnetized state and as the field is increased in the positive direction, the magnetic induction increases from zero to the

saturation induction, B_S (Figure 1.18). When the field is reduced to zero after saturation, the induction decreases from B_S to the residual induction or retentivity, B_r. The reversed field required to reduce the induction to zero is called coercivity, H_C.

Many FM materials have been used in a wide range of applications. Besides the conventional pure metals (Fe, Co, Ni) and rare-earth magnets, a series of compounds present significant FM properties, such as: spinels γ-Fe_2O_3, $CoFe_2O_4$ and $NiFe_2O_4$ among others.

1.2.3.1 Ferromagnetism at the nanoscale: size effect and applications

The design of nanofeatures, uniformed in size and shape at a reasonable large-range order, *i.e*. "nanopatterning", allows to extend the thin films utility as intermediate heterogeneous surfaces in the design of complex functional devices with tunable surface properties.[63,64,65] Magnetic nanopatterned surfaces have became particularly interesting systems as innovative magnetic materials and devices in different applications such as ultra-high-density magnetic storage, magnetic random access memory (MRAM), patterned recording media, magnetic switches, and ''quantum'' magnetic disks.[66,67] In the patterned surfaces, each element is a single magnetic domain, with uniaxial magnetic anisotropy so that the magnetization points in one of the only two directions at remanent magnetization and the magnetic anisotropy axis can be parallel to the plane, or perpendicular to the plane. In longitudinal thin film media, there has been a trend to increase coercivity and decrease the product of thickness and remanent magnetization of the film to achieve sharp transitions in magnetization and maximize the density of data along the track.[68,69] However, the size reduction needed due to the miniaturization of the integrated circuits can lead to the superparamagnetic behavior in which thermal energy can reverse the magnetization direction. On other hand, to increase the data density needed for several applications, the dimensions need to be extremely reduced. It is found in the literature that the grain diameters and film thicknesses are currently in the range of 10 - 20 nm.[69] These values can be decreased, but it is necessary to take into account that the decrease of the grain volume is often compensated by the increase of the magnetic anisotropy energy of the grain. For high values of magnetic anisotropy energy, it becomes difficult to write the data on the medium.

1.2.4 MFs materials

MF materials are materials that couple simultaneously two or more primary ferroics properties as: ferroelectricity, ferromagnetism and / or ferroelasticity, Figure 1.20.[70] These properties exist in the presence of an electric polarization, magnetization or elastic deformation and can be hysterically switched by the action of an electric field, a magnetic field or a stress.[70] The MF materials are divided in two types: single-phase and composites materials.

1.2.4.1 Single - phase MFs

Single-phase MFs are formed just by one crystallographic phase. However, single-phase MF materials are rare and the trend is to extend the definition to the materials that possess the corresponding antiferroics as well, e.g., anti-FM FEs.[71] The scarcity of MF materials can be explained through a number of factors including symmetry, electronic properties, chemistry, size of the small cations and structural distortions.[25] As a result of this scarceness, only a small subgroup of all magnetically and electrically polarizable materials are either FM or FE and very few exhibit simultaneously both ferroic properties, Figure 1.20.[70]

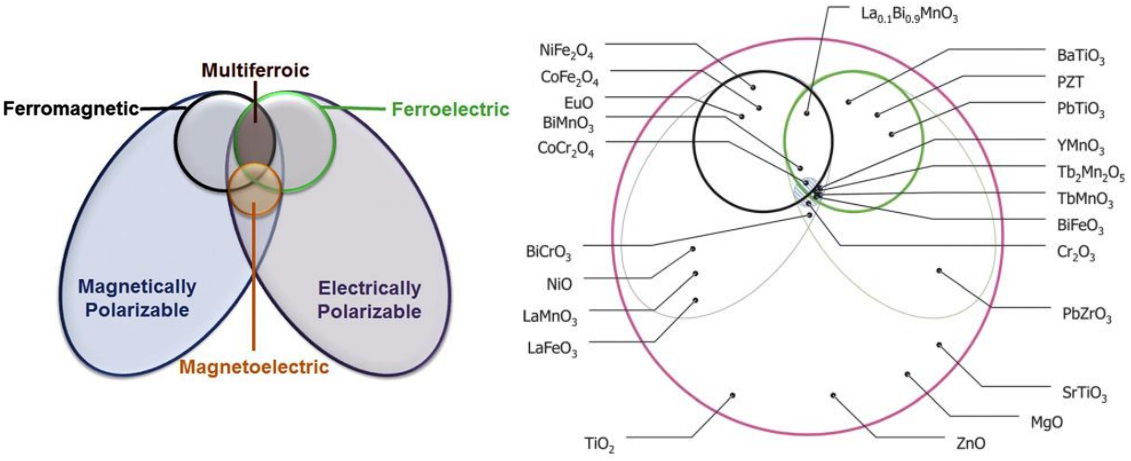

Figure 1.20: Relationship between MF and magnetoelectric materials, illustrating the requirements to achieve both properties in a material, as well as some examples of each ferroic material [adapted from reference 10 and 70].

Thus, the magnetoelectric coupling is only present in materials that typically possess the so-called linear magnetoelectric effect manifested as an induction of magnetization by an electric field or polarization by a magnetic field.[70]

$BiFeO_3$, with rhombohedral distorted perovskite structure, is one of the few interesting single-phase MF materials presenting the coexistence of large P_S and magnetization in a single compound and coupling between these functionalities.[28,72,73] This material is considered as the MF archetype and an example of lead-free materials that exhibits a strong FE behavior with a T_C of 1103 K and an apparent anti-FM order of magnetic moments which results in a weak magnetic response below T_N of 643 K, turning this material particularly interesting for many applications, including multifunctional sensors, resistive memories, information storage, sprintronics, among others. Its properties are a result of the two distorted perovskite blocks, connected along the pseudocubic – [111], building a rombohedral unit cell, Figure 1.21.

A clockwise and a counterclockwise rotation of the two oxygen octahedra connected along the [111], as well as a shift of the Fe ions also along the [111], are responsible for P_S, Figure 1.21.[74,5] As shown in Figure 1.21 there are three possible rotations: 71 º, 109 º and 180º. The 71 º and 109 º rotations result in the rotation of the anti-FM planes, providing an evidence for a magnetoelectric behavior. Because of symmetry reasons, in the 180º rotation, the initial magnetic ordering is preserved. Up to now, the reported FE measurements have confirmed a large polarization value of 55 - 60 μCcm^{-2} along the surface normal, corresponding to a spontaneous polarization of 90 - 95 μCcm^{-2} along the [111] directions of the rhombohedral unit cell.[72] It is the biggest known switchable polarization in perovskites and it is almost the double of the remanent polarization of PZT (Figure 1.10).[74] In addition, the reported magnetic measurements have shown a weak, saturated magnetic moment of 8 - 10 $emucm^{-3}$, which is consistent with the magnitude of the canting of the anti-FM sublattices calculated for $BiFeO_3$ in the absence of the long-wavelength spin spiral observed in bulk single crystals.[72]

Although the possibility of coupling between the FE polarization and the weak ferromagnetism has been investigated using first-principles density functional theory,[72] there have been no theoretical previous investigations of the coupling between ferroelectricity and antiferromagnetism in this material. Consequently, one of the most widely accepted model using the density functional theory was the model in which the

weak ferromagnetism of the Dzyaloshinskii-Moriya type was considered. The Dzyaloshinskii-Moriya interaction corresponds to spin-exchange in combination with the spin-orbit coupling, leading to canting of the magnetic sublattices.[10,72]

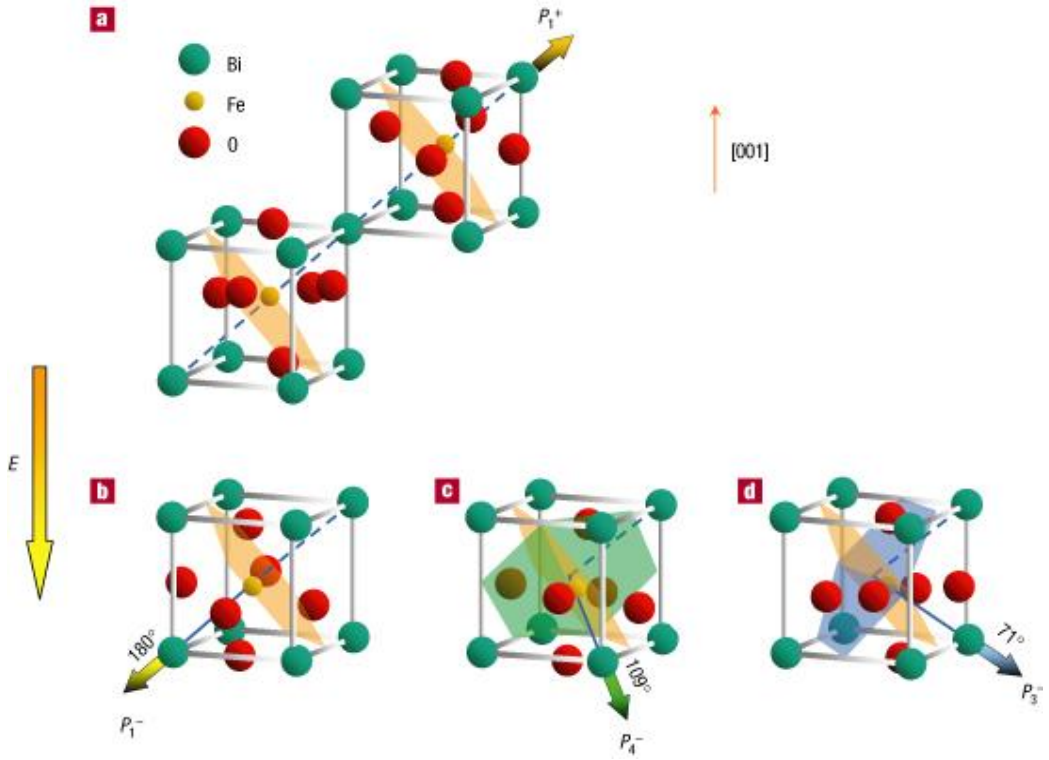

Figure 1.21: Scheme of [001] - oriented $BiFeO_3$ crystal structure and the FE polarization (bold arrows) and anti-FM plane (shaded planes): a) Polarization with an up out-of-plane component before electrical poling; b) 180º polarization switching mechanism with the down out-of-plane component after an applied external electrical field; c) and d 109º and 71º polarization switching mechanisms, with the down out-of-plane component switched by an external electrical field, respectively. [adapted from reference 75].

Due to these properties, $BiFeO_3$ is being considered promising lead-free FE and MF materials. However, the magnetoelectric response of this as well as of others single-phase MF materials is usually lower than the theoretical predictions, occurring at a temperature below room temperature. None of single-phase MF materials display reasonably large electrical and magnetic polarization simultaneously at room temperature.[76] This feature limits the applicability of single-phase MFs in the microelectronics industry. From this point of view it is necessary to design a multifunctional composite material with a sufficiently high magnetoelectric coupling at

room temperature. In this way, different strategies have been proposed and consequently recent improvements have been achieved through the development of nanocomposites MFs materials.

1.2.4.2 Nanocomposites MFs

Within the nanocomposites MFs, the particulate nanocomposite (0-3), horizontal heterostructure (2-2) and vertical heterostructure MF composites (1-3), are the three architectures mostly considered (Figure 1.22). The notations such as (0-3), (2-2), (1-3) describe the structure of each phase of the composite.[14]

The (0-3) composite (Figure 1.22a) consists in zero-dimensional (0D) magnetic nanoparticles distributed in three-dimensional (3D) FE matrix. Horizontal heterostructures (2-2) (Figure 1.22b) are formed by two-dimensional (2D) alternating layers of a FE perovskite and conventional magnetic spinel that usually exhibit weak magnetoelectric effects due to a large in-plane constraint from the substrate. Vertical heterostructures (1-3) are composed by one-dimensional (1D) nanoparticulates of the ferro/ferrimagnetic phase embedded in a (3D) FE matrix (Figure 1.22c).[13]

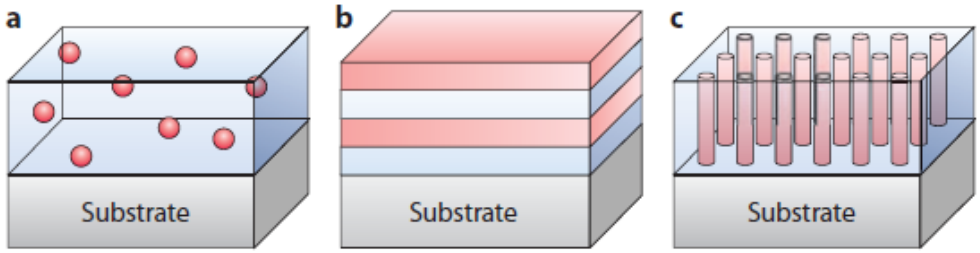

Figure 1.22: Schematic illustration of three kinds of composite nanostructures: a) particulate nanocomposite films (0-3) with magnetic particles (0D) embedded in a FE film matrix (3D); b) horizontal heterostructure (2-2) with alternating FE (2D) and magnetic (2D) layers, or simply a FE (or magnetic) thin film grown on a magnetic (or FE) substrate; and c) vertical heterostructure (1-3) with one-phase nanopillars (1D) embedded in a matrix of another phase (3D), [adapted from reference 14].

Horizontal heterostructures are easy to prepare and due to their processing simplicity and device integration, these heterostructures are the most widely investigated of the magnetoelectric composite nanostructures.[25] However, these heterostructures exhibit a weak magnetoelectric effect due to large *in-plane* constrains

from the substrate when compared to the vertical ones. The vertical heterostructures show thus many advantages over the horizontal heterostructures. Vertical heterostructures promote a larger interfacial surface area and are intrinsically heteroepitaxial in three dimensions; which should allow, theoretically, a stronger coupling between FE and FM components.[13] Beyond these reasons, the mechanical clamping imposed by the substrate, which is known for reducing both the piezoelectric response and the magnetoelectric coupling mediated by lattice deformation in thin geometries, can be controlled in this kind of heterostructures.[13] In this heterostructure type the strains can be thus considered as the sum of different strains type: the lateral strain that results from the tension induced by the substrate, the out of plane compression and the vertical strain at the interface (Figure 1.23).[77] The efficacy of the vertical strain depends on the quality of the columnar interfaces and contact area of the film with the substrate. In others words, in the case of a perfect strain coupling at the interface, the transition from lateral strain control to vertical strain control occurs when the vertical interface area for a particular column is larger than the contact area of the film with the substrate.[77] Thus, in these heterostructures, in which the interface is perpendicular to the substrate, the effect of substrate clamping is removed and allows a better strain-induced coupling between the two phases achieving, theoretically, strong magnetoelectric coupling.[77]

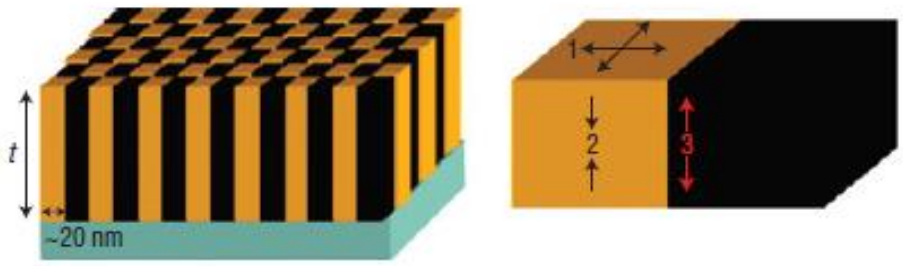

Figure 1.23: Strain concept in heteroepitaxial vertical heterostructures. For simplicity an ordered arrangement of phases is showed. In a pure epitaxial film, the phase is simply strained to the isostructural substrate [adapted from reference 77].

Nanocomposites MF films in comparison with bulk MF composites present some advantages such as: the FE / piezoelectric and magnetostrictive phases that could be tuned and controlled at the nanoscale representing a new scale to explore

magnetoelectric coupling mechanisms. Different phases can be combined at the atomic level allowing a significant reduction of the interface losses. Furthermore, the combination of different phases with similar crystal lattices, epitaxial growth or superlattice can also allow the design of new MF magnetoelectric composites films, which facilitates the understanding of magnetoelectric coupling at the atomic scale.[78] Composites MF materials are particularly interesting because the interactions between the magnetic and electric orders lead to additional functionalities.[71,79] In the Table 1.1 are present some types and literature examples of MF composite thin films.

A special attention have been paid for the development of a self-organized columnar composite such as: $BaTiO_3$ - $CoFe_2O_4$, $CoFe_2O_4$ - $BiFeO_3$[80,81,82,83] or $CoFe_2O_4$ - $PbTiO_3$.[84]

In 2004 Ramesh *et al.*[85] reported the preparation of nanopillars of $CoFe_2O_4$ epitaxially embedded into $BaTiO_3$ films. Such vertical heterostructures present a strong coupling manifested as a distinct drop in the magnetization of *ca.* 16 emu/cm^3 (5% of magnetization at 100 Oe external field) around the FE T_C. In these heterostructured composites different types of strains should be taken into consideration. Typically, the substrate induces a tension (lateral strain), giving rise to out-of-plane compression. Additionally, the presence of two different crystallographic phases originates a vertical strain at the interface. In $CoFe_2O_4$-$BaTiO_3$ horizontal heterostructures with a layer thickness of 30 nm, no temperature dependence of magnetization at 100 Oe was observed around the FE T_C. However, the magnetoelectric coupling values, limited by the clamping of the films to the substrate, were much lower than required for applications. In case of horizontal heterostructures, the clamping effect of the substrate effectively suppresses any in-plane strain in the film.

Later, in 2005 and taking in account these interesting advantages of the vertical heterostructures, Ramesh *et al.*[81] showed to be possible to induce magnetization reversal by the application of an electric field in a columnar $CoFe_2O_4$-$BiFeO_3$ epitaxial nanocomposite. This result was possible due to a significant elastic strain - mediated magnetoelectric coupling between the two ferroic phases. This electric-field magnetization reversal at room-temperature allows the use of these heterostructures type in a number of applications ranging from energy conversion to information technology. However, to achieve full control over the electric-field induced switching of the

magnetization in each bit, the superposition of a weak perpendicular magnetic field during the electrical writing might be necessary.

Levin *et al.*[84] in 2006 demonstrated that the epitaxial self-assembly of two largely immiscible phases, $CoFe_2O_4$ - $PbTiO_3$, on a single-crystal substrate is driven by the elastic interactions and, under appropriate growth conditions, these elastic interactions dominate over the kinetic factors and determine the resulting phase morphology and arrangement. The morphological characteristics of the nanostructures can be controlled by modifying the stress state in the film, which can be accomplished, for example, by using different substrate orientations and phase fractions.

In 2010, Yan *et al.*[82] measured the different ferroic properties in $CoFe_2O_4$-$BiFeO_3$ epitaxial thin films deposited on [001], [110], and [111] $SrTiO_3$ single crystal substrates. The results showed a dependence on the orientation of the substrate. The maximum values of the relative dielectric permittivity, saturation polarization, longitudinal piezoelectric coefficient, saturation magnetization and magnetoelectric coupling coefficient at room temperature were ~144 $\mu m.cm^{-2}$, 50 $pm.V^{-1}$, 400 $emu.cm^{-3}$ and 20 $mVcm^{-1}Oe^{-1}$ respectively for the thin films deposited on [001] substrate. However the values remain low for practical applications.

As the magnetoelectric properties are related with the strain transferred from the phase boundaries and, thus, are critically dependent on their geometry on the nanoscale, a relatively simple strain field distribution may be favorable for developing a good coupling. Thus, it is of great interest to explore composites with simpler strain field by creating various pre-designed structures as a strategy for constructing new candidates with promising properties. From this point view, in 2010, Gao *et al.*[76] proposed a new nanofabrication technique combining pulsed laser deposition and a nanoporous anodic aluminum oxide membrane mask to prepare various types of MF nanocomposites, namely periodically ordered $CoFe_2O_4$ dots covered by a continuous $Pb(Zr,Ti)O_3$ layer, $Pb(Zr,Ti)O_3$ dots covered with $CoFe_2O_4$, and $Pb(Zr,Ti)O_3$-$CoFe_2O_4$ bilayer heterostructure dots. By properly tuning the processing parameters, epitaxial nanodot-matrix composites were obtained. An unexpected out-of-plane magnetic easy axis induced by the top $Pb(Zr,Ti)O_3$ layer and a uniform microdomain structure can be observed for the composite consisting of $CoFe_2O_4$ nanostructures covered by a $Pb(Zr,Ti)O_3$ film. The nanocomposites exhibited strong piezoelectric signals, and they

also display magnetoelectric coupling revealed by magnetic-field dependent capacitance measurements.[76]

Table 1.1: Types and literature examples of MF composite thin films.

Types	Examples	Preparation technique	Observations	References
Single-Phase	$BiFeO_3$	Pulsed Laser Deposition	Magnetoelectric coefficient – 3 $Vcm^{-1}Oe^{-1}$ – Low for practical applications.	73
Vertical Heterostructure	$BiFeO_3$-$CoFe_2O_4$	Electron Beam Litography	Magnetoelectric coupling was observed however, none value was reported.	83
	$CoFe_2O_4$-$Pb(Zr,Ti)O_3$	Combination between Pulsed Laser Deposition and anodic aluminum oxide membrane mask	Display low magnetoelectric coupling for practical applications. This coupling seems to be a strain field transfer between diferent phases.	76
	$CoFe_2O_4$-$BiFeO_3$	Pulsed Laser Deposition	Magnetoelectric coefficient – 20 $mVcm^{-1}Oe^{-1}$ – Low for practical applications.	82
	$CoFe_2O_4$-$BiFeO_3$	Pulsed Laser Deposition	Magnetoelectric susceptibility - 1.0 x 10^{-2} Gcm/V.	81
	$CoFe_2O_4$-$BaTiO_3$	Pulsed Laser Deposition	Strong magnetoelectric coupling manifested by a drop in the magnetization of 16 emu/cm^3.	85
Horinzontal Heterostructure	$CoFe_2O_4$-$BaTiO_3$	Pulsed Laser Deposition	Low magnetoelectric coupling due to the clamping of the films to the substrate. Negligible change around the FE T_C was observed.	85

More recently, Ross *et al.*[83] using nanolithographic techniques based on the combination of templated self-assembly method with electron-beam litrography (also termed soft electron-beam lithography) prepared self-assembled $BiFeO_3$-$CoFe_2O_4$

nanocomposites in which the ferrimagnetic $CoFe_2O_4$ pillars form square arrays of periods 60-100 nm in a FE $BiFeO_3$ matrix. The FE phase presented a clear domain structure with domain sizes on the order of the pillar period and a coercive field of 200 $kV.cm^{-1}$. The magnetic switching field of the FM pillars was measured from the remanent curve derived from MFM measurements, yielding a remanent coercivity of around 5 kOe. The remanent curves of templated and untemplated nanocomposites were similar, which indicated that magnetostatic interactions between pillars had a minor effect on the switching of the array. Magnetoelectric coupling was observed by applying an ac voltage to the FE matrix, which caused the reversal of magnetization in some of the FM pillars.

Although several efforts have been made, a careful control of the geometry of the films at the nanoscale in order to obtain a relatively simple strain field distribution and to optimize and enhance the coupling is still necessary. The physical methods generally applied in the preparation of vertical heterostructures such as: top-down approaches or the bottom-up approaches as pulse laser deposition, usually provide a relatively low control of the nanostructure[85,80,81,83,84] and even though the magnetoelectric coupling values are comparable to those of bulk MFs, the magnetoelectric voltage output signal depends on the films thickness and the values are far too low for application.[15]

1.2.4.3 Applications

These materials have potential applications as micro-devices in a range of technological applications such as: magnetic field sensors, transducers, filters, oscillators, phase shifters, heterogeneous read / write devices and memory devices.[71,79] Due to the coexistence of several order parameters and magnetoelectric coupling, the composites MF materials can be also applied in novel types of memory devices. This can be explained by the fact that FE polarization and magnetization can be used to store binary information in FeRAM and MRAM, respectively. Thus, the coexistence of magnetization and polarization in a composite MF material is expected to allow the four-state logic in a single device.[86]

Beyond these applications, the electrical control of magnetization via magnetoelectric coupling as well as the combination of ferroic properties in a single

device, offer the opportunity to combine the respective advantages of FeRAM and MRAM in the form of non-volatile magnetic storage bits that are switched by an electrical field.[14,86] In 2008 Bibes *et al.*[86] designed a possible magnetoelectric RAM (MERAM) device. In this MERAM device, the binary information is stored by the magnetization direction of the bottom FM layer and is read by the resistance of the magnetic trilayer when the magnetizations of the two FM layers are parallel. The writing is made by applying a voltage across the MF FE – anti-FM layer.[14,86]

Another current application of these materials is in tunnel junction devices in which the required thickness is <10 nm.[10]

1.2.5 Preparation method: Top - Down approach versus Bottom - Up

In the semiconductor and MEMS industries, extensive efforts to develop nano - fabrication techniques have been made so far. As explained before, the features of the FE properties of FE oxides are very sensitive to the compositional homogeneity, the crystalline quality, and the physical dimension of the materials. Within this context, the understanding and control of the intrinsic / extrinsic effects on FE properties should be made by the choice of an appropriate preparation method. This should take into account several parameters such as: the shape and size of the materials, the lattice strain at the interface of FE and the substrate, and the arrange materials on a substrate of considerably large size for practical applications of FEs in ultrahigh density non-volatile memories. In addition, the method should be cheap and easily accessible, allowing an easy control of the size and shape below 100 nm as well as mass production of desired structures with a narrow size distribution. Up to now, the fabrication strategies employed for the fabrication of structurally well-defined FE nanostructures[87] can be classified into two groups: top-down and bottom-up approaches.

Top-down approaches consist on the reduction of feature size through etching or removal of material from a large structure. These methods are mainly based on lithography processes by utilizing energized particles such as: photons, ions, or electron beams. Some examples of these techniques are the focused ion beam (FIB), electron beam (EB) and electron beam direct writing (EBDW). The main advantage of these methods includes the positioning with high-precision, size and shape control.

Alexe *et al.*[56] demonstrated the fabrication of periodic patterns of FE SBT and $Pb(Zr_{0.7}Ti_{0.3})O_3$ with a pattern density of ca. 1 $Gbit.cm^{-2}$ by EBDW technique. The FE nanostructures were polycrystalline with grains of 20 nm diameter or less.[56] Muralt *et al.*[88] combining bottom-up and top-down approaches reported the preparation of epitaxial 200 nm thick film of $Pb(Zr_{0.4}Ti_{0.6})O_3$ by reactive rf magnetron sputtering on conductive Nb-doped and the patterning process involving electron-beam lithography of polymethylmethacrylate, fabrication of a 75 nm thick Cr hard mask layer by means of a lift-off process, and dry etching of PZT to obtained a nanopatterned FE surface. The smallest PZT features obtained were 100 nm in lateral dimensions.[88]

Some others examples of patterning FE domains through top-down approaches can be found in the review report published by Bonnell *et al.*,[89] where the fundamental aspects of polarization switching relevant to patterning are summarized, with an emphasis on poling mechanisms. In addition, problems related to the stability of domain patterns and limitations on the smallest domain size are discussed as well as the demonstration of FE patterning by lithography for a number of complex systems.[89] Another important report on this subject was published by Lee *et al.*[87], where various fabrication methods based on top-down and bottom-up approaches are reviewed. Special emphasis on advantages and limitations of the processes as well as the structural effect of FE nanocapacitors on the domain switching behavior and cross-talk between neighboring capacitors under external electric field are discussed.[87]

Top-down approaches have also been applied to prepare magnetic nanopatterned surfaces.[66,67] The first domains structure observation in magnetic patterned surfaces prepared through lithography were reported in 1985 by Ozimek group.[90] However, due to the resolution limit determined by the radiation wavelength used in this technique, it was necessary to find new top-down techniques such as: dip-pen nanolithography,[91] UV-lithography,[92] X-ray lithography,[93] nanosphere lithography,[94] ion beam lithography[95] or even microcontact printing[94] and near-field photolithography;[96,97] in order to circumvent the diffraction limit and achieve feature sizes as small as 50 nm.[98,99] A variety of magnetic patterned surfaces have been obtained through these novel techniques such as: simplest cases of dots and lines;[100] complex patterns as rectangles, diamonds,[101] triangles and pentagons,[102] dots and lines connected by small

constrictions,[103] or dot super- lattices[104] among others used for the study of magnetization reversal processes.[64]

In the last decade, using focused ion-beam,[105] UV photolithography[106] or combining templated self-assembly method with electron-beam litrography (also named soft electron-beam lithography)[83,107,108] nanopatterned MF structures including $BiFeO_3$ have been produced.

Although top–down methods are well suited to prepare nanopatterned surfaces, they are unfortunately limited to processe small areas in a reasonably short time and are expensive compared to the bottom-up methods. In order to overcome these disadvantages, some methods have been developed to prepare nanostructured FM thin films, such as: electrodeposition,[109] sol-gel techniques,[110] and plasma laser deposition (PLD).[111]

Bottom-up approaches consist in the self-assembly of atoms, molecules, or nanoparticles to obtain FE, FM and MF nanostructures. The approach provides several distinct advantages over top-down approaches. The bottom-up approaches allows to easily access the critical size of ferroic materials (below which ferroic properties vanishes completely), to obtain defect free nanostructures, excellent stoichiometry, thickness, size, array and porous distribution control and high homogeneity in the structure. Typical bottom-up approaches for ferroic nanostructures include chemical solution deposition (CSD), physical vapor deposition (PVD), chemical vapor deposition (CVD) and metalorganic chemical vapor deposition (MOCVD). Within the CSD methods, the sol-gel method, more specifically the EISA methodology, is the lowest cost method that offers high versatility for creation of a wide range of compositions, nanostructures and properties.[87,112,113] Thus, and taking into account the main disadvantages of the top-down approaches which include the effect on crystallographic orientation of the materials, presence of impurities, high cost of the equipments and the difficulty to cover extensive surfaces areas, the EISA methodology provides a versatile platform to prepare functional nanostructured materials, namely mesostructured oxide thin films, due to its capability to form large pores and thick walls, apart from being industrially available and hazard-free. The block-copolymers used in this methodology are easy to remove from the mineral framework and have high thermal stability avoiding the dehydration of the nanoporous network before the organic decomposition.

Moreover, the etching methods usually associated with the top–down techniques (namely lithographic techniques) are typically harmful to the electric and magnetic properties of the ferroic materials.[114]

1.2.5.1 Sol-Gel method and chemical solution deposition

The sol-gel process involves the connection of metal centers with oxo or hydroxo – bridges, consequently generating metal – oxo or metal – hydroxopolymers in solution. The hydroxylated metal species can react with others metal centers leading to condensation reactions, where an oligomer is formed by bridging two metal centers. In most sol-gel processes, the inorganic network is built by successive hydrolysis and condensation reactions.[115] The formation of such networks can be extremely important for microstructure and crystalline phase development when the films are submitted to heat treatments to obtain the crystalline nanostructures.[27] This processing technique has several advantages over other processing techniques such as low temperature preparation, homogeneity, purity, dopant incorporation possibility, stoichiometric control, low-cost and ability to coat large and complex substrate areas. However, the sol-gel process exhibits an inherent disadvantage due to the evolution of organic matter and gases during drying which can affect the porosity organization. Consequently, the structural and electrical properties of sol–gel derived thin films depend strongly on the thermal processing, both on the pre-sintering and final sintering temperatures.[116,117,118]

In general the soft chemistry routes, and more specifically the sol-gel processes have been used to obtain a great variety of organic-inorganic hybrid materials, which exhibit several different interesting and functional properties.[119] The sol-gel technique has been applied to the preparation of various types of FE, FM and MF thin films including $PbTiO_3$, $PbZrO_3$, $BaTiO_3$, $Pb(Zr,Ti)O_3$, $CoFe_2O_4$, $BiFeO_3$, among others.

The dip-coating and spin-coating processes are the most used chemical solution deposition techniques to prepare inorganic layers from sol-gel solutions. These techniques are very versatile to produce homogeneous coatings through the spreading of a solution (by dip-coating or spin-coating) onto a substrate and evaporation of volatile compounds and solvents (Figure 1.24).[120,121]

The solutions used in dip-coating are non-Newtonian fluids, especially the sol-gel solutions in which the solvent evaporates, simultaneously inducing a modification of the

viscosity, density, surface tension and also often starting the polycondensation of the inorganic species through pH change and spatial assembly of the precursors. The alcohols are appropriate solvents because they have low surface tension and are reasonably volatile to promote fast evaporation, being these properties necessary to obtain highly homogeneous films.[121]

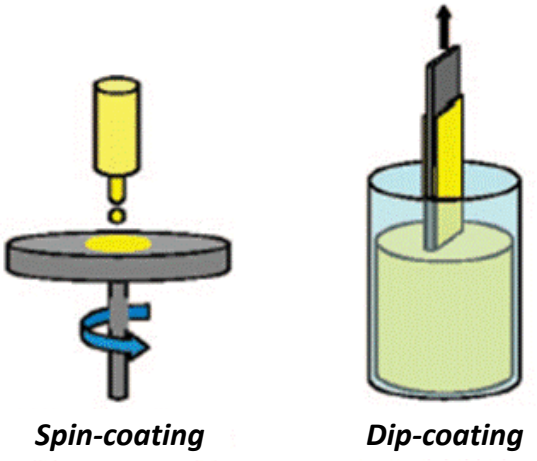

Figure 1.24: Different liquid techniques deposition [adapted from reference 120].

During the dip-coating, the film thickness is governed by factors that include viscous drag, gravitational forces and the surface tension in the concavely curved meniscus among others. In the case of dip-coating from sol-gel solutions, the characteristics of the precursor, aggregation and gelation behavior also play a key role in defining both the thickness and nature of the formed film.[122]

1.2.6 Porous / nanostructured ferroic materials prepared by EISA

Since 1992, when Kresge *et al.*[123] discovered that the micellar and lyotropic liquid-crystal phases could behave as templates for the formation of ordered silica mesoporous materials,[123,124] an explosive growth of research in this field has occurred envisaging their application in catalysis, adsorption, gas sensoring, photonics, ultra-low density materials, nanodevices, etc.[125,120]

Mesoporous materials have been the target of an increasing and interesting research because of their desirable characteristics, such as: *i)* high specific surface area; *ii)* narrow distributed pore size (between 2 and 50 nm, according to the IUPAC definition[126]); *iii)* tunable mesoporous pore size; *iv)* composition controllable; *v)*

thermal and chemical stability.[120]In addition, these materials allow post-functionalization to facilitate the further introduction of other functional moieties at the surface. A significant number of mesoporous silica-based materials were synthesized generally through sol-gel chemistry using template structure-directed synthesis strategy.[127]

Other porous inorganic materials, such as: various oxides,[120,128,129] metal sulfides,[130] phosphates[131] and metals[132] were prepared through the liquid-crystalline mechanism, in which inorganic precursors (metal alkoxides or chlorides precursors) were self-assembled in the presence of amphiphilic block-copolymer templates via chemical interactions including electrostatic attraction, hydrogen bonding, and hydrophobic/hydrophilic interactions.[133] However, the extension of the typical silica-base procedures to transition metals based systems was not trivial due to the differences between Si and most of the metals in terms of reaction kinetics and coordination aspects.

The great attraction on mesoporous non-silica oxides started in 1995 when porous powder TiO_2 organized network was first prepared.[134] Only in 2000 the first stable non-silica based amorphous titanium oxide mesoporous thin films were reported.[135] The synthesis conditions were optimized by controlling the high reactivity of Ti(IV) towards hydrolysis and condensation reactions. The films were obtained by sol-gel method and EISA under a careful control of the solvent evaporation.[135] The EISA is a denomination given by Brinker *et al*.[136] to the synthesis method from which it is possible to obtain ordered hybrid mesophases from dilute solutions, upon solvent evaporation. This methodology can be considered as a liquid crystal templating-based method (LCT), whereas the inorganic phase condenses around a stabilized surfactant mesophase.[137] On the other hand, it can be also considered as cooperative self-assembly-based method (CSA), in which surfactant molecules and inorganic species combine in a first step to form hybrid intermediate entities that behave as independent surfactant species building blocks of hybrid structures.[138] Hybrid materials result from the combination of both methods depending on the chemical and processing critical parameters. These parameters are: *i)* the chemical factors that govern the relative quantity of surfactant and inorganic precursor; *ii)* the kinetics of hydrolysis/condensation reactions and *iii)* the processing conditions that govern the

diffusion of volatile molecules into or out of the film, fixing the dry film composition and its final thickness.[120] The self-assembly is started during evaporation of the deposited solution layer on the substrate.[112,139] This is a complex step that involves at least four simultaneous mechanisms that may be ruled by the following parameters: *i)* fast evaporation of the solvent; *ii)* film water content equilibration with the atmosphere; *iii)* formation and *iv)* stabilization of the template/inorganic biphasic homogeneous layer and consolidation of the inorganic network through evaporation (Figure 1.25).[120]

Due to these chemical and processing critical parameters, the coexistence of crystallinity and meso-ordering in the mesoporous thin films were shown to be notably difficult. A careful control of the chemical, processing and treatment conditions on the synthesis is required to avoid the collapse of the meso-ordering during the thermal crystallization. In 2004, a controlled process of preparation of ordered mesoporous crystalline networks and mesostructure nano-island single layers, composed of multimetallic oxides having perovskite or ilmenite type structures was reported.[63] Nanocrystalline mesoporous films of $SrTiO_3$, $MgTa_2O_6$ and $Co_xTi_{(1-x)}O_{(2-x)}$ were then prepared starting from metal chloride precursors and using a copolymer (KLE) with higher chemical and thermal stability than the often used Pluronic copolymers (polyethylene oxide–polypropylene oxide; PEO–PPO). The chemical stability of these kind of templates permit fast self-assembly in a broad range of solvents and the high thermal stability allows dehydration of the network before the organic decomposition, thus preventing the structure collapse. Careful control of the self-assembly (by in-situ techniques) and of the kinetics allowed the preservation of the meso-ordering and prevented cations separation during the crystallization.[63] Although the nanostructured multimetallic oxide porous thin films can be achieved by EISA,[112] this procedure / study was not followed to prepare other perovskites up to 2011, when Brezesinski *et al.*[140] reported the preparation of mesoporous $BiFeO_3$ thin films with anisotropic crystallites combined with a continuous mesoporosity using the same soft-templating methodology. During the thermal treatment a substantial loss of the porous order was observed and only the photocatalytic activity was studied.

Within the photocatalytic application, another photocatalyst based on ordered mesoporous $NaTaO_3$ thin films were successfully prepared through EISA by Brezesinski *et al.*.[141] The nanocrystalline materials not only exhibit enhanced UV-light

photocatalytic activity but are also able to maintain stable performance.[141]

In 2012, our group reported the preparation and characterization of nanoporous $BaTiO_3$ and $PbTiO_3$ thin films with around 100 nm of thickness. Our designation of porous thin films (nanoporous) differs from the traditional one (mesoporous) because ours films do not present a very well-ordered porous structure. We have probed the piezo- and ferro- electric behaviour at nanoscale. However, the main difficulty in this work was the control of the porosity order during thermal treatment to achieve the tetragonal crystallographic phase. This problem was more relevant for $BaTiO_3$ films as the crystallization temperature to obtain the required tetragonality is significantly higher (700 °C) than the temperature of decomposition of the block-copolymer (350 ºC).[142]

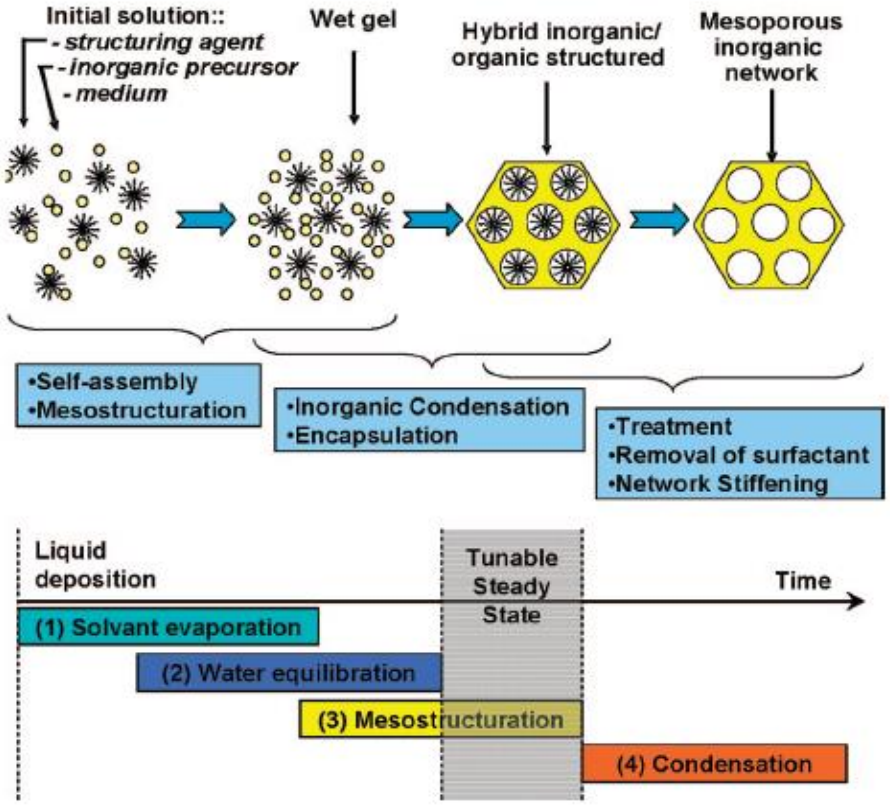

Figure 1.25: Scheme illustrating the templating approach combined with the various steps involved in the EISA process during thin film formation by liquid deposition techniques, [adapted from reference 120].

In 2014, Brezesinski *et al.*[143] reported the possibility to prepare PZT thin film nanostructures with a high degree of biaxial texturing and good FE properties. The authors showed that cubic mesostructured films with 16 nm diameter pores could be

crystallized to produce PZT perovskite phase with the retention of the nanoscale order. The coercive field and P_r of approximately 100 nm - thick films derived from dynamic P - E experiments are ∼250 $kVcm^{-1}$ and ∼25 μCcm^{-2} (∼7 μCcm^{-2} after subtracting the non-switching components).[143] However, more studies are necessary in order to reduce the amount of non-switching components to further improve the overall FE performance.

More recently, our group using one of the crystalline phases prepared in our first work reported the role of nanoporosity on the local piezo and FE properties of $PbTiO_3$ thin films and the results were compared with electrical properties of dense counterparts. We observed that porosity promotes the crystallization of tetragonal $PbTiO_3$ at a lower temperature when compared with the dense counterparts. Moreover for the same thermal conditions, the porous films exhibit enhanced piezoelectric coefficients, switchable polarization and low local coercivity.[142,144]

In terms of FM with spinel structure, in 2010, Brezesinski *et al.*[145] reported the synthesis of periodic mesoporous $CoFe_2O_4$ thin films with tunable room temperature ferrimagnetism. The inverse spinel framework possesses a strong preference for out-of-plane oriented magnetization, which is unique in the thin film system. This preference is explained based on in-plane tensile strains, combined wih a competing magnetic anisotropy within these mesoporous films that can overcome the shape anisotropy to produce an easy axis for magnetic alignment normal to the substrate.[145] In 2014, the same group using the same chemical method prepared mesoporous thin films of ferrimagnetic $Ho_3Fe_5O_{12}$.[146] The results provide evidence of the presence of single-phase garnet with 27 nm diameter crystallites and few defects after being heated to 850 °C in air. Furthermore, dc magnetometry measurements showed that the thin films are magnetically stable with a room-temperature coercivity of ∼170 Oe and exhibit an out-of-plane easy axis with a significant perpendicular magnetic anisotropy. A strong preference for out-of-plane magnetic alignment makes these thin films attractive for application in spintronics and nanomagnetics.[146]

Mesoporous $CuFe_2O_4$[147] and $NiFe_2O_4$[148] thin films were also prepared combining sol-gel chemistry with polymer templating strategies. Although these compositions exhibit multiple functionalities, including FM behavior, most of the attention has been given to the redox - and photoactivity applications as well as for

lithium batteries. Some examples of mesoporous thin films prepared by EISA to be used in lithium batteries applications can be found in the literature: β - $MgMoO_4$,[149] $NiMoO_4$[150] and α - Fe_2O_3.[151]

In the current competition for the miniaturization of microelectronic devices, nanopatterned surfaces with well-ordered arrays and distributed on metallic or semiconductor substrates are of great interest. Nanopatterned surfaces are defined as solid / environment interfaces composed of ordered features (for examples pores) with size between 1 and 100 nm.[152] Control over the dispersion, organization, and dimension of the pores spread over the substrate becomes a special challenge when their diameters are below 50 nm and bottom-up approaches are applied. In 2004, Grosso *et al.* [63] adjusted the EISA procedure to prepare the first nanopatterned thin films of $SrTiO_3$, $MgTa_2O_6$ and $Co_{0.15}Ti_{0.85}O_{1.85}$. Basically, the adjustments consisted in the use of highly diluted initial solutions and low withdrawal rates. The distance between the centres of pores can be increased by increasing the solution dilution. Indeed, the thickness of the film, pores diameter and the distance between the pores can be adjusted by the initial copolymer volumetric fraction (φ) and the hydrophobic and hydrophilic chain lengths (number of units a and b respectively) present in the block-copolymer.[63] Although the preparation procedure and structural characterization were addressed, the properties of these nanostructures have not been reported yet.

In 2008 Grosso *et al.*[153] extended this procedure to prepare TiO_2, Al_2O_3, and ZrO_2 films patterns composed of ordered nanomotifs of various morphologies (i.e. perforations (craters), rings, canyons, wires, dots, or channels) with typical lateral dimensions less than 40 nm and thickness below 15 nm. So far, there are no other nanopatterned thin films with different compositions and prepared by EISA reported in the literature.

Besides their functional properties porous films are very promising to achieve MF composites with applicable magnetoelectric coupling as typically porosity may be tuned to be vertically oriented, reducing the substrate clamping effect. Moreover the high specific surface of this type of porous films may be also very favorable for composite formation. Additionally, the chemical-assembly method can allow the direct nanopatterning of large substrate areas with a functional oxide at a cost-effective price,

in the absence of expensive equipment or etching processes (which typically affect negatively the ferroic properties).

1.3 Motivation and objectives

As mentioned above, a strong and real effort to fabricate new multifunctional thin films, namely MF composites thin films with a precise control of composition, morphology, atomic arrangements and interfaces is required in order to answer the microelectronic industry needs.

The design and control of such heterostructured MF composites remains a great challenge, Figure 1.4. The majority of the works described up to now are based on top-down approaches, which do not allow a careful control of the nanostructure. Hence considerable advances in the fabrication of MF thin films complex heterostructures are necessary. Through self-assembly chemical methods it is expected to construct vertical nanostructures in which the FE and the FM phases are arranged with long-range ordering and with a good control of the stoichiometric composition, phases distribution, interfaces and strain coupling between phases.

Within this context, the main motivation of this work is to contribute to the development of new nanocomposite ferroic thin films with optimized and required performance for microelectronic applications. By using a chemical based method porous ferroic films with high specific surface and vertical ordered porosity will be prepared. These structures will be further functionalized by filling the nanoporosity with ferroic nanoparticles of different nature. This original idea can be viewed as a new concept to prepare MF nanocomposite heterostructures.

The Figure 1.26 shows how our contribution can be useful to produce the future nanocomposite MF structures with enhanced strain-coupling properties at a cost-effective way. According to previous studies,[77] the transition from substrate strain control to vertical strain control occurs when the vertical interface area within ferroic phases exceeds the one with the substrate. By extrapolating the latest study results to nanoporous or nanopatterned thin films, we expected to control the vertical strains over the lateral ones when the film thickness be lower than half of the diameter of the vertical pore. These new multifunctional materials with promising properties could be applied in several devices such as: ultra-sensitive solid state magnetic sensors, computer memory that combines the best properties of FE storage and magnetic read/write, solid-state microwave and high-power devices, energy harvesting, and other novel and smart

circuit devices with high integration level, high performance and enhanced power management.

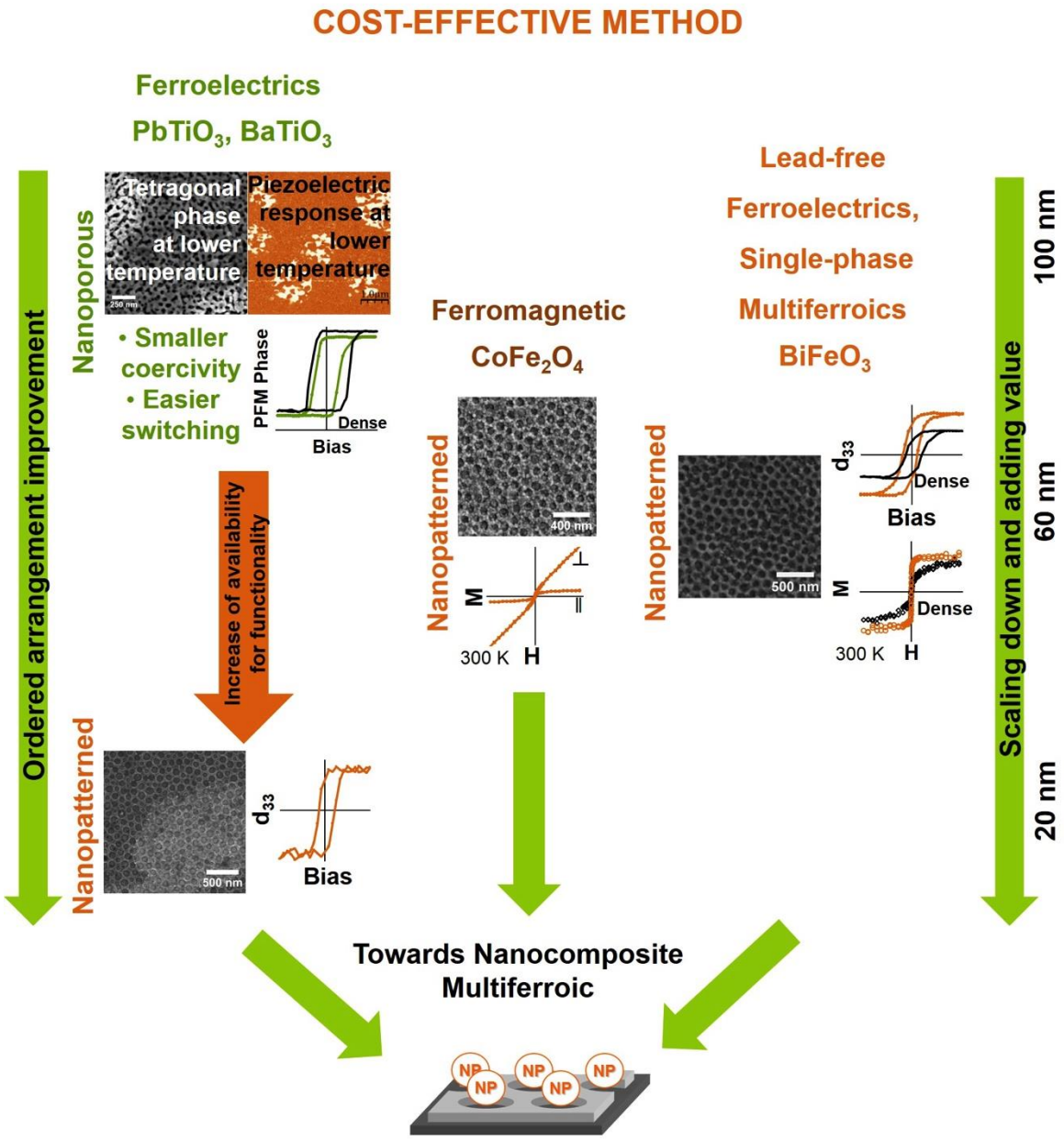

Figure 1.26: Strategy to achieve functional nanocomposite MFs applied in this Thesis.

Thus, the main objectives of this Thesis are:

- To prepare different FE, FM and MF nanoporous and nanopatterned thin films such as: $PbTiO_3$, $BaTiO_3$ (both FE), $CoFe_2O_4$ (FM) and $BiFeO_3$ (MF),

- To understand the role of nanoporosity on the microstructure evolution, crystallization and ferroic properties of the required phase,

- To functionalize the porous films with ferroic nanoparticles in order to achieve the magnetoelectric nanocomposite thin films,

- To characterize the ferroic properties of the nanocomposite thin films.

CHAPTER 2

Films preparation and characterization techniques

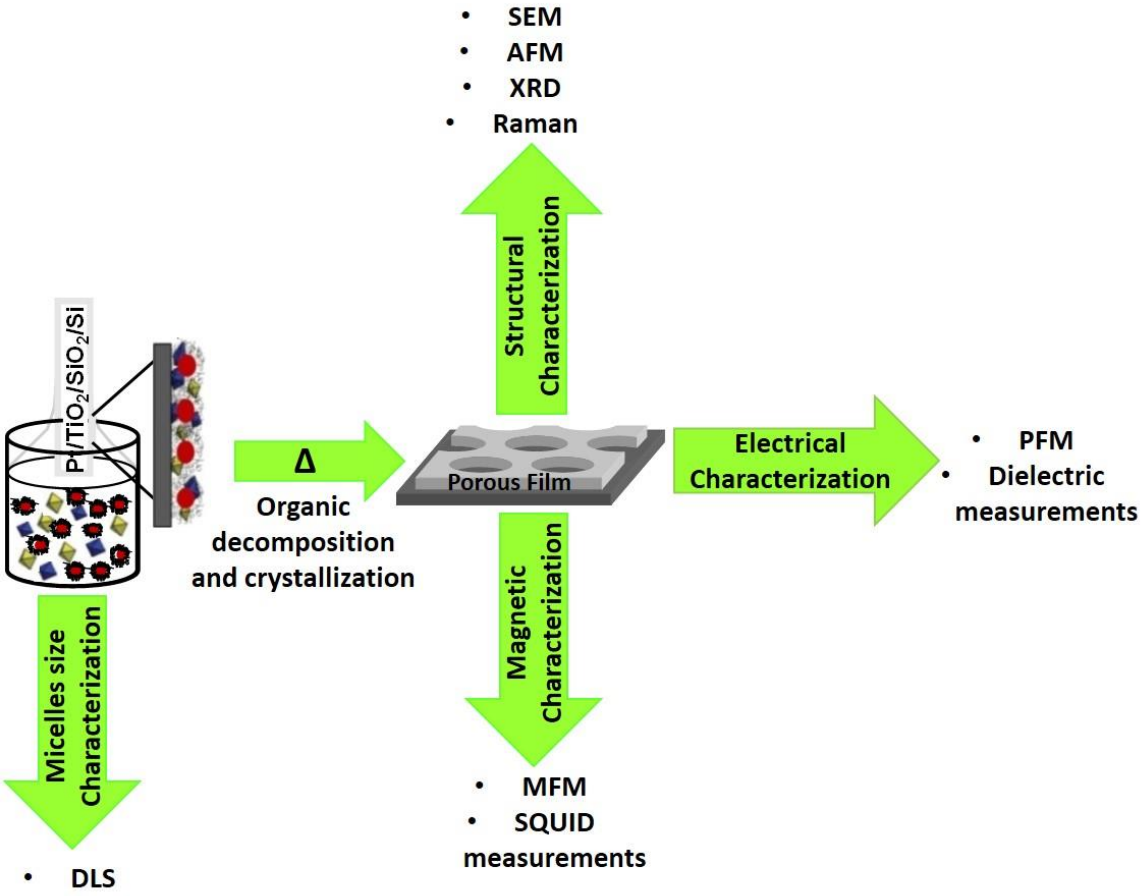

Graphical abstract: Overview of the experimental setup for material's preparation and characterization.

Abstract

This chapter will describes the experimental procedure followed to prepare the ferroelectric, ferromagnetic and single – phase multiferroic thin films as well as the used techniques to functionalize ferroelectric thin films with ferromagnetic nanoparticles to achieve the nanocomposites multiferroic thin films. The used characterization techniques are also described. Ferroelectric, ferromagnetic and single – phase multiferroic thin films nanoporous and nanopatterned thin films under study include $BaTiO_3$, $PbTiO_3$, $CoFe_2O_4$ and $BiFeO_3$ compositions. The multiferroic nanocomposites thin films are $BaTiO_3$ porous matrices functionalized with cobalt and nickel metal nanoparticles. All dense and porous thin films are prepared by EISA methodology using sol-gel solutions in absence or in the presence of an amphiphilic block-copolymer. The

attempts to functionalize the pores of the thin films are made using electrochemical or CO_2 supercritical fluid depositions.

Different characterization techniques are used to characterize the sol-gel solutions and the thin films including dynamic light scattering; thermal analysis; scanning electron microscopy, transmission electron microscopy, X-ray diffraction, Raman spectroscopy, atomic force microscopy, piezoresponse force microscopy, magnetic force microscopy, superconducting quantum interference device and dielectric measurements.

Index

2.1 Films preparation

Thin films can be prepared through a different number of techniques. However, just a few are suitable to produce ordered porous thin films as mentioned in the section 1.2.5 of the Chapter 1. Dip-coating technique is one of the most commonly used in electronics and optics industries to prepare inorganic layers from sol-gel solutions.[154,155] As described before, the combination of sol-gel method with EISA is the most used method to prepare ordered porous thin films. Figure 2.1 represents schematically the methodology used in the preparation of the films of this work.

EISA methodology is based on the use of micellar and lyotropic liquid-crystal phases, which act as structure-directing agents, regulating the nucleation, growth, morphology and orientation of inorganic crystals. After evaporation during the thermal treatment, the structure-directing agents form periodically organised porous structures.

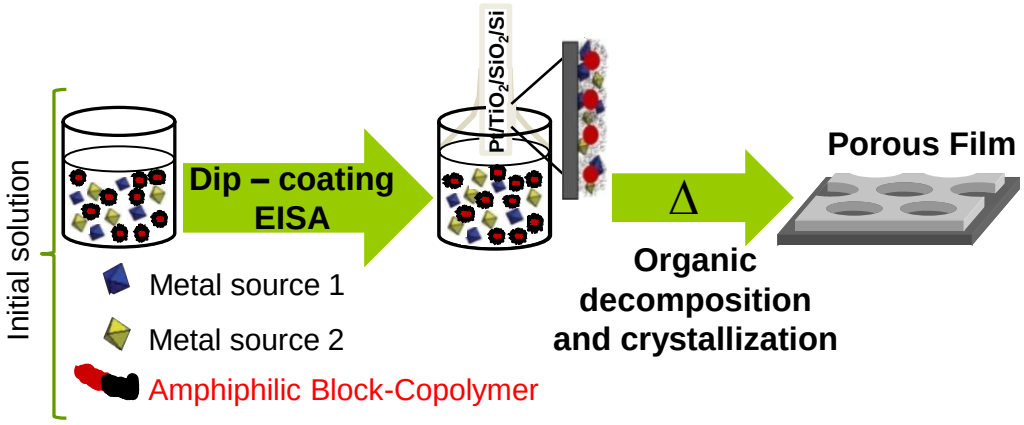

Figure 2.1: Scheme of evaporation-induced self-assembly associated to dip-coating.

The structure-directing agents self-assembly is started during evaporation of the deposited solution layer on the substrate.[112,139] However, this is a complex step that involves at least four simultaneous mechanisms that may be ruled by the following parameters: *i)* fast evaporation of the solvent; *ii)* film water content equilibration with the atmosphere; *iii)* formation and *iv)* stabilization of the template/inorganic biphasic homogeneous layer and consolidation of the inorganic network through evaporation (Figure 1.25).[120]

The structure-directing agents consist of hydrophilic and hydrophobic parts. The hydrophilic chains are selectively brought in contact with polar solvent, bringing the hydrophobic ones shielded within the spherical or cylindrical micelle. Above the critical micelle concentration and with the increase of the structure-directing agents molecular weight, spherical and cylindrical micelles are formed producing thus different pore sizes. Further increasing of the structure-directing agents concentration, periodic hexagonal, cubic or lamellar structures can be achieved.[115]

Whereas the nature of the sol-gel solutions is non-Newtonian, the evaporation of the solvents takes place during dip-coating deposition with simultaneous self-assembly of inorganic species around the structure-directing agents micelles leading for mesophase formation. The hydrolysis and condensation reactions take place throughout whole procedure, up to final heat treatment, determining the degree of condensation, density and species structure. The dip-coating of sol-gel solutions is a complex dynamic process, difficult to model because it is associated with time-dependent evaporation-induced concentration and viscosity gradients in solution.[156]

Faustini *et al.*[156] reported a systematic study on the preparation of sol-gel films by dip-coating under extreme conditions, Figure 2.2. At low withdrawal speeds, the film thickness is governed by the interdependence of continuous evaporation of the solvent at the meniscus and the capillary rise at the drying line. At high speeds, the final thickness is mainly dependent on the viscous drag. However, for thinner films, there is a low thickness limit that cannot be overcome only by using the high diluted solutions.[156]

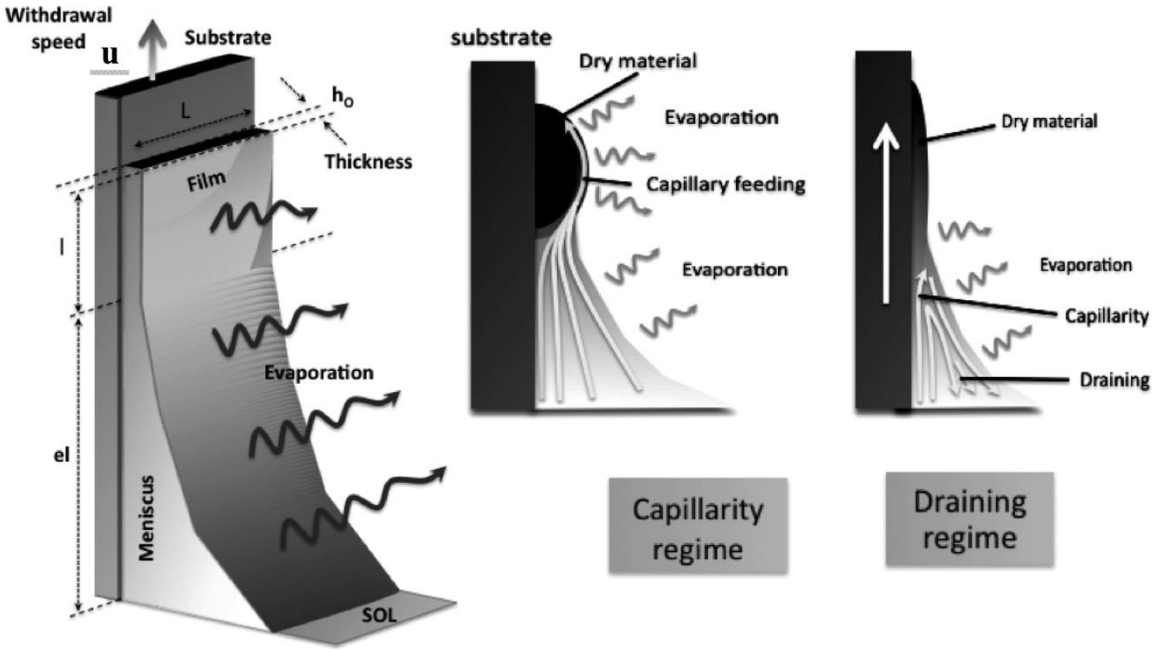

Figure 2.2: Schematic illustration of sol-gel method during the dip-coating process. Two different regimes taking place through dip-coating process: capillary and draining for slow and fast withdrawal rates, respectively [adapted from reference 156].

The as-prepared thin films are xerogels in which the organic template is embedded into the inorganic matrix. Different block-copolymers were used as structure-directing agents to prepare the nanoporous and nanopatterned thin films. After deposition, the films must be submitted to a thermal treatment to promote: *i)* the stabilization of the mesophase; *ii)* the decomposition and elimination of the organic moieties creating the porosity; and *iii)* the crystallization of the network. The crystallization occurs through nucleation and growth mechanisms. A fast nucleation leads usually to a large number of homogeneously distributed crystallite seeds along the inorganic network. Their subsequent growth into nanocrystallites is made by diffusion

of the adjacent atoms towards the nucleus surface to occupy atomic sites of lower energy.[115]

Thus the thin film preparation procedure consisted in three main steps: *i)* synthesis of the sol-gel solution, *ii)* dip-coating deposition, and *iii)* thermal treatment. After thermal treatment the pores are typically empty, being available for the functionalization (in this Thesis the functionalization step not involves covalent bonds) with nanoparticles of different ferroic nature.

2.1.1 Sol-gel process and dip-coating deposition

All the thin films were deposited *via* dip-coating, where the substrate is dipped into the sol-gel and subsequently withdrawn at a constant speed (Figure 2.1). The dip-coater used for the deposition was the Single Vessel Small Dip Coater from KSV Instruments (Finland) model DC with adjustable withdrawal rate from 0.1 to 85 mm/min. The equipment was modified with a homemade drying chamber, which allow to submit the just deposited films to a temperature between 50 and 100 ºC. Prior to the deposition step, Pt(111)/TiO_2/SiO_2/Si(100) substrates from Inostek Inc. and Radiant Inc. were cut in rectangles of 1.0 x 2.0 cm^2 and subsequently ultrasonically cleaned with ethanol and acetone during 10 min respectively. This substrate type is the most similar substrate to the one used in the microelectronic industry. For some compositions, low temperature (90 ºC) to quickly dry the sol was employed to maximize the adhesion of the sol to the substrate. This drying temperature applied during the deposition promotes the solvents evaporation allowing the domination of the viscous drag regime upon gravity forces. In order to get the desired thickness of the thin films different withdrawal rates were used.

2.1.2 Thermal treatment

Different thermal treatments were used to optimize the crystallization. In the case of porous thin films, a compromise between obtaining the crystalline phase and maintain the ordered porosity was necessary to be established during the thermal annealing. In some cases, a more controlled procedure for evaporation of solvents and block-copolymer removal was followed. For dense films, one more additional step was introduced before the thermal treatment. Immediately after the deposition films were

placed on a hot-plate at 120 ºC for 2/3 min and subsequently calcined and thermal treated at the desired temperatures.

2.1.3 Functionalization

The functionalization (in this Thesis the functionalization step not involves covalent bonds) was carried out using the electrochemical deposition and Supercritical Fluid Deposition (SCFD) techniques. The electrochemical deposition technique was performed in LCMCP-UPMC in Paris under Supervision of Professor Christel Laberty and Professor Clément Sanchez. The Supercritical Fluid Deposition (SCFD) technique was carried out in the Department of Chemistry-Physics I, Universidad Complutense in Madrid with Professor Albertina Cabañas.

The electrochemical deposition of nanoparticles films was carried out in a potenciostatic galvanostat (Princeton Applied Research – PAR262) equipment using an aqueous solution as supporting electrolyte. The counter electrode used was platinum and the reference electrode was a saturated calomel electrode (SCE-E = −0.241 V/NHE) (NHE - normal hydrogen electrode). Solutions were aerated with argon and the temperature maintained constant in the 20 - 25 ºC range. More details about the experimental conditions can be found in the Chapter 5.

The experiments using the Supercritical Fluid Deposition (SCFD) technique were conducted in a *ca*. 100 mL stirred high-pressure reactor (Autoclave Eng. Inc.) in the batch mode. Several pieces of 1.0 x 1.0 cm^2 of the nanopatterned thin films were placed vertically inside the high-pressure reactor and in contact with the wall. The precursor, previously dissolved in ethanol, was placed in a vial located at the bottom of the reactor without contacting the substrates. More details about the experimental conditions can be found in the Chapter 7.

2.2 Structure characterization

The attainment of ordered porous thin films is dependent of several parameters such as: precursors dilution; solvent polarity; dissolution conditions; organic: inorganic ratio; substrate surface energy; thermal treatment and aging of the solutions; withdrawal rate and thermal treatment conditions.

Sol-gel solutions were mainly characterized by Dynamic Light Scattering (DLS) and thermal analyses (TGA/DTA and TGA/DSC). The films were regularly structural and morphological characterized by X-ray diffraction (XRD), Raman spectroscopy, scanning electron microscopy (SEM), and atomic force microscopy (AFM). Piezoresponse force microscopy (PFM), dielectric measurements, magnetic force microscopy (MFM), and superconducting quantum interference device (SQUID) were used to obtain information about piezoelectric, electrical and magnetic properties. These characterization techniques allowed us to study the microstructural features, the role of processing conditions, and investigate the polarization switching, magnetic domains and stability of the FE / FM phase of the prepared nanostructures.

2.2.1 Dynamic Light Scattering (DLS)

DLS, also known as Photon Correlation Spectroscopy, is used to measure the size or size distribution profile of molecules or particles in suspension or polymers in solution, normally in the submicron region and / or lower than one nanometer.[157]

The size measured in DLS is the diameter of the sphere that diffuses at the same speed as the particle being measured. DLS measures Brownian motion of nanoparticles (the movement of particles due to the random collision with the molecules of the liquid surrounding the particles) and relates this to the particles size through the Stokes - Einstein equation. The scattered light introduced through the light source into the cell is collected at either 90° or 173° as shown in the Figure 2.3.

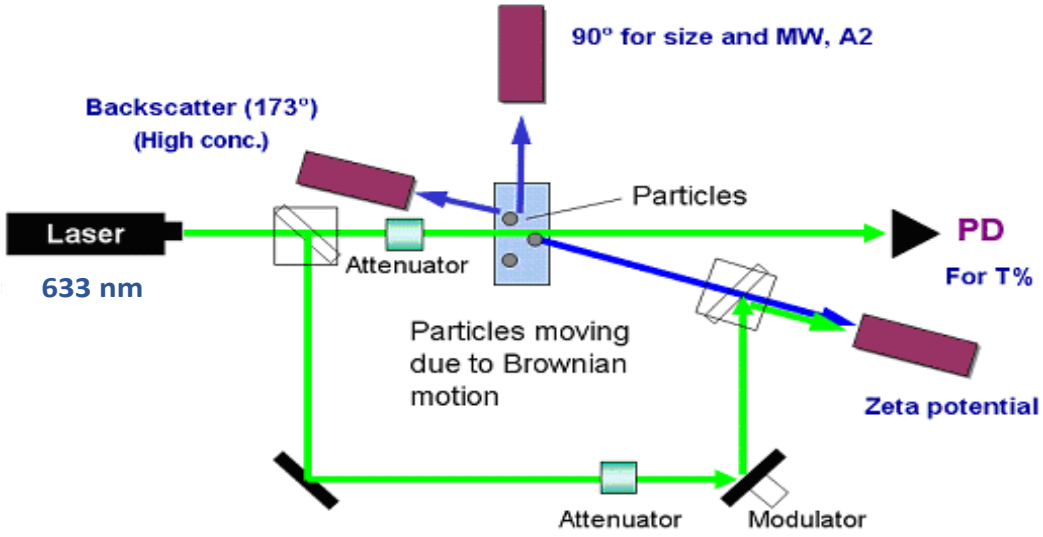

Figure 2.3: Working principle of the DLS thecnique [adapted from reference 158].

Within the cell, the scattered light signal is fed into a multi-channel correlator that creates a function, which is used to determine the translational diffusion coefficient of the particles. As mentioned the Stokes-Einstein equation is then used to calculate the particle size.[159] If a small particle is illuminated by a light source such as a laser, the particle will scatter the light in all directions. In contrary, if a screen is held close to the particle, the screen will be illuminated by the scattered light. In this technique, small particles in the solution diffuse rapidly resulting in a rapid fluctuation on the intensity signal while larger particles diffuse more slowly.[159] These fluctuations are caused by interference effects arising from the relative Brownian movements of an ensemble of a large number of particles within a sample, i.e. these fluctuations are the result of variations in the position of an essentially fixed number of particles in the scattering volume. In summary, the DLS measures the rate of these intensity fluctuations and then uses this to calculate the size of the particles.[159]

DLS has been used to investigate the dynamics of block-copolymers in dilute solutions, semi-dilute solutions, and concentrated solutions. In the Chapter 4 we use this technique to measure the micelle size in different solutions where the effect of several parameters such as: *i)* addition of inorganic precursors / organic solvent; *ii)* heating of solution and *iii)* solution aging time on the micellization process and, consequently, on the development of the micelles of block-copolymer in the solution of $BaTiO_3$ were studied.

The DLS measurements were carried out using a Nano ZetaSizer, Malvern equipment with a ‘‘red’’ laser operating at 633 nm and a detector positioned at 173º at room temperature.

2.2.2 Thermal analysis (TGA/DTA and TGA/DSC)

In general thermal analyses measure a change in a material as a function of the temperature.

Differential thermal analysis (DTA) is based on the heat loss or gain due to the structural changes in material as a function of temperature. On the other hand, the thermal gravimetric analysis (TGA) is based on the measuring of the weight loss during the heating. This weight loss that occurs in amorphous gels prepared by solution is mainly due to the evaporation of water, solvents, organic matter oxidation with release

of carbon dioxide and, in some cases, phase formation. DTA and TGA can be performed separately or simultaneously under different atmospheres and heating rates. The equipment uses two set of identical columns, one for the reference and other for the sample.[21]

From the DTA and TGA plots, several chemical and physical characteristics can be extracted, among them: thermal stability, exothermic and endothermic reactions, phase formation and transition, glass transition temperature, melting temperature, among others.

Differential scanning calorimetry (DSC) consists in the determination of the temperature and heat flow associated with phenomena suffered by a certain material as a function of time and/or temperature. DSC measures a heat quantity, which is radiated or absorbed excessively by the sample on the basis of a temperature difference between the sample and the reference material.

The DSC is mainly used to study phase transitions and / or exothermic decompositions assessed through the enthalpy values.[160]

In this work, a DSC50 Shimadzu system and SETSYS Setaram system were used with a heating rate of 5 °C/min under flowing air up to 600 and 800 °C respectively. TGA-DSC analyses were used to study the exothermic and endothermic reactions, phase formation and transition. These techniques were carried out on dried porous and dense powders obtained by drying the deposition solutions in open vessels at 60 ºC for few days. A Setaram Labsys™ TGA-DSC16 system was used with a heating rate of 10 °C/min under flowing air between 600 and 800 °C.

2.2.3 Transmission Electron Microscopy (TEM)

TEM is an excellent and versatile tool for the characterization of complex structures over spatial ranges from atomic scale, through nano up to the micrometer level and beyond.[161] The TEM technique consists in the emitting of electron beam from an electron gun. This electron gun emits a highly coherent beam of electrons of exceedingly small wavelength and that are accelerated by a high voltage, normally 100-300 kV, producing thus, the electron beam. This electron beam is focused by electromagnetic lenses to be incident on a small area of sample (less than 200 nm^2). The interaction between electron beam and the sample produces a wide range of different

signals. This happens because, the electrons are one type of ionizing radiation, which is the general term given to radiation that is capable of removing the strongly bound, inner-shell electrons from the attractive field of the nucleus by transferring some of its energy to individual atoms in the sample, producing thus a wide range of secondary signals from the sample.[161,162] TEM has no inherent ability to distinguish atomic species; but, electron scattering is very sensitive to target elements. Heavy atoms with large, positively charged nuclei scatter electrons more effectively and to higher angles than light ones. Electrons interact primarily with the potential field of an atomic nucleus, and to some extent the electron cloud surrounding the nucleus. The scattering of an electron by an atomic nucleus occurs by a Columbic interaction known as Rutherford scattering. This is equivalent to the elastic scattering, without energy loss. The scattering of an electron by the electron cloud of an atom is most often an inelastic interaction, i.e., exhibiting energy loss. This energy loss can be measured by Electron Energy Loss Spectroscopy (EELS) and is responsible for the characteristic X-Ray Fluorescence that is measured in Energy-Dispersive X-Ray Spectroscopy (EDS) and Wavelength-Dispersive X-Ray Spectroscopy (WDS).[161,162] TEM offers two modes of sample observation, image mode (bright-field and dark-field) and diffraction mode. High-resolution transmission electron microscopy (HRTEM) has been often used for qualitative and quantitative characterization of nanometric scale features due to its high image resolution (< 2Å), easiness of calibration and high precision and accuracy.

TEM samples of thin film can usually be prepared by several methods, namely by: a) etching the samples using a mixture of nitric acid with hydrofluoric acid for a short time; b) cross-section, c) scratching of the film followed by deposition of of the scratchs in a TEM grid; and d) FIB through cross sectional and lifted out onto TEM supports.

In the first method, the main difficulty is to get rid of the platinum layer of the substrate ($Pt(111)/TiO_2/SiO_2/Si(100)$) keeping the morphology/chemical features of the film. For the cross-section, the film specimens were cut with 2-3 mm the thickness using diamond pen. These specimens were cleaned and glued with a thin layer of M-Bond 650 – Vishay glue. After this step, the final samples, constituted by various wafers and glued films face to face were placed in a clamp type device to press the cross section samples. Then the samples were introduced in the oven at 125 ^oC during at least

2h to guarantee a strong adhesion between the films. The following step consisted in fixing the final sample to the surface of grinder sample holder with thermoplastic glue and to polish it until approximately half of the initial thickness. Grinding and parallel polishing should be slow and soft, changing constantly the grinding direction. The sample side must be turned in order to polish the other sample side until approximately 20-30 μm. The grinding paper sequence was P320, P1200, P2500 and P4000. The last step consisted in the placing of the copper ring with 2 mm (AGAR) of hole using epoxy glue (Araldit – Gattan) and in the removing of the sample from the grinder sample holder. For this it was necessary to heat the grinder sample holder with the sample until be able to remove slowly and carefully the sample with the copper ring. Then, samples were introduced in the ion milling to make the center hole. The ion milling conditions used were: double ion beam, 5 keV of beam voltage, 4º of beam angle during 2 hours and 8º during more 2 hours. After these steps samples are ready to be observed.

TEM samples were also prepared through scraping films from the substrate. The scraped films were suspended in ethanol and the copper grid without film (AGAR) was then immersed in the suspension and left to dry before observation in TEM. The main problem of this method is to scrap only the film and avoid the platinum.

In the case of FIB method the stronguests difficulty in this kind of samples is the selection of the most adequate laser intensity to avoid to deteriorate the samples.

All the methods were tried in this Thesis, however, many difficulties related with film thickness and porosity turned the preparation of good samples an impossible task.

The microscopes used in this work were Hitachi H9000-NA and HR–TEM200–SE/EDS: HR-(EF)TEM, 2200FS model, Jeol.

The research leading to these results has received funding from the European Union Seventh Framework Programme under Grant Agreement 312483 - ESTEEM2 (Integrated Infrastructure Initiative–I3). The results obtained through the different approaches are not presented in the following Chapters due to experimental difficulties related with the porosity and thin thickness of the films.

2.2.4 Scanning Electron Microscopy (SEM)

SEM is a widely used to obtain information about morphology, texture, chemical composition, crystalline structure and orientation of materials contained in the sample.

This technique in analogy to the TEM requires a focused beam of high energy electrons. This energy, when interacts with the sample produces a variety of signals including secondary electrons, backscattered electrons, diffracted backscattered and characteristic X-rays. The secondary electrons are used to obtain images, revealing the morphology and topography of the samples. Backscattered electrons are used to illustrate contrasts in composition of multiphase samples. Diffracted backscattered electrons are used to determine crystal structures and orientations of minerals and photons. Characteristic X-rays are used in elemental analysis.[162]

SEM technique can also be applied to perform local chemical analyses. These analysis are especially useful in qualitatively or semi-quantitatively determination of chemical compositions by Energy-Dispersive X-Ray Spectroscopy (EDS), crystalline structure and crystal orientations by Electron Backscatter Diffraction (EBSD).

SEM is a fast technique for quick identification of elements present in the samples, having a good depth of field. It is a versatile tool that supports others techniques. However, this technique presents some limitations: *i)* it requires vacuum compatibility; and *ii)* the final resolution is strongly dependent on the sample and on its preparation. Insulating samples may need to be coated.[163,164,165,166]

Prior to the analysis the thin films described in this Thesis, these were fixed with carbon tape on an aluminum support with no coating. For the cross-sections analysis, an aluminum cross-section support was used. Through SEM analysis the porous order and periodicity of the nanostructure, porous size, pore size distribution, film thickness and the chemical composition of the surface was investigated. A SU-70 Hitachi microscope was used to peforme the microstructure analyses.

2.2.5 X-ray diffraction (XRD)

The discovery of the X-ray diffraction (XRD) was realized in 1912 by Von Laue, Friedrich and Knipping. XRD is a non-destructive technique, sample preparation

is easy and the measurements can be performed in different atmospheres and temperatures.[167]

When X-ray radiation penetrates the matter, the radiation interacts with the electrons present in the atoms, resulting in the scattering of the radiation, Figure 2.4.

If the atoms are organized in planes and the distances between the atoms are of the same magnitude as the wavelength of the X-rays, constructive and destructive interference will occur. The peaks of XRD are produced by constructive interference of a monochromatic beam of X-rays scattered at characteristic angles for each set of lattice planes in the sample.[168] The possibility of constructive interference to the inter-planar separations (Figure 2.5) is related by the classical Bragg law:

$$n\lambda=2d\sin\theta \qquad \textbf{Eq. 2.1}$$

where λ is the wavelength of X-rays, θ is the Bragg angle, d is the inter-planar separations and n is the order of diffraction. This law is a fundamental equation for the interpretation of X-ray diffraction data.[168]

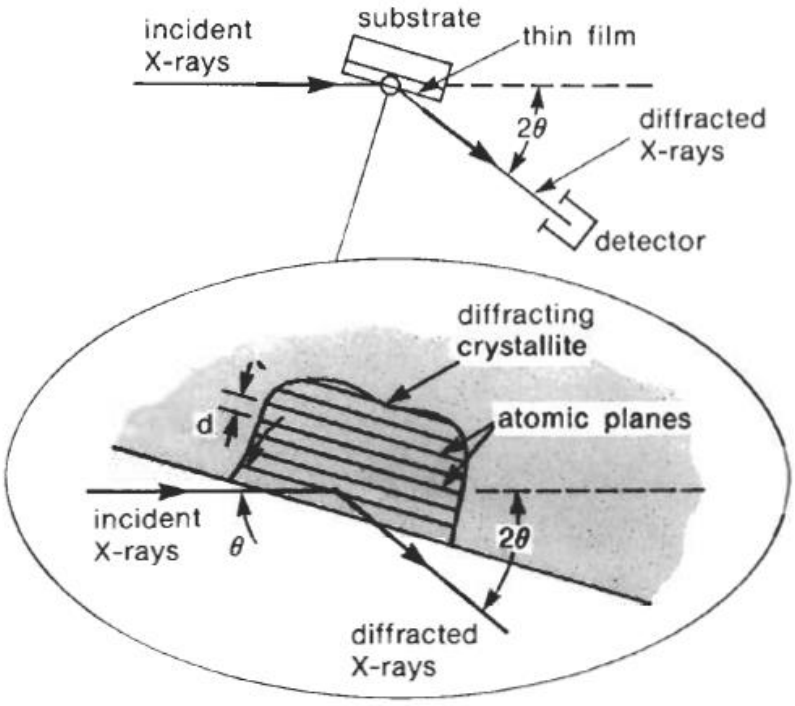

Figure 2.4: Working principle of XRD, [adapted from reference 162].

The arrangement of atoms or of the population of electrons is determined by angular dependence analysis of scattered X-ray. The peak intensities typically observed in the range of diffraction angle from 10 to 150° are determined by the atomic position within the lattice planes and consequently, the X-ray diffraction pattern reveals the periodic atomic arrangements present in a material.[168]

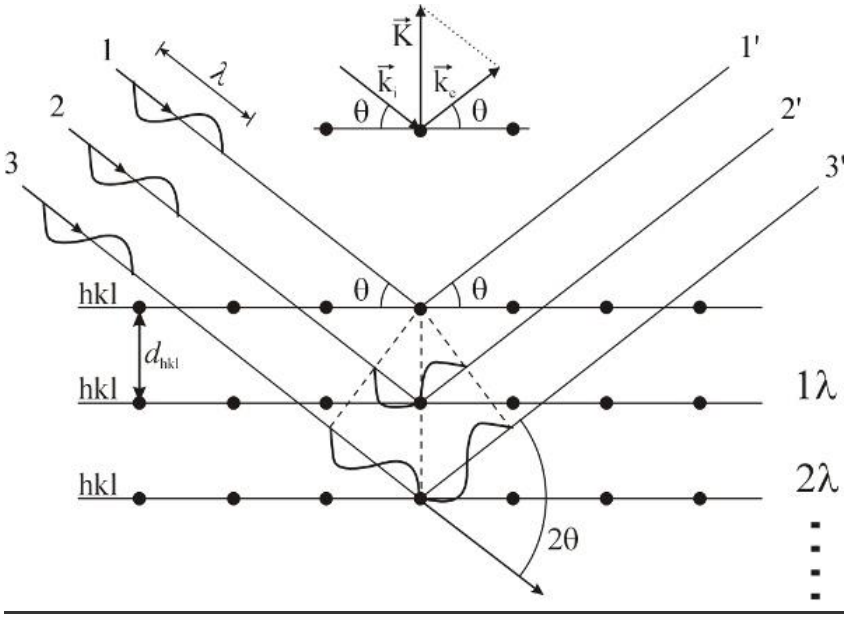

Figure 2.5: Schematic drawing of Bragg law, [adapted from reference 162].

Using this technique, information about structure, phases, preferential orientations in thin films and other structural parameters, such as average grain size, crystallinity, strain or micro-strain effects in bulk and thin film and crystal defects can be obtained. Beyond identifying the crystalline phases for a wide variety of bulk and thin films, it is also possible to identify and quantify the lattice parameters.[21]

For polycrystalline films it is possible to determine the crystallite size, the percentage of material in crystalline form and amorphous, and measure residual stress, as well.

The crystalline phases in the films and *in-situ* phase formation in the powders were identified by XRD using a Philips X'Pert MPD X-ray diffractometer with Cu Kα radiation and 2° grazing incidence angle. More details about the conditions can be found the following Chapters.

2.2.6 Raman spectroscopy

Raman spectroscopy is also known as a vibrational spectroscopy method. Normally it is used to study the interaction between light and matter in which the light is inelastically scattered. Laser light such as visible, infrared and near ultraviolet can be used as light source in the Raman spectroscopy.

When this laser light interacts with the molecules or bonds inside the samples it gives rise to different scattering phenomena, namely Rayleigh, Stokes Raman and Antistoke Raman scattering[169] (Figure 2.6). During this interaction the laser light photon excites the molecules from ground state to the virtual energy states, where it stays for some time and return to the ground state in different or same vibration levels after emitting the photon.[162]

If the excited molecule from first vibration level returns back to the same vibration level, this energy transfer model is known by Rayleigh scattering or elastic scattering. Rayleigh scattering or elastic scattering (no change in the frequency of photons) is thus based on elastic scattering of the photons that interacts with molecules. Rayleigh scattered photons have the same wavelength as the incident light (Figure 2.6).[162]

However, if the molecule returns to different vibrational level, then the difference between the original state and the new state leads to a shift in the emitted photon's frequency, away from the excitation wavelength. In this case, the energy transfer model is known as Raman scattering. When the photon frequency is shifted towards lower wavelength this is known as Stokes scattering, otherwise it is known as Anti-stokes scattering. The Stokes scattering (Stokes shift) is the most common energy transfer model. This shift happens when a photon interacts with the electron cloud of the functional groups bonds, exciting an electron into a virtual state. The electron then relaxes into an excited vibrational or rotational state leading to a loss of some energy of the photon, which is detected as Stokes Raman scattering (Figure 2.6). In this case the photon frequency is shifted towards lower wavelength. This loss of energy is directly related to the functional group, the structure of the molecule to which it is attached, the types of atoms in that molecule and its environment.[169]

However, factors such as the polarization state of the molecule (which determines the Raman scattering intensity) must be considered in the interpretation of

the Raman scattering, i.e. some vibrational or rotational transitions, which exhibit low polarizability cannot be active in the Raman and consequently cannot appear in a Raman spectra.[170]

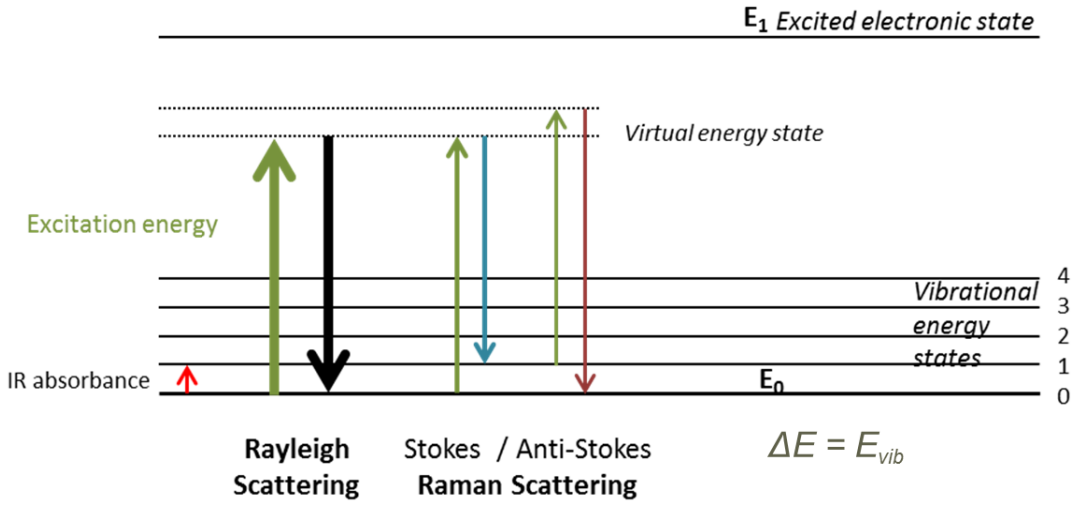

Figure 2.6: Energy-level diagram showing the states involved in Raman spectroscopy, [adapted from reference 171].

Raman spectroscopy gives very valuable information, which is useful for chemical identification, characterization of molecular structures, effects of bonding, environment and stress on a sample.

In this Thesis, Raman spectroscopy was used to prove the presence of the tetragonal phase in the perovskite thin films. Raman spectroscopy was performed directly in the thin films using a JY Horiba LabRam model HR800 equipment, with a high-resolution 800 mm focal length spectrometer. An argon ion laser beam at a wavelength of 325 nm was utilized.

2.2.7 Atomic Force Microscopy (AFM)

Atomic force microscopy (AFM) was developed in 1985 by Binning, Quate and Gerber.[172] This technique is a variant of scanning probe microscope (SPM) and it is used to image surface profile. SPM is the general term describing a crescent number of techniques which use a sharp probe to scan over a surface and to measure certain properties of this surface. Some examples are scanning tunneling microscopy (STM), AFM and Near-Field Scanning Optical Microscopy (NSOM).

AFM was developed to overcome a basic drawback of STM, which is applicable to conducting or semiconducting surfaces.

AFM works on two basic modes: contact mode and non-contact mode. In contact mode AFM, the tip (scanning probe) mounted on the cantilever is in perpetual contact with the sample and this is scanned using piezoelectric actuators (Figure 2.7 a). The deflection in Z of the cantilever is monitored by laser spot reflected from the cantilever to the mirror and photodiode. This signal passed to the feedback system which allow the mapping of the sample surface. In feedback mode, output signal usually adjusts the Z position of the scanner to maintain a deflection setpoint. During the interaction between the tip and the sample surface, the tip amplitude, frequency, magnitude change. These signals are converted to get topography profile of the samples.[173]

As mentioned, the other mode of AFM operation is non-contact or tapping mode (Figure 2.7 b). In this mode the cantilever is placed at some particular Z distance from the sample, where the tip mechanically oscillates near to its resonance frequency (usually the fundamental resonance). When the tip is in contact with the sample forces the oscillation amplitude of the tip vibration reduces or increase by nm. In feedback mode, output signal usually adjusts the Z position of the scanner to maintain an amplitude setpoint. In simillary to the contact mode, this change in amplitude is monitored by the photodiode in order to acquire the topography of the sample. The major advantages of the tapping over contact mode are the better resolution due to the negligible lateral forces and less wear of the tip.[173]

AFM technique can be applied to almost any type of surface, conducting or insulating samples.[174] Through AFM it is possible to obtain real topographical image of surfaces. The typical horizontal and vertical distance resolutions are about 0.2 nm and 0.01 nm respectively. The later value is much better than the values achieved using SEM and TEM.

Moreover, the scanning area is from several nanometers to hundred of nanometers. In terms of the resolution, AFM technique is comparable to TEM and it can provide higher resolution than normal SEM. One of the most important characteristics of AFM is that it can be applied easily used in vacuum, ambient air or even at liquid environment without lossing atomic resolution. Worthwhile to mention as well that this

technique is used not only for characterization, like surface observation but also for fabrication, namely as microfabrication of surfaces as in the semiconductors industry.[175]

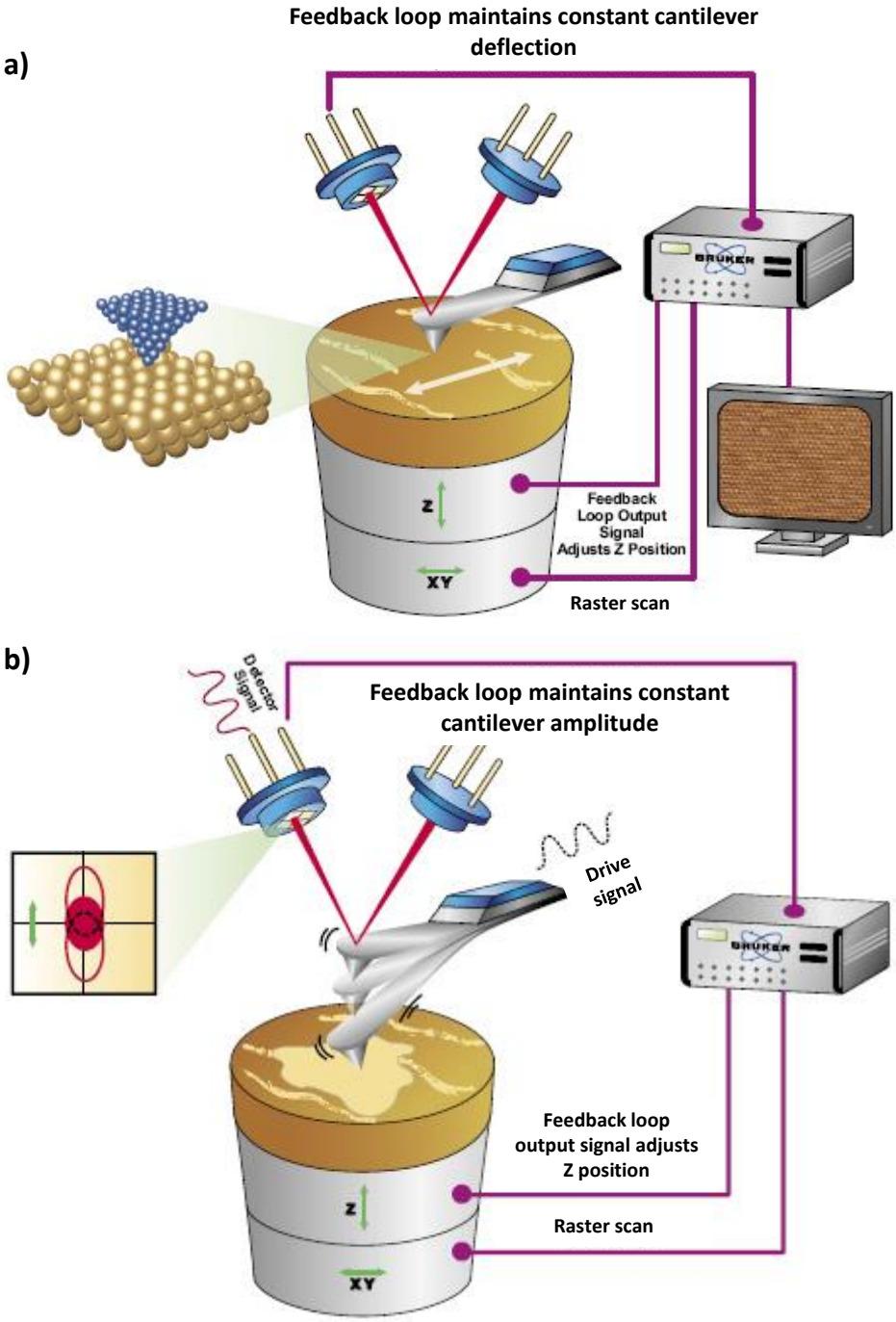

Figure 2.7: Schematic representation of the AFM working principle: a) contact mode and b) tapping mode or non-contact [adapted from reference 176].

Within the context of this thesis, through AFM it was possible to assess nanoporous and nanopatterned thin films, quantifying porous diameters and wall thickness between the pores. As different equipments were used, more details about them and experimental conditions can be found in the Chapter 4, 6 and 7.

2.2.8 Piezoelectric Force Microscopy (PFM)

Nowadays, PFM is a powerful tool for the characterization of ferroic thin films. This technique became a standard method during the past years to study of FE behavior, namely domain dynamics and switching, fatigue and retention mechanisms, as well as of phase transitions in ferroic materials.[177]

In general, PFM is carried out in contact mode using a conductive tip (moveable nano electrode).

The working principle of PFM is based on the detection of local vibrations of a FE or piezoelectric sample induced by an alternative current (AC) signal with an optional direct current (DC) offset bias applied between the conductive SPM tip and the bottom electrode of the sample, thus establishing an external electric field within the sample.[177] Due to the converse piezoelectric effect, the samples will locally expand or contract according to the applied electric field as illustred in Figure 2.8.

When the applied electric field is parallel to the material polarization direction, the material expands. The contraction of the material happens if the applied electric field is anti-parallel.[178] The local oscillations of the sample surface are transmitted to the tip and detected using a usual lock-in technique, Figure 2.9.[179]

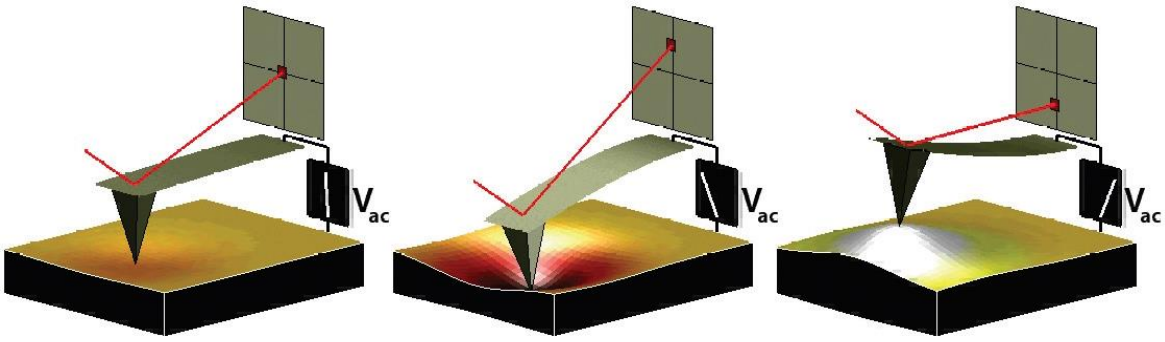

Figure 2.8: Illustration of PFM working principle. The change of cantilever deflection is directly related to the expansion or contraction of the sample electric domains, and hence proportional to the applied electric field [adapted from references 180].

The signal at the lock-in output is denoted piezoresponse signal (PRS).[177] The PRS oscillates in-phase with the AC modulating field if the polarization is parallel to the field, and out-of-phase if anti-parallel.[178,181]

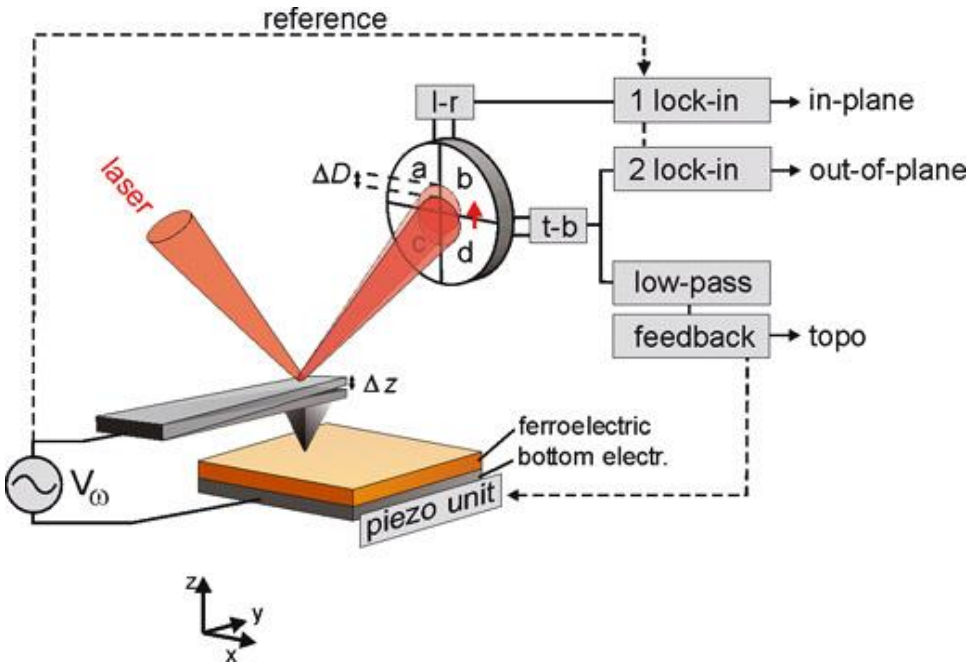

Figure 2.9: Schematic PFM setup, acquiring simultaneously the topography and the in- and out-of-plane component of the polarization. A function generator is used to apply an alternating voltage Vω between the tip and the bottom electrode of the FE, [adapted from reference 182].

In order to observe domain switching, the applied AC voltage in PFM imaging should be much lower than the coercive bias because otherwise, the local domain structure of the studied sample can be modified. Moreover, the frequency of the applied AC voltage, should be also lower than the fundamental resonance frequency and the first contact resonance of the AFM cantilever in order to observe the true response from the sample.[177,178,181]

Three typical PFM modes were used in this Thesis: Vertical-PFM (VPFM), Lateral-PFM (LPFM), and piezoresponse force spectroscopy (PFS). For the VPFM and LPM, the phase contrast obtained reflects the domain polarity in different sample locations, while from the magnitude of the amplitude signal local piezoelectric coefficient of the sample can be observed.

VPFM imaging is based on measuring the out-of-plane polarization by recording the tip deflection signal at the frequency of modulation. This out-of-plane piezoresponse signal (OPPRS) is extracted from the z-deflection signal given by the detector electronics, and represents the local oscillations perpendicular to the plane of the sample surface (Figure 2.10a).[177,183]

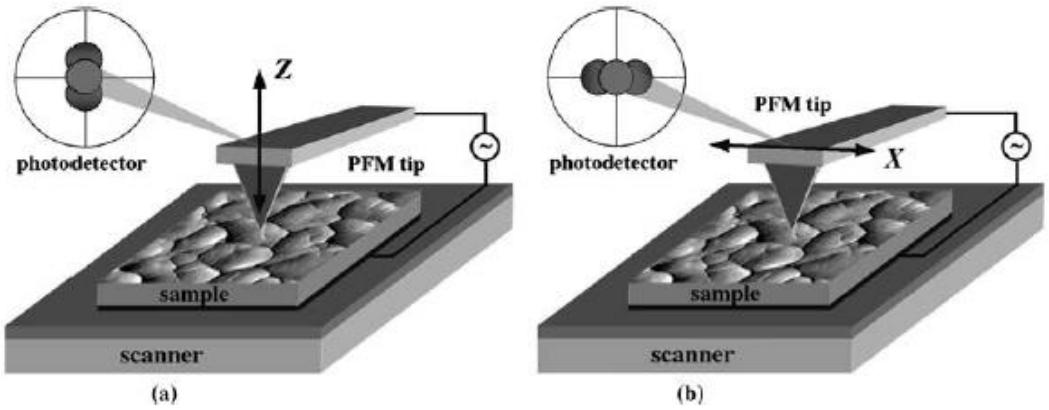

Figure 2.10: Schema of the vertical (a) and lateral (b) PFM signal detection. [adapted from reference 183].

Similarly, LPFM imaging is based on measuring the in-plane component of the polarization reflected as the lateral motion of the cantilever due to bias-induced surface shearing, Figure 2.10b. Thus, the in-plane polarization is obtained from the x-deflection signal (usually denoted friction). It represents the oscillations of the surface perpendicular to the cantilever, in the plane of the film, and is denoted in-plane piezoresponse signal (IPPRS).[177,183]

PFS is a non-imaging, point spectroscopy technique that complements the PFM. In PFS, the piezoresponse of the sample at a given location on the sample can be mapped versus, for example, the DC bias ($V_{DC\text{-}tip}$), or the frequency of the AC signal (V_{AC}) applied to the sample using the tip. Thus, PFS can be used to generate the local hysteresis loops in FE material locally, Figure 2.11.

During the hysteresis loop, a sine wave is carried by a square wave that steps in magnitude with time, as illustrated in Figure 2.11. Between each voltage step, the offset is stepped back to zero. The AC bias is applied in order to determine the bias-induced change in polarization distribution (e.g., the size of the switched domain). It is then

possible to see the hysteresis curve of the switching of the polarization of the surface, bottom diagram in Figure 2.11.[179,184,184]

From these techniques it is possible to evaluate the piezoelectric behavior through the PFM imaging of the samples as well as the FE by the hysteresis loop. From the hysteresis loops it is possible to obtain detailed information on the local FE behavior such as critical voltage, coercivity, imprint, switchable polarization, remanent piezoelectric coefficient and effective piezoelectric coefficient $(d_{33})_{eff}$.

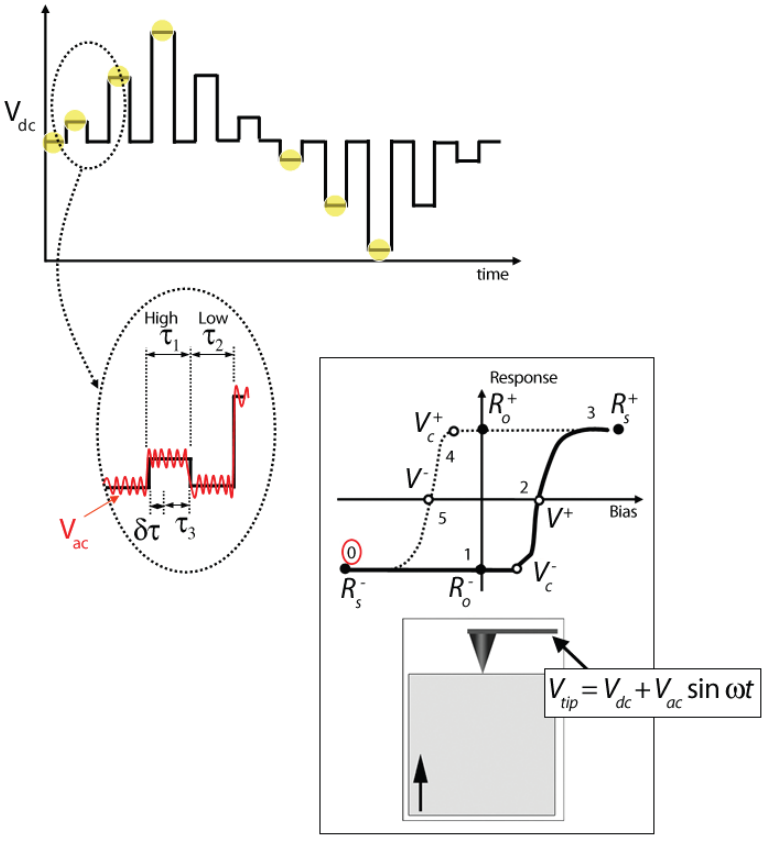

Figure 2.11: Switching spectroscopy PFM diagram, [adapted from reference 184 and 185].

As different equipments were used, more details about the equipments and experimental conditions can be found in the next Chapters.

We acknowledge COST Action MP0904 SIMUFER for funding my Short Term Scientific Mission in Nanoscale Function group of Conway Institute of Biomolecular and Biomedical Research in Ireland to deep learning about all PFM theory and experimental conditions details.

2.2.9 Magnetic Force Microscopy (MFM)

MFM, is another powerful technique for the characterization of FM thin films. In this technique, the interaction force should be dominated by the magnetic force between the magnetized tip and magnetic sample. However, in addition to the magnetic forces, Van der Waals forces always exist between the tip and the sample. These Van der Waals forces vary according to the tip-sample distance, which are therefore used to measure the surface topography.[178]

A MFM image is obtained by measuring either the amplitude or the phase change of the cantilever oscillation as a result of the magnetic force between the surface and the magnetized MFM cantilever at a certain distance from the surface (i.e., a lift mode technique). The collected images contain information on magnetic domain distributions at the sample surface.[178] Figure 2.12 illustrates the working principle of MFM technique.[178]

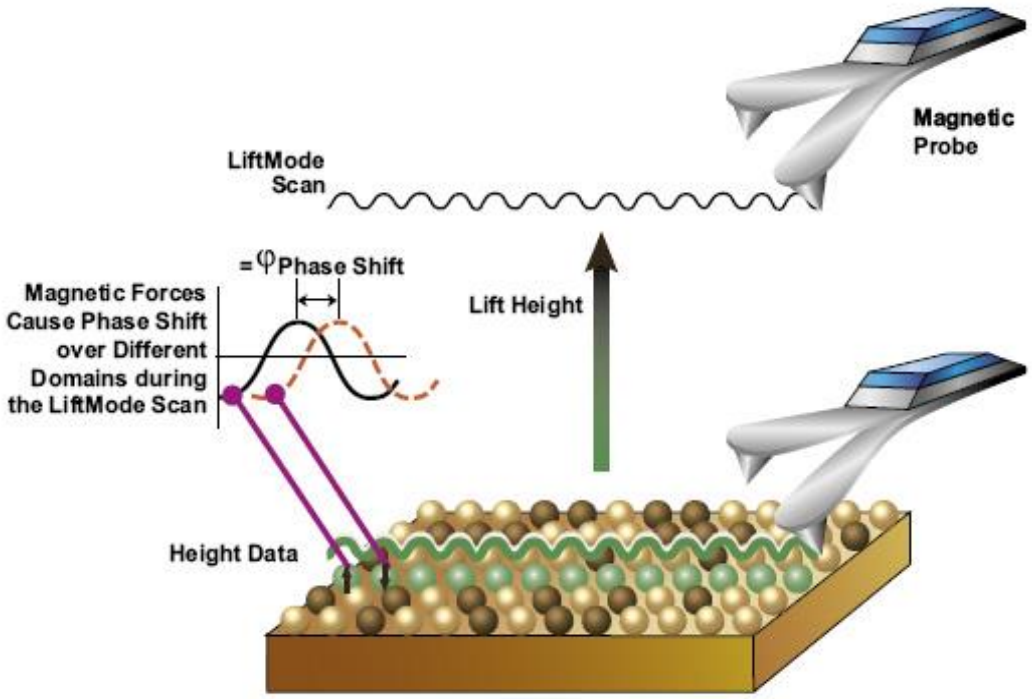

Figure 2.12: Illustration for MFM measurements, [adapted from reference 176].

Basically in the MFM technique, a first scan to obtain the sample topography is performed in tapping mode. In this case, as the tip-sample distance is reduced, the Van der Waals forces are dominant. After this scan, the set-point is varied to place the tip in

the region where the magnetic forces are dominant and used to scan the MFM imaging. In this second scan, the tip-sample distance is increased and the biased tip is scanned along with the topography line (Figure 2.12). The tip is only affected by the magnetic force and a MFM image is obtained.[178]

Through MFM it was possible to assess the local magnetic behavior in the nanoporous composites, nanopatterned and dense thin films as well as in nanopatterned composite thin films.

As different equipments were used, more details about the equipments and experimental conditions can be found in the Chapter 5, 6 and 7.

2.2.10 Superconducting Quantum Interface Device Magnetometer (SQUID)

Superconducting Quantum Interface Device Magnetometer, SQUID equipment consists of Josephson junctions that have two superconductors, separated by a thin insulating layer and acts as a flux-to-voltage transducer, Figure 2.13.

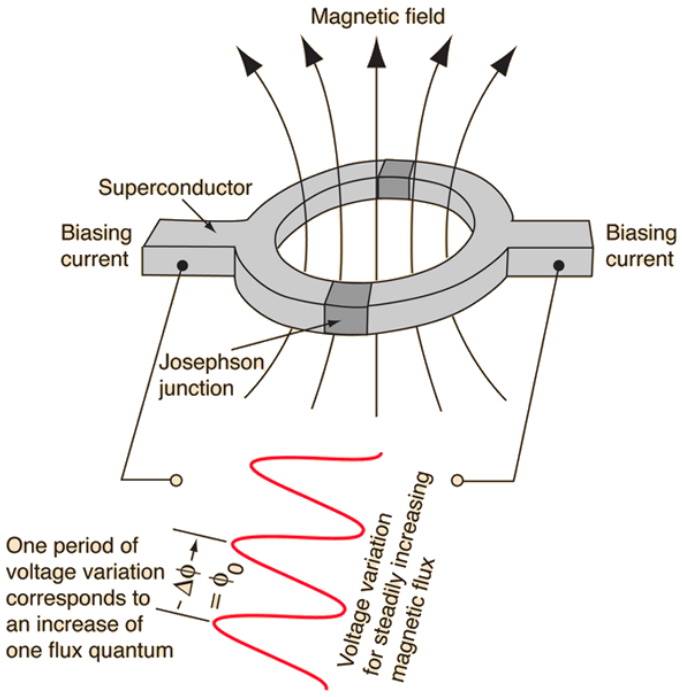

Figure 2.13: Schematic of a SQUID system, [adapted from reference 186].

The SQUID uses the properties of electron-pair wave coherence and Josephson Junctions to detect very small magnetic fields allowing to determine the magnetization

of a sample with high precision as a function of parameters as external magnetic field or temperature.[186] Separately from the shielding currents in the superconducting loop, only currents induced by the movement of the magnetic sample inside the gradiometer pickup coils are flux-coupled into the SQUID loop.[186] Through SQUID measurements it was possible to assess the macroscopic magnetic behavior in the nanoporous composites, nanopatterned and dense thin films as well as in nanopatterned composite thin films. SQUID measurements in parallel and perpendicular film configurations relative to the applied field direction were performed using a Quantum Design MPMS magnetometer.

As the experimental conditions depending on the measured sample, more details can be found in the Chapter 5, 6 and 7.

All measurements were performance by Professor Liliana Ferreira and Professor Margarida Godinho at the Biosystems and Integrative Sciences Institute (BioISI), Faculdade de Ciências, University of Lisbon.

CHAPTER 3

Role of the nanoporosity on the local FE properties of $PbTiO_3$: modelling and experimental observation

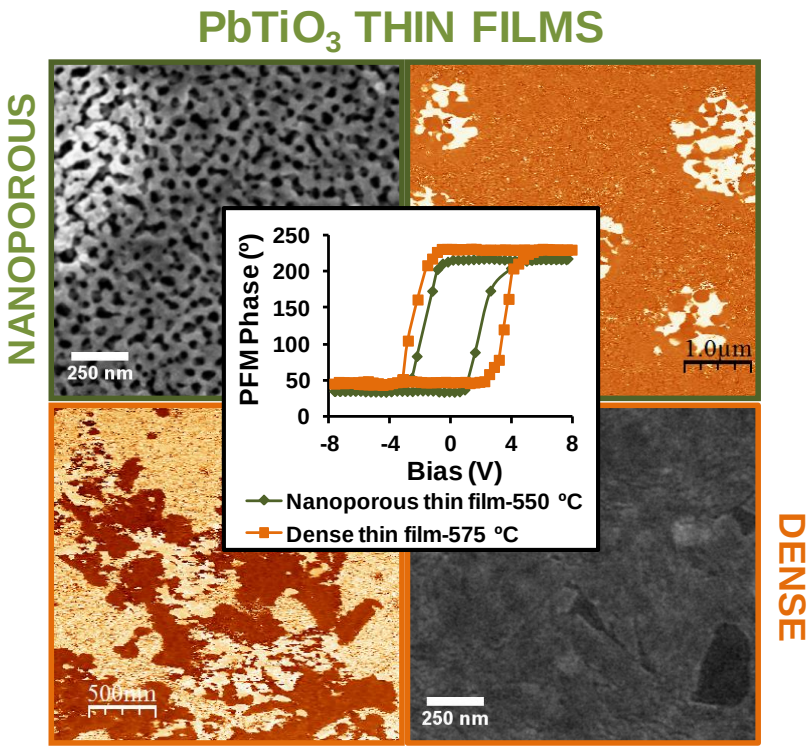

Graphical abstract: Nanoporous films with improved tetragonality at lower temperature than the dense films exhibit enhanced piezoelectric coefficients, switchable polarization and low local coercivity.

Abstract

Nanoporous and dense ferroelectric PbTiO3 thin films are prepared by a modified sol-gel process. The presence of nanoporosity, with ~ 50 nm pore size formed using a block polymer as a structure-directing agent, markedly affects the microstructure, crystallization and ferroelectric film´s properties. The crystallization of the tetragonal phase is enhanced in nanoporous films. It is suggested that the decomposition of the block-copolymer in porous films triggers the crystallization of the perovskite phase at low temperatures via the local increase of temperature.

Finite Element Model is used to exploit the possibility of improving the coercivity (here meaning the coercive field) of thin and ultrathin films by engineering the material microstructure. It is theoretically predicted that nanopores with sizes and interdistances lower than the ferroelectric domain sizes act as dispersion centers and

create electric field instabilities. The polarization switching is facilitated, decreasing the coercive field. These predictions are proved experimentally by VPFM, which clearly show that nanoporous films with improved tetragonality exhibit enhanced piezoelectric coefficients, switchable polarization and low local coercivity. Nanoporosity markedly affects the microstructure, crystallization and ferroelectric properties. By providing a means of achieving enhanced properties, nanoporosity may have a broad impact in applications of ferroelectric thin films. Our work clearly demonstrates that nanoporosity contributes to decrease the coercive field of thin and ultrathin films and, as so to solve a main limitation of scaling ferroelectrics. This demonstration has broad implications in the micro- and nano-electronic applications of ferroelectrics.

Index

3.1 Introduction

As mentioned in the Chapter 1 owing to the trend of device miniaturization, integration and multi-functionalization, FE thin films have attracted the attention due to their original properties which can be used in the development of advanced functional devices such as: non-volatile memories, mechanical sensors and actuators, pyroelectric detectors and tunable microwave and electro-optical devices, among others. With miniaturization of circuitry and devices new fundamental challenges arise and in what concern the materials: *i)* how thin a thin film can be before ferroelectricity is vanished due to intrinsic size effects?; *ii)* how domain structure and related properties behavior, as transport depend on thickness?; and *iii)* how to enhance the surface and interface areas? are some of the questions that need to be answered.

During the last two decades a variety of computer-based simulations and calculation methods scaling from the atomic level to meso- and macroscale, have been developed to study in detail FE domain structures and new emerged functionalities in FE and FM materials for nanoelectronics applications. Some examples of these methods are the first-principles calculation, molecular dynamics (MD) simulation, Monte Carlo (MC) simulation, effective Hamiltonian method and phase field method. Other theoretical models such as the phenomenological Landau theory, soft mode theory and Ising model have been also established to understand the FE phase transition behaviors and FE domain configurations.[11,28,35,187] Nevertheless, none of these models and

simulation techniques predict the functional properties in the most composite nanostructures.

For these materials, methods as: *i)* Maxwell-Garnett (MG) approximation; *ii)* Bruggeman (BG) approximation and *iii)* Lichtenecker (LI) mixing formulae are the most common effective medium approximations (EMA) models for predicting electrical properties (as the permittivity) in composites.[188]

The Finite Element Model (FEM) is another approach to calculate the electric field distribution inside a composite and the effective dielectric permitivity.[188] By comparison with EMA approaches, FEM is the most complete method because takes into consideration the microstructure of the composites, the local permittivity, and performs a more rigorous calculation of the local potential without supplementary approximations.[188] As porous thin films can be considered as composites due to the FE / air interface existence, the FEM approximation can be used to model the role of the nanoporosity on the FE properties, as is the case of the present work.

In one of our recent works,[142] we already described the preparation of $BaTiO_3$ and $PbTiO_3$ nanoporous thin films however, the role of the nanoporosity on the microstructure development and phase evolution and the relations between nanoporosity and the electrical properties at the nanoscale have not been addressed. Up to now, the porosity is considered as a defect (or secondary phase) with a detrimental effect in the electrical macroscopic response.

$PbTiO_3$ with a high polarizibility, strong spontaneous polarization (81 $\mu C/cm^2$), high T_C (around 490 °C), a large tetragonality (c/a = 1.06) and high pyroelectric coefficient is the material choice for this study.[189,190,191] Nanoporous $PbTiO_3$ thin films were prepared through sol–gel templating using a commercial amphiphilic block-copolymer, PS40-*b*-PEO53, as a structure-directing agent. The structure and microstructure evolution is followed by X-ray diffraction (XRD), Raman spectroscopy and scanning electron microscopy (SEM). The local electromechanical response of the nanoporous and dense thin films is, for the first time, theoretically predicted by FEM and experimentally assessed by VPFM and piezoresponse force spectroscopy (PFS). By comparing the structure and properties of nanoporous and dense $PbTiO_3$ films, prepared under identical conditions, the relations between nanoporosity and local piezoelectric

response are established. The role of nanoporosity on the phase and microstructure development of FE $PbTiO_3$ films is proposed.

3.2 Experimental part

Nanoporous $PbTiO_3$ films were prepared based on the procedure described in reference.[142] Polystyrene-*b*-poly(ethylene oxide) (PS-*b*-PEO) block-copolymer with MW_{PS} = 40 000 $gmol^{-1}$, MW_{PEO} = 53 000 $gmol^{-1}$, PS40-*b*-PEO53, from Polymer Source, was used as a structure-directing agent. Three solutions were prepared. In solution A, PS40-*b*-PEO53 block-copolymer (75 mg, Polymer Source) was dissolved in tetrahydrofuran (5.62 mmol, Sigma-Aldrich, purity ≥ 99.5%) at 70 ºC. Subsequently, and under stirring, absolute ethanol (26.42 mmol, BRAND) was added drop by drop. Solution B was prepared by the dissolution of lead (II) acetate trihydrate (0.60 mmol, Fluka, purity ≥ 99.5% w/w) in glacial acetic acid (Merck). Solution C was prepared from mixing 2,4-pentanedione (0.43 mmol, Fluka, purity 99.3% w/w) with titanium (IV) n-butoxide (0.60 mmol, Merck, 98.0% w/w) under stirring at room temperature. Afterwards, solutions B and C were added to solution A, forming the final solution. For the dense thin films, a similar procedure was used, however solution A was prepared without the block-copolymer.

Nanoporous and dense thin films were deposited by dip-coating onto 1.0 x 2.0 cm^2 sized slides of platinized silicon substrates ($Pt(111)/TiO_2/SiO_2/Si(100)$) (Inostek Inc.). In order to get similar film thicknesses (around 100 nm), the withdrawal rates were adjusted to 0.493 mm/s (nanoporous) and 0.761 mm/s (dense). All films were thermally treated in air at 350 °C in order to complete the inorganic condensation (mesostructuration) of the matrix and to decompose the organic content. Films were then annealed for 5 min at the desired temperatures to achieve crystallization. To follow the phase formation process, TGA-DSC were carried out on dried nanoporous and dense powders obtained by drying the solutions described above in open vessels at 60 ºC for few days. TGA was carried out on a Setaram Labsys™ TGA-DSC16 system with a heating rate of 10 °C/min under flowing air up to 600 °C. DSC was performed in a DSC50 Shimadzu system with a heating rate of 5 °C/min under flowing air up to 600 ºC. The crystalline phases in the films were identified by XRD using a Philips X'Pert MPD X-ray diffractometer with Cu Kα radiation, 2 ° grazing incidence angle

and a step length of 0.02 °. Raman spectroscopy was performed in JY Horiba LabRam model HR800 equipment, with a high resolution 800 mm focal length spectrometer. An argon ion laser beam at a wavelength of 325 nm was utilized. The film microstructure was investigated by high-resolution SEM using a SU-70 Hitachi microscope.

VPFM was carried out on an AFM system (JPK, Nanowizard II, with a lock in amplifier, SRS Stanford Research Systems), using DPE-18 cantilevers with Pt-coated tips (Mikromasch, resonant frequency of 60−100 kHz, force constant of 1.1−5.6 N/m). Topography signals of the film surface were taken simultaneously with the amplitude and phase signals and were collected in contact mode. Since the results were obtained with the same type of cantilevers and under identical scanning and acquisition conditions, comparison between films can be made. PFS as function of the applied potential between the platinized substrate and the conducting tips was performed on an MFP-3D AFM (Asylum). Several hysteresis loops with bias from - 8 to + 8 V were obtained for each sample to ensure the reproducibility of the results, and representative loops are presented. The piezoelectric and FE properties are mean values taken from several hysteresis loops, at least twenty for each sample. The imprint is defined as $I_m = (V^+ + V^-) / 2$, where V^+ correspond to the positive coercive bias and V^- to the negative coercive bias and these bias values were taken from the phase signal. Remanent piezoelectric coefficients were taken from amplitude signal for zero bias values. Switchable polarization corresponds to the difference between the positive saturated piezoresponse and negative ones ($R_m = (R_S)^+ - (R_S)^-$) taken from the mixed hysteresis loops. As the effective piezoelectric coefficient ($(d_{33})_{eff}$) is proportional to the amplitude signal, this can be defined as $(d_{33})_{eff} \propto$ (amplitude signal . cos(phase signal)) / V_{ac}, where V_{ac} is the ac voltage applied. The absolute values of d_{33} were not determined, but as the results were acquired with the same cantilever and under identical scanning and acquisition conditions, the comparison of the relative values of piezoelectric coefficients for each film can be established.

3.3 Results and discussion

3.3.1 Microstructure and structure characterization

Figure 3.1 presents TGA-DSC analyses of nanoporous and dense $PbTiO_3$ precursor gels. The TGA curves (Figure 3.1a) of these gels have a similar profile and three main regions can be identified: region I from room temperature up to 200 ºC, in which the weight losses for both gels is around 5% and attributed to the loss of residual water and evaporation of organics; region II in which the weight losses are 20% for the case of dense gels (from 200 to 330 ºC) and 32% for the porous ones (from 200 to 450 ºC) and assigned to decomposition of organics; and region III in which the weight losses are almost constant up to 600 ºC, reaching a value of 5% for both gels and attributed to the decomposition of residual species. Note that the temperature interval of region II is wider for nanoporous than for dense precursor gels.

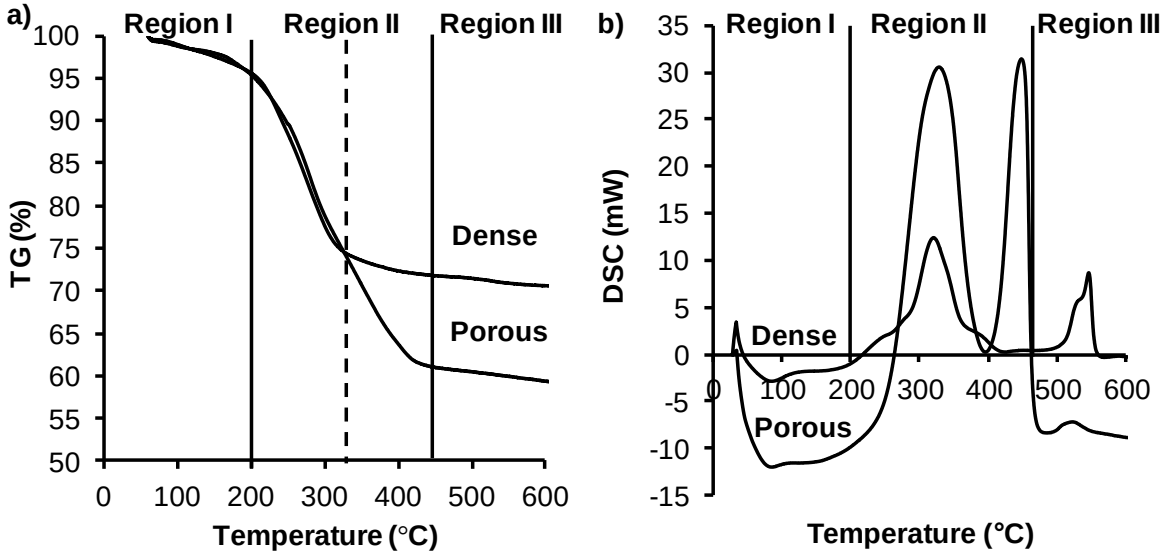

Figure 3.1: TGA-DSC of precursor gels of nanoporous and dense $PbTiO_3$ films. The TGA curves of nanoporous and dense gels are quite similar, with a significant weight loss from room temperature up to 450 ºC. The DSC curves clearly show that the crystallization occurs at an earlier temperature in the case of the nanoporous films when compared with the dense ones.

DSC analysis (Figure 3.1b) of nanoporous and dense gels also present similar thermal profiles, although the intensity of the thermal effects is different. These curves are characterized by three main thermal effects in the case of nanoporous gels and just

two in the case of the dense ones. For nanoporous gels, the two intense exothermic peaks between 200 and ≈450 ºC corresponding to region II in DSC are related with the decomposition of organics and block-copolymer degradation. The block-copolymer used in the solution preparation is formed by two different copolymers (PS and PEO) with different degradation temperature. The third exothermic peak, between 450 and 600 ºC (region III) is attributed to the crystallization of the perovskite phase. In the case of dense gels, just one and less intense peak is observed in region II. This fact is due to the absence of the block-copolymer in this case and it is in line with the TGA behavior indicating that the energy released in this temperature interval is higher when compared with dense precursor gels. The peak observed in region III corresponds to the crystallization phase as observed in the nanoporous case. However, in the case of nanoporous the crystallization occurs at lower temperature than in the dense ones.

Figure 3.2 depicts top view SEM micrographs of nanoporous and dense $PbTiO_3$ thin films thermally treated at different temperatures and illustrates the different microstructure evolution of both films. Nanoporous thin films thermal treated at 500 ºC (Figure 3.2) present a porous microstructure with a certain degree of order and periodicity. Pore size is around 50 nm. Pore order and periodicity results from the self-assembly of micelles of the amphiphilic block-copolymer, followed by condensation of the inorganic species around the micelle arrays. During the thermal decomposition of the block-copolymer void motifs are created. According to the thermal analysis, this takes place between 200 and 450 ºC (Figure 3.2). As the temperature of the heat treatment increases, the microstructure of the porous films varies, from a somehow organized pore arrangement to an interconnected porosity. At 550 ºC, the walls between the pores start to collapse and pores become connected, but the film remains porous. For high temperature treatments, pore connectivity increases and simultaneously the relative area of dense zones increases as well, corresponding to film densification promoted by the heat treatment. For thin films treated at 600 and 625 ºC, the organization of the pores is significantly degraded. In addition, as the treatment temperature increases, bright areas appear (~ 550 ºC), which become increasingly larger. Comparatively and as expected, the microstructure is denser and crack-free for the case of dense films. These films heat treated at 550 ºC are amorphous.

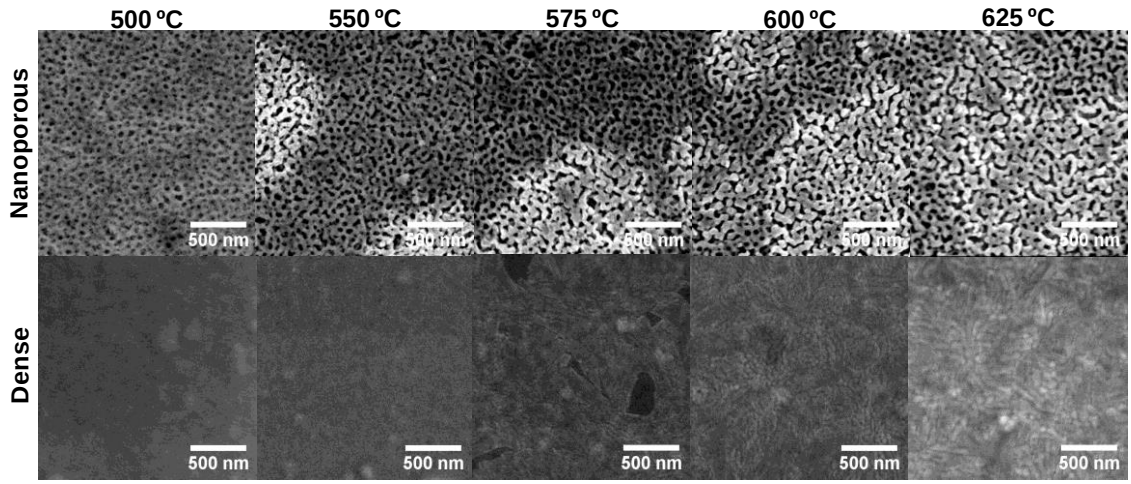

Figure 3.2: SEM micrographs illustrating the typical morphology of nanoporous and dense $PbTiO_3$ thin films after thermal treatment at: 500, 550, 575, 600 and 625 ºC. As the temperature of the thermal treatment increases, the porosity order is lost, pores become interconnected and dense areas increase. A well-defined grain pattern with increasing of grain size with annealing temperature characterizes $PbTiO_3$ dense films.

As the annealing temperature increases, dense films crystallize and a well-defined grain pattern can be observed. The growth of the grains is evident in films annealed at 625 ºC.

Figure 3.3 shows the XRD patterns of nanoporous and dense $PbTiO_3$ thin films treated at different temperatures. Nanoporous thin films heat treated at 550 ºC are mainly amorphous but some diffraction peaks associated with crystalline $PbTiO_3$ are already visible at *ca.* 22, 32 and 45º 2θ. At this temperature, it is not possible to differentiate between the cubic and tetragonal structure of $PbTiO_3$ (JCPDS no. 00-040-0099 and 00-003-0721, respectively). For heat treatments at and above 575 ºC, the film crystallinity increases and the tetragonal phase can be easily identified by the splitting of the diffraction peaks at 22.43, 31.92 and 45.79 into 21.45, 22.78, 31.47, 32.77, 43.69 and 47.56 º 2θ, respectively. However, the concomitant presence of both cubic and tetragonal phases is possible. In the case of the dense films, those heat treated at 550 ºC are clearly amorphous (Figure 3.3). At 575 ºC, dense thin films start to show some degree of crystallinity.

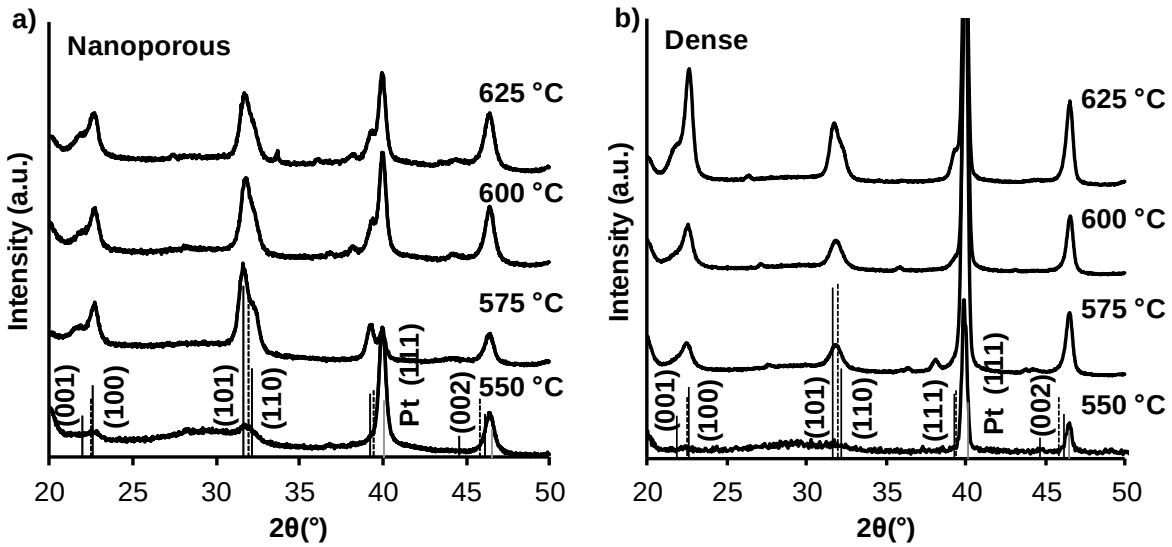

Figure 3.3: X-ray diffraction patterns of nanoporous and dense $PbTiO_3$ thin films thermally treated at: 500, 550, 575, 600 and 625 ºC. Solid black vertical lines correspond to the tetragonal (JCPDS no 00-003-0721) and dashed vertical lines correspond to cubic (JCPDS no 00-040-0099) crystalline phase of $PbTiO_3$. The gray lines correspond to the Pt layer of the substrate. Tetragonal $PbTiO_3$ phase crystallizes at lower temperatures in the case of nanoporous films (575 ºC).

The tetragonal crystallographic phase is visible for the heat treatment of 625 ºC, with a clear splitting of the diffraction peaks as described above. These results confirm the previous indications that $PbTiO_3$ nanoporous thin films crystalize at lower temperatures than their dense counterparts.

To verify these observations, Raman spectroscopy studies were conducted (Figure 3.4). Nanoporous thin films treated at 525 ºC do not present the typical Raman modes of the tetragonal phase. The main peak of the tetragonal phase is the peak that appears at 324 cm^{-1}. For films heat treated at 575 ºC or 625 ºC, the presence of E+B1, A1 (2TO), E(3TO) and A1(3TO) bands at 287, 324, 503 and 599 cm^{-1}, respectively, indicate the presence of the tetragonal phase, as previously reported for other $PbTiO_3$ and lead zirconate titanate thin films.[192,193,194] The Raman peaks are slightly shifted to low wavenumber in relation to single crystal values,[195] probably due to strains induced by the substrate. In the case of dense thin films, tetragonal modes start to be observed only at 625 ºC, in agreement with the XRD observations. The formation of the tetragonal phase in nanoporous $PbTiO_3$ thin films occurs at a lower temperature than in the case of dense ones. Because the tetragonal phase is the one responsible for

ferroelectricity in ABO_3 perovskite type materials, we therefore expect some differences in terms of the electrical/electromechanical behavior between these thin films.

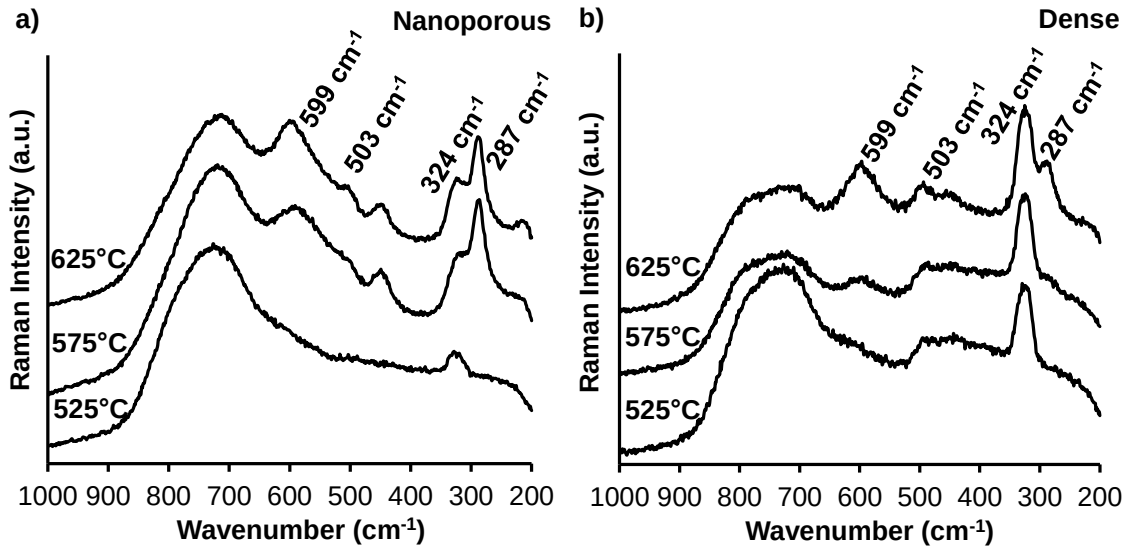

Figure 3.4: Raman spectra of nanoporous and dense $PbTiO_3$ thin films thermally treated at: 525, 575 and 625 ºC. Raman spectroscopy proves the early crystallization of tetragonal $PbTiO_3$ phase in nanoporous films.

3.3.2 Modelling of local electric properties using FEM

In order to predict and understand the role of porosity on FE properties, FEM was applied to our films by Dr. Leontin Padurariu during a Short Term Scientific Mission at the University of Aveiro financed by the COST Action MP0904 SIMUFER. This work was supervised by Professor Liliana Mitoseriu from University "Alexandru Ioan Cuza", Iasi, Romania.

Through the FEM model different types of microstructures similar to the ones observed by SEM, Figure 3.2, were numerically generated. The numerically generated microstructure represented in Figure 3.5a shows a good representation of the nanoporous thin films heat treated at 625 ºC with 35% of porosity. For comparison and to investigate the role of the porosity on switching properties the numerically generated microstructure of dense thin film counterpart is represented in the Figure 3.5b. The heat treatment temperature was chosen take into account the high degree of crystallinity for both thin films. Considering these microstructures, the local field was computed by solving the Laplace's equation, $\nabla.(\varepsilon \nabla V) = 0$, considering the permittivity of the FE

bulk 1000 and 1 for air. The film thickness was kept constant and the potential on the bottom electrode was considered zero and 1 Volt on the top electrode. A top layer of air was also considered due to the presence of the empty pores. However, its thickness do not affected the final results whereas a FE / air interface always removes the normal component of the field on the interface inside the FE. In other words, the electric field inside the FE is tangent at interfaces with air. The real local electric field inside the system was thus computed as the gradient the potential: $\vec{E}_{local} = -\nabla V$. Figures 3.5a and 3.5b show the electric potential and field distribution at an applied bias under the same scaling dimensions for nanoporous and dense thin films, respectively. For the dense thin films, Figure 3.5b, the local field is located under the PFM tip and it is not enough to switch the dipoles. As a consequence, a high applied bias value is necessary to switch a very small FE volume. Such high applied bias value is not favorable since it leads to the appearance of the cross-talk effect provoked by the domain movement or thermal diffusion.

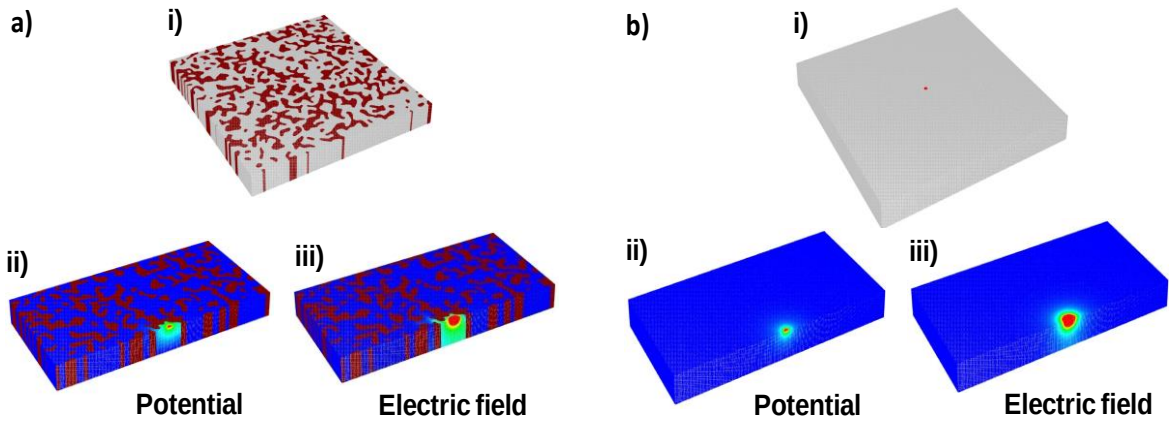

Figure 3.5: Simulations of the electric potential and electric field distribution on; a) nanoporous and b) dense thin films with the same thickness and under a nanosized PFM tip. A FE/air interface was considered.

Otherwise, for nanoporous thin films, when the FE / air interfaces (pores) are close to the PFM tip, the field goes more deeply inside the material, needing a lower applied bias to be switched. The introduction of vertical FE / air interfaces (vertical porosity) in FE thin films leads thus to a favorable local field distribution of the switching process since the pores inhibit the dipole-dipole interactions at long-range and cross-talk phenomena, favoring the reverse polarization for lower applied bias when

compared to the dense structures. This is a relevant observation, since our model predicts that the existence of nanoporosity in a FE thin film can facilitate domain switching and so overcome one of the major hurdles of thin films related with the increase of the coercive field. Hence, the local domains (bits of memory) written in various positions are more stable in time in this kind the structures because they are separated by pores (no dipole-dipole interactions and no crosstalk).

These very interesting predictions were checked by experimental observations. Using VPFM and PFS the local piezoelectric and FE behavior of nanoporous and dense sol-gel based $PbTiO_3$ thin films were assessed.

3.3.3 Local electric properties: Experimental observation

Figures 3.6 and 3.7 represent the topography and VPFM amplitude and phase images of nanoporous and dense $PbTiO_3$ thin films thermally treated at different temperatures. The dark domains in the VPFM phase images correspond to domains in which the polarization is oriented towards the substrate (phase = -180 °), while bright regions correspond to domains with polarization oriented towards the free surface of the films (phase = 180 °). Since sol-gel and self assembly methods have as drawback a random size distribution of the deposited nanograins and VPFM is sensitive to the component of polarization normal to the film surface, grains with in-plane polarization exhibit an intermediate contrast. Nanoporous thin films thermally treated at 500 and 525 ºC do not present piezoelectric response what is related with their incipient degree of crystallinity. In the topography images of the different nanoporous thin films, pores and grains are not clearly defined due to the use of contact mode, in which the tip convolution effect is more evident.[142] For all nanoporous thin films, the topography and VPFM amplitude and phase images reveal the presence of two distinct phases exhibiting different piezoelectric behavior, in analogy with the two regions (bright and dark) observed in the SEM microstructures (Figure 3.2). The dimension of the area with strong piezoelectric response (the bright areas in SEM micrographs) increases with the increase of the heating temperature, and in accordance with the enhancement of the degree of crystallinity and tetragonal distortion as observed by XRD and Raman (Figure 3.3 and 3.4).

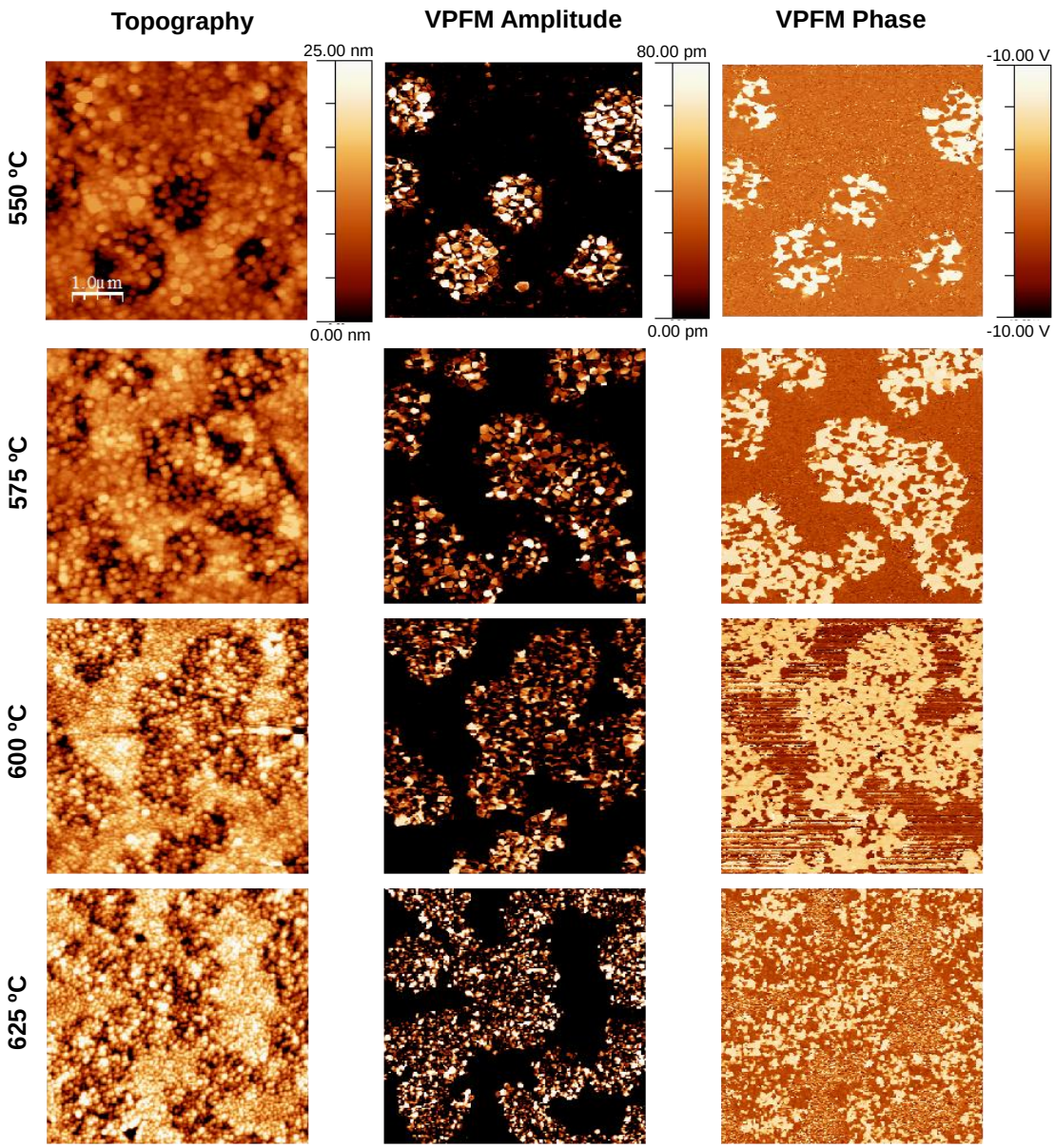

Figure 3.6: Topographic and VPFM amplitude and phase images of nanoporous $PbTiO_3$ thin films after thermal treatment at 550, 575, 600 and 625 ºC. The data scale for all topographic images is between 0 to 25 nm, for amplitude at 575, 600 and 625 ºC is between 0 to 250 pm and for all phase images is between -10 to 10 V. This 20 V scale corresponds to 360 º, thus opposite domains oscillate 180 º out-of-phase, as expected. The dimension of the areas with strong piezoelectric behavior increases as the heating temperature increases as a consequence of the increasing crystallinity and tetragonal phase content.

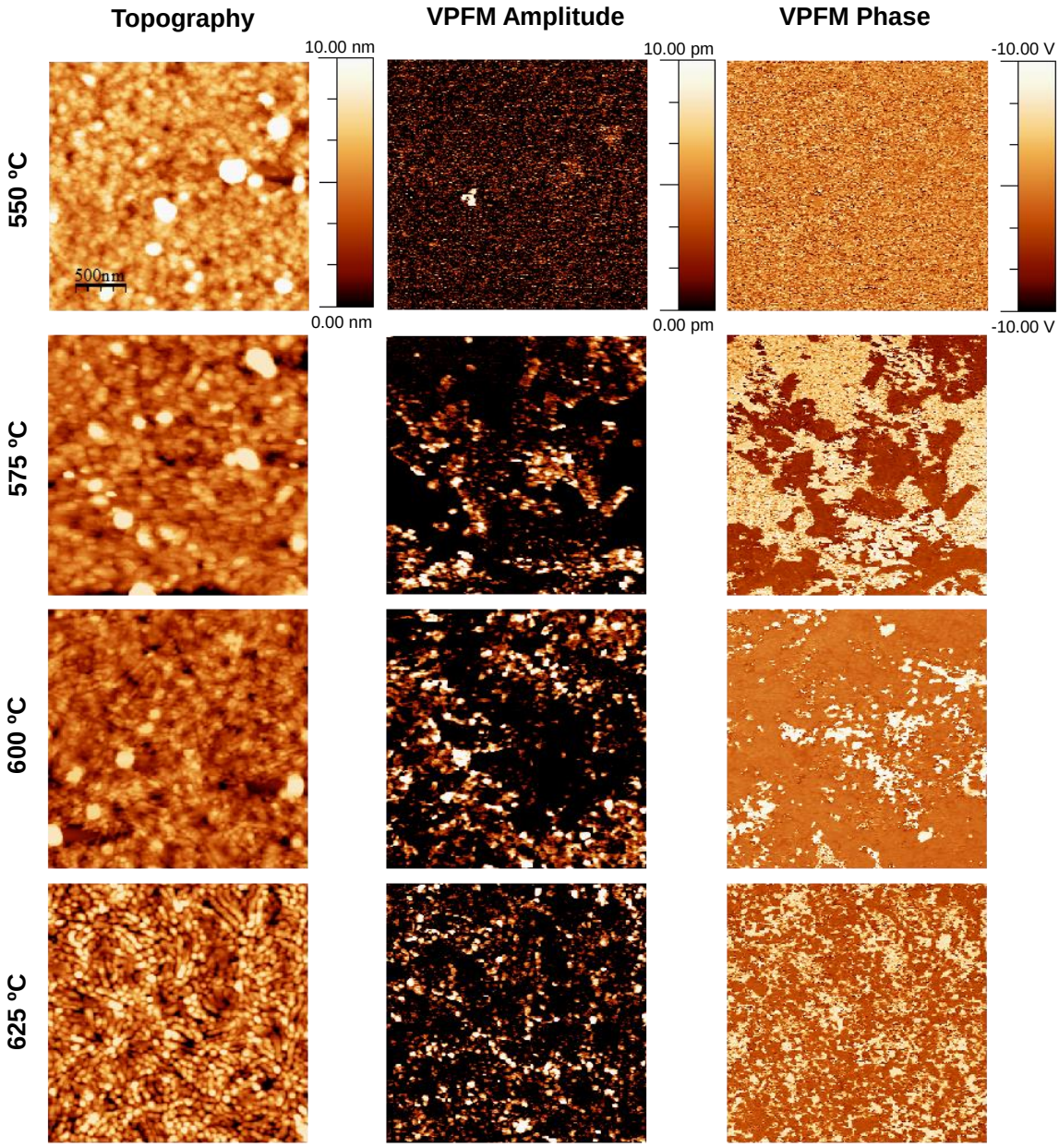

Figure 3.7: Topographic and VPFM phase and amplitude images of dense $PbTiO_3$ thin films after thermal treatment at: 550, 575, 600, and 625 ºC. The data scale for all topographic images is between 0 to 10 nm, for amplitude at 575, 600 and 625ºC is between 0 to 60 pm and for all phase images is between -10 to 10 V. This 20 V scale corresponds to 360 º, thus opposite domains oscillate 180 º out-of-phase, as expected. Piezoelectric domains in these films are smaller and less defined than in porous films. In this case, PFM amplitude response appears in films treated at higher heating temperatures when compared with nanoporous ones.

The bright areas formation can be related with a kinetic process of nucleation and as these bright areas are more defined in the nanoporous films than in dense ones,

the pores in the nanoporous case probably act as nucleation defects contributing for an early crystallization. This is well known from the nucleation and crystal growth classic theories.[21] However, experimentally, it was difficult to maximize the areas with strong piezoelectric behavior without losing the porosity order.

VPFM amplitude and phase images of dense films (Figure 3.7) show that the piezoelectric domains in these thin films are smaller and less defined than in the case of nanoporous ones, as observed through the domain size analysis, Table 3.1. This fact is a consequence of the high crystallinity present in the nanoporous thin films. However, as the annealing temperature increases in the case of nanoporous ones, the domain size decreases showing that the grains of these films are polydomains as consequence of the grain size and the methodology used in the preparation. At 550 ºC, no VPFM response could be observed in dense films, corroborating the observations of XRD and Raman spectroscopy. VPFM response is only observed for films heat treated at temperatures above 575 ºC. An increase of the area exhibiting VPFM response is also observed with enhanced annealing temperature.

Table 3.1: Average domain size for nanoporous and dense thin films calculated from the amplitude image.

Heating temperature (ºC)	Nanoporous (nm)	Dense (nm)
550	210.8 ± 15.9	
575	206.4 ± 16.9	49.3 ± 7.9
600	196.2 ± 14.6	49.8 ± 6.9
625	119.2 ± 14.1	51.5 ± 8.3

The representative PFS results obtained from the bright areas of these thin films are shown in Figure 3.8. The representative remanent hysteresis loops (amplitude and phase) reveal that the switched polarization remains after bias removal. For each film, hysteresis loops were measured from individual domains.

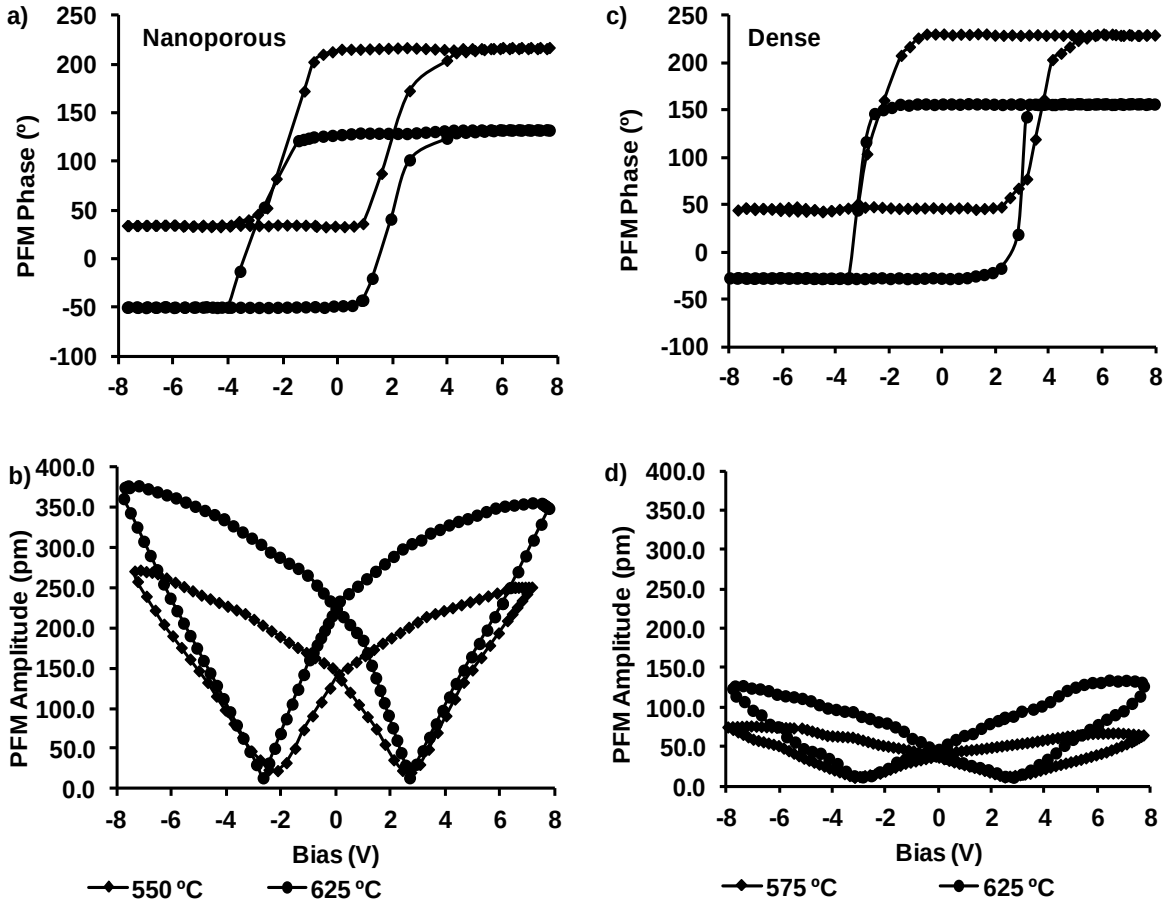

Figure 3.8: Representative remanent local hysteresis loops: phase (a and c) and amplitude (b and d) obtained in nanoporous and dense $PbTiO_3$ films after thermal treatment at: 550, 575, 600 and 625 ºC. FE properties are enhanced in nanoporous films.

The well-defined hysteresis loops clearly confirm the FE behavior at room temperature of nanoporous and dense $PbTiO_3$ thin films heat treated at different temperatures: 550 and 625 ºC in the case of nanoporous and 575 and 625 ºC for dense ones. However, the obtained phase hysteresis loops are not symmetric in terms of coercive voltage and remanent polarization for all films. This effect is known as imprint and is usually caused by the preference of a certain polarization state over the other. Thus, the horizontal shift present in all the hysteresis loops provides a measure of the internal field, and the vertical shift present in the same hysteresis loops provides information on regions with frozen polarization, i.e., can be associated with regions having a non-switching or preferentially oriented polarization.[196] Imprint behavior can also be related to self-polarization that depends, to a large extent, on the film deposition technology. The phenomenon of self-polarization occurs due to the presence of an

internal electric field, which is at least as large as the coercive field at the T_C. In the case of sol–gel deposited films, it was reported that the self-polarization effect is thickness dependent, suggesting that the alignment of domains occurs locally near the film–bottom electrode interface.[197,198,199] As in our work, the thickness is practically the same for nanoporous and dense thin films (around 100 nm), the vertical shift is not evaluated. Table 3.2 presents mean values of imprint, critical voltage, coercivity (here meaning the coercive field), and remanent piezoelectric coefficients calculated from several phase and amplitude hysteresis loops measured for nanoporous and dense thin films. Table 3.2 presents also the switchable polarization and $(d_{33})_{eff}$, calculated from mixed hysteresis loops.

From the imprint values, the imprint effect can be associated with an incipient crystallization of the tetragonal phase. Thus, as the heating temperature increases, imprint is slightly decreased (Table 3.2). Another explanation for this imprint effect is the presence of defects in the film, including oxygen vacancies and surface / interface defects (lattice distortion due to the difference of the thermal expansion coefficient between the film and the substrate). From critical voltage and coercivity values of Table 3.2, it is observed that nanoporous thin films present values slightly lower when compared with the dense thin films, suggesting that the crystallinity degree and porosity present in nanoporous films can affect the switching ability. Thus, and whereas the critical voltage values are usually used to evaluate the switching capability, nanoporous thin films show a higher switching ability than the dense films as supported by our results of FEM modelling, Figure 3.5. The switching process starts with the nucleation of a new domain just under the tip. This newly formed domain expands until it reaches an equilibrium size, which depends on the value of the applied voltage. This nucleation and growth of reverse domains are responsible for the reverse polarization. As discussed previously, porosity in the films triggers the crystallization at lower temperature than in dense counterparts. Thus, we propose that this earlier crystallization of the tetragonal perovskite phase (prompted by the presence of porosity) leads to a reduction of the energy necessary to reorient the dipoles in the FE structures and, consequently a reduction of coercivity when compared with dense films. On the other hand, as the porosity induces instability in the dipole-dipole interactions, the reverse polarization can be favoured for low bias values, Table 3.2.

Table 3.2: Average values of critical voltage, coercivity, imprint, switchable polarization, remanent piezoelectric coefficients and $(d_{33})_{eff}$ calculated from several phase, amplitude and mixed hysteresis loops for all nanoporous and dense thin films. The lower coercivity values present in nanoporous films show that the nanoporosity favors the switching in this kind of structure.

	Heating temperature (º C)	Critical voltage (V)	Coercivity values (V)	Imprint values (V)	Switchable polarization (pm/V)	Remanent piezoelectric coefficient (pm)	$(d_{33})_{eff}$ (pm/V))
Nanoporous films	**550**	1.0±0.1	2.0±0.1	0.9±0.1	254.7±6.8	149.1±5.3	137.0±5.7
	600	1.0±0.1	2.4±0.1	1.0±0.1	261.3±6.6	172.4±5.8	148.8±5.5
	625	1.4±0.1	2.3±0.1	0.5±0.1	534.7±8.3	241.9±6.0	218.8±6.3
Dense films	**575**	2.1±0.1	3.1±0.1	1.1±0.1	65.0±2.9	40.7±0.6	33.4±0.9
	600	1.8±0.1	2.5±0.1	1.2±0.1	85.1±2.0	45.5±0.5	35.7±0.8
	625	2.4±0.1	2.9±0.1	0.8±0.1	107.7±1.3	44.4±1.3	37.8±0.6

All these experimental results are in good agreement with the results obtained by FEM model specially developed for this kind of structures, Figure 3.5.

Thus, in this work we show theoretically and experimentally that both the presence and increasing of porosity content decreases the effective coercive field in nanoporous films. Remanent piezoelectric coefficients, $(d_{33})_{eff}$ coefficients and switchable polarization are higher for nanoporous than for dense films, revealing that porosity leads to better FE properties. This can be also related to the crystallinity of the films, probably to the high content of tetragonal phase present in the nanoporous films and associated with a smaller constraining effect of the substrate as well, when compared with equivalent dense films. Porosity is known to decrease the polarization and the dielectric permittivity of a polar media. Though deleterious, the decrease of permittivity can be beneficial to the pyroelectric coefficients of a FE material, as previously observed in several perovskites, like lead calcium titanate porous films.[200]

However, the effect of porosity on the intrinsic behavior of switching of a FE has never been reported before.

The increase of the piezoelectric coefficient and decrease of the coercive field for nanoporous films as observed and reported for the first time in this work are very important results, since they can be used as a tool to tailor the coercive field of FE nanostructures. Thus, nanoporosity can be viewed as a strategy to respond to the current miniaturization requirements of microelectronics; a good example is the application of these structures in FE capacitors for NV-FeRAMs in which the switchable remanent polarization should be reversed by application of short bias voltage.[201]

3.4 Conclusions

Nanoporous and dense $PbTiO_3$ thin films were prepared by a modified sol-gel route. The porosity structure and arrangement is very dependent on the heat treatment; as the temperature of annealing increases, the porosity tends to collapse and films tend to densify. An earlier crystallization of the tetragonal perovskite phase was verified to occur in nanoporous films when compared with the dense counterparts. A possible explanation for the observed effect can be related with the exothermic degradation of the block-copolymer (strengthened by the intense peaks observed in the DSC) concomitant with the presence of the pores that act as nucleation defects contributing for the formation of tetragonal phase at lower temperature in nanoporous films than in dense ones.[21] This enhancement of the tetragonality of the nanoporous films is reflected in the enhancement of the local ferroelectric properties as corroborated by FEM modelling and experimental observations. Under the same processing conditions, porous films show a higher local piezoelectric response and, importantly a lower local coercive field than the dense counterparts. In this work we proved that nanoporosity might be a tool to improve the switching behavior of ferroelectric thin films.

CHAPTER 4

Designing $BaTiO_3$ porous thin films

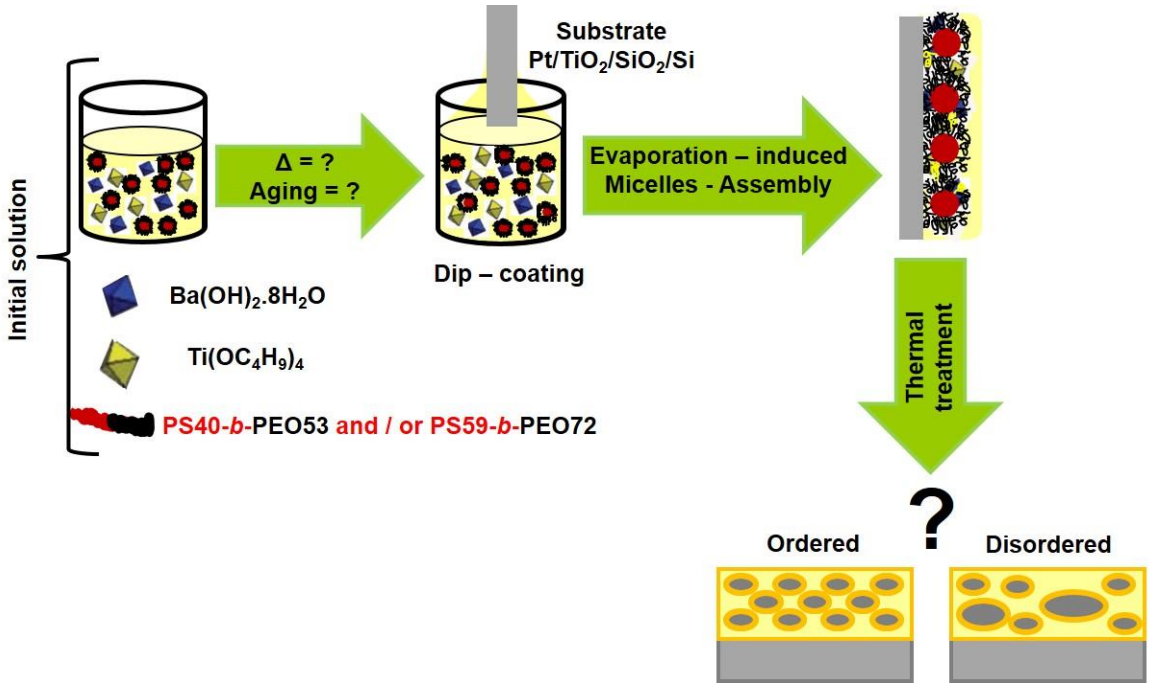

Graphical abstract: Optimization of the $BaTiO_3$ initial solution parameters such as: block-copolymer, solution aging time and solution heat treatment in order to achieve ordered nanoporous films. The use of fresh solutions and long block sizes of the PS-PEO copolymer allows the preparation of thin films with ordered nanoporous arrays.

Abstract

This chapter is about the effect understanding of several parameters such as: *i)* solution heat treatment; *ii)* addition of inorganic precursors/ organic solvent; and *iii)* solution aging time on the micellization process and, consequently, on the development of the micelles of block-copolymer in the solution of $BaTiO_3$. The study of these parameters on the micelles organization as well as the effect of the size of the blocks of block copolymers based on polystyrene (PS) and poly(ethylene oxide) (PEO) on the porous structure and order arrangement evolution is of vital importance in the attainment of a mesostructure with an ordered and periodic nanoporosity array.

Solutions without and with addition of inorganic precursors/organic solvents have a narrow micelle size distribution at least up to 1440 min of solution aging time, suggesting a micellization process following the closed association mechanism.[202,203] For the solutions prepared in the absence of inorganic precursors, the micellization process is rapid and spontaneous. In the other cases, the micellization process seems to

occur in two steps. When the solution containing the inorganic precursors/organic solvents is submitted to heating, the first step of the micellization process occurs within 180 min. In the case of the preparation of $BaTiO_3$ porous thin films, it is preferable to use a precursors fresh solution without any heating cycle.

PS40-*b*-PEO53 block-copolymer with MW_{PS} = 40 000 $gmol^{-1}$, MW_{PEO} = 53 000 $gmol^{-1}$ (hereafter designed 40-53) was compared with PS59-*b*-PEO72 block-copolymer with MW_{PS} = 59000 $gmol^{-1}$, MW_{PEO} = 72000 $gmol^{-1}$ (hereafter designed 59-72). An earlier crystallization of the tetragonal perovskite phase was verified to occur in nanoporous films prepared with the copolymer with blocks with higher molecular weight (59-72) when compared with nanoporous thin films prepared with a lower molecular weight block-copolymer (40-53). The use of the 59-72 allows the preparation of the microstructures with enhanced number of pores with smaller diameter (average value 35 nm), which seems to facilitate the formation of tetragonal phase at lower temperature. The highest tetragonality in this last nanoporous thin film is reflected on the enhancement of the local piezoelectric properties.

Index

4.1 Introduction

$BaTiO_3$ is a well-known lead-free FE material that has been used in various applications because its ferroelectricity, piezoelectric properties and, dielectric permitivity. $BaTiO_3$ has the ideal perovskite structure (cubic phase) above 120 ºC (T_C). At below temperatures to 120 ºC, the titanium ion shifts off its ideal symmetric position at the center of each octahedral interstice. This shift creates an electric dipole that polarizes the structure electrically and, causes the distortion in the cell lattice.[21,204]

Among the various applications, $BaTiO_3$ thin films have been used as transducers and actuators (piezoelectric effect), as high-K dielectric and capacitors, which are promissing for creating FRAM and paraelectric DRAM with high density, which depend on the hysteresis between two stable states of polarization, as well as in high speeding microprocessors and communication systems.[25,54,205]

As demonstrated in a previous work of our research group,[142] the preparation of ordered $BaTiO_3$ nanoporous thin films is not a trivial task. It is very critical to obtain ordered arrays of pores in multimetallic oxides. Moreover, the organization of the pores degrade upon the thermal treatment necessary for crystallization of the tetragonal phase. In order to understand the initial solution parameters and the chain size of the block-copolymer effect in obtaining a crystalline ordered mesostructure, the present work will be divided in two main sections. In section 4.2, we report the development of the

micelles of block-copolymer in a $BaTiO_3$ solution as well as the effect of several parameters, *i)* solution heat treatment; *ii)* addition of inorganic precursors/ organic solvent; and *iii)* solution aging time, on the micellization process. In section 4.3, the effect of the use of two PS-*b*-PEO based block-copolymers containing blocks with different molecular weights on the mesostructure order, crystallization of phase as well as on the local FE properties is studied.

4.2 Study of the block-copolymer micelles organization in a multimetallic oxide solution by DLS

The self-assembly of block-copolymers provides a versatile platform to produce nanostructured porous oxide thin films.[137,154,206] The physical and chemical properties of these nanostructured films can be tuned by changing the initial solution parameters.[120,207]

We have reported in one of our recent work[142] and in the Chapter 3, that the nanoporosity induced by the block-copolymer templates can be used to functionalize the thin films or even to tune and enhance the local electrical properties[144].[142,144] Although, these results are quite interesting and promising for microelectronic applications, the microstructures reported, namely for $BaTiO_3$, do not present a well-ordered crystalline porous structure and the porosity order is partly lost as the temperature of the thermal treatment increases.

The understanding of the micelles organization in solution for these particular multimetallic solution, as well as the micelles organization evolution, is crucial for the formation of a periodic ordered mesostructure whereas, the pores organization is associated to the self-assembly of block-copolymer micelles in solution or on the surface. In fact, since the discovery of organized mesoporous silica in 1992,[123] several materials were prepared using a large variety of amphiphilic or surfactant molecules as templates.[128,130,120] An important overview about the mechanisms involved in the mesostructuring that takes place during the formation of templated inorganic materials by evaporation was reported in 2004 by Grosso *et al.*[112] These mechanisms were based on the meso-organization of silica thin films using tetraethylorthosilicate (TEOS) as the inorganic source, and cetyltrimethylammonium bromide (CTAB) as the strutucturing agent.[112] The authors also studied TiO_2-based mesostructured thin films using F127 block-copolymer. It was thus demonstrated that the micelles organization depends mainly on the chemical composition of the film when it reaches the modulable steady state in which the inorganic framework is still flexible. This state occurs just after the evaporation. During this time the film water and volatile contents are in equilibrium with the environment and the final structure is defined and stabilised.[112] Nevertheless,

the comprehension of the effect of several physical and chemical parameters on micelles organization for this particular multimetallic oxide system ($BaTiO_3$) has not yet been reported. This is the intent of this Chapter. However, before going deep in the understanding of such parameters on micelles organization, it is vital to first understand the micellization process in dilute solutions.

The micellization process and the structural parameters of the micelles depend on the composition, structure and molar mass of the copolymer, interactions between the copolymer blocks and the solvent, copolymer concentration, temperature and on the preparation methods.[208] In diluted solutions, a block-copolymer can inter-molecularly associate forming micelles according to the closed association model, which assume a dynamic equilibrium between free copolymer chains and micelles with a determined association number of unimers.[209] The copolymer micelles are spherical and are formed by a core and an external shell. The core consists of poorly soluble sequences of block-copolymer, and the shell consists of solvated sequences, which prevent macroscopic flocculation of the copolymer.[210] According to the closed association model, above the critical micelle concentration (CMC), free copolymer chains and micelles coexist in solution. For block-copolymers undergoing closed association in dilute solution to form micelles with an appreciable association number,[208] the standard Gibbs energy of micellization process, ΔG^o, can be determined by following expression:

$$\Delta G^o \approx RT \times \ln (CMC),$$

where, R is the ideal gas constant, T is the temperature and CMC is the critical micelle concentration.[211] CMC is defined as the concentration above which micelles are spontaneously formed. If the association number is temperature independent, the standard enthalpy of micellization process, ΔH^o, can be determined by measuring the temperature dependence of the critical micelle concentration, by the following expression:[211]

$$\Delta H^o \approx R \times [(d\ln(CMC))/d(T^{-1})]$$

When the block-copolymers are used in organic solvents, as in our case, the enthalpy contribution to the Gibbs energy change of the micellization process is uniquely responsible for micelle formation. Thus characteristics of the micelles and the mechanism of micellization are strongly dependent upon the selective solvent.[212] However, the presence of solvent in the cores of the block-copolymer micelles increases

the rate at which the free chain-micelle equilibrium is achieved. Consequently, the existence of solvent in the micelle cores and its concentration can be important factors to reach the thermodynamic equilibrium.[213] The block-copolymer micellization is a heterogeneous process, which occurs in different time scales, varying from nanoseconds to milliseconds for the initial stages of the micelle formation to hours, days, or even years until the final stage of micelle equilibrium is reached.[214]

In this present work, we aim to report the development of the micelles of block-copolymer in a solution of $BaTiO_3$ as well as the effect of several parameters such as: *i)* heating of the solution; *ii)* addition of inorganic precursors/ organic solvent; and *iii)* aging time of solution on the micellization process. These parameters, among various critical parameters such as: dilution, solvent polarity, dissolution conditions and substrate surface energy, are important for the preparation of the solution used in the dip-coating process and, consequently are responsible for the formation of an ordered mesostructure. This study was followed by DLS.

4.2.1 Experimental part

Porous $BaTiO_3$ solutions were prepared based on the description of reference.[142] However, some changes in the procedure were necessary. Six solutions (solutions 1 to 6) with different chemical compositions and treated differently were studied as detailed in Table 1. 40-53 block-copolymer with MW_{PS} = 40 000 $gmol^{-1}$, MW_{PEO} = 53 000 $gmol^{-1}$ from Polymer Source was used as a structure-directing agent. Solutions 1 and 2 consisted uniquely of solution A. Solution A was prepared by the dissolution of the block-copolymer 40-53 in tetrahydrofuran (C_4H_8O, THF) (Sigma Aldrich, purity ≥ 99.5% w/w), followed by heating at 70 ºC for 10-15 min. Then, absolute ethanol (CH_3CH_2OH) (Panreac, purity ≥ 96% v/v) was slowly added drop-by-drop, under stirring. The solution A became turbid when the absolute ethanol was progressively added as a result of the block-copolymer micellization.

Solutions 3, 4, 5 and 6 were prepared by the addition of the solution B to the solution C, as indicated in the Table 4.1, in order to prepare the inorganic precursors solution. These precursor solutions were slowly added to the solution A forming the final solutions. Solution B was prepared by dissolution of barium hydroxide octahydrate

($Ba(OH)_2.8H_2O$) (Merck, purity ≥ 98.0% w/w) into glacial acetic acid (CH_3COOH) (Sigma Aldrich, purity ≥ 99.7% w/w) at 70 °C for 10 min. The solution C results from the addition of acetylacetone ($C_5H_8O_2$) (Fluka, purity ≥ 99.3% w/w) to the titanium (IV) n-butoxide ($Ti(OC_4H_9)_4$) (Merck, purity 98.0% w/w) precursor. The chemical composition of solutions 2 and 4 are not displayed in Table 4.1 as they have similar composition to solutions 1 and 3, respectively. The only difference among solutions 1 and 2, and solution 3 and 4 is that solutions 2 and 4 were submitted to three cycles of heating at 70 ºC during 10 min in order to study the effect of the heating of solution on the micellization process. Solutions 3, 5 and 6 were prepared to evaluate the inorganic/organic precursors effect in the micelles size and consequently on the micellization process by comparison with solution 1. The aging time of the solutions was analyzed over 2880 min (48 hours). This aging time was enough to verify the stability of the solutions and the existence of any degradation on the micellization process. The DLS measurements were carried out using a Nano ZetaSizer, Malvern equipment with a ‘‘red’’ laser operating at 633 nm and a detector positioned at 173º at room temperature. The DLS measurements were performed after 5, 10, 20, 30, 40, 50, 60, 75, 90, 105, 120, 180, 240, 300, 360, 1260, 1320, 1380, 1440 (24 hours), 1500, 1560, 1620, 1680 and 2880 min (48 hours) of aging time. The solutions were kept under stirring during the DLS analysis. The data was analyzed using Malvern Zetasizer Software v. 6.20.

Nanoporous $BaTiO_3$ thin films were deposited by dip-coating at a withdrawal rate of 0.49 mm/s onto 1.0 x 2.0 cm^2 sized slides of platinized silicon ($Pt(111)/TiO_2/SiO_2/Si(100)$) substrates (Inostek, Inc.) after 1, 3, 5 and 7 hours of solutions aging. All the films were thermally treated in air at 350 °C during 5 min in order to complete the inorganic condensation of the matrix and to decompose the organic parts of the precursors and block-copolymer template. Subsequently, thin films were calcined at 650 ºC for 5 min to achieve crystallization.

SEM (SU-70 Hitachi) was used to monitor the microstructure evolution of the thin films prepared with the described solutions.

Table 4.1: Chemical composition of the $BaTiO_3$ final solutions used for DLS measurements.

	Reagents	Solutions 1 and 2	Solutions 3 and 4	Solution 5	Solution 6
Solution A	**40-53**	0.083 g	0.083 g	0.083 g	0.083 g
	C_4H_8O	0.93 g (12.90 mmol)	0.93 g (12.90 mmol)	1.23 g (17.06 mmol)	0.93 g (12.90 mmol)
	CH_3CH_2OH	2.78 g (60.36 mmol)	2.78 g (60.36 mmol)	2.78 g (60.36 mmol)	2.78 g (60.36 mmol)
Solution B	**$Ba(OH)_2.8H_2O$**		0.445 g (1.415 mmol)	0.445 g (1.415 mmol)	0.445 g (1.415 mmol)
	CH_3COOH		1.714 g (28.54 mmol)	1.714 g (28.54 mmol)	2.014 g (33.54 mmol)
Solution C	**$Ti(OC_4H_9)_4$**		0.480 g (1.410 mmol)	0.480 g (1.410 mmol)	0.480 g (1.410 mmol)
	$C_5H_8O_2$		0.100 g (0.998 mmol)	0.100 g (0.998 mmol)	0.100 g (0.998 mmol)

4.2.2 Results and Discussion

Figure 4.1 presents the time evolution of micelles average size (Z) for the different solutions measured by DLS.

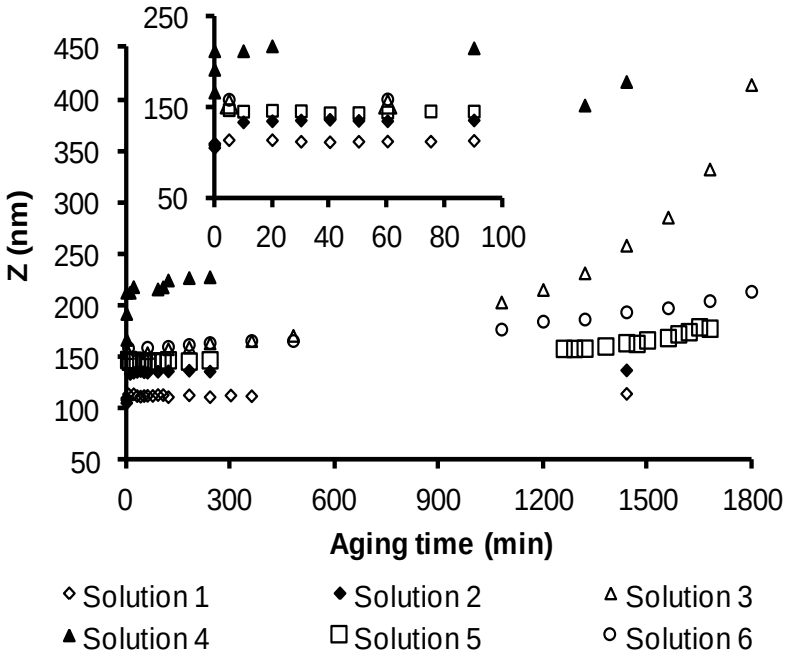

Figure 4.1: Study of the time evolution of micelles average size, Z, for different solutions using DLS. The inset shows the zoom of first 100 min of the evolution of micelles average size. The micellization process can probably be divided in two steps: *i)* the first step corresponds to the first 360 min; and *ii)* the second step occurs between 480 and 1800 min.

DLS determines the particle size by measuring the Brownian motion of the particles in solution and, further interpreting of this using established theories. As the two used solvents have a very similar refractive index, the cancelation of eventual contributions of selective adsorption to the light scattering was verified.

Whereas DLS allows measuring the micelle size and assess their time evolution, in this work we used the technique to study the different parameters effect on micellization process and, consequently verify if micelles formation occurs in solution or if they are just formed under evaporation on the substrate surface. This fact is very important because well dispersed and separated motifs can only be formed if the micelles are formed in the solution, prior to deposition.[207]

Through Figure 4.1, one can observe that for all solutions the micelles are formed prior to deposition. Solution 1 has a constant behavior with time, *i.e.* the block-copolymer micelles, in appropriate solvent achieves very quickly the thermodynamic equilibrium (equilibrium size). More specifically, in the used solvent mixture the block-copolymer chains are quickly and reversibly associated, leading to the formation of micellar aggregates. This happen because the solvent mixture contains a thermodynamically good solvent for one of the blocks and another solvent that precipitate the other block. In this particular system, the micelles are formed by PEO chains (polar chains) in the shell and PS (apolar chains) in the core. These micellar aggregates can be compared in most of their aspects to those obtained with classical low molecular weight surfactants. In particular, the block-copolymer active surface and their self-associative characteristics leading to micellar systems are directly related to their segmental incompatibility. The micelles formed by these non-ionic surfactants are generally spherical and have a narrow size distribution, but may change in shape and size distribution under certain conditions. The narrow micelle size distribution for the solution 1 measured after 5, 1440 and 2880 min of aging time is represented in Figure 4.2.

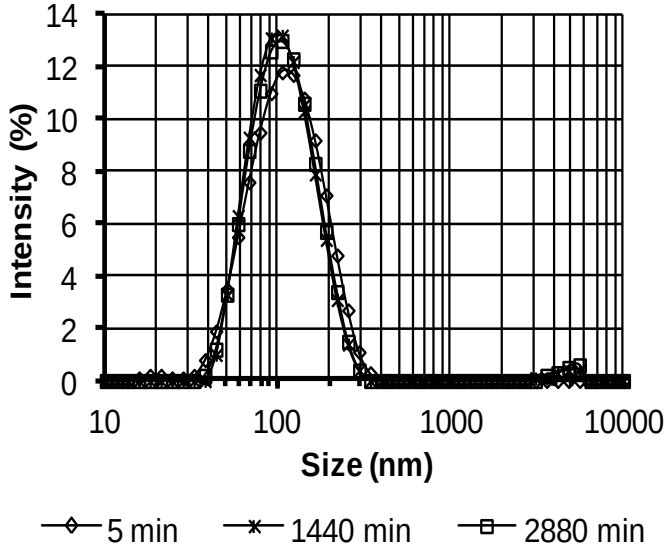

Figure 4.2: Micelle size distributions of solution 1 after 5, 1440 and 2880 min of aging time. Narrow size distributions for this solution can be observed.

The mean diameters (intensity distribution) are 98.94 nm for 5 min, 99.29 nm for 1440 min, and 101.2 nm for 2880 min. These values suggest that the micellization process obeys to the closed association mechanism, characterized by a certain CMC, below which only molecularly dissolved copolymer is present in solution, usually as unimers. Above CMC, multi-molecular micelles are in equilibrium with the unimers.

Moreover, the high solubility and stability of the block-copolymer in the used solvents mixture lead to the formation of micelles with quasi-equilibrium size very quickly, i.e. the micellization process proceeds fast and spontaneously ($\Delta G<0$). Consequently, it is possible to verify that there is a very quick increase of the micelles number with an almost fixed micelle size. Quintana *et al.*[209] showed through a micellization thermodynamics study that the standard Gibbs energy of micellization is negative when the selectivity of the medium increases, favoring the micelle formation. If the block-copolymer is used in organic solvents, the entropy is negative and, consequently, the micelle formation is unfavorable.[212] For this reason and for spontaneous micelle formation it is necessary $\Delta H<0$. The main factor responsible for this, is probably the relatively large exothermic interchange of energy accompanying the replacement of copolymer segment / solvent interactions by copolymer segment / copolymer segment and solvent/solvent interactions upon formation of the micelle cores, as observed by Quintana *et al.*[208] Furthermore, the presence of solvent molecules in the cores of the block-copolymer micelles will give rise to a certain disorder in micelles, increasing the rate at which the free chain-micelle equilibrium is reached. The peak at several thousand nanometers observed also in Figure 4.2, probably corresponds to some elongated micelles dispersed in solution, as observed by Cameron *et al.*[25] For the sake of understanding, the results will be discussed in three sections.

- **Addition of inorganic precursors/ organic solvent**

Solution 3, used to understand the effect of the addition of the inorganic precursors to solution 1, presents a significant increase of micelle size upon inorganic precursors addition (Figure 4.1). This may be attributed to the complexation of the cations with the PEO chains, which leads to thicker and / or denser micellar shells. The cations addition probably decreases the dissolution ability of the system, leading to the accommodation of large micelles with lower interface curvatures. Figure 4.3 shows the

size distribution of solution 3 and, as it was observed for solution 1, this solution presents micelles with a narrow size distribution at least up to 1440 min of aging time. After 1440 min of aging, a progressive and quick increase in the micelle size and size distribution is observed becoming multimodal and revealing the presence of different size populations in the system. The micelle size increase is probably due to the rise in the solution viscosity with aging time.

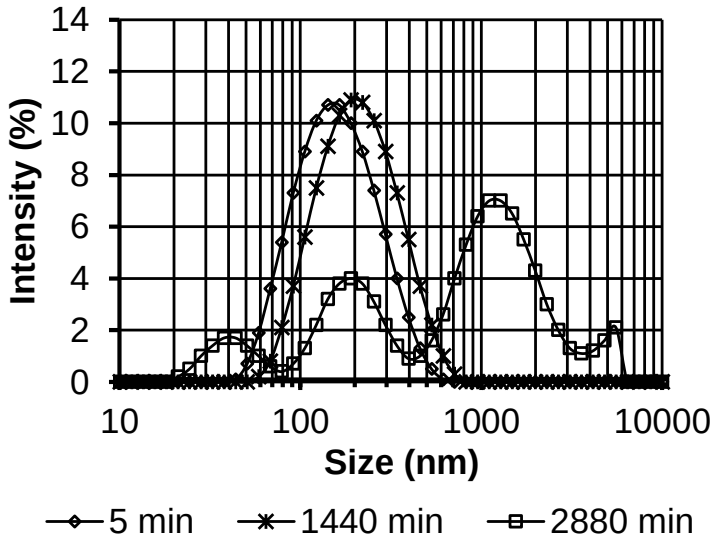

Figure 4.3: Micelle size distribution of Solution 3 after 5, 1440 and 2880 min of aging time showing a wide micelle size distribution for long aging times.

Figure 4.4 represents the viscosity increase with aging time for solution 3. This enhancement in viscosity leads to the formation of large particles or aggregates thereby making the solution polydisperse over time. In addition, large particles of the copolymer reduce the entropy and consequently, the thermodynamic equilibrium and stable copolymer aggregation states are sometimes difficult to reach.

For this solution and by comparison with several studies realized namely, by Gérard *et al.*[157] and Quintana *et al.*[215], the micellization process can probably be divided in two steps:

i) 1st Step attributed to unimer ↔ micelle equilibrium at constant micelle concentration (Figure 4.1);

ii) 2nd Step corresponding to an association ↔ dissociation equilibrium (Figure 4.1).

The first step, occurring during the first 360 min, is characterized by the micelles number increase with an almost fixed micelle size as observed in the Figure 4.1. The growth rate of micelles achieving quasi-equilibrium size (≈ 150 nm) is higher than the formation rate of new micelles.

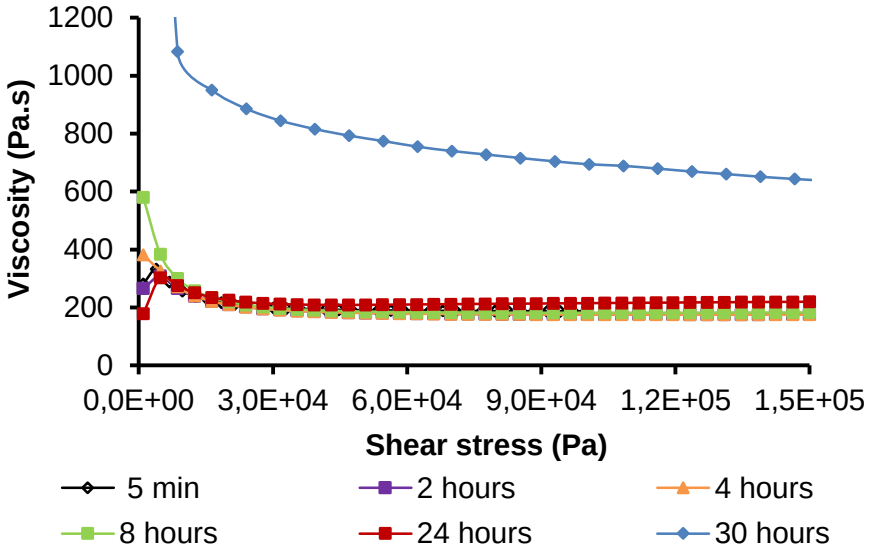

Figure 4.4: Time evolution of the viscosity as function of shear stress for solution 3. The enhancement in viscosity leads to the formation of large particles or aggregates thereby making the solution polydisperse over time. The total gelation of the solution occurs between 24 hours and 30 hours. The maximum viscosity value can be observed at 30 hours.

In the second step, which occurs from the 480 to 1800 min, the growth of the micelles seems to be reached by decomposition of some micelles in favor of others, and by entry or expulsion of unimers into or from micelles. The growth of micelle size must be relatively fast. In this step there is an increase of the association number and a decrease of the micelle number. Thus, the first step is considered as the dominant step over the second one.

In Figure 4.1, one can also find the results related to the organic solvent effect in the micelles size and, consequently, on the micellization process. Solutions 5 and 6 contain higher amount of organic solvents, namely 0.300 g of THF and 0.300 g CH_3COOH respectively, than solution 3 (Table 4.1). Comparing the behavior of these two solutions with solution 3, one can observe the decrease of the micelle size and the

presence of a narrow micelle size distribution at least up to 1440 min of aging time. The reduction in the micelle size may be explained by the high dissolution/solubility degree of solutions 5 and 6, which allow to accommodate small micelles. These results reveal that the medium polarity or solubility may affect the formation of micelles and the size of the formed micelles. For solutions 5 and 6, the micellization process seems to occur in two steps as observed for solution 3.

- **Heating of solution**

The results of the effect of solution heating on micellization are also presented in Figure 4.1 for solutions 2 and 4. Three points at zero time which refer to the three consecutive heating cycles are observed. Solution 2 presents a size decrease with heating cycles, followed by an increase that is then kept constant with time. The micelle size diminution is due to the decrease of the solution viscosity with consequent increase of the species mobility and solubility in the solution. As observed by Grosso *et al.*[207] and Bahadur *et al*.,[216] high solubility leads to small micelles and ultimately to small pores in the films. Such as for solution 1, the micellization process in the solution 2 occurs very fast. In solution 4, the behavior was considerably different. The micelle size increases gradually with the heating cycles, stabilizes and then increases significantly. A significant increase in the viscosity during the heating cycles was observed, probably as a result of a fast gelation of the solution. This viscosity increment leads to the formation of large particles, and consequently reduces the solution entropy, which precludes the formation of stable copolymer aggregation states. As observed in solution 3, the micellization process seems to occur in two steps, however in this case, the first step is only up to 180 min.

All these results point to the benefits of using fresh initial solutions without heating cycles to attain thin films with porous narrow size distribution. In other words, from the previous observations, to obtain thin films with better quality it is necessary to use solutions before the beginning of the second step of the micellization process.

- **Aging time**

The aging time effect on micellization process is also studied. $BaTiO_3$ thin films were deposited using the solution 3 with different aging times.

Figure 4.5 shows the SEM micrographs obtained for $BaTiO_3$ thin films deposited after 5 min, 1, 3, 5 and 7 hours of solution aging and thermally treated at 650 ºC during 5 min. The microstructures reveal a porous structure with a certain degree of order and periodicity evidencing that there are no significant differences in the microstructure development of films prepared with 5 min or 1 hour aged solutions (Figure 4.5a and 4.5b). Pore order and periodicity results from the self-assembly of micelles of the amphiphilic block-copolymer, followed by condensation of the inorganic species around the micelle arrays. During the thermal decomposition of the block-copolymer, void motifs are created. According to the thermal analysis presented in Chapter 3 (Figure 3.1), this takes place between 200 and 450 ºC.

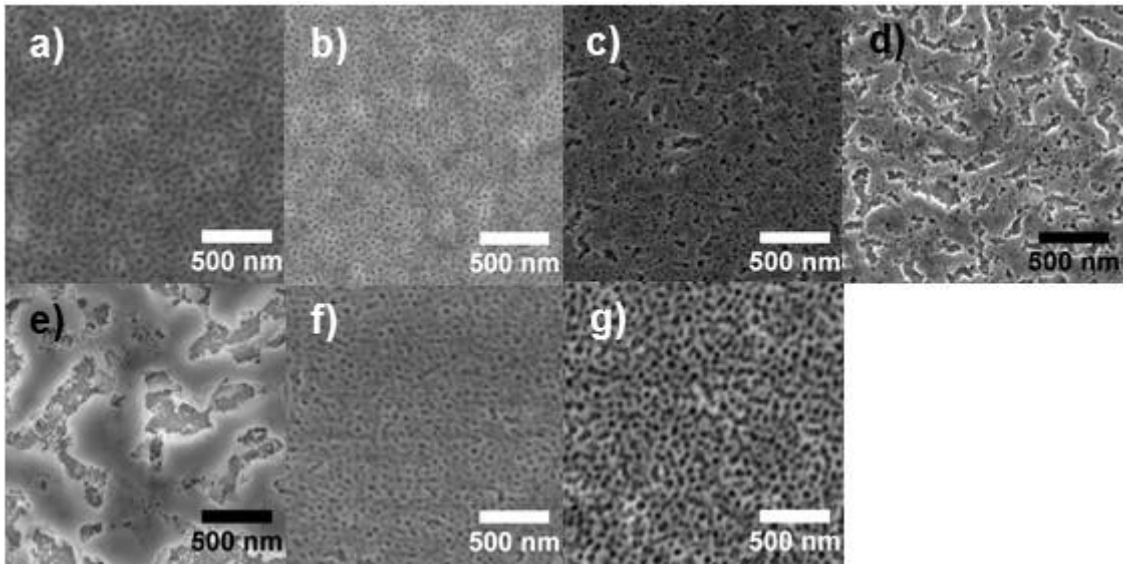

Figure 4.5: SEM images showing the morphology of $BaTiO_3$ nanoporous thin film after thermal treatment at 650 ºC. The thin films were deposited using solution 3 aged during: a) 5 min; b) 1 hour; c) 3 hours; d) 5 hours; and e) 7 hours. The Figure 4.5f and 4.5g compare the thin films obtained after 1 hour aging time with solutions 5 and 6, respectively. The Figure 4.5a and 4.5b reveal a porous structure with a certain degree of order and periodicity. After 3, 5 and 7 hours of aging time (Figures 4.5c, 4.5d and 4.5e), the porous size of thin films increases due to the solution viscosity increase, which occurs naturally in the sol-gel process. In the Figure 4.5f and 4.5g, the microstruture lose some porosity order and periodicity, which can be attributed to the different solvent evaporation rates during the deposition or to the different decomposition rates during the thermal treatment due to the higher volatile organic solvent amount in the solution.

The pore size for the aging time of 5 min and 1 hour is around 50 nm. As expected, the pore size is lower than the micelle size obtained by DLS due to the evaporation of the organic and volatile solvents present in the hybrid mesostructure. In addition, during the thermal treatment the mesostructuration of the inorganic framework and crystallization take place, leading to thus a contraction of the pores size. As a careful control of processing and thermal treatment conditions was undertaken, the collapse of the meso-ordering during crystallization did not occurr. However, as the aging time of the solution increases, the microstructure of the porous films varies, from a somehow organized pore arrangement to a disorder and larger porosity. After 3, 5 and 7 hours of aging time (Figures 4.5c, 4.5d and 4.5e), the porous size of thin films increases. According to the Figure 4.1, the first step of the solution 3 should occur during the first 360 min (6 hours) where a narrow size distribution is observed (Figure 4.3). This result should result in a similar microstructure to the Figure 4.5a and 4.5b. However, significant differences in the pores size, porosity order and periodicity can be observed for the thin films deposited after 3 and 5 hours. This can be explained by the progressive increase of the solution viscosity during the aging and consequent micelle size enhancement (Figure 4.3). As aging time increases, the solution viscosity naturally increases due to the gelation of the solution. This viscosity increment leads to the formation of large particles which is reflected in a disordered mesostructure. As expected, after 7 hours of aging time, the porous size signaficatly increases as consequence of the micelle size increase, which occurs during the second step of the micellization process. In this step, the growth of the micelles seems to be reached by decomposition of some micelles in favor of others, and by entry or expulsion of unimers into or from micelles.

Comparing these thin films with the thin films obtained from solutions 5 and 6 after 1 hours of aging time (Figures 4.5f and 4.5g) one can observe that the porous size is practically the same that the obtained with solution 3 (Figures 4.5a and 4.5b). In this case, the pore size did not follow the trend of the DLS results (Figure 4.1) where the micelles size of solutions 5 and 6 is slightly lower than the obtained with solution 3. As observed for solution 3, a contraction of the pore size due to the evaporation of the organic and volatile solvents during the condensation and mesostructuration of the inorganic framework also occurs for films derived from solutions 5 and 6. However, as

solutions 5 and 6 present high dissolution / solubility degree, the consequent adhesion to the substrate is higher and the flattening effect of the micelles, which probably took place during the thermal treatment, is higher increasing thus the pore size. This pore size can be thus compared with those obtained for the thin films derived from the solution 3. The mesostructure obtained through these solutions, solution 5 and 6, lose some porosity order and periodicity. This can be attributed to the different solvent evaporation rates during the deposition or to the different decomposition rates during the thermal treatment due to the higher volatile organic solvent amount in the solution.

From these results, the heating and the aging time of the precursor solutions are not means to maximize the degree of ordering of the porous $BaTiO_3$ structure. Otherwise, it is preferable to use just prepared precursor solutions without any heating cycle. Figure 4.5 indicates that only the thin films deposited using solution 3 aged during 5 min and/or 1 hour present a reasonable degree of periodic order.

4.3 Block-copolymer effect on mesostructure of multimetallic oxide: $BaTiO_3$

The choice of the appropriate block-copolymer to prepare an ordered and periodic mesostructure is also a crucial parameter. Besides the all parameters related to the initial solution mentioned in the previous section, the correct block-copolymer choice plays an important role in the attainment the desired mesostructure.

Amphiphilic block-copolymers consist in two or more polymeric segments covalently bonded together and that are capable of self-assembly into ordered arrays of micro and nano-domains with dimensions on the order of 5-100 nm.[217]

Brinker[218] and Ozin[219] groups are pioneered in the preparation of mesostructured silica thin films using EISA method. Since then, several transition metals have been used as inorganic precursos in order to prepare others mesoporous materials.[120,115] However, only in 2003 the first titanium oxide mesoporous thin film with high crystallinity was obtained by using PEO-based nonionic diblock (Brij 56 or Brij 58) or triblock-copolymers (Pluronic P123 or Pluronic F127) as structure directing agents.[220] Nevertheless, this kind of templates leads, after crystallization, to mesostructures with relatively low porous order and periodicity. One possible explanation is the low wall thickness in comparison with the critical nucleation size.[125,221] It is well reported that the large amphiphilic copolymers such as poly(ethylene-co-butylene)-*b*-poly(ethylene oxide), also known as KLE, produce high crystalline metal oxides with well-defined nanoscale periodicity. These block-copolymers allow the formation of inorganic-organic composites with sufficiently thick pore walls that can be fully crystallized without compromise the order.[140]

Indeed, the self-assembly characteristics of block-copolymers permit the structure control, varying the typical length scales and adding specific functions.[145,222] Moreover, their properties can be continuously changed by adjusting solvent composition, molecular weight or polymer architecture. This kind of amphiphilic block-copolymers have more hydrophobic character comparing to Pluronic P123 block-copolymer and, consequently increases the stability of micelles in less polar solvents

such as ethanol as well as their very low polydispersity form spherical micelles exclusively.[145,222]

The amphiphilic block-copolymers may have different combinations of hydrophilic (polar) and hydrophobic (apolar) components so that their interactions with the metal species can be controlled. The PEO is widely used as the hydrophilic part since it can forms thicker walls, which remain after crystallization preserving thus, an ordered mesostructure. Among different hydrophobic polymers PS, polypropylene (PPO), polyisoprene (PI), or polyvinylpyrrolidone (PVP)), PS seems to be the best hydrophobic one because this can serve as a scaffold for the mesostructure crystallization before their decomposition at ≈ 450 ºC, which is much higher than the traditional F127 or P123 templates that decomposes at ≈ 250 ºC.[125,115,120] Thus, conjugating the properties of PEO and PS, the block-copolymer PS-*b*-PEO seems to be a good templating agent to prepared well-ordered mesostructures.

In Chapter 3, we showed that the crystallization of the tetragonal phase and the local FE properties is significantly improved by the introduction of nanoporosity. In those studies and the previous section we used PS40-*b*-PEO53 block-copolymer. In order to investigate the effect of size of the blocks of the block-copolymer on the porous arrangement, longer PS and PEO block sizes are tried. Thus, using a similar preparation method but with a different block-copolymer, we intent to obtain a crystalline $BaTiO_3$ ordered mesostructure and improve its FE properties. For this, a comparative study using two PS-*b*-PEO block-copolymers, 40-53 and 59-72, as structure-directing agents, is carried out.

4.3.1 Experimental part

Porous $BaTiO_3$ films were prepared by sol-gel method and EISA methodology using based PS-*b*-PEO block-copolymers (see Chapter 2). 40-53 block-copolymer with MW_{PS} = 40 000 $gmol^{-1}$, MW_{PEO} = 53 000 $gmol^{-1}$ and 59-72 block-copolymer with MW_{PS} = 59000 $gmol^{-1}$, MW_{PEO} = 72000 $gmol^{-1}$ both from Polymer Source, were used as a structure-directing agents.

For each block-copolymer, three solutions were prepared. In solution A, 40-53 block-copolymer or 59-72 block-copolymer (83 mg) was dissolved in tetrahydrofuran

(12.90 mmol for 40-53 or 15.31 mmol for 59-72, Sigma-Aldrich, purity ≥ 99.5%) at 70 ºC. Subsequently, and under stirring, absolute ethanol (60.36 mmol for 40-53 or 71.89 mmol for 59-72) was added drop by drop. Solution B was prepared by the dissolution of barium hydroxide octahydrate (1.42 mmol, Merck, purity ≥ 98.0% w/w) in glacial acetic acid (28.54 mmol, Merck) at 70 ºC. Solution C was prepared from mixing 2,4-pentanedione (0.99 mmol, Fluka, purity 99.3% w/w) with titanium (IV) n-butoxide (1.41 mmol, Merck, 98.0% w/w) under stirring at room temperature. Afterwards, solutions B and C were added to solution A, forming the final solution. For dense thin films, a similar procedure was used, however solution A was prepared without the block-copolymer.

Nanoporous and dense thin films were deposited by dip-coating onto 1.0 x 2.0 cm^2 sized slides of platinized silicon (Pt (111)/TiO_2/SiO_2/Si(100)) (Inostek Inc.). In order to get similar film thicknesses (around 100 nm), the withdrawal rates were adjusted to 1.6 mm/s (nanoporous) and 3.0 mm/s (dense). All films were thermally treated in air at 350 °C to complete the inorganic condensation (mesostructuration) of the matrix and to decompose the organic content. The films were then annealed for 20 min at the 650 ºC and 5 min at 700 ºC to achieve the desired crystalline phase.

To follow the phase formation process, TGA-DSC were carried out on dried nanoporous and dense powders obtained by drying the solutions described above in open vessels at 60 ºC for few days. TGA was performed in a Setaram Labsys™ TGA-DSC16 system with a heating rate of 10 °C/min under flowing air up to 800 °C. DSC was carried out on a DSC50 Shimadzu system with a heating rate of 5 °C/min under flowing air up to 800 °C.

The crystalline phases in the thin films and *in-situ* phase formation in the powders were identified by XRD using a Philips X'Pert MPD X-ray diffractometer with Cu Kα radiation, 2° grazing incidence angle and a step length of 0.02 °.

Raman spectroscopy was performed in JY Horiba LabRam model HR800 equipment, with a high resolution 800 mm focal length spectrometer. An argon ion laser beam at a wavelength of 325 nm was utilized. The film mesostructure was investigated by high-resolution SEM using a SU-70 Hitachi microscope.

VPFM was carried out on Nanoscope III, Digital Instruments system with a lock-in amplifier, SRS Stanford Research Systems, using DPE-18 cantilevers with Pt-

coated tips (Mikromasch, resonant frequency of 60−100 kHz, force constant of 1.1−5.6 N/m), respectively. For the VPFM measurements, the topography signal of the film surface was taken simultaneously with the mixed signal. Both were collected in contact mode. Since the results were obtained with the same type of cantilevers and under identical scanning and acquisition conditions, comparison between films can be made.

4.3.2 Results and discussion

Figure 4.6 presents TGA-DSC analyses of nanoporous and dense $BaTiO_3$ precursor gels prepared using different block-copolymers: 40-53 and 59-72.

The TGA curves (Figure 4.6a) of these gels have a similar profile in the four main regions identified: *i)* region I from room temperature up to 200 ºC, in which the weight losses for both gels is around 5% for the nanoporous and 10 % for the dense, and attributed to the loss of residual water and evaporation of organics; *ii)* region II in which the weight losses are 22% for the case of dense gels (from 200 to 400 ºC) and 35% for the porous ones (from 200 to 450 ºC) and assigned to the decomposition of organics; *iii)* region III in which the weight losses are almost constant up to 700 ºC, reaching a value of 3% for both gels and attributed to the decomposition of residual species; and *iv)* region IV in which the weight losses are 5% and assigned to the decomposition of residual species more strongly bonded. Note that the temperature interval of region II is wider for nanoporous than for dense precursor gels.

DSC analyses (Figure 4.6b) of nanoporous and dense gels also present similar thermal profiles, although the intensity of the thermal effects is different for both block-copolymers and dense gels. In the case of nanoporous gels, the intense exothermic peaks between 200 and 400 ºC corresponding to region II in DSC curve are related with the decomposition of organics and block-copolymer degradation. In the case of dense gels, a less intense peak is observed in region II. This fact is due to the absence of the block-copolymer in this case and it is in line with the TGA behavior indicating that the energy released in this temperature interval is higher for the nanoporous when compared with dense precursor gels. The exothermic peaks between 400 and 700 ºC (region III) is attributed to the perovskite phase formation. The peaks observed in region IV corresponds to the crystallization process. The nanoporous thin films crystallize at

slightly lower temperature than the dense ones, as can be observed through the DSC (Figure 4.6b).

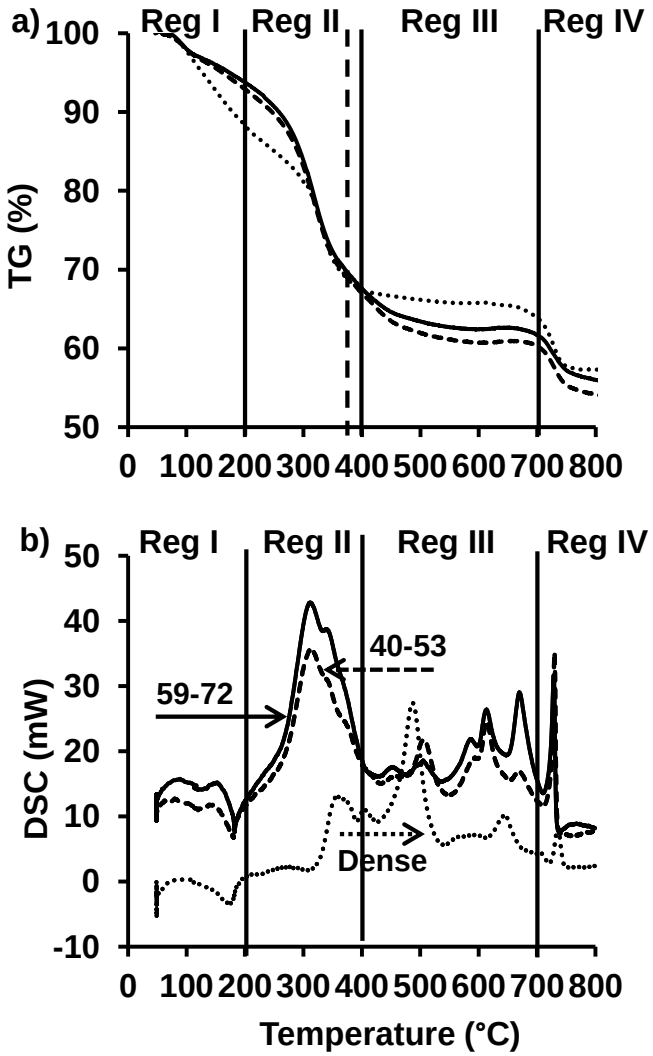

Figure 4.6: TGA-DSC of precursor gels of nanoporous and dense $BaTiO_3$ films. The TGA curves of nanoporous and dense gels are quite similar, with a significant weight loss from room temperature up to 450 ºC. The DSC curves clearly show that the crystallization occurs at an earlier temperature in the case of the nanoporous films when compared with the dense ones.

Figure 4.7 shows the in-situ XRD patterns of nanoporous and dense $BaTiO_3$ powders (obtained by drying at 60 °C the dip-coating solutions) treated at different temperatures. Nanoporous powders prepared with block-copolymer 40-53 and 59-72 start the crystallization at 650 ºC while the crystallization of the dense powders starts to occur at 750 ºC.

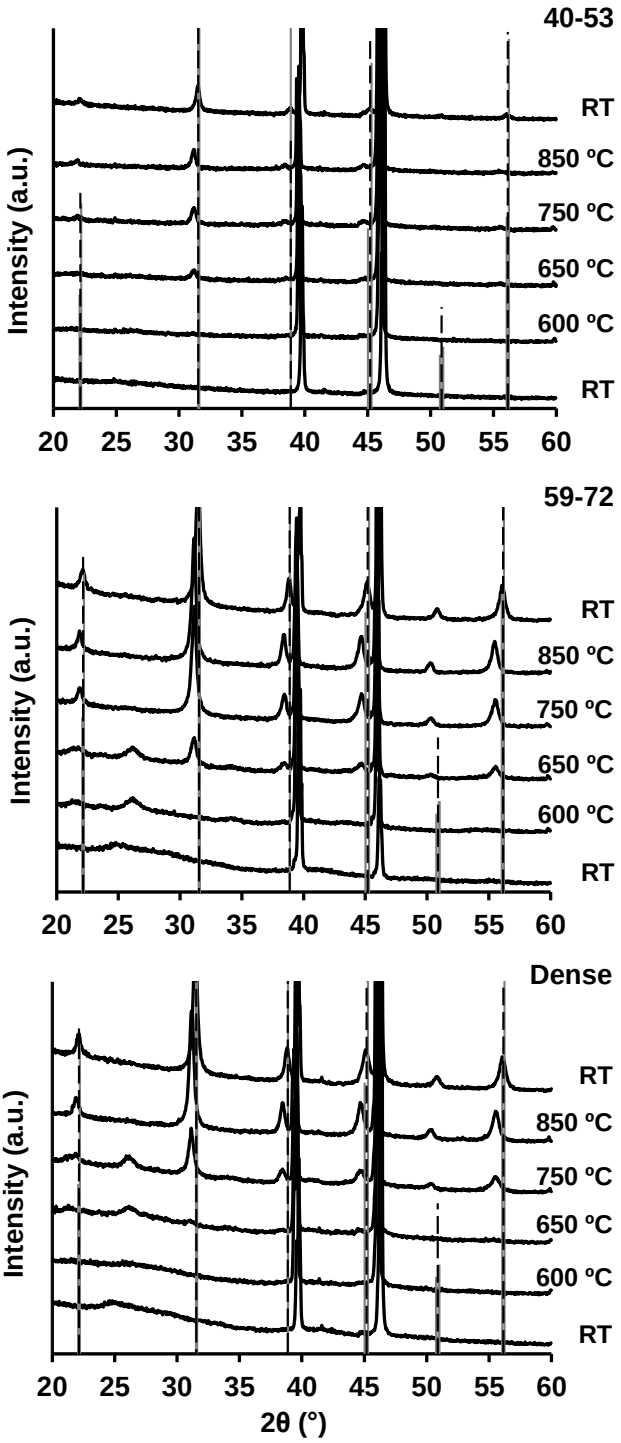

Figure 4.7: In situ X-ray diffraction patterns of nanoporous and dense $BaTiO_3$ powders treated from room temperature up to 850 ºC. Solid gray vertical lines correspond to the tetragonal (JCPDS no 01-070-9164) and dashed black vertical lines correspond to cubic (JCPDS no 01-070-9165) crystalline phase of $BaTiO_3$. The peaks at *ca*. 40 and 47º 2θ correspond to the platinum foil used to perform the measurements. Crystalline $BaTiO_3$ phase occurs at lower temperatures in the case of nanoporous films (~ 650 ºC).

Comparing the nanoporous prepared with different block-copolymer and dense powders, the powder prepared with the block-copolymer 40-53 is mainly amorphous but some diffraction peaks associated with crystalline $BaTiO_3$ are already visible at *ca*. 32 and 45º 2θ. At the mentioned temperatures it is impossible to differentiate between the cubic and tetragonal structure of $BaTiO_3$ (JCPDS no. 01-070-9165 and 01-070-9164, respectively).

For thermal treatments at and above 650 ºC, the powders crystallinity increases. However, the concomitant presence of both cubic and tetragonal phases is observed. The early crystallization is more evident for the nanoporous thin films prepared with the block-copolymer 59-72. These results are in agreement with the previous indications that $PbTiO_3$ nanoporous powders crystalize at lower temperatures than their dense counterparts.[144]

Figure 4.8 depicts top view SEM micrographs of nanoporous and dense $BaTiO_3$ thin films thermally treated at different temperatures, illustrating the microstructure evolution of the three films. Nanoporous thin films prepared with block-copolymer 59-72 and thermal treated at 350 ºC present a porous microstructure with a higher degree of order and periodicity when compared with thin films prepared with block-copolymer 40-53. This is a consequence of the chain size of the block-copolymer. Pore order and periodicity result from self-assembly of micelles of the amphiphilic block-copolymer, followed by condensation of the inorganic species around the micelle arrays. From the image contrast at 350 ºC for both nanoporous thin films, it can be observed that the block-copolymer may be completely decomposed since the majority of the pores are empty. According to the thermal analyses, the block-copolymer decomposition takes place between 200 and 400 ºC (Figure 4.6). Average pore size is around 35 nm for thin films prepared with block-copolymer 59-72 and 50 nm for thin films prepared with block-copolymer 40-53.

Thin films XRD patterns are shown in Figure 4.9. The nanoporous thin films prepared with different block-copolymers and the dense ones were thermal treated at 650 and 700 ºC. The absence of the characteristic peaks of $BaTiO_3$ perovskite structure at 650 ºC points to an amorphous character of the dense films. The formation of the crystalline phase occurs at a lower temperature in nanoporous than in dense thin films.

Theses results are in accordance to our previews observation in $PbTiO_3$ thin films.[144] The thermal analyses and diffraction patterns of the dried solution powders thermally treated in similar conditions as the films also supported the formation of crystalline perovskite phase at lower temperature in nanoporous than in non-porous materials.

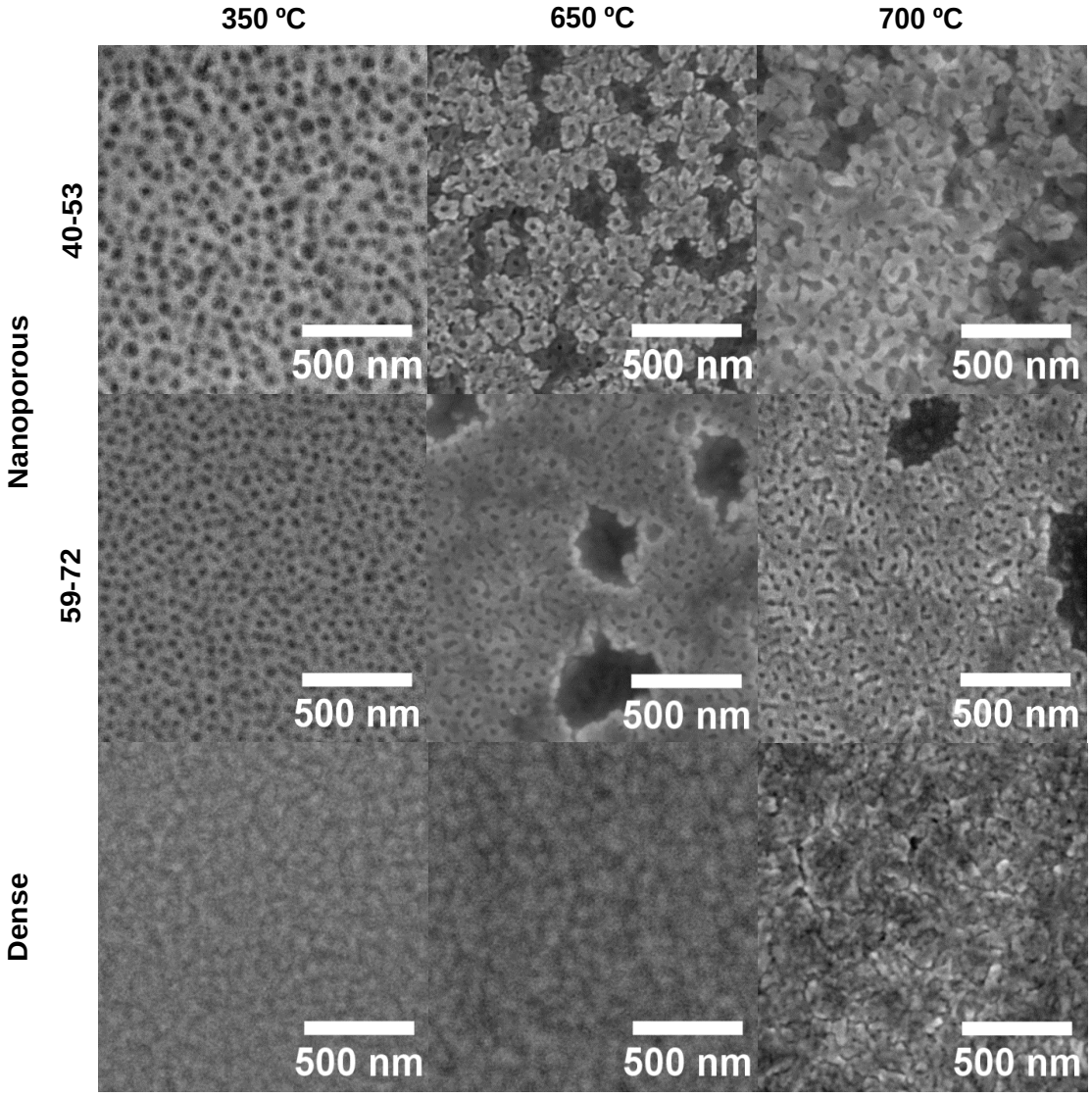

Figure 4.8: SEM micrographs illustrating the typical morphology of nanoporous and dense $BaTiO_3$ thin films after thermal treatment at: 350, 650 and 700 ºC. As the temperature of the thermal treatment increases, the porosity order is lost and bright areas appear as a consequence of the crystallization. Defined larger grains (in comparison to porous films) characterize the $BaTiO_3$ dense films.

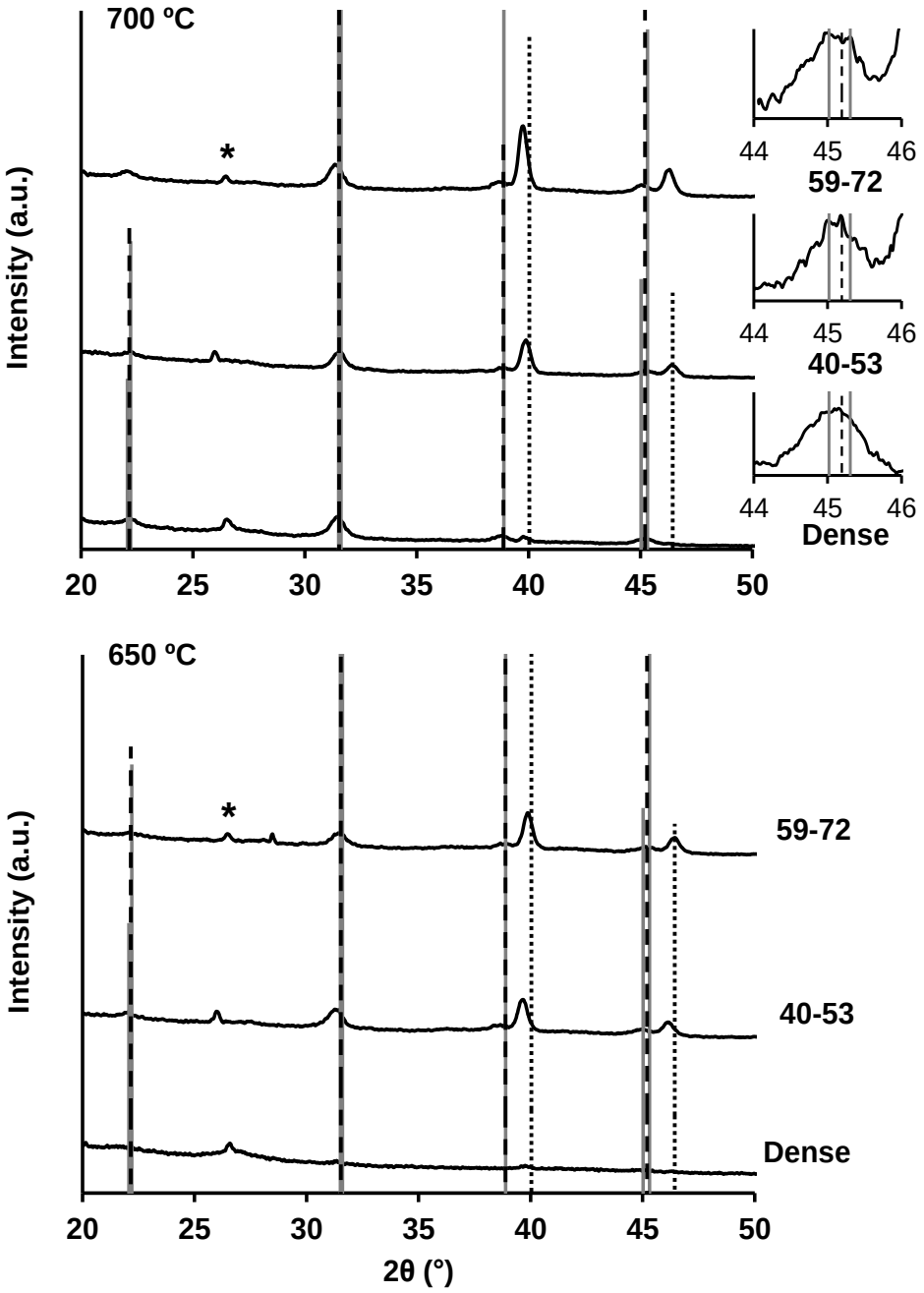

Figure 4.9: X-ray diffraction patterns of nanoporous and dense $BaTiO_3$ thin films thermally treated at 650 and 700 ºC. Solid gray vertical lines correspond to the tetragonal (JCPDS no 01-070-9164) and dashed black vertical lines correspond to cubic (JCPDS no 01-070-9165) crystalline phase of $BaTiO_3$. The dotted black lines correspond to the platinum layer of the substrate. The asterisk corresponds to the titanium oxide already presence in the substrate when thermally treated at 650 ºC. Tetragonal crystalline $BaTiO_3$ phase occurs at lower temperatures in the case of nanoporous films prepared with the block-copolymer 59-72 (700 ºC).

A possible explanation for this effect can be related with the exothermic degradation of the block-copolymer concomitant with the presence of the pores that act as nucleation sites / defects facilitating to the formation of the crystalline phase.[21] However, at this temperature it is not possible to differentiate between the cubic and tetragonal structure of $BaTiO_3$ (JCPDS no. 01-070-9165 and 01-070-9164, respectively).

For heat treatments at 700 ºC, the film crystallinity increases but the tetragonal phase can only be identified in thin films prepared with the block-copolymer 59-72 by the splitting of the diffraction peak at 45.19 into 45.02 and 45.30 º 2θ (for comparison, the reflections corresponding to $BaTiO_3$ in the tetragonal and cubic phase according to the JCPDS no. 01-070-9164 and 01-070-9165 respectively are shown in more detail in Figure 4.9b). No other crystalline phases could be detected.

The heat treatment at 700 °C seems to be sufficient to achieve crystallization and a good compromise in terms of keeping the nanoporosity.

In order to confirm the XRD observations, Raman spectroscopy studies were performed in nanoporous and dense films thermal treated at 700 ºC, Figure 4.10.

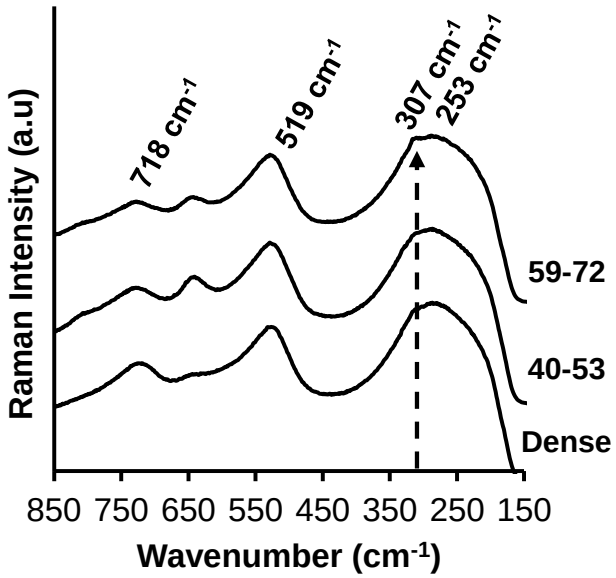

Figure 4.10: Raman spectra of nanoporous and dense $BaTiO_3$ thin films thermally treated at 700 ºC. Raman spectroscopy proves the enhancement of the tetragonal $BaTiO_3$ phase in nanoporous film prepared with the block-copolymer 59-72.

Eight Raman active modes are expected for tetragonal $BaTiO_3$ with a space group *P*4*mm*, 3A1g + B1g+ 4Eg.[223] All Raman patterns display peaks which can be assigned to tetragonal $BaTiO_3$. The broad peaks at around 519 and 253 can be assigned to the fundamental TO modes (transverse component of the optical mode) of A1 symmetry. The peak at 307 cm^{-1} more evident in the film prepared with 59-72 block-copolymer is assigned to the B1 mode, indicating an asymmetry within the TiO_6 octahedra of $BaTiO_3$ on a local scale. The broadband at around 718 cm^{-1} is related to the highest frequency longitudinal optical mode (LO) of A1 symmetry. In the case of nanoporous thin films prepared with the block-copolymer 59-72, the peak at 307 cm^{-1} is better defined than in dense films or films prepared with 40-53, indicating an enhancement of the tetragonal phase in those films.

In order to investigate the piezoelectric behavior in the different nanoporous $BaTiO_3$ and dense thin films thermal treated at 700 ºC, a modified AFM was used, VPFM.

The topographic and piezoresponse domain images of thin films are shown in Figure 4.11. Topographic images reveal the clearly resolved morphological features, mainly for the nanoporous films prepared with the block-copolymer 59-72 (Figure 4.11c) indicating the crystallite structure of these films. The pores in the topography images are not clearly defined due to the use of contact mode, which is the required mode for PFM but not the best suited one for resolving film topography. Clearly, an increase of the nanocrystalline size is verified in nanoporous thin films when the block-copolymer 59-72 is used.

Both nanoporous thin films reveal the presence of two distinct phases exhibiting different piezoelectric behavior, in analogy with the two regions (bright and dark) observed in the SEM microstructures (Figure 4.8). The bright areas formation can be related with a kinetic process of nucleation and consequent crystalline phase formation. These bright areas with strong piezoelectric response are more defined in the nanoporous thin films, mainly in the nanoporous thin films prepared with the block-copolymer 59-72, than in dense ones, whereas the pores in the nanoporous case probably act as nucleation sites contributing for an early crystallization and consequent piezoelectric response. The same behavior was observed in nanoporous $PbTiO_3$ thin films prepared through the same methodology.[144]

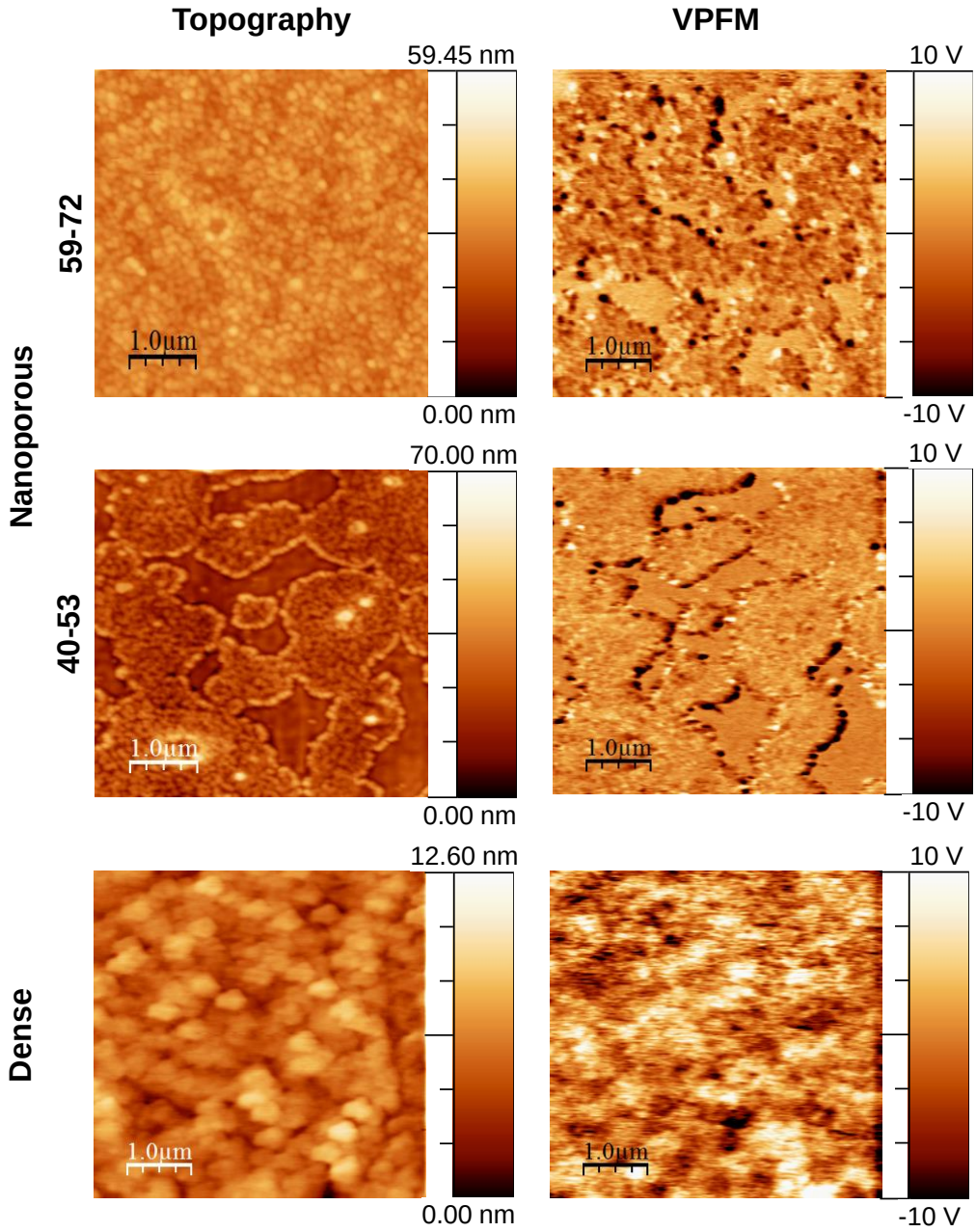

Figure 4.11: Topography and VPFM mixed signal scanning probe microscopy images of dense and nanoporous $BaTiO_3$ films (prepared with different Mw block-copolymers), all thermally treated at 700 ºC. The scale of the VPFM mixed signal image ranges between -10 to 10 V. This 20 V scale corresponds to 360º, thus opposite domains oscillate 180º out of phase. The piezoelectric response is stronger in the nanoporous thin film prepared with the larger block-copolymer (59-72) than in dense counterpart or nanoporous thin film prepared with block-copolymer 40-53.

All thin films exhibit piezoelectric domains (Figure 4.11b, d, f). Different contrasts can be observed in VPFM, indicating opposite polarities. Dark regions correspond to domains with polarization oriented toward the substrate and bright regions to domains with polarization terminated at the free surface of the film. The grains are randomly splited into domains of opposite polarities. However, and as expected, based in the XRD and Raman results, the better defined domains are observed in the nanoporous thin films prepared with the block-coplymer 59-72 than in the nanoporous films prepared with the block-coplymer 40-53 or dense ones. This can be explained, as previously mentioned, by the enhancement of the degree of crystallinity and tetragonal distortion in the nanoporous thin film prepared with higher block-copolymer. In these particular films, the piezoelectric response is more homogeneously distributed within the crystalline areas. However, experimentally, it was difficult to maximize the areas with strong piezoelectric behavior without losing the porosity order.

The ferroelctric properties were not evaluated due to the weak FE response of this perovskite structure mainly prepared by EISA methodology. Although the nanoporous thin films exhibit the tetragonal phase, in $BaTiO_3$ the out-of-plane piezoelectric response signal does not simply describe the out-of-plane polarization due to the high value of d_{15} compared to d_{33}, so a very weak out-of-plane piezoelectric response signal means a weak spontaneous polarization perpendicular to the film plane.[177] As a consequence, and as well documented in the literature, the out-of-plane piezoresponse of $BaTiO_3$ films acquire by PFM is generally weak.

4.4 Conclusions

The optimized conditions to prepare an ordered nanoporous $BaTiO_3$ thin film are presented in the Figure 4.12.

From the study of the initial solution effect on structural properties of $BaTiO_3$ it was possible to conclude that the solutions without inorganic precursors and with addition of the inorganic precursors/organic solvents have a narrow size distribution suggesting that the micellization process obeys the closed association mechanism.

The micellization process for the solutions with addition of the inorganic precursors/organic solvents seems to occur in two steps. In the first step, the number of micelles with similar size increases due to very quick formation of micelles in quasi-equilibrium. In the second step, the association number increases and the micelle number decreases. This fact can be explained by the growth of micelles through decomposition and by entering or expulsion of unimers into or from micelles. The increase of the number of micelles with similar sizes is considered as the dominant step over the micelle size growth. For the solutions without inorganic precursors, the micellization process occurs too fast. The addition of more organic solvents, THF and CH_3COOH, leads to the increase of the solubility degree of the solvation systems, allowing the accommodation of smaller micelles. We have concluded that for the preparation of $BaTiO_3$ porous films in the described conditions, it is preferable to use very fresh solutions with no heating cycle. The understanding of the effect of these parameters on the micellization process, allowed finding that under the applied conditions solution 3 is the most suitable to achieve almost ordered $BaTiO_3$ nanoporous films.

From the second study, we can conclude that the order of the porosity structure and arrangement is very dependent on the structure-directing agent. An earlier crystallization of the tetragonal perovskite phase was verified to occur in nanoporous films prepared with the 59-72 block-copolymer. A possible explanation for the observed effect can be related with the exothermic degradation of block-copolymer concomitant with the presence of smaller and higher volume of pores that act as nucleation sites contributing for the formation of tetragonal phase at low temperature in nanoporous films prepared with the higher block-copolymer.[21] This enhancement of the tetragonality in these nanoporous thin films is reflected in the enhancement of the local piezoelectric properties. However, the ferroelctric properties were not probed due to the weak ferroelectric response of this perovskite structure mainly prepared by EISA. Although, the local ferroelectric properties were not observed, these nanoporous films were used as matrices for the preparation of multifunctional materials as described in the next Chapter.

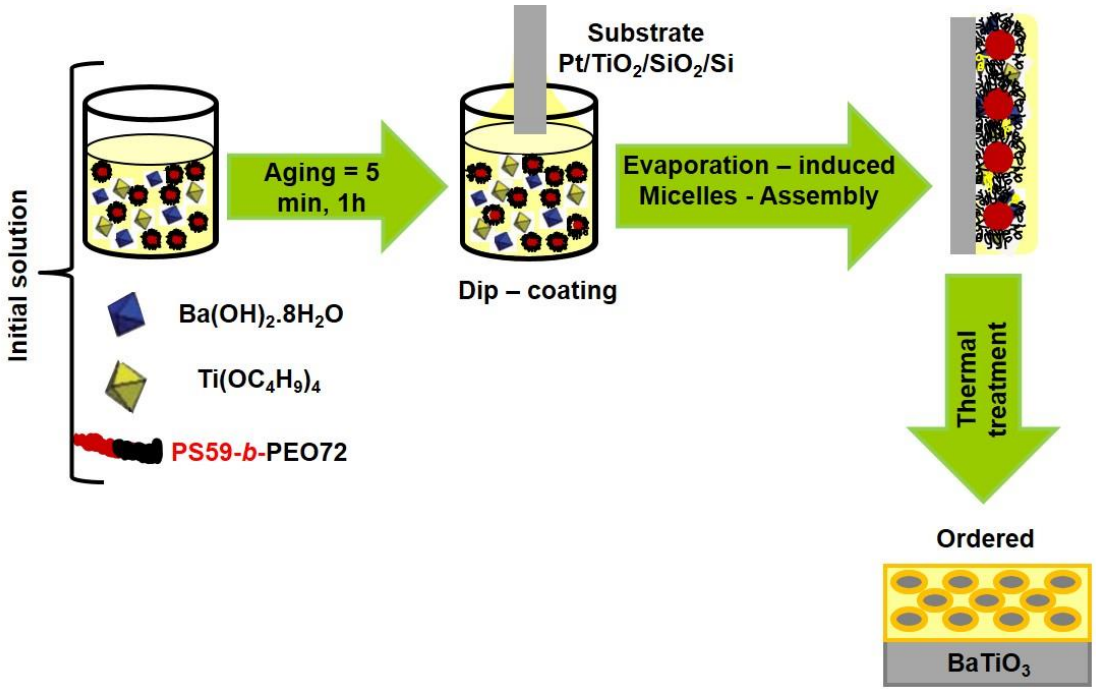

Figure 4.12: Optimized conditions of the $BaTiO_3$ initial solution parameters in order to achieve ordered nanoporous films.

CHAPTER 5

Chemical designed MF nanocomposite films: original design

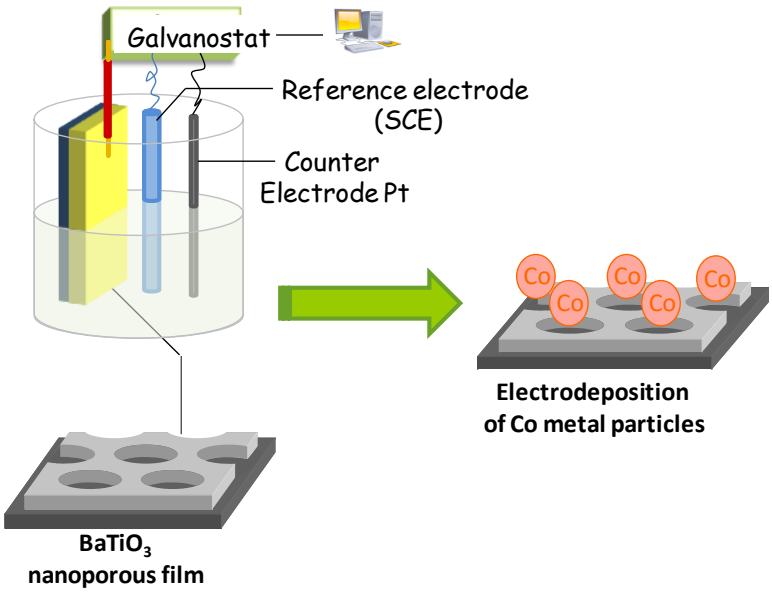

Graphical abstract: Schematic representation of the electrochemical functionalization of the $BaTiO_3$ ferroelectric porous matrix with Co metal ferromagnetic nanoparticles.

Abstract

Multifunctional (in this Chapter and in the Chapter 7 the multifunctional material is designed as multiferroic material) thin films are prepared by electrochemical deposition of ferromagnetic cobalt nanoparticles into the ferroelectric $BaTiO_3$ porous matrix prepared as described in the last chapter. The piezoelectric properties are investigated at the nanoscale by PFM. Ferromagnetic properties are assessed by MFM together with macroscopic measurements using a SQUID magnetometer. The composite films display both ferroelectric and ferromagnetic properties pointing for their great potential as a new generation of multiferroic systems for multifunctional applications.

Index

5.1 Introduction

Multifunctional materials combining two or more order parameters in the same material seem to be the answer to present and future needs in terms of microelectronic materials and devices.

The combination of the FE properties with other functionality such as FM and/or ferroelasticity in the same physical volume forming a MF material is an interesting approach towards miniaturisation and creation of new functionalities.[70]

As mentioned before MF thin films offer the possibility to fabricate a new type of storage devices combining the best qualities of FeRAMs and MRAMs like fast low-power electrical write operation and non-destructive magnetic read operation.[7] Generally, two types of MF thin films are considered: the single-phase MFs and the nanocomposite MFs.[13,14] It is believed that in order to reach an applicable MF material it would be important to engineer a multiphasic composite material with a sufficiently high magnetoelectric coupling.[13,14] Horizontal multilayered composite thin films consist of alternating layers of FE and FM phases. Usually they exhibit a weak magnetoelectric effect due to large in-plane constrains from the substrate. Vertical heterostructured thin composite films consist of vertical structures of one of the ferroic phases embedded vertically within the other phase.

Under the context, the preparation of low cost MFs by a simple methodology is necessary. Here, we describe a new methodology to prepare a MF based on the use of a nanoporous $BaTiO_3$ thin film with 100 nm of thickness and of an electrochemical deposition strategy to insert the FM species into the pores. The technique is particularly attractive for commercial applications due to its relatively high deposition rate and thickness uniformity of the deposited film.

Some studies concerning the correlation between electrodeposition parameters (pH solution, current density, and electrolyte composition) and magnetic properties in cobalt thin layers (coercivity, remanence, squareness of the hysteresis loop) have been investigated.[224,225,226,227] It is well established that the magneto-transport properties of the electrodeposited films are very sensitive to their crystallographic and chemical structure. Generally, by changing the current density and deposit composition one could obtain very different magnetic properties. To the best of our knowledge, this is the first report on the use of electrochemical depositon to funcionalize pores of a porous FE film matrix aiming the preparation of a MF composite material.

5.2 Experimental part

$BaTiO_3$ nanoporous thin films were prepared according to reference.[142]

The electrochemical deposition of cobalt films was carried out in a potenciostatic method in an aqueous solution of 0.1 M cobalt(II) sulphate heptahydrated (Aldrich, ≥ 99%), 10 mM of cobalt (II) chloride hexahydrated (Aldrich, 99%) as source of metal ions and 1 M sodium sulphate (Aldrich, ≥ 99%) as supporting electrolyte. The solution pH was adjusted to 4.2 by the addition of boric acid (Sigma, ≥ 99.5%, 0.5 M) for all experiments to minimize the hydrogen evolution and the possible precipitation of hydroxylated species. The counter electrode used was platinum wire and the reference electrode was a saturated calomel electrode (SCE-E = −0.241 V/NHE (normal hydrogen electrode)). For all the electrochemical experiments, the geometrical surface area of the working electrode was 0.192 cm^2. Solutions were aerated with argon and the temperature maintained constant in the 20-25 ºC range. The applied potentials were varied between -1 and 1 V versus SCE. A potentiostat galvanostat (Princeton Applied Research – PAR262) was used for the electrosyntheses and voltammetric measurements.

The film mesostructure was investigated by SEM using a SU-70 Hitachi microscope. VPFM were carried out on Nanoscope III, Digital Instruments system with a lock-in amplifier, SRS Stanford Research Systems, using DPE-18 cantilevers with Pt-coated tips (Mikromasch, resonant frequency of 60−100 kHz, force constant of 1.1−5.6 N/m), respectively. For the VPFM measurements, the topography signal of the film

surface was taken simultaneously with the mixed signal. Both were collected in contact mode. Since the results were obtained with the same type of cantilevers and under identical scanning and acquisition conditions, comparison between films can be made.

MFM was carried out on an Agilent (Molecular Imaging, PicoSPM LE), using Bruker cantilevers with Co-Cr coated tips (MESP, resonant frequency of 50−100 kHz, force constant of 2.8−5.0 N/m). Topography signals of the film surface were taken in AC mode simultaneously with the deflection and phase signals. The MFM signals were collected using a lift height mode. A dynamic mode was used to record the phase.

Magnetization measurements as a function of temperature, M(T), and applied magnetic field, M(H), were performed using a SQUID magnetometer (Quantum Design MPMS). The M(T) curves were collected at 50 mT in increasing temperature from 10 to 370 K, after zero-field cooling (ZFC) or field cooling (FC) procedures. The hysteresis loops were obtained at 10 and 300 K for magnetic fields between -5.0 T and 5.0 T.

5.3 Results and discussion

Cobalt electrodeposition conditions was firstly performed and optimized with platinum surface using electrochemical methods. In order to select the potential for electrodeposition, current-potential measurements were realized. Figure 5.1 shows a current-potential curve of cobalt on platinum wafers, in 0.1 M in $CoSO_4$, 10 mM $CoCl_2$ and 1 M Na_2SO_4 solution with 0.5 M H_3BO_3 at pH 4.2.

The scan potential rate was 50 mVs^{-1}. The cobalt began to be deposited from around -0.850 V versus SCE. The cathodic current, corresponding to nucleation and growth phenomena, increases rather fast with increasing negative potential. In the potential range where reduction of cobalt (Co^{2+}) occurs, hydrogen evolution is observed simultaneously. At more negative potentials, the rate of hydrogen reaction increases. As it is shown, only one oxidation peak was obtained at -0.280 V, which can be associated with cobalt deposition.

Figure 5.2 shows the current transient for the electrodeposition of cobalt in the pores of nanoporous $BaTiO_3$ surface obtained at applied potentials of -1 V. These transients show an initial increase stage followed by a decrease in the current that

attained a quasi-stationary value. This feature is consistent with the nucleation and the growth processes, indicating a growth mechanism controlled by diffusion.

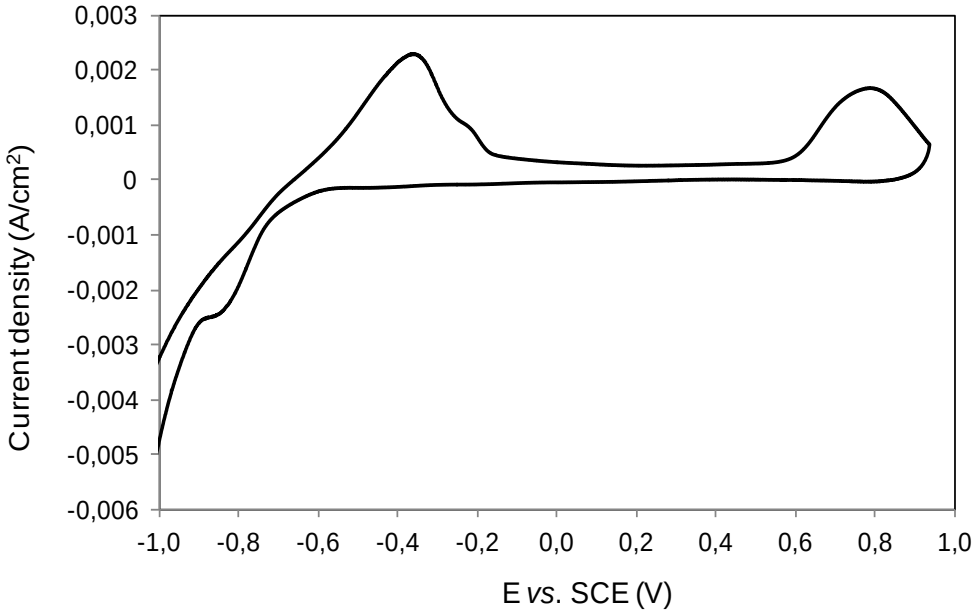

Figure 5.1: The current potential curve for platinum / nanoporous $BaTiO_3$ electrode in 0.1 M in $CoSO_4$, 10 mM $CoCl_2$ and 1 M Na_2SO_4 solution with 0.5 M H_3BO_3 at pH 4.2. The scanning was 50 mVs^{-1}. The cobalt began to be deposited from around -0.850 V versus SCE. Only one oxidation peak was obtained at -0.280 V, which can be associated with cobalt deposition.

The desired architecture consists on the deposition of the metal inside the nanoporosity of the matrix. To obtain this goal is necessary to control the process; particles should be smaller than the porosity order to get an adequate interface between $BaTiO_3$ and cobalt. Different electrodeposition attempts were used, between 2 and 20 s, in order to determine the correct time to avoid the growth of the particles. The films resulting of the deposition experiments consisting of a sequential of two cycles of 5 s were selected for further characterization.

SEM micrographs in Figure 5.3 display the surface morphology of nanoporous $BaTiO_3$ thin films thermally treated at 650 °C and functionalized with cobalt nanoparticles. The porous matrix used to be filled in the electrodeposition presented a considerable degradation of the meso-organization, having pores of different sizes and

interconnected. As reported in the previous chapters, during the mesostructure crystallization, crystal growth occurs with consequent collapse of pore walls and interconnection of pores, leading to the formation of large pores.[142,144]

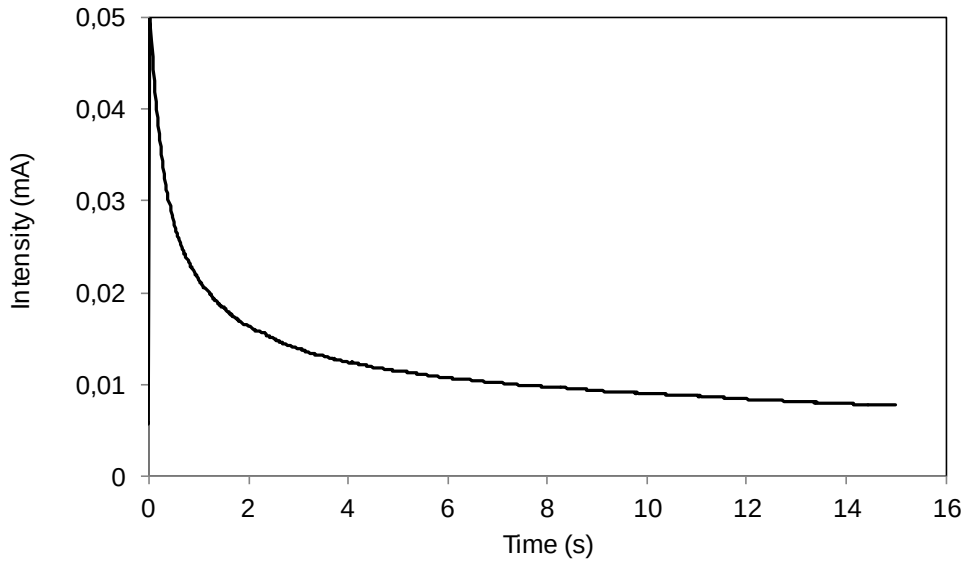

Figure 5.2: Current transient for the electrodeposition of cobalt on platinum / nanoporous $BaTiO_3$ electrode from the solution 0.1M in $CoSO_4$, 10mM $CoCl_2$ and 1M Na_2SO_4 solution with 0.5M H_3BO_3 at pH 4.2 and at -1V vs. SCE. This current transient is consistent with the nucleation and the growth processes, suggesting a growth mechanism controlled by diffusion.

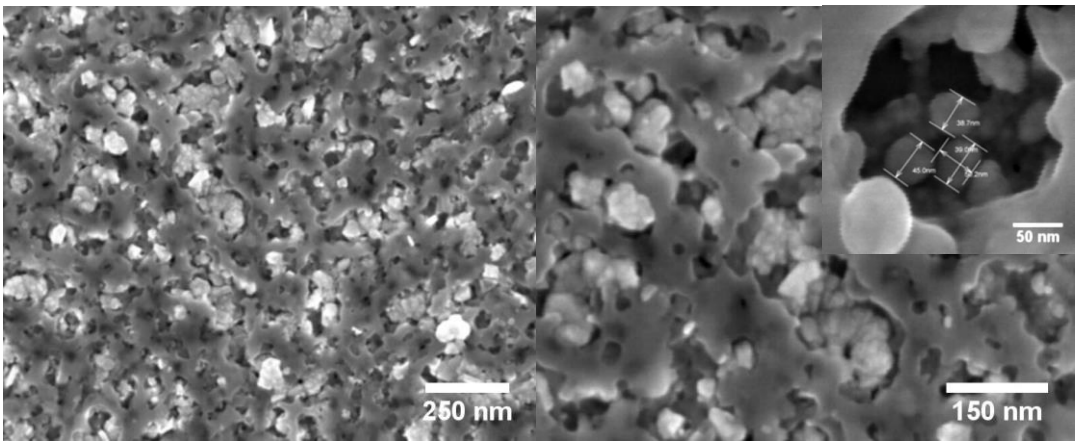

Figure 5.3: SEM images showing the typical morphology of $BaTiO_3$ porous thin film functionalized with cobalt nanoparticles. Not all pores are filled with cobalt nanoparticles. In the inset, one can observe some nanoparticles located just at the entrance of the pore and others accommodated inside the pores. The nanoparticles seem to be very aggregated being the typical size of the particles above 50 nm.

From the analysis of the micrographs and as expected, it seems that the larger pores are easily filled with cobalt particles through the electrochemical deposition than the smaller ones. The reason for this behavior is supposed to be the higher availability of the platinum substrate in these pores than in the smaller ones. Consequently the smallest pores are practically empty. As observed through the inset, some nanoparticles are located just at the entrance of the pore and others are accommodated inside the pores. The nanoparticles seem to be very aggregated being the typical size of the particles below 50 nm.

In order to investigate the local piezo and FE behavior of these matrices, VPFM was used and the local piezoelectric response of the films was obtained as a function of the applied electric ac bias between the platinized substrate and the conducting AFM tip. The topographic and domain images are shown in Figure 5.4.

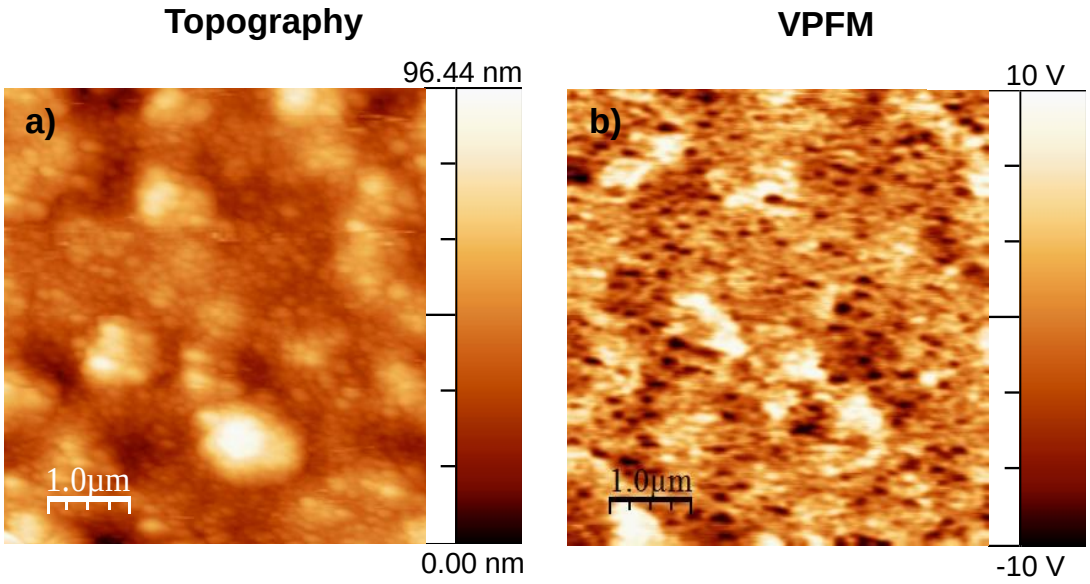

Figure 5.4: Scanning probe microscopy images of nanoporous $BaTiO_3$ film functionalized with cobalt nanoparticels by electrochemical deposition: a) topography image; b) VPFM mixed signal. The scale of the VPFM mixed signal image ranges between -10 to 10 V. This 20 V scale corresponds to 360º, thus opposite domains oscillate 180º out of phase.

Topography reveals that pores are not clearly defined suggesting that the majority of the pores are filled with the cobalt nanoparticles. Bright and well-defined grains corresponding to the crystalline grains can be observed. Although weak, the film exhibits piezoelectric response. Different contrasts are observed, indicating opposite

polarities. Dark regions correspond to domains with polarization oriented toward the substrate and bright regions to domains with polarization terminated at the free surface of the film.

The grains are randomly split into domains of opposite polarities. The piezoelectric response is not homogenously distributed along the surface. This can be explained by the presence of the cobalt nanoparticles inside the pores. Although several attempts were made in order to prove the FE properties, hysteresis loops were not obtained maybe due to the weak effective piezoelectric coefficient, d_{33}, of $BaTiO_3$. It is well reported that in the $BaTiO_3$ perovskite the out-of-plane piezoelectric response signal does not simply describe the out-of-plane polarization due to the high value of d_{15} compared with d_{33}, consequently the longitudinal piezoelectric coefficient has not a linear relation with the out-of- plane polarization, so a weak out-of-plane piezoelectric response signal means a weak spontaneous polarization perpendicular to the film plane.[177] In addition, it is also well known that the FE behavior is dependent on the particle size or of the crystallinity of the film. In one of ours previous works, we could observe that the hysteresis loops of $BaTiO_3$ at 750 ºC were better defined and more symmetric than that the hysteresis loops obtained at 700 ºC.[142] Moreover a progressive reduction of tetragonal distortion, heat of transition, Curie temperature, and relative dielectric permittivity were observed with a decrease of the physical size of the FE particles and, consequently ferroelectricity can be vanished below a critical size which is very dependent on the synthesis method of preparation.[228]

The local FM properties of the cobalt nanoparticles were evaluated by MFM, Figure 5.5. The acquisition of MFM signals was performed using lift height mode with dynamic tip defection. Different contrasts can be observed in the MFM response proving the FM behavior of the cobalt nanoparticles placed inside the pores. However, in order to distinguish the difference between topographic image and MFM response, two line profiles along of the red lines were taken from the topographic and MFM response image, Figure 5.5 c) and d) respectively. As observed by the line profiles, MFM profile is not coincident to the topographic one. In addition, the composite film was tilted 45 and 90 º clockwise, Figure 5.5 e-h, and one can observe that the MFM response is always in the same area.

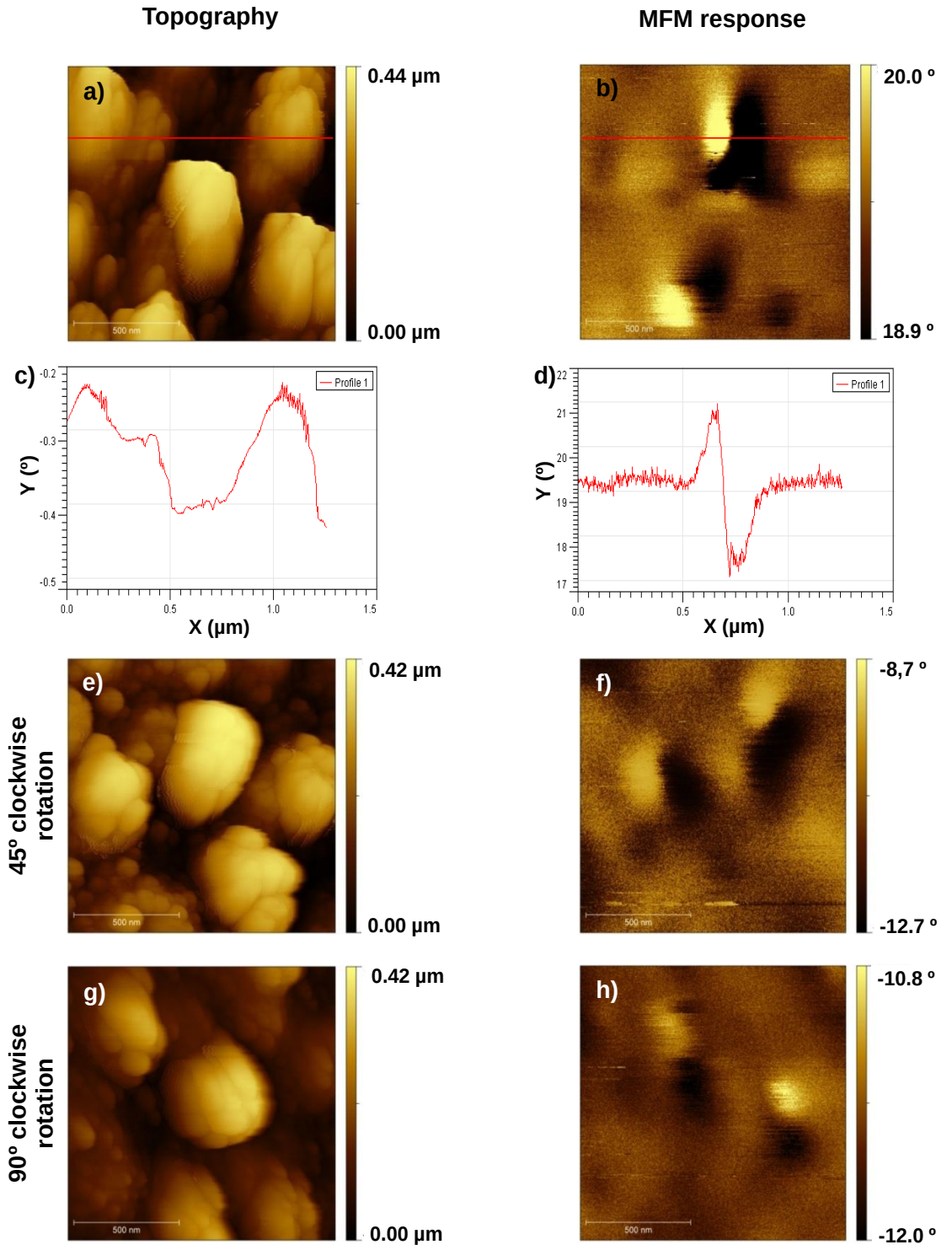

Figure 5.5: AFM images (1500 x 1500 nm^2) (a, e and g) and MFM images (b, f and h) of the nanoporous $BaTiO_3$ functionalized with cobalt nanoparticles by electrochemical deposition. The images c) and d) show line profiles of the topography and MFM response signal. The MFM response proves the local FM properties of the composite film induced by the presence of the cobalt nanoparticles inside the pores of the nanoporous $BaTiO_3$ films.

Figure 5.6 shows the magnetization measurements as a function of temperature and applied magnetic field after subtraction of the diamagnetic components due to the substrate and $BaTiO_3$ film. Although these results are preliminary and are not normalized to the film volume, the magnetic behavior is consistent with the presence of FM cobalt nanoparticles, characterized by a T_C well above room temperature and coercive field values around 435 Oe at 300 K and 1100 Oe at 10 K.

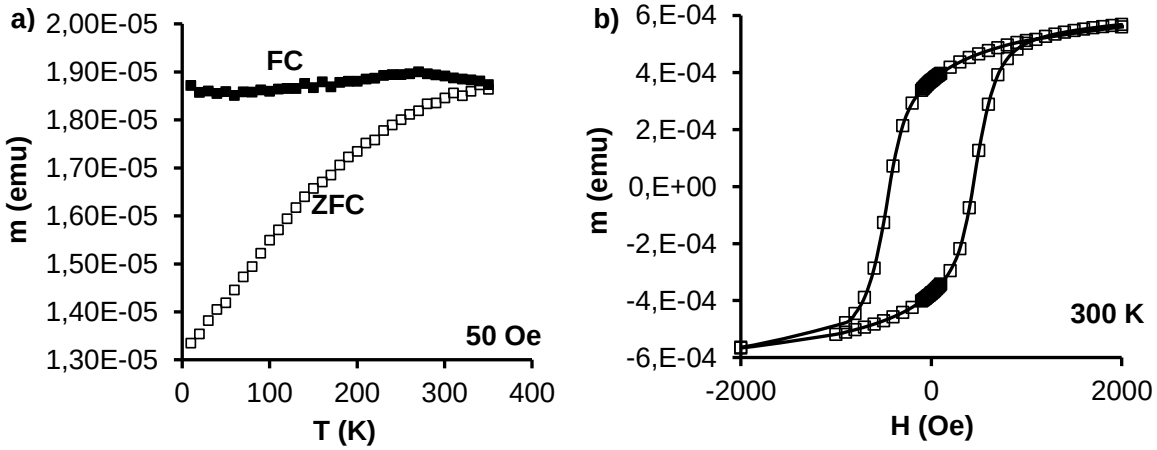

Figure 5.6: Magnetization measurements a) as a function of temperature, for zero field cooling (ZFC curve) and cooling under the measurement field (FC curve) and b) as a function of the magnetic applied field (only showing the range between ± 2000 Oe).

5.4 Conclusions

Multiferroic thin films were prepared by combining EISA methodology for the deposition of a porous matrix with an electrochemical deposition for the functionalization of the film with cobalt nanoparticles. Pores filling was successfully proved by SEM. However, the smallest pores were not filled. Cobalt nanoparticles were quite aggregated being the typical size of the particles below 50 nm. PFM characterization proves the piezoelectric behavior of the composite film, however local ferroelectric hysteresis loops were not obtained. The weak out-of-plane piezoelectric coefficient of the $BaTiO_3$ together with the small particle size and low degree of crystalinity of these films may be the reason for such observations. In addition the ferroelectricity can be completely vanished below a critical size, which is very dependent on the synthesis method of preparation. MFM together with macroscopic

measurements using a SQUID magnetometer proved the ferromagnetic behavior of the composite.

CHAPTER 6

Chemical-based nanopatterning

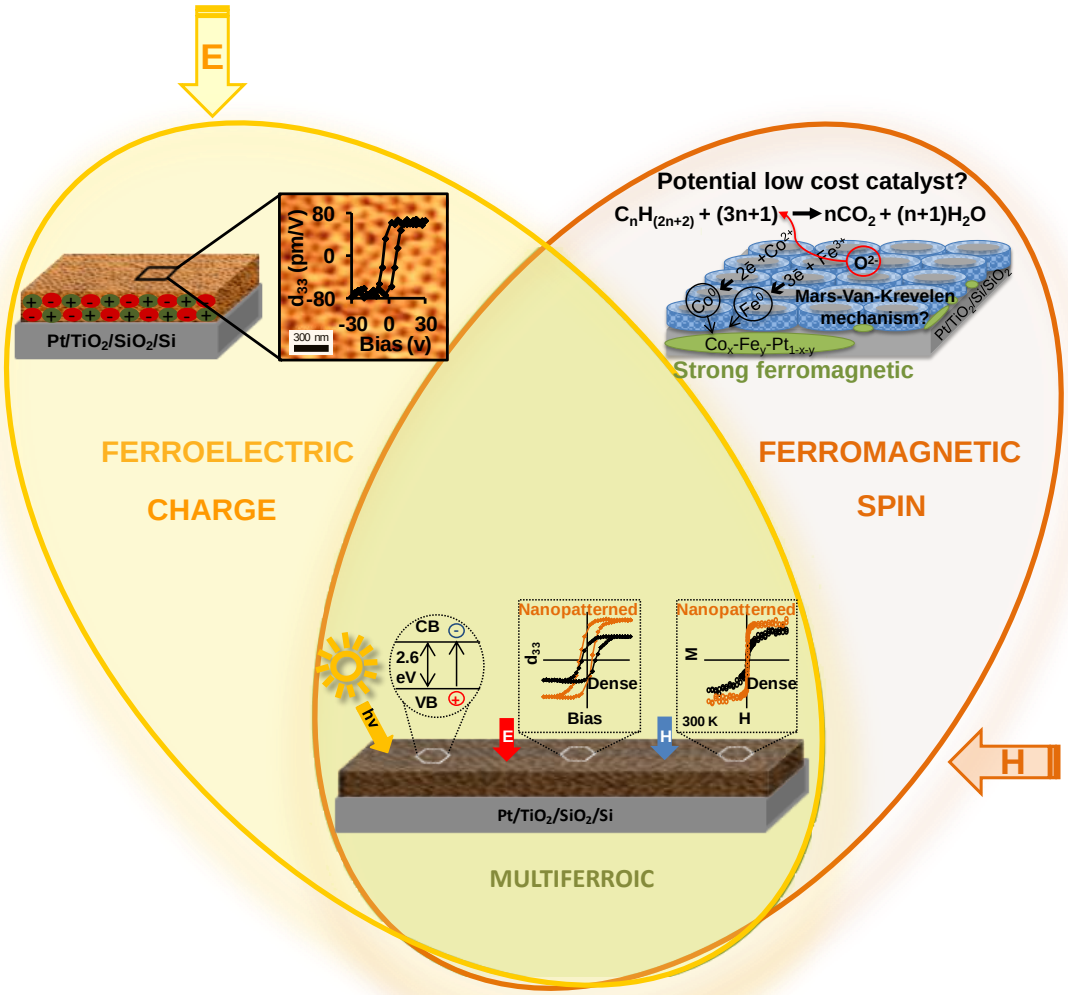

Graphical abstract: Nanopatterning functional porous thin films using an easy and low-cost block-copolymer chemical self-assembly methodology.

Abstract

Chemical self-assembly of functional ferroelectric, ferromagnetic and multiferroic materials, namely of $PbTiO_3$, $CoFe_2O_4$ and $BiFeO_3$, using amphiphilic block-copolymers, is used to prepare low-cost nanopatterned porous thin films. The approach developed in this Chapter is highly effective on patterning porosity, avoiding costly high-resolution lithography techniques and harmful etching processes. Thus, nanopatterned thin films present honeycomb-like arrangement of pores and vertical open porosity from the film surface to the substrate which, lead to around of 50 to 60%

of the substrate surface accessible to further functionalization. Pores with diameters between 80 and 140 nm are obtained. The ordering and thickness of the films are discussed as a function of the precursors concentration and withdrawal rate used for films dip-coating.

The nanopatterned $PbTiO_3$ porous films with thickness of 22 nm exhibit tetragonal perovskite crystallographic phase and ferroelectric response at the nanoscale. The piezoelectric coefficient (d_{33}) value obtained for these nanopatterned films is approximately 50 pm/V, which is slightly better than the $(d_{33})_{eff}$ obtained for the single crystal nanoislands (resulting from complex preparation approaches) where the crosstalk effect provoked by the domain movement or thermal diffusion is inherently excluded (39.4 pm/V).[40]

$CoFe_2O_4$ thin films present a preferential in-plane orientation in opposite to the other $CoFe_2O_4$ films[110,229] prepared by sol-gel methods and with low thickness (≈ 65 nm) where the out-of-plane magnetization prevails. The local and macroscopic magnetic properties are assessed as a function of the thickness and of the porosity by MFM and SQUID magnetometry, respectively. A high saturation magnetizations (close or higher than in bulk $CoFe_2O_4$) were determined for all films, pointing to the presence of a ferromagnetic impurity compatible with a platinum-rich metal alloy. The presence of this impurity not only enhances the magnetic performance but also provides evidence for the use of these $CoFe_2O_4$ films as catalysts with large specific surface area in energy impact process such as the combustion of biogas at low temperature, avoiding the use of the cost prohibitive noble metal catalysts.[230,231]

Crystalline nanopatterned 66 nm thick $BiFeO_3$ layers with an average pore diameter of 100 nm were obtained after heat treatment at 600 ºC. The large vertical porosity markedly enhances the local electric and macroscopic magnetic properties when compared with the dense counterparts. The porous structure also has a positive effect on the parallel magnetic characteristics of the system, displaying a 50% larger ferromagnetic component and enhanced remanent magnetization when compared to the dense thin films counterpart. The porosity is also important for photocatalytic applications conjugating the low direct band gap (2.58 eV) and extended porous area (*ca*. 57 %).

Index

6.1 Introduction

For many of the nanoelectronic applications it would be a challenge to prepare FE thin films with lateral sizes (thickness) well below 100 nm.[232] The design of nanofeatures, uniformed in size and shape at a reasonable large-range order, *i.e*. "nanopatterning", would extend the FE thin films utility for electronic devices and integrated circuits, which require that each pixel feature can be individually addressable. Additionally, nanopatterned porous FE thin films may be of interest to develop vertical composite nanostructures. As mentioned in the Chapter 1, in these vertical nanostructures, the vertical strain control occurs when the vertical interface area between FE and FM phases of the composite exceeds the contact area between the film and substrate. In opposite way, the lateral (substrate) strain controls. When the vertical strain controls, perfect strain coupling at the interface can be obtained.[77]

Nanopatterning in microelectronics is currently conducted by lithographic techniques. Nevertheless, most of these techniques are time consuming, difficult to apply to large areas and have limitations for feature sizes below 100 nm, thereby becoming extremely expensive.[88,56,113,89] Honeycomb ordered arrays can be prepared using amphiphilic block copolymers depending on the chemical compositions of the

block copolymers.[233] The interfacial tension between polymer solutions and water droplets is a key point to prevent water droplets coalescence, thus contributing to preparing ordered honeycomb-patterned films.[233] Nguyen *et al.*[234] reported the replication of the porosity of block copolymer films to achieve a sílica-based porous network. The use of block-copolymers as masks together with lithography has been highlighted as promising for future integrated circuit technology patterning extendable to large areas.[113,235] However, fabrication methodologies involving chemical etching in ferroic materials should be avoided as they cannot be etched easily, and etching creates important structural defects degrading the electric and magnetic properties. Therefore, it is interesting to use the liquid-crystal template mechanism developed by the scientists of Mobil Research and Development Corporation, in 1992,[236] to directly self-assembly the ferroic materials into ordered porous array. In 2004, a high thermally stable block-copolymer was used to prepare nanocrystalline multimetallic inorganic mesoporous thin films of ternary oxide films of $SrTiO_3$, $MgTa_2O_6$ and $Co_xTi_{(1-x)}O_{(2-x)}$.[63] The wet chemical methods using a template agent allow preparing large surface areas with high reproducibility at low-cost without expensive and/or specialized equipment.[207,123,136,120,220]

Although we tried to optimize and improve the coexistence of mesostructural order and crystallization through the study of the initial solution parameters and block-copolymer choice, as described in Chapter 4, the drawback of the procedure remains in the partial loss of the organization of the porous structure during the thermal treatment required to achieve the crystalline phase. Based on those observations, in this Chapter, we try to overcome those limitations by preparing thin films with thickness below 100 nm and using a large amphiphilic copolymer such as poly(butadiene(1,4 addition)-*b*-ethylene oxide) (PB-*b*-PEO), which seems to form inorganic-organic composites with sufficiently thick pore walls that can be fully crystallized without compromise the order. It is well reported that the large amphiphilic copolymers PB-based, namely KLE, produce high crystalline metal oxides with well-defined nanoscale periodicity.[140] Moreover, this amphiphilic block-copolymer presents high chemical and thermal stability that allows the dehydration of the network before the organic decomposition, preventing thus the structure collapsing. Accordingly we report here for the first time a

low-cost and optimized sol-gel method coupled with amphiphilic block-copolymer to prepare nanopatterned thin films of different compositions.

Thus, we believe that decreasing the thickness of the films and using a PB-*b*-PEO block-copolymer, we are able to enhance the order of the nanostructure, achieving highly ordered nanopatterned films with a hexagonal type arrangement of the pores and directed vertical porosity to the substrate. Moreover from previous results, Chapter 3 and Chapter 4, the local FE properties can be markedly enhanced through the nanoporoisty presence. Depending on the composition structural, optical, electric and magnetic characterization are addressed.

In the section 6.2 the importance of the inorganic precursor concentration, withdrawal rate and thermal treatment on the crystallographic phase formation, porosity size and ordering, film thickness and accessibility to the substrate underneath is discussed. Local piezo and FE properties are reported.

Section 6.3 describes the use of sol-gel and EISA to prepare nanopatterned porous thin layer of $CoFe_2O_4$ with 40 or 65 nm thick and very ordered pores with diameter between 60 to 80 nm. The local and macroscopic magnetic properties are studied and compared with the dense counterparts.

The electrical and magnetic properties at macro and local scale of highly ordered nanopatterned porous $BiFeO_3$ thin films with *ca.* 66 nm of thickness and average pore size of 100 nm are addressed in section 6.4. To understand the porosity effect on these properties the comparison with bulk counterparts is established. Optical absorption behavior was also analyzed to exploit the multifunctional character of nanopatterned porous $BiFeO_3$ thin films and their potential for a wide range of applications.

6.2 Block-copolymer-assisted nanopatterning of porous $PbTiO_3$ thin films

As mentioned before and despite of the presence of lead in its composition, $PbTiO_3$ is one of the best room temperature FE perovskite with a high transition temperature (~ 490 ºC) presenting interesting applications in microelectronics such as multilayer capacitors, infrared pyroelectric sensors, nonvolatile and dynamic random access memories, and ultrasonic transducers,[237,55,238,28] for which the FE behavior is one of the most important requisites.[239]

However, based on Devonshire-Ginzburg-Landau (DGL) theory, as the physical dimensions of a FE material are reduced the stability of the FE state is altered. This leads to the existence of a critical size below which ferroelectricity is suppressed.[36] For $PbTiO_3$ thin films, it was predicted that the *c* lattice parameter and, consequently, the tetragonality (*c/a*) substantially decrease below a thickness size of 20 nm.[45] However, the FE critical size values vary considerable and are directly dependent on the methodology of preparation.[11,46]

Here we report an optimized wet chemical method using a different block-copolymer, solution concentration, withdrawal rate and temperature of processing, in which the nano ordered porosity is preserved. The prepared FE nanopatterned $PbTiO_3$ thin films exhibit an ordered hexagonal-like array of pores perpendicular to the substrate. To the best of our knowledge, highly hexagonal ordered $PbTiO_3$ porous thin films prepared by direct block-copolymer self-assembly have never been achieved before for a film thickness below 100 nm.

6.2.1 Experimental part

Nanopatterned porous $PbTiO_3$ thin films were prepared using a diluted sol-gel solution and EISA methodology (see Chapter 2), Scheme 6.1. In the present work, we employed a different amphiphilic block-copolymer from our previous works.[142,144] PB51-*b*-PEO62 with MW_{PB} = 51000 $gmol^{-1}$ and MW_{PEO} = 62000 $gmol^{-1}$, was used as a micellar templating agent. Three solutions were prepared. In solution A, PB51-*b*-PEO62 block-copolymer (45 mg, Polymer Source) was dissolved in absolute ethanol (98.15 mmol, Riedel-de Haën) at 70 ºC. Solution B was prepared by the dissolution of lead (II)

acetate trihydrate (0.60 mmol, Fluka, purity ≥ 99.5% w/w) in glacial acetic acid (8.93 mmol, Merck) at room temperature. Solution C resulted from mixing 2,4-pentanedione (0.43 mmol, Fluka, purity 99.3% w/w) with titanium (IV) *n*-butoxide (0.60 mmol, Merck, 98.0% w/w) under stirring at room temperature. Afterward, solutions B and C were added to solution A, forming the final solution. The films prepared with the inorganic quantities described above were named High C. To optimize the inorganic precursors concentration, we have reduced the concentration of inorganic sources (lead (II) acetate trihydrate and titanium (IV) *n*-butoxide) in solutions B and C to half of the quantity. The films derived from these solutions were denoted Low C. Nanopatterned $PbTiO_3$ thin films were deposited at room temperature and 30% relative humidity by dip-coating onto platinized silicon ($Pt(111)/TiO_2/SiO_2/Si(100)$) (Radiant Inc.) at 0.76 and 1.6 mm/s. All films were thermally treated in air at 350 °C during 5 min in order to complete the inorganic condensation (mesostructuration) of the matrix and to partially decompose the organic content. The films were also annealed at 550 and 600 ºC during 5 min in order to achieve crystallization.

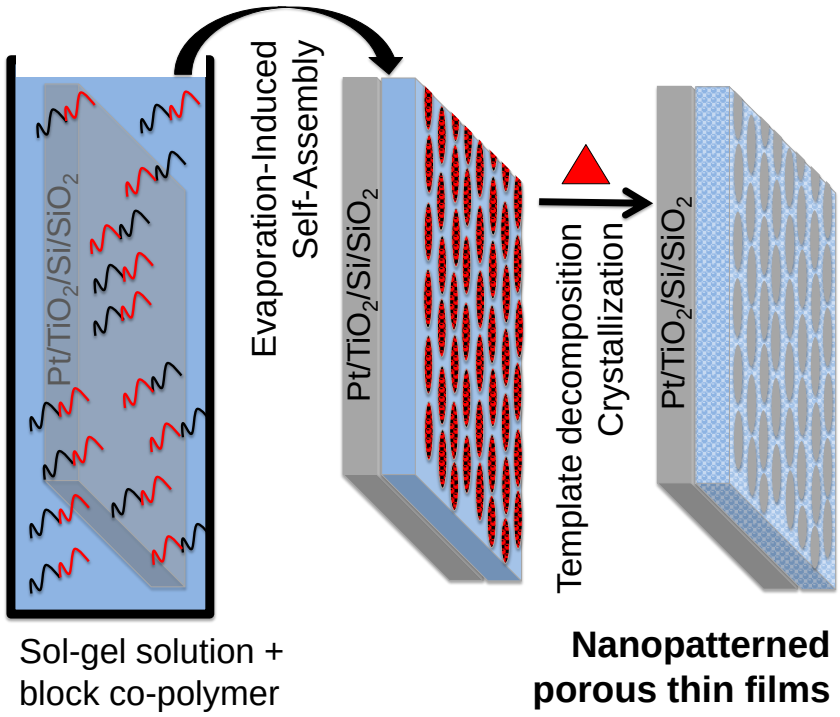

Scheme 6.1: Illustration of the preparation of porous thin films with self-patterned nanopores.

Films microstructure was investigated by high-resolution SEM using a SU-70 Hitachi microscope. To follow the phase formation process, TGA-DTA were carried out on dried nanoporous and dense powders obtained by drying the solutions described above in open vessels at 60 ºC for a few days. A Setaram Labsys™ TGA-DSC16 system was used with a heating rate of 10 °C/min under flowing air up to 700 °C. The crystalline phases were identified by XRD using a Philips X'Pert MPD X-ray diffractometer with Cu Kα radiation, 2 ° grazing incidence angle and a step length of 0.02 °. Raman spectroscopy was performed in JY Horiba LabRam model HR800 equipment, with a high-resolution 800 mm focal length spectrometer. An argon ion laser beam at a wavelength of 325 nm was utilized.

AFM and VPFM were carried out on Nanoscope III, Digital Instruments system with a lock-in amplifier, SRS Stanford Research Systems, using Tap300 cantilevers with Al-coated tips (Budget Sensors, resonant frequency of 200−400 kHz, force constant of 20−75 N/m) and DPE-18 cantilevers with Pt-coated tips (Mikromasch, resonant frequency of 60−100 kHz, force constant of 1.1−5.6 N/m), respectively. For VPFM measurements, the topography signal of the film surface was taken simultaneously with the mixed signal. Both were collected in contact mode. The AFM measurements were also collected in contact mode. Since the results were obtained with the same type of cantilevers and under identical scanning and acquisition conditions, a comparison between films can be made. Several hysteresis loops with bias from -30 to +30 V were obtained to ensure the reproducibility of the results, and representative loops are presented. The piezoelectric and FE properties are mean values taken from several (at least ten) hysteresis loops. The critical voltage is defined as the necessary voltage for the nucleation of a new domain. The imprint is defined as $I_m = (V^+ + V^-)/2$, where V^+ corresponds to the positive coercive bias and V^- to the negative coercive bias. Switchable polarization corresponds to the difference between the positive saturated piezoresponse and negative ones ($R_m = (R_S)^+ - (R_S)^-$). As the effective piezoelectric coefficient ($(d_{33})_{eff}$) is proportional to the amplitude signal, this can be defined as $(d_{33})_{eff} \propto$ (amplitude signal·cos(phase signal)) / V_{ac}, where V_{ac} is the ac voltage applied, and its value can be taken from the mixed signal at zero voltage.

6.2.2 Results and discussion

Figure 6.1 shows top view SEM micrographs of nanopatterned $PbTiO_3$ thin films deposited starting from solutions with high and low inorganic precursor concentration (High C and Low C), using two distinct withdrawal rates (0.76 and 1.6 mm/s) and heated at 350, 550 and 600 ºC.

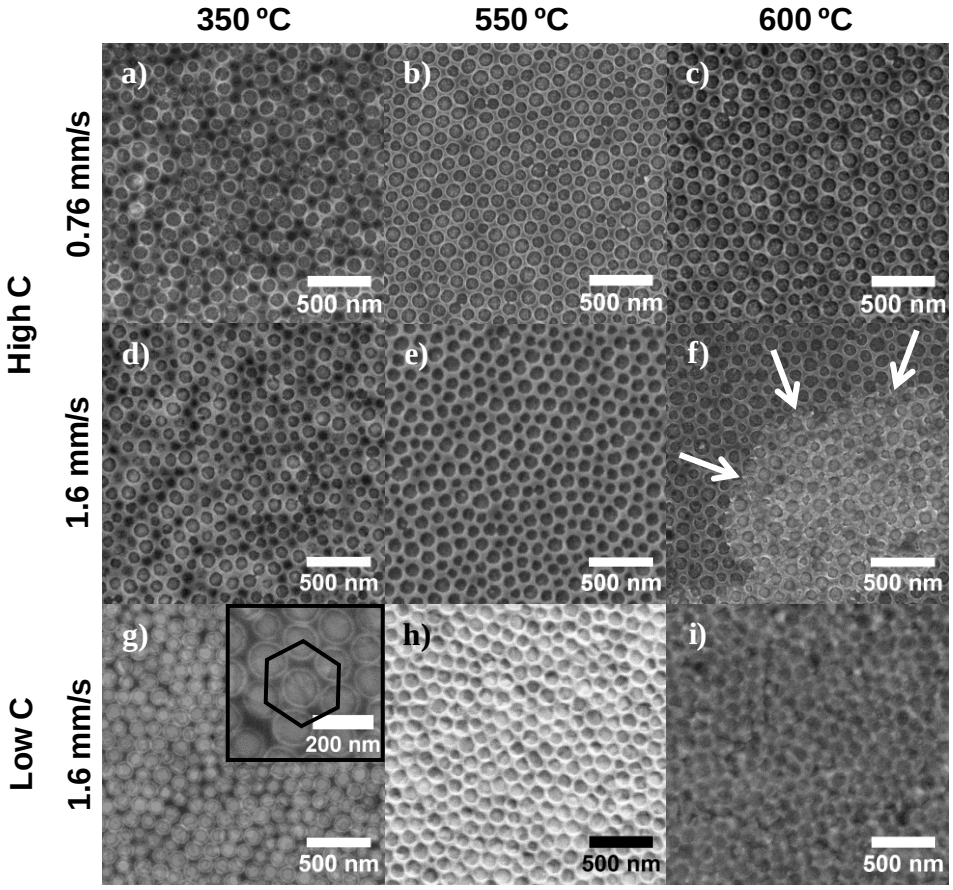

Figure 6.1: SEM micrographs illustrating the typical morphology of nanopatterned $PbTiO_3$ films deposited with high concentration (High C) (6.1a-6.1f) and low concentration (Low C) (6.1g-6.1i) of inorganic precursors; using withdrawal rates of 0.76 mm/s (6.1a-6.1c) and 1.6 mm/s (6.1d-6.1i) and treated at 350 (6.1a, 6.1d and 6.1g), 550 (6.1b, 6.1e and 6.1h) and 600 ºC (6.1c, 6.1f and 6.1i). As the inorganic precursors concentration increases, the distribution of pores sizes becomes wider. The thin film deposited with High C solution and fast withdrawal rate presents different contrasts in the SEM image after treatment at 600 °C (bright areas indicated with arrows in Figure 6.1i). All films present a well-ordered hexagonal arrangement of pores as shown in the inset of Figure 6.1g.

These micrographs are representative of the entire covered surface. All films present well-ordered arrays of pores forming honeycomb-like patterns. After heat treatment at 350 ºC for 5 min, films appear amorphous and some pores seem to remain closed due to the incomplete removal of the block-copolymer (Figure 6.1a, 6.1d and 6.1g). The complete PB-*b*-PEO decomposition occurs between 200 and 450 °C as observed through the TGA-DTA analyses (Figure A1.1 in Appendix). The void motifs result from the thermal decomposition of the block-copolymer.

Independently from the solution concentration, the films treated at 550 and 600 ºC present arrays of hexagonal-like ordered porous structures (Figure 6.1b, 6.1e, 6.1f and 6.1c, 6.1f, 6.1g, respectively). High C films deposited at 0.76 mm/s and treated at 600 ºC (Figure 6.1c) have pores with larger diameters than High C films deposited at 1.6 mm/s and treated at the same temperature (98.1 ± 13.3 nm versus 86.9 ± 13.7 nm calculated from the SEM micrographs) (Figure 6.1c and 6.1f; and Table 1). The latter films present thicker walls than the former ones (91.9 ± 13.1 nm versus ~77.2 ± 14.4 nm). According to the literature, the high withdrawal rate provides more matter at the substrate, thereby generating thicker films with thicker walls and reducing the pore diameter.[240,153]

At 600 °C, the film deposited with the highest concentrated solution and withdrawal rate (Figure 6.1f) shows different contrast areas in the SEM top view (bright areas). Despite this fact, the order and periodicity of the framework remain after this high temperature treatment. The variation on the brightness contrast may be related with the presence of different crystalline phases as observed in our previous work, Chapter 3.[144] Bright areas may be related with the presence of a tetragonal perovskite phase. The imaging of the Low C films treated at 600 ºC is difficult, this is probably due to the reduced film thickness and high exposure of the platinum of the substrate (very bright contrast). The average pore diameter and wall thickness, calculated from the SEM micrographs, are 127.0 ± 11.6 nm and 66.1 ± 14.8 nm, respectively (Table 1). Under these conditions, some of the pores become interconnected (Figure 6.1i). At Low C, the inorganic precursors concentration seems to be insufficient to allow the formation of a homogeneous continuous layer after heat treatment. According to the literature, the inorganic/organic ratio of the initial precursors solution has a determinant influence on the final mesostructure of the mesoporous and nanopatterned thin films.[112,220,207,241]

Ethanolic solutions containing PB-*b*-PEO were reported to form high quality monolayers of oxides with homogeneous pore sizes and ordered arrangements.[156,207,241] The formation of the well-ordered monolayers is mainly dependent on the nature of the used amphiphilic block copolymer, solvent, solution dilution and withdrawal rate.[156,207,241] High C films deposited with the same withdrawal rate and treated at 600 ºC exhibit a higher thickness than the films prepared from Low C. The high content of inorganic precursors enhances interactions with PEO chains, leading to thicker walls and turning pore sizes more heterogeneous (wider distribution of pore sizes) as observed when comparing Figure 6.1e and 6.1h. When the concentration of precursors increases as a consequence of the viscous drag regime[156] a slight increase on the film thickness is expected.

To acquire more data on the effect of the inorganic precursor concentration and withdrawal rate on the structure of nanopatterned films, AFM was carried out in the High C films deposited at both withdrawal rates (0.76 and 1.6 mm/s) and in Low C films deposited at 1.6 mm/s, all treated at 600 ºC (Figure 6.2). The AFM profiles (not presented here) taken from the AFM images allowed the calculation of: pore diameter (d_{pore}), wall thickness, film thickness, fraction of accessible substrate surface (S_{Pt}) and root mean square surface roughness (RMS).

Average values are presented in Table 6.1. For thin films deposited with High C, the AFM images present a good periodicity of pores with wide distribution of pore sizes, confirming SEM results. The AFM images of Low C films (Figure 6.2e and 6.2f) show narrow distribution of pore sizes and a homogeneous wall thickness. Indeed, from the values presented in Table 6.1, d_{pore} is higher in Low C (140.9±6.2 nm) than in High C for 1.6 mm/s (82.3±11.4 nm) or 0.76 mm/s (93.8±13.6 nm). A decrease of d_{pore} when the withdrawal rate increases was observed, which is consistent with SEM observations. Simultaneously, the wall thickness between the pores increases and the S_{Pt} slightly decreases. These results are only consequence of the withdrawal rate.

At 600 ºC, as a result of the phase formation, the nanopatterned films deposited at 1.6 mm/s present a significant number of well-defined nanograins and the hexagonal array is not well-defined. As the AFM measurements were performed in contact mode with high-resolution tips (tip radius < 10 nm and tip height of 17 μm), the pore depth can be related with film thickness.

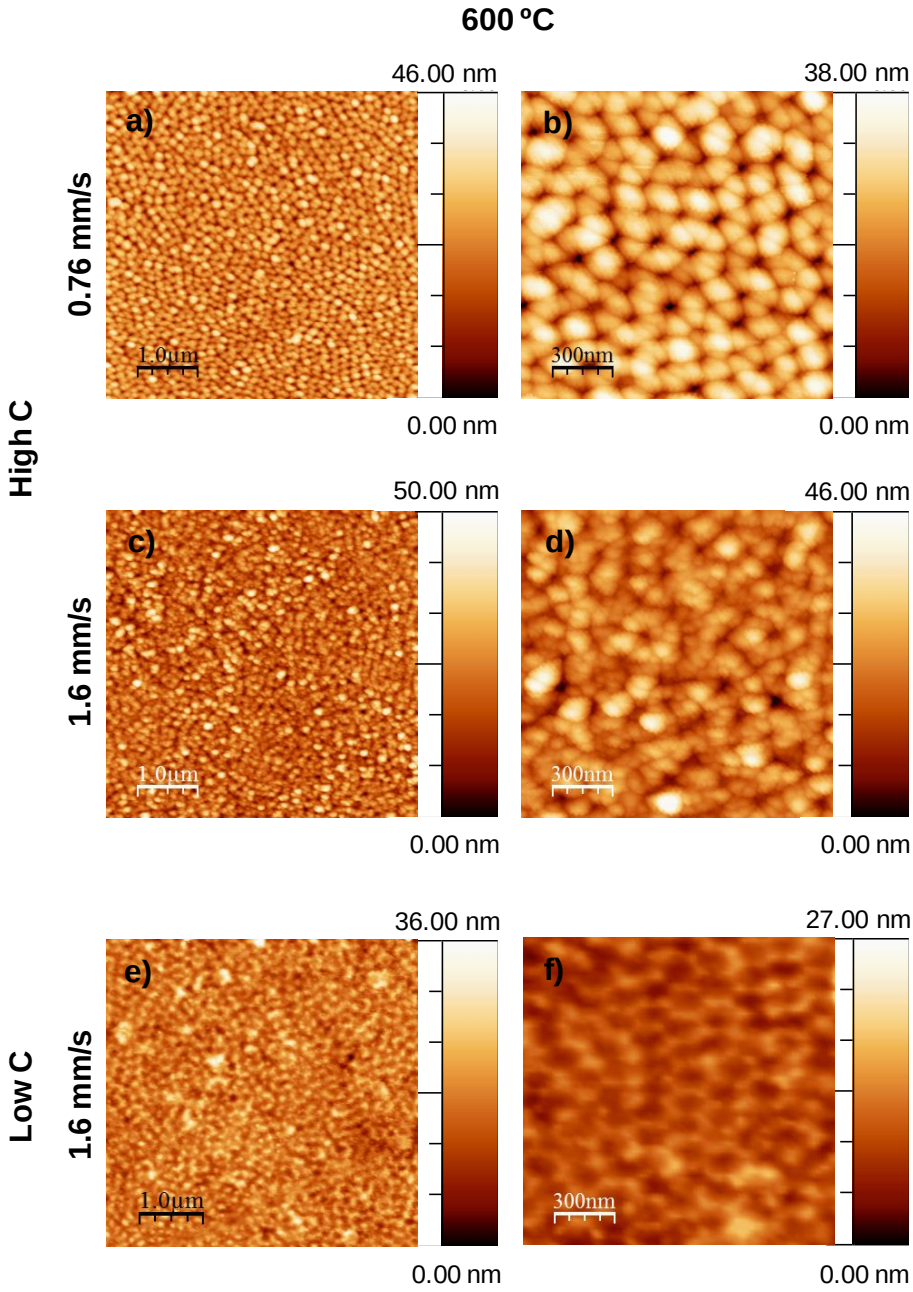

Figure 6.2: AFM topographical images of nanopatterned $PbTiO_3$ films (5 µm x 5 µm and 1.5 µm x 1.5 µm) obtained with High C (a-d) and Low C (e-f) solutions, deposited at 0.76 mm/s (a and b) and 1.6 mm/s (c-f) and thermal treated at 600 ºC. All nanopatterned $PbTiO_3$ films present ordered hexagonal arrays of pores.

According to the values of Table 6.1, the film thickness increases as the inorganic precursors concentration and withdrawal rate increase. The increase of the inorganic precursor concentration increases the solution viscosity improving film

thickness. In fact, as the highest value of film thickness is below the tip height, the pore depth can be related with the film thickness without big error.

Furthermore, the thickness value obtained for thin films deposited with High C and 1.6 mm/s is in good agreement with the value measured by SEM cross-section image (not presented here). Thus, the porosity seems to be completely open and practically directed to the substrate. It is worth noting the remarkable porous order of all the studied films, despite the different film thicknesses (varying from ~ 5 to 22 nm).

Table 6.1: Nanopatterned $PbTiO_3$ films features: pore diameter (d_{pore}), wall thickness between the pores (both calculated using AFM and SEM images), film thickness, fraction of accessible platinum substrate surface (S_{Pt}) and root mean square (RMS) surface roughness (calculated from AFM images). As the inorganic precursor concentration and withdrawal rate increase, film thickness and wall thickness also increase, with concomitant decrease of the pore diameter.

	High C		**Low C**
	0.76 mm/s	**1.6 mm/s**	**1.6 mm/s**
d_{pore} – AFM (nm)	93.8±13.6	82.3±11.4	140.9±6.2
d_{pore} – SEM (nm)	98.1 ± 13.3	86.9 ± 13.7	127.0 ± 11.6
Wall thickness – AFM (nm)	76.2±13.6	89.4±11.5	40.8±10.6
Wall thickness – SEM (nm)	77.2 ± 14.4	91.9 ± 13.1	66.1 ± 14.8
Film thickness – AFM (nm)	18.9±2.1	22.4±1.7	5.7±1.4
S_{Pt} – AFM (%)	52.1±2.4	47.7±2.1	59.9±2.6
RMS surface roughness – AFM (nm)	5.6	6.7	2.9

Figure 6.3 shows the XRD patterns of nanopatterned $PbTiO_3$ thin films deposited with different inorganic precursors concentrations (High C and Low C), different withdrawal rates (0.76 and 1.6 mm/s) and thermally treated at 600 °C. Solid black and dashed vertical lines correspond to the tetragonal (JCPDS no. 00-003-0721) and cubic (JCPDS no. 00-040-0099) crystalline $PbTiO_3$ phases, respectively. The gray lines at 2θ 40.4 and 47.0° correspond to reflections of the platinum layer of the substrate (JCPDS no. 04-010-5118). Only the nanopatterned thin films prepared with High C of inorganics and deposited with the faster withdrawal rate present the main diffraction

peaks associated to the crystalline $PbTiO_3$ phase. In all other cases, the XRD patterns do not show the typical reflections of the perovskite phase. A potential explanation may be the size of the crystallites that can be too small to be detected by XRD diffraction.

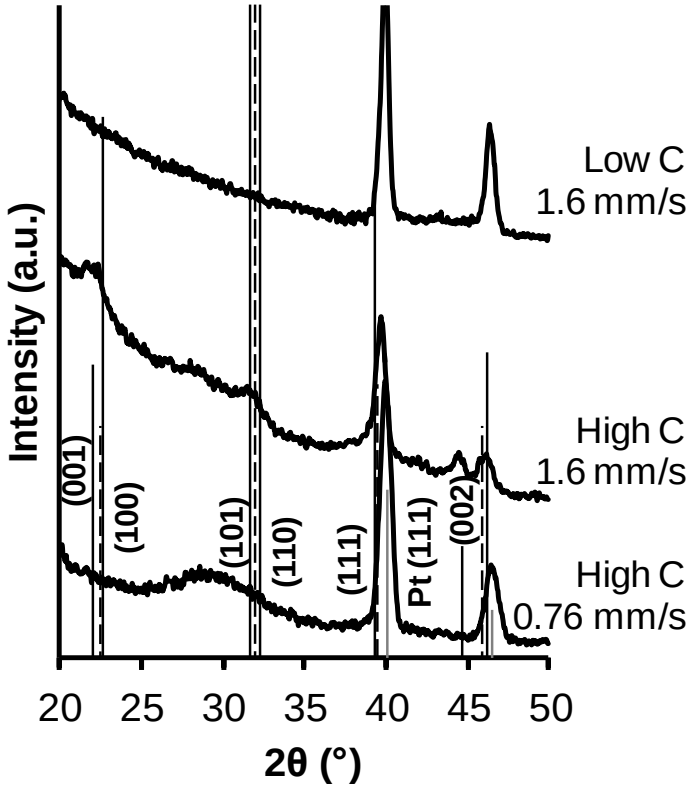

Figure 6.3: X-ray diffraction patterns of nanopatterned $PbTiO_3$ films prepared with High C and Low C solutions, deposited at 0.76 or 1.6 mm/s and treated at 600 ºC. Solid black and dashed vertical lines correspond to the tetragonal (JCPDS no. 00-003-0721) and cubic (JCPDS no. 00-040-0099) crystalline phases of $PbTiO_3$, respectively. The gray lines correspond to the platinum layer of the substrate. Crystalline $PbTiO_3$ phase only appears in thin films deposited with High C and 1.6 mm/s withdrawal rate.

For the films prepared with High C and a withdrawal rate of 1.6 mm/s, it is not possible to differentiate between the cubic and tetragonal structure of $PbTiO_3$ (JCPDS no. 00-040-0099 and 00-003-0721, respectively) by XRD. As the thickness of the nanopatterned films is low (~22 nm, see Table 6.1), the intensity of the diffraction pattern is weak. Another issue to consider is the relation between thickness and tetragonality. One must consider that it is possible that the thickness of the film affects the tetragonality. As reported by Lichtensteiger *et al.*[45], the tetragonality of $PbTiO_3$ thin

films progressively decreases as thickness of the film decreases below 20 nm due to the in-plane strain relaxation and the constraining effect of the substrate.

To verify the presence of the tetragonal phase, Raman spectroscopy was performed in $PbTiO_3$ thin films deposited with High C and 1.6 mm/s of withdrawal rate and treated at 600 ºC (Figure 6.4). These films present the typical Raman modes of the tetragonal phase (E+B1, A1 (2TO), E(3TO) and A1(3TO) bands) at 287, 324, 503 and 599 cm^{-1}, as previously reported for other $PbTiO_3$ and lead zirconate titanate thin films.[192,193]

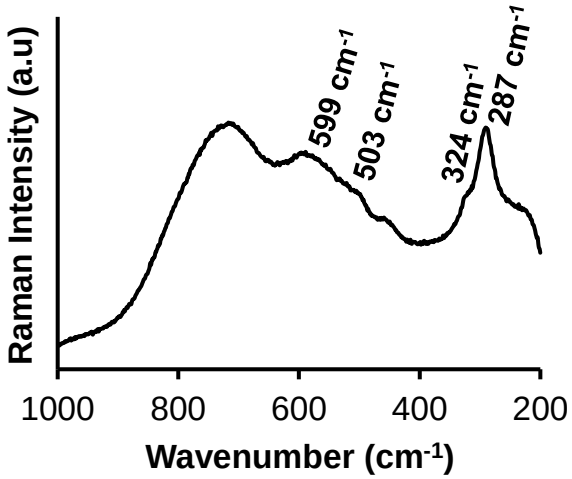

Figure 6.4: Raman spectrum of nanopatterned $PbTiO_3$ films deposited with High C solution at 1.6 mm/s and treated at 600 ºC. Raman spectroscopy proves the presence of the tetragonal $PbTiO_3$ phase in nanopatterned films deposited with High C and fast withdrawal rate.

The Raman peaks are slightly shifted to low wavenumber in relation to single crystal values,[195] probably due to strains induced by the substrate. The Raman results clarify the XRD results.

As the presence of tetragonal phase leads to the appearance of ferroelectricity in ABO_3 perovskite type materials, the local piezoelectric and FE behavior of High C films deposited at 1.6 mm/s and treated at 600 ºC was investigated through VPFM and PFS. Figure 6.5 shows the topographic image, VPFM mixed signal, and the three-dimensional image of the topography with mixed signal. The dark domains in the VPFM mixed signal image correspond to domains in which the polarization is oriented towards the substrate (phase = -180 °), while bright regions correspond to domains with

polarization oriented towards the free surface of the films (phase = 180°). Grains with in-plane polarization exhibit an intermediate contrast. The VPFM mixed signal image presents two distinct piezoelectric behaviors (Figure 6.1f). In analogy to our previous work,[144] the areas with strong piezoelectric response correspond to the bright areas observed in SEM micrographs and can be assigned to crystalline $PbTiO_3$ tetragonal phase. The extension of those areas may be enlarged by treating the films at a temperature above 600 ºC or increasing the heating time.[144] However, experimentally, it was difficult to maximize the areas with strong piezoelectric behavior without losing the porosity order (see Figure A1.2 in Appendix).

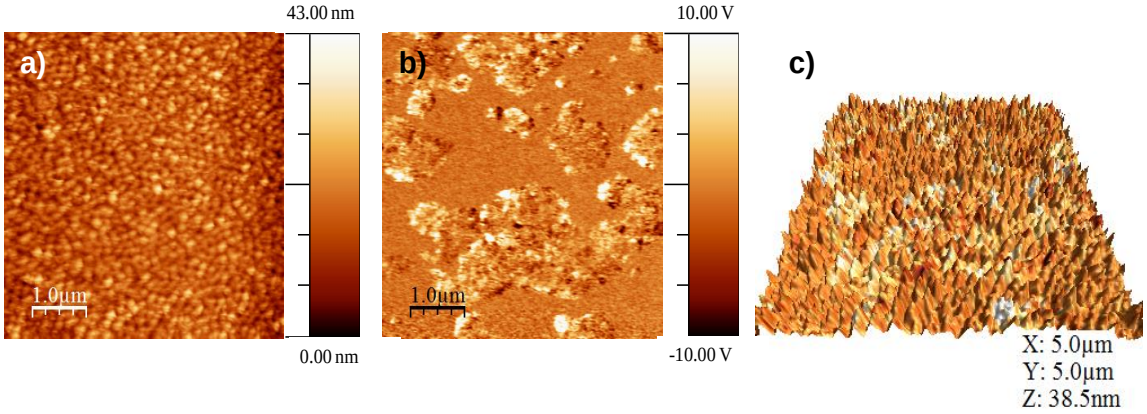

Figure 6.5: Scanning probe microscopy images of nanopatterned $PbTiO_3$ film deposited with High C at 1.6 mm/s and treated at 600 ºC: a) topography image; b) VPFM mixed signal and c) three dimensional image of the topography with mixed signal. The scale of the VPFM mixed signal image ranges between -10 to 10 V. This 20 V scale corresponds to 360º, thus opposite domains oscillate 180º out of phase.

To investigate the FE behavior of these nanopatterned films, we measured their local piezoelectric response as a function of an applied bias between the platinum substrate and the conducting AFM tip. Figure 6.6 shows a representative example of the local remanent out-of-plane piezoelectric hysteresis loop obtained directly from the PFM equipment/software and measured from individual domains with bias from −30 V to +30 V. The hysteresis loop reveals that the switched polarization remains after bias removal and clearly confirms the FE behavior at room temperature of these films. For a quantitative analysis, the FE properties such as critical voltage, coercivity (here meaning the coercive field), imprint, switchable polarization and $(d_{33})_{eff}$, were

calculated from several mixed hysteresis loops and are presented in Table 6.2. The values obtained in our previous work,[144] described in Chapter 3, for dense and nanoporous 100 nm thin films are also included in Table 6.2 for comparison proposes.

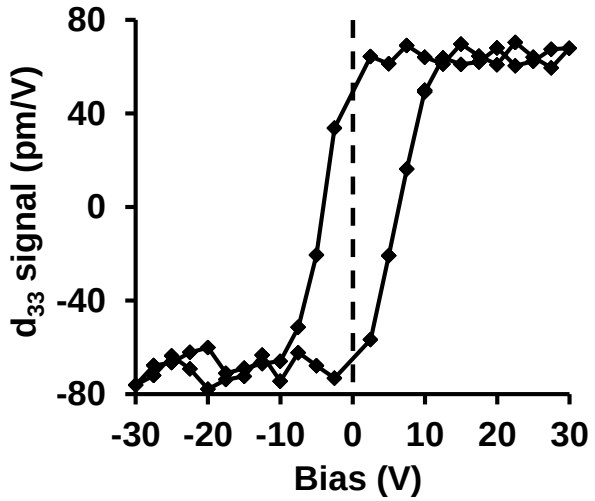

Figure 6.6: Representative remanent local hysteresis loop obtained in nanopatterned $PbTiO_3$ film deposited with High C solution at fast withdrawal rate and treated at 600 ºC. The dashed vertical line indicates the bias = 0 V.

The critical voltage (2.0 ± 0.5 V) and coercivity value (5.3 ± 0.5 V) of the nanopatterned nanoporous $PbTiO_3$ thin films are higher than the values observed in ~ 100 nm thick nanoporous $PbTiO_3$ films prepared in our previous work (1.0 ± 0.1 V and 2.4 ± 0.1 V, respectively).[144] These results clearly demonstrate how the FE behavior is affected by the low thickness of the nanopatterned thin films. The hysteresis loops obtained for these films show an imprint effect in terms of coercive voltage (1.3 ± 0.5 V). This effect is usually caused by the preference for a certain polarization state over the other and provides a measure of the internal field.[196] Imprint behavior can also be related with the self-polarization that depends, on a large extent, on the film deposition technology. In the case of sol–gel deposited films, it was reported that the self-polarization effect is thickness dependent, suggesting that the alignment of domains occurs locally near the film-bottom electrode interface.[197] In the nanopatterned thin films prepared in the current work the imprint value is slightly higher than the value obtained in 100 nm thick $PbTiO_3$ nanoporous films of our preview work (1.0 ± 0.1 V).[144] This variation can be associated with the incipient crystallization degree of the

tetragonal phase of the nanopatterned thin films and/or surface/interface defects (lattice distortion due to different thermal expansion coefficients of the film and substrate). The switchable polarization and $(d_{33})_{eff}$ piezoelectric coefficient of the nanopatterned porous thin films (137.6 ± 6.7 pm/V and 49.6 ± 0.7 pm/V, respectively) are lower than the ones of 100 nm thick $PbTiO_3$ nanoporous films (261.3 ± 6.6 and 148.8 ± 5.5 pm/V, respectively). The degradation of the electrical properties may result from the decrease of the film thickness with consequent reduction of the tetragonality.

Table 6.2: Average values of critical voltage, coercivity, imprint, switchable polarization and $(d_{33})_{eff}$ calculated from at least ten phase, amplitude and mixed hysteresis loops (Piezoresponse Force Microscopy loops) for dense and nanoporous with 100 nm of thickness of our previous work[144] and nanopatterned porous thin films of this work. The higher coercivity values present in nanopatterned thin films show how the FE behavior is affected by the low thickness of the nanopatterned thin films. However in terms of the vertical shift, nanopatterned thin films present reduced imprint effect probably due to the high porosity area of this kind of structure. Consequently, the switchable polarization and $(d_{33})_{eff}$ coefficient are slightly higher than those obtained for dense ones where the crosstalk effect provoked by the domain movement or thermal diffusion is not excluded.

Films	Critical voltage (V)	Coercivity (V)	Imprint (V)	Switchable polarization (pm/V)	$(d_{33})_{eff}$ (pm/V)
Dense–100[144]	1.8±0.1	2.5±0.1	1.2±0.1	85.1±2.0	35.7±0.8
Porous-100[144]	1.0±0.1	2.4±0.1	1.0±0.1	261.3±6.6	148.8±5.5
Nanopatterned	2.0±0.5	5.3±0.5	1.3±0.5	137.6±6.7	49.6±0.7

The decrease of the tetragonality leads to a drop on the spontaneous polarization of the films, due to a residual unscreened depolarization field. The depolarization field increases as the thickness of the FE film decreases and, consequently it has a detrimental effect on the homogeneous polarization state, leading to either a reduction of the spontaneous polarization or formation of FE domains.[242,243] Moreover comparing the values obtained for nanopatterned films with the values reported for dense films in our previous work,[144] nanopatterned films present higher switchable polarization and $(d_{33})_{eff}$ piezoelectric coefficient than dense ones (137.6 ± 6.7 pm/V and 49.6 ± 0.7 pm/V

versus 85.1±2.0 pm/V and 35.7±0.8 pm/V, respectively). These results clearly demonstrate that the porosity even in films with low thickness (20 nm) and consequent low tetragonality degree leads to enhanced local FE properties. Although, nanopatterned films present higher coercivity than nanoporous 100 nm thick films,[144] the nanopatterned ones can be stwiched at lower power thus being interesting for applications in memory devices. The piezoelectric coefficient (d_{33}) value obtained for the nanopatterned films is approximately 50 pm/V, which is slightly better than the $(d_{33})_{eff}$ obtained for the single crystal nanoislands (resulting from complex preparation approaches) where the crosstalk effect provoked by the domain movement or thermal diffusion is inherently excluded (39.4 pm/V).[244] Thus, comparing the nanopatterned with porous films of $PbTiO_3$ synthesized by different methods[239,245] or with $PbTiO_3$ nanoislands,[244] nanopatterned films here prepared by an easy and low-cost method present enhanced FE properties. Furthermore, the porosity is completely open and directed to the substrate, with the platinum underneath almost 50% accessible.

6.3 FM properties in nanopatterned porous $CoFe_2O_4$ thin films

Efforts have been also dedicated to develop an alternative within the bottom-up methods to prepare magnetic nanopatterned surfaces. As mentioned before, in 2004, Grosso *et al.*[63] using a bottom-up strategy reported the preparation of nanoislands of $Co_{0.15}Ti_{0.85}O_{1.85}$ with 6 nm thickness via a wet chemical method with a non-commercial block-copolymer template. The properties of those nanostructures were not reported. FM mesoporous 200 nm thick films of $CuFe_2O_4$,[147] and $CoFe_2O_4$[145] were recently prepared by EISA.[145] Although, the macroscopic magnetic properties of these mesoporous thin films with three-dimensional interconnected nanoscale architecture were reported, the relation between nanoporosity and magnetic properties was not addressed.

$CoFe_2O_4$ is one of the most interesting materials of the magnetic ferrites with inverse spinel structure and T_C of 793 K.[246] $CoFe_2O_4$ has a moderate saturation magnetization, good chemical stability, large permeability at high frequency, large magnetostriction and large magnetocrystalline anisotropy. These properties allows to use it in spin filtering, MFs, audio recording tapes, read/write heads and high-density magnetic recording media[110] if the grain size is lower than 10 nm.[110,246]

However, for a variety of applications, such as ultralow-power memory and logic devices, the preference for out-of-plane magnetization is desirable.[145] It is well know that the thermal stability have becomes an increasingly important limitation in longitudinal recording devices.[247]

The tailoring of magnetic anisotropy in $CoFe_2O_4$ films can be achieved by tuning the stress state of the films using different substrates, employing a buffer layer, as well as varying film thickness.[248,249] In previous studies it has been observed that for strained epitaxial dense $CoFe_2O_4$ films with thickness bellow a certain value ($\approx$ 60 nm), the tensile strain can distort the cubic lattice, leading to a perpendicular anisotropy that overcomes the shape anisotropy and prevails.[249,250,251]

Tolbert *et al.*[145] reported another way to tailor the magnetic anisotropy in $CoFe_2O_4$ films. The authors reported that in $CoFe_2O_4$ mesoporous thin films the shape anisotropy within the pore walls can cause a preference for the out-of-plane

magnetization which is uncommon in dense $CoFe_2O_4$ thin films. Beyond this, the nanoscale structure itself imparts a strain anisotropy to the material that overcomes the in-plane shape anisotropy of thin films producing a perpendicular anisotropy to the plane of the substrate showing thus, that the porous structure can be used to tailor the magnetic properties.[145]

Within this context and taking into account the results presented in previous Chapters and section 6.2, here we intent to study the nanopososity effect on the magnetic properties. In addition, in the previous Chapters and section 6.2 we reported that the nanoporosity can provide the means of achieving enhanced local FE properties. Through the FEM modelling and PFM results we demosntrated that the porosity can reduces the energy necessary to reorient the dipoles in the FE structures and induce instability in the dipole-dipole interaction, producing thus a significant increase in the spontaneous polarization.[144]

To the best of our knowledge, we report here for the first time, the use of sol-gel and EISA to prepare nanopatterned porous thin layer of $CoFe_2O_4$ with thickness of below 70 nm and very ordered pores with diameter between 60 to 80 nm. The porosity is perpendicular to the substrate and open from the top of the surface to the substrate. The local and macroscopic magnetic properties of the prepared samples are presented and compared with dense counterparts.

6.3.1 Experimental part

Nanopatterned porous $CoFe_2O_4$ thin films were prepared using a sol-gel method and EISA methodology (see Chapter 2 and Scheme 6.1). PB51-*b*-PEO62 with MW_{PB} = 51000 $gmol^{-1}$ and MW_{PEO} = 62000 $gmol^{-1}$, from Polymer Source, was used as a micellar templating agent. Two solutions were prepared. In solution A, PB51-b-PEO62 block-copolymer (37 mg) was dissolved in a mixture of ethanol (51.38 mmol, Riedel-de-Haën) and 2-methoxyethanol (38.05 mmol, Sigma-Aldrich, purity ≥ 99.8% w/w) at 70 ºC. Solution B was prepared by the dissolution of cobalt (II) nitrate hexahydrate (0.38 mmol, Sigma-Aldrich, purity ≥ 98% w/w) and iron (III) nitrate nonahydrate (0.77 mmol, Sigma-Aldrich, purity ≥ 98% w/w) in a mixture of 2-methoxyethanol (12.68 mmol, Sigma-Aldrich, purity ≥ 99.8% w/w), ethanol (17.13 mmol) and glacial acetic

acid (0.35 mmol, Sigma-Aldrich, ≥ 99.7% w/w). Afterwards, solution B was added to solution A, forming the final deposition solution. For the dense thin films, a similar procedure was used but excluding the block-copolymer.

Nanopatterned porous and dense $CoFe_2O_4$ thin films were deposited by dip-coating onto 1.0 x 2.0 cm^2 sized slides of platinized silicon ($Pt(111)/TiO_2/SiO_2/Si(100)$) (Radiant Inc.) at 90 ºC. Nanopatterned porous thin films were deposited at 0.76 mm/s and 1.6 mm/s while the dense ones were deposited at 0.34 mm/s and 0.76 mm/s depending on the required thickness. The dense thin films were heated at 120 ºC for 3 min after deposition. All templated films were thermally treated in air at 300 °C during 20 h in order to complete the inorganic condensation (mesostructuration) of the matrix and to decompose the organic content. The films were then annealed at 500 °C during 10 min and using a 5 °C/min ramp rate. After that and in order to achieve crystallization, all films were thermally treated at 750 ºC for 10 min.

Films microstructure was investigated by high-resolution SEM using a SU-70 Hitachi microscope. The thickness values were taken from the cross-section images not present here. The crystalline phases in the films were identified by XRD using a Philips X'Pert MPD X-ray diffractometer with Cu Kα radiation, 2° grazing incidence angle and a step length of 0.02 °. MFM was carried out on an MFP-3D AFM (Asylum), using Bruker cantilevers with Co-Cr coated tips (MESP, resonant frequency of 50−100 kHz, force constant of 2.8−5.0 N/m). Topography signals of the film surface were taken simultaneously with the deflection and phase signals and were collected in amplitude modulation mode using a MFM phase channel. The signals were collected using a lift height mode and a dynamic mode where the phase was recorded. Since the results were obtained with the same type of cantilevers and under identical scanning and acquisition conditions, comparison between films can be made. SQUID measurements were performed using a Quantum Design MPMS magnetometer. The thermal dependence of the magnetization was measured between 10 K and 370 K under 15 mT, after cooling the sample from room temperature to 10 K in zero applied field (ZFC) and after cooling the sample under the measurement field (FC). Hysteresis curves for magnetic fields up to 5.5 T were obtained at 300 K, in parallel and perpendicular film configurations relative to the applied field direction.

6.3.2 Results and discussion

Figure 6.7 depicts top view SEM micrographs of nanopatterned porous and dense $CoFe_2O_4$ thin films with 40 and 65 nm of thickness and thermally treated at 300 and 750 °C. This set of micrographs illustrates the differing microstructure evolution of both nanopatterned porous and dense thin films and they are representative of the entire coated surfaces. The microstructures of the nanopatterned porous thin films reveal hexagonal-like arrays of pores. The pore order and periodicity result from the self-assembly of micelles of the amphiphilic block-copolymer, followed by condensation of the inorganic species around the micelle arrays.

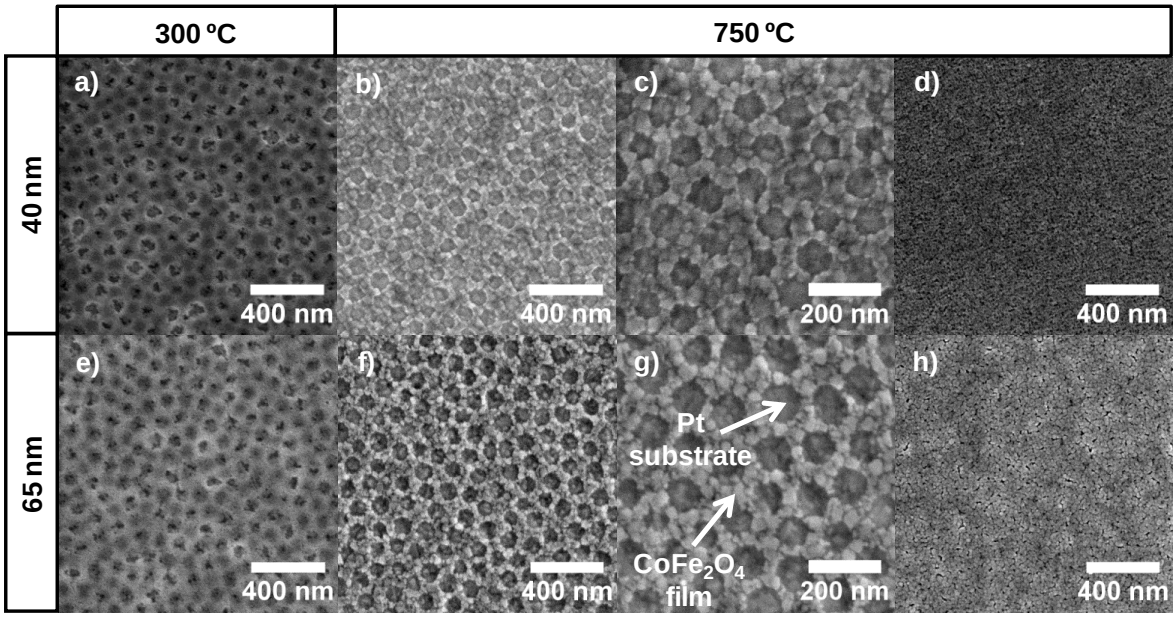

Figure 6.7: SEM micrographs illustrating the morphology of nanopatterned porous and dense $CoFe_2O_4$ thin films. a-c - nanopatterned thin films with nearly 40 nm and thermally treated at 300 and 750 ºC, respectively; e-g - nanopatterned thin films deposited with around 65 nm and thermally treated at 300and 750 ºC, respectively; d and h - dense thin films deposited with 40 nm and 65 nm respectively, and thermally treated at 750 ºC. As the thickness increases the grains in dense thin films become more well-defined. A very well-defined porous pattern in nanopatterned porous thin films is obtained with increasing of the annealing temperature.

Figure 6.7a and 6.7e reveal an amorphous character of the structure after thermal treatment at 300 °C for 20 h. In these micrographs some pores are closed due to the

block-copolymer presence within them. The PB-*b*-PEO decomposition occurs between 200 and 450 ºC (see Figure A1.1 in Appendix). During the thermal decomposition of the block-copolymer, a cross-linked and amorphous metal oxide framework with an ordered network of void pores is created.

Upon thermal treatment at 750 ºC (Figure 6.7b and 6.7f) the porous structure is completely open due to the total decomposition of the block-copolymer, leading to the formation of pores at the locations formerly occupied by polymer micelles. Moreover, at this temperature (Figure 6.7c and 6.7g), well-defined and crystalline grains around the motifs are evident as well as a highly ordered nanoporosity for both film thicknesses. A slow thermal treatment is required for the crystallization of $CoFe_2O_4$ spinel phase in avoid the loss of the ordered porosity.

In the nanopatterned porous thin films, the average pore size determined using the software Image J (version 1.45s),[252] ranges between 60 to 80 nm and the porosity is completely open from the top of the film towards the substrate. The thickness values were determined using the SEM cross-section micrographs for the different thin films treated at 750 ºC and are presented in Table 6.3.

Table 6.3: Thickness values measured from the cross-section SEM micrographs of the nanopatterned porous and dense $CoFe_2O_4$ thin films deposited with different withdrawal rates and thermally treated at 750 ºC. As the withdrawal rate increases the thickness value increases.

Thickness (nm)	
Nanoporous	**Dense**
40.8±2.5	40.1±1.8
65.0±1.4	65.8±1.5

Comparing both thickness, ≈ 40 and 65 nm, for the case of nanopatterned porous thin films, it is possible to observe a better organized pattern and with a better homogeneity in the pore size for the thin films with higher thickness.

Upon increasing temperature, some of the walls collapse and, consequently some pores become interconnected (compare Figure 6.7b and 6.7c with 6.7f and 6.7g).

The formation of such a pattern is a consequence of the lack of material for the formation of a continuous and homogeneous porous coating. It is well documented that the formation of well-ordered monolayers is mainly dependent on the solution dilution and withdrawal rate used, resulting in different film thicknesses.[156,240] Attaining a homogeneous layer is possible within narrow ranges of concentration and/or deposition rates.[156,240] The degree of porosity calculated from the SEM micrographs (Figure 6.7b and 6.7f) for the nanopatterned porous thin films treated at 750 ºC varies between from 51.0 to 47.0% for the thin films with ≈ 40 nm and 65 nm, respectively.

Comparing nanopatterned porous and dense thin films treated at higher temperature and with different thickness, the grain sizes are better defined for nanopatterned porous and dense thin films with ≈ 65 nm than for the ones with 40 nm. Indeed, during film growth, it is expected that as the film gets thicker, the average in-plane grain size also increases. This phenomenon is relate with surface energy differences or growth-velocity anisotropies.[253] Observing the dense films, upon 750 °C treatment, these become more compact as the withdrawal rate and, consequently the film thickness increases (Figure 6.7d and 6.7h).

The XRD patterns collected to ensure the achievement of the correct crystallization phase are shown in Figure 6.8. The XRD patterns for the nanopatterned porous and dense $CoFe_2O_4$ thin films thermally treated at 750 ºC confirmed the presence of all diffraction peaks associated with $CoFe_2O_4$ phase, proving that all films formed the inverse spinel $CoFe_2O_4$ crystalline phase as corroborated with JCPDS no. 22-1086.

Figure 6.9 shows the AFM topography and magnetic domain structure determined by MFM of nanopatterned porous and dense $CoFe_2O_4$ thin films with similar thickness and both thermally treated at 750 ºC. The MFM measurements were performed on as-prepared films by AFM / MFM using the tapping lift mode. The AFM topography images (Figure 6.9a and 6.9c), like the SEM micrographs, reveal a hexagonal-like array of pores and crystalline grains around the motifs for the nanopatterned porous thin films and well-defined grains for the dense ones. The RMS (root mean square) surface roughness of the nanopatterned porous thin films is 3.5 nm while in the dense thin films the surface roughness is about 1.5 nm. The surface roughness difference is due to the nanopatterned porous structure of the films.

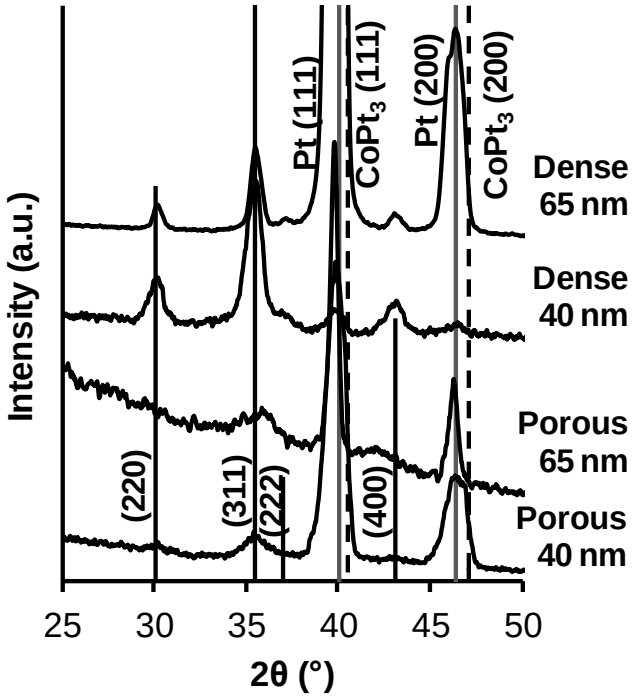

Figure 6.8: X-ray diffraction patterns of nanopatterned porous and dense $CoFe_2O_4$ thin films with thicknesses around 40 nm and 65 nm and treated at 750 ºC. Solid black vertical lines correspond to the inverse spinel $CoFe_2O_4$ (JCPDS no. 22-1086) crystalline phase of $CoFe_2O_4$. The gray lines correspond to the platinum layer of the substrate (JCPDS no. 04-010-5118) and the hatched line to the crystalline phase of $CoPt_3$ (JCPDS no. 01-072-9179).

The MFM images (Figure 6.9b and 6.9d) reveal weak magnetic domains with a cluster-like structure, similar to that observed for $CoFe_2O_4$ thin films deposited using sol-gel method on silica substrate or by PLD on MgO substrate.[249,254] Contrarily to epitaxial $CoFe_2O_4$ films with strong perpendicular anisotropy and low coercivity, [249] no typical stripe structure was observed in our thin films deposited by EISA and with polycrystalline structure. Comparing both thin films, it is clear that the nanopatterned porous ones display less pronounced contrast in the magnetic domains than the dense films showing that the porosity tends to reduce the local magnetic properties. This result reveals that the magnetocrystalline anisotropy and the shape anisotropy induced by the porosity in the nanopatterned porous thin films overcame the perpendicular anisotropy even for films with a thickness similar to the critical thickness (≈ 60 nm).[110,145,255,254]

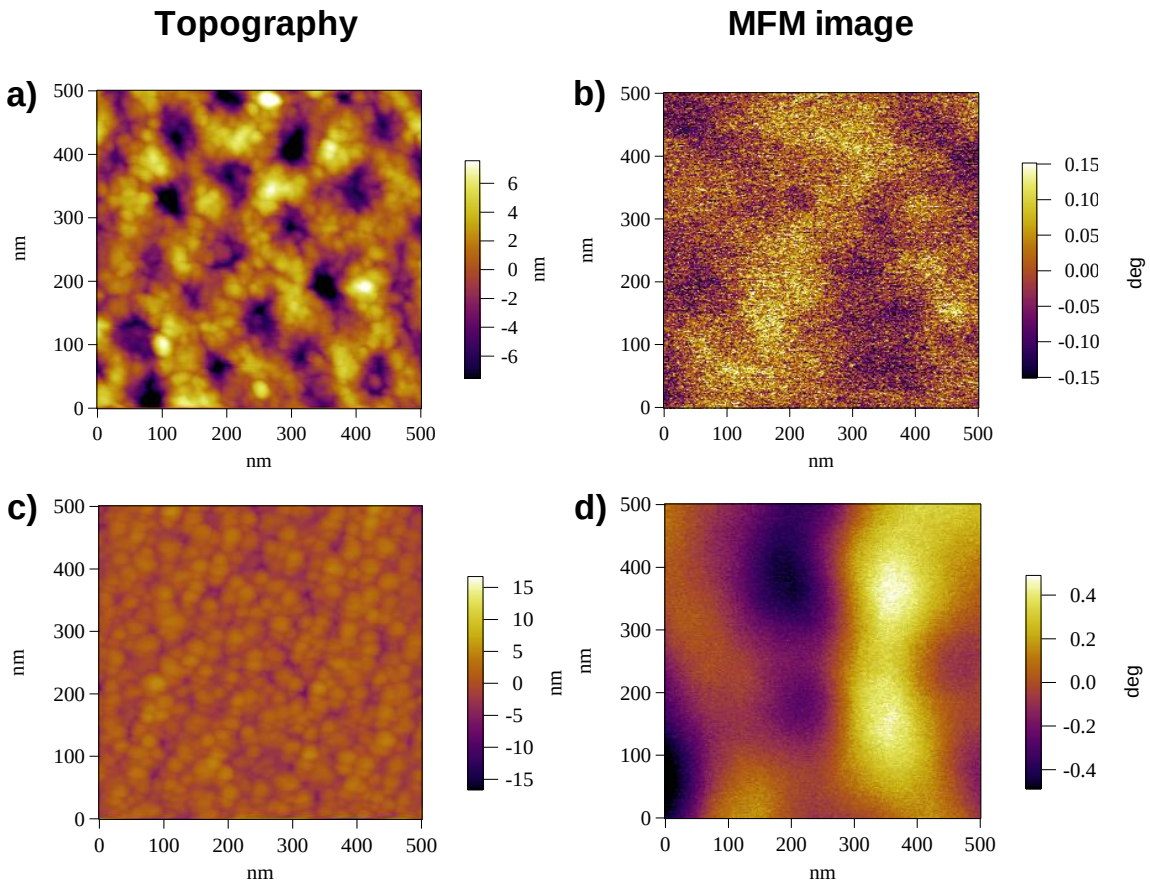

Figure 6.9: AFM images (500x500 nm^2) (a and c) and MFM images (b and d) of nanopatterned porous and dense $CoFe_2O_4$ thin films deposited with around 65 nm and thermally treated at 750 ºC. The nanopatterned thin films present a less pronounced out-of-plane magnetization than the dense films.

As the MFM measurements were performed perpendicular to the substrate, the in-plane orientation cannot be observed. In order to evaluate the magnetic properties of the nanopatterned porous and dense thin films for in-plane and out-of-plane geometries, the magnetization versus field measurements were performed with the films oriented parallel and perpendicularly to the external magnetic field. The diamagnetic component due to the substrate was subtracted from the measured data and the results, normalized to the films volume, with uncertainties varying between 3.5 and 4.5%, are shown in Figure 6.10.

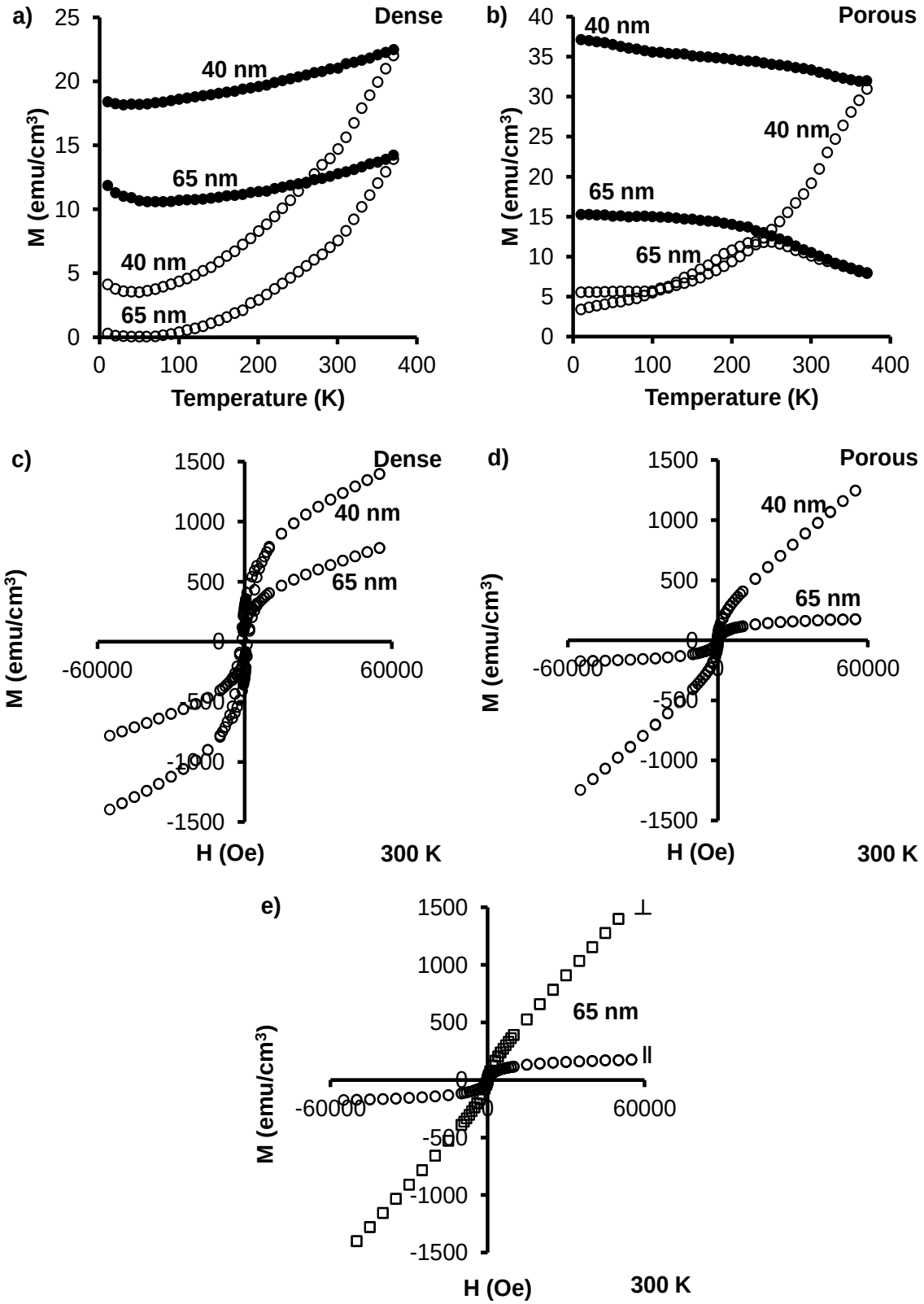

Figure 6.10: Thermal variation of the magnetization of the: a) nanopatterned porous thin films with thicknesses of 65 nm and 40 nm and b) dense thin films with thicknesses of 65

nm and 40 nm measured under 15 mT: ZFC curves (open symbols) and FC curves (solid symbols). Hysteresis loops at 300 K with the thin films parallel to the applied magnetic field for: c) nanopatterned porous thin films with thicknesses of 65 nm and 40 nm; d) dense thin films with thicknesses of 65 nm and 40 nm. Hysteresis curves of the: e) nanopatterned porous thin films with 65 nm of thickness obtained at 300 K with the applied field perpendicular (□) and parallel (○) to the film surface.

For the nanopatterned porous films, the estimated film volume was based on the SEM micrographs considering a porosity of 51% and 47% for the thin films with 40 nm and 65 nm, respectively.

The temperature dependence of the in-plane magnetization was measured for all the films. In Figures 6.10a and 6.10b this dependence is illustrated for a dense and a nanopatterned porous film. For the dense film, as expected for a ferrimagnetic behavior with a T_C well above room temperature, the ZFC magnetization values increase monotonically up to 370 K corresponding to the progressive alignment of domains. The FC curve displays a magnetization, which is almost constant indicating that thermal fluctuations have no influence on magnetization. For the nanopatterned porous thin film (65 nm), the ZFC and FC curves overlap for temperatures above 250 K showing a transition temperature much lower than in the dense case. The ferrimagnetic behavior of all thin films is also expressed in the hysteresis curves obtained at 300 K, as shown in Figures 6.10c and 6.10d for both films. As can be seen from the magnetic parameters in Table 6.4, at 300 K, the nanopatterned porous films display saturation magnetization (M_s) values much lower than dense films with similar thicknesses and almost no remanence or coercivity properties. These features can be understood as an effect of porosity. In opposite to observed in the Chapter 3 and Chapter 4, where the nanoporosity can provide the means of achieving enhanced local FE properties, here the nanoporosity has a negative effect.

Bulk $CoFe_2O_4$ displays a saturation magnetization around 80 emu/g,[256] corresponding to 430 emu/cm^3 for a bulk density of 5.3 g/cm^3. Table 6.4 presents for dense and nanopatterned porous thin films for both thicknesses, the values of the saturation and remanent magnetization (M_r) and coercive field (H_c). The 65 nm thick dense films have H_c values of the expected order of magnitude ($\approx$ 0.5 T)[257], but M_s

values close to bulk $CoFe_2O_4$. This last result was unexpected as films usually present values of M_s significantly lower than bulk. The M_s value is even more intriguing in the case of the 45 nm thick dense films, as the value is almost the double of the M_s of bulk $CoFe_2O_4$.

Table 6.4: Saturation magnetization (M_s), remanent magnetization (M_r) and coercive field (H_C) for all measured nanopatterned porous and dense thin films. The uncertainties were majored from the volume uncertainties.

Films	Thickness (nm)	M_s (±5%) (emu/cm^3)	M_r (±5%) (emu/cm^3)	H_C (±5%) (mT)
Dense	65.4 nm	399	132	118
	40.1 nm	819	290	157
Porous	65.0 nm	143	1.1	1.4
	40.8 nm	266	43	24

A possible explanation for this behavior would be the presence of traces of a FM phase. By analysis of the XRD pattern, it is not clear that a secondary phase is present. However, it is reasonable to consider the possibility of the formation of a platinum-rich alloy by reduction of the metal ions, Co^{2+} and / or Fe^{3+}, followed by reaction with the platinum of the substrate. To exemplify the similarity between a platinum-rich alloy, platinum and $CoFe_2O_4$ phase, Figure 6.8 also displays the reflections of Pt and $CoPt_3$ according to the JCPDS card nos. 04-010-5118 and 01-072-9179, respectively. In the literature, both Co-Pt_3[258] or Fe_x-Co_y-$Pt_{100-x-y}$[259] present strong ferromagnetism. In order to achieve one of these alloys, it would be necessary the reduction of the metal ions in the $CoFe_2O_4$ lattice which is usually achieved by using a reductive atmosphere. Although the film was thermally always in air, during the thermal treatments and where the organic matter decomposition occurs a local reductive atmosphere can be created, which can favour the the alloys formation at low temperature. However, it is reported that the creation of the reductive atmosphere during the thermal treatment of sol-gel films essentially occurs in thick films.[260] Another potential explanation may be the occurrence upon thermal treatments of oxidation of organic moieties of the metal precursors and block-copolymer over the reducible Co^{2+} and Fe^{3+} ions, following a

Mars-Van-Krevelen mechanism.[230,231] This mechanism is based on the mobility of the oxygen in the lattice. Certain mixed oxides have the capacity of gather up or release gaseous oxygen from crystal lattice in order to maintain the charge balance associated to hydrocarbon decomposition and modification of the valence charges of the metal ions.[231] Dumitru *et al.*[230], using temperature-programmed reduction, showed the reduction of $CoFe_2O_4$ in three steps with temperature maximums at 232, 328 and 640 ºC. The Fe^{3+} was totally reduced to iron metal while only half of Co^{2+} was reduced to cobalt metal. The reduced metal can diffuse through the grain boundaries of the platinum substrate forming a platinum-rich phase.[261] The formation of this alloy seems to occur in both dense and nanopatterned porous thin films at both thicknesses, having more impact on the magnetic properties of the thinner than of the thicker films. This result can be explained due to the lower $CoFe_2O_4$ amount in the thinner films and consequently the magnetic effect of the platinum-rich phase is more pronounced.

The field variation of the magnetization was measured with the magnetic field perpendicular to the film surface, for all thin films. As illustrated in the Figure 6.10e, a high susceptibility remains up to the highest applied fields, indicating a progressive alignment of magnetic moments with the increasing field and that no complete out-of-plane magnetization is achieved, contrary to other published results for $CoFe_2O_4$ thin films of similar thickness.[254] These out-of-plane magnetization curves indicate a preferential in-plane orientation, differing from other $CoFe_2O_4$ films prepared by sol-gel methods with such low thickness.[110,229] It is well known, that in magnetic thin films with thickness above certain values (such as 60 nm), the stress will relax partly or mostly, leading to magnetic isotropy or in-plane anisotropy due to the strong effect of the shape anisotropy.[110,145,254]

6.4 Functional $BiFeO_3$ nanopatterned porous thin films

$BiFeO_3$ has been one of the most studied ferroic material in the last decades. In fact, in 2003, Ramesh *et al*.[73] reported that heteroepitaxial constrained $BiFeO_3$ thin films present a substantial magnetization (~150 emu/cm^3) and enhanced FE polarization (50 to 60 μC/cm^2) comparable to the lead-based materials.[73] Beyond these attractive ferroic properties, $BiFeO_3$ also presents interesting optical properties and, consequently considerable potential for applications in solid state devices that utilize heterojunction effects and as photovoltaic and photocatalytic devices due to its small direct band gap (around 2.7 eV).[262,263,264] However, in practice it is challenging to obtain single-phase $BiFeO_3$, free from secondary and ternary FE oxides like Bi_2O_3, $Bi_{25}FeO_{39}$ and $Bi_2Fe_4O_9$.[265] The high volatility of bismuth cation at the required crystallization temperatures, results in the control of nucleation and growth processes that ensure the characteristics at micro and nanoscale of the thin films.[74,266,267]

To the best of our knowledge, up to now, nanopatterned structures involving $BiFeO_3$ were mainly produced by nanolithography based on the combination of templated self-assembly method with electron-beam litrography (also termed as soft electron-beam lithography),[83,107,108] focused ion-beam[105] or UV photolithography.[106] Although, these thin films present well-defined structures, the application of such methods is limited by the high cost of equipment and the difficulty to cover extensive surface areas. Moreover the etching methods usually associated with lithography are typically harmful to the electric and magnetic properties of ferroic materials. In 2011, Brezesinski *et al.*[140] reported the preparation of $BiFeO_3$ thin films with anisotropic crystallites combined with a continuous mesoporosity using the same soft-templating methodology that we intent to use in this study. However, these thin films do not present a porosity directed to the substrate. In addition only the photocatalytic activity was studied and not the magnetic or electric properties.

The present study addresses the electrical and magnetic properties at macro and local scale of highly ordered nanopatterned porous $BiFeO_3$ thin films with *ca.* 66 nm of thickness and average pore size of 100 nm. In similarly to the developed in the previous works described in the preceding Chapters and sections, the understanding of the porosity effect on these properties is established by the comparison with bulk

counterparts. Optical absorption behavior was also analyzed to exploit the multifunctional character of the nanopatterned porous $BiFeO_3$ thin films and their potential for a wide range of applications.

6.4.1 Experimental part

Nanopatterned porous $BiFeO_3$ thin films were prepared using a sol-gel method and EISA methodology (see Chapter 2 and Scheme 6.1). PB51-*b*-PEO62 block-copolymer with MW_{PB} = 51000 $gmol^{-1}$, MW_{PEO} = 62000 $gmol^{-1}$, from Polymer Source, was used as a structure-directing agent. Two solutions were prepared. In solution A, PB51-*b*-PEO62 block-copolymer (37 mg) was dissolved in a mixture of ethanol (51.4 mmol, Riedel-de Haën) and 2-methoxyethanol (38.1 mmol, Sigma-Aldrich, purity ≥ 99.8% w/w) at 70 ºC. Solution B was prepared by the dissolution of iron (III) nitrate nonahydrate (0.77 mmol, Sigma-Aldrich, purity ≥ 98% w/w) and bismuth (III) nitrate pentahydrate (0.77 mmol, Sigma-Aldrich, purity ≥ 98% w/w) in a mixture of 2-methoxyethanol (12.7 mmol, Sigma-Aldrich, purity ≥ 99.8% w/w), ethanol (17.1 mmol, Riedel-de Haën) and glacial acetic acid (0.35 mmol, Sigma-Aldrich, ≥ 99.7% w/w). Afterwards, solution B was added to solution A, forming the final solution. For the dense thin films, a similar procedure was used. However, in this case, the solution with the block-copolymer was not added.

Nanopatterned porous and dense $BiFeO_3$ thin films were deposited by dip-coating onto 1.0 x 2.0 cm^2 sized slides of platinized silicon ($Pt(111)/TiO_2/SiO_2/Si(100)$) (Radiant Inc.) at 90 ºC. In order to get similar film thicknesses, the withdrawal rates were adjusted to 0.34 mm/s (dense) and 0.76 mm/s (nanopatterned). All films were thermally treated in air at 300 °C during 20 h in order to complete the inorganic condensation (mesostructuration) of the matrix and to decompose the organic content. The dense thin films were heated at 120 ºC for 3 min after deposition and before the thermal treatment at 300 ºC. The films were then annealed at 500 °C during 10 min and using a 5 °C/min ramp rate. After that and to achieve crystallization, all films were thermally treated at 550 and 600 ºC for 5 min. The film microstructure was investigated by high-resolution SEM using a SU-70 Hitachi microscope. The thickness values were taken from the cross-section images (data not shown). The crystalline phases were

identified by XRD using a Philips X'Pert MPD X-ray diffractometer with Cu Kα radiation, 2° grazing incidence angle and a step length of 0.02 °.

The topography, piezoelectric and FE properties were evaluated using AFM, VPFM and PFS techniques. These techniques were carried out on Nanoscope III, Digital Instruments system with a lock-in amplifier, SRS Stanford Research Systems, using Tap300 cantilevers with Al-coated tips (Budget Sensors, resonant frequency of 200−400 kHz, force constant of 20−75 N/m) and DPE-18 cantilevers with Pt-coated tips (Mikromasch, resonant frequency of 60−100 kHz, force constant of 1.1−5.6 N/m), respectively. For the VPFM measurements, the topography signal of the film surface was taken simultaneously with the mixed signal in contact mode. The AFM measurements were collected in tapping mode. Since the results were obtained with the same type of cantilevers and under identical scanning and acquisition conditions, comparison between films can be established. Several hysteresis loops with bias from -45 to +45 V were acquired to ensure the reproducibility of the results, and the achievement of a representative hysteresis loop. The piezoelectric and FE properties are average values taken from at least ten hysteresis loops. Switchable polarization corresponds to the difference between the positive saturated piezoresponse and negative ones ($R_m = (R_S)^+ - (R_S)^-$). The imprint is defined as $I_m = (V^+ + V^-) / 2$, where V^+ correspond to the positive coercive bias and V^- to the negative coercive bias and these bias values were taken from the phase signal. As the effective piezoelectric coefficient ($(d_{33})_{eff}$) is proportional to the amplitude signal, this can be defined as $(d_{33})_{eff} \propto$ (amplitude signal·cos(phase signal)) / V_{ac}, where V_{ac} is the ac voltage applied, and its value can be obtained from the mixed signal at zero voltage. Optical absorption measurements were carried out on a JASCO V-560 (UV-Vis) spectrophotometer with a wavelength range from 900 to 190 nm and a resolution of 0.1 nm in diffuse reflectance mode. A clean platinized silicon ($Pt(111)/TiO_2/SiO_2/Si(100)$) substrate was used as reference for diffuse reflectance measurements before the analysis of $BiFeO_3$ thin films. Magnetization measurements as a function of temperature, M(T), and applied magnetic field, M(H), were performed using a SQUID magnetometer (Quantum Design MPMS). The M(T) curves were collected at 20 mT in increasing temperature from 10 to 370 K, after zero-field cooling (ZFC) or field cooling (FC) procedures. The hysteresis loops were obtained at 35 and 300 K for magnetic fields up to 5.0 T.

6.4.2 Results and discussion

During the deposition process, at 90 ºC, the evaporation of volatile solvents (2-methoxyethanol and ethanol) occurs leading to the co-assembling of the system to form a hybrid inorganic/organic nanostructure with long-range periodicity and good homogeneity. The block-copolymer is removed through calcination at low temperatures (300 ºC) to impart porosity and fully condense the inorganic network. Figure 6.11 shows a set of top view SEM micrographs of nanopatterned porous and dense $BiFeO_3$ thin films thermally treated at 500, 550 and 600 ºC

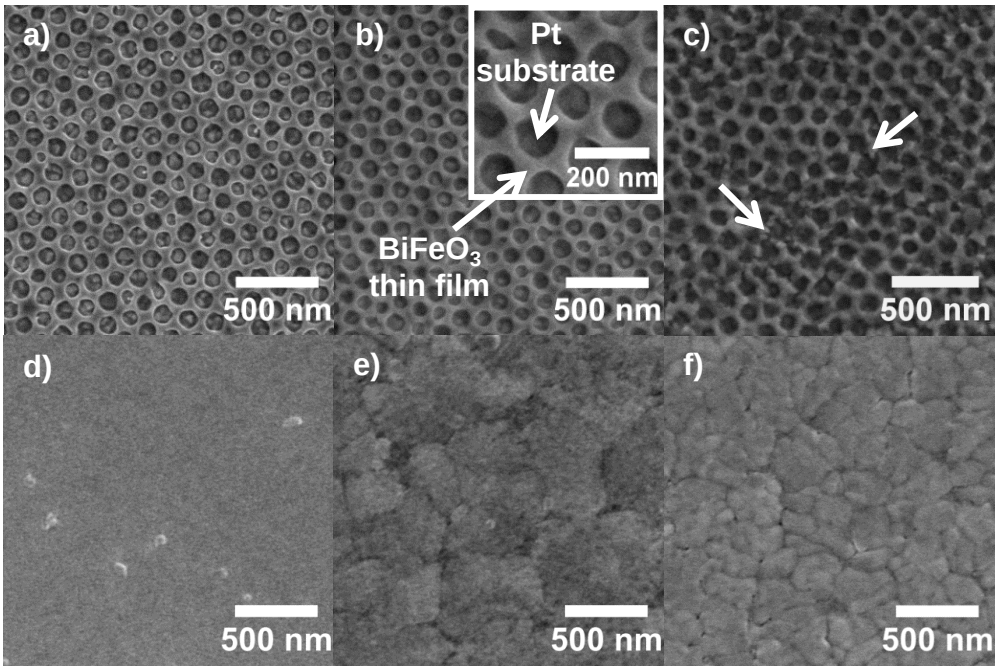

Figure 6.11: SEM micrographs of nanopatterned porous (6.11a, 6.11 b and 6.11c) and dense (6.11d, 6.11e and 6.11f) $BiFeO_3$ films thermally treated at 500 °C for 10 min (6.11a and 6.11d), 550 °C for 5 min (6.11b and 6.11e) and 600 ºC for 5 min (6.11c and 6.11f). The nanopatterned porous films show for all heating conditions well-ordered hexagonal arrays of pores (6.11a-6.11c). The inset present in the SEM micrograph 6.11b shows that the pores of the nanostructure are completely empty and the porosity is directed to the substrate. The nanopatterned films treated at 600 °C present some interconnected pores as shown by the white arrows, but the order and porosity at a long range remain. The dense films present crack-free surfaces with the grain size increasing as a function of the heating temperature (6.11d-6.11f).

The micrographs are representative of the entire covered surfaces and reveal hexagonal-like arrays of pores with diameter of 98.5 ± 8.6 nm and wall thickness

between the pores of 77.9 ± 8.0 nm. Figure 6.11a displays the nanopatterned films after 20 h of thermal treatment at 300 ºC followed by 10 min at 500 ºC. One can see that the pores of the nanostructure are completely empty and the porosity is directed to the substrate. Upon thermal treatment at 550 ºC (Figure 6.11b), the periodicity of the nanostructure is retained. This happened because the walls formed between the pores through this block-copolymer template are sufficiently thick allowing the nucleation and growth of the crystalline phase, as well as the shrinkage, without collapsing the porosity order. At 600 ºC (Figure 6.11c) the nanostructure slightly changes due to the shrinkage of the inorganic component. Some walls between the pores slightly collapse and consequently some pores are connected. However, the hexagonal array of nanopores is clearly kept throughout the films. The percentage of porosity calculated from analysis of the SEM micrographs (Figure 6.11c) is 56.5 ± 2.4 %. In what concerns the dense films these are crack-free and the presence of major structural defects can be ruled out. As the temperature of the thermal treatment increases and concomitant with the crystallization dense films develop a well-defined grain structure; the growth of the grains is evident in the films thermal treated at 600 ºC (Figure 6.11f). In order to get similar film thicknesses, the withdrawal rates during the film deposition were adjusted to 0.34 mm/s for dense and 0.76 mm/s for nanopatterned films. The thickness values for both films were measured using SEM cross-section micrographs. The thicknesses are 66.2 ± 1.9 nm and 65.7 ± 1.4 nm for nanopatterned porous and dense films, respectively.

The phase composition and structure of nanopatterned porous and dense $BiFeO_3$ thin films were analyzed by XRD for films thermally treated at 600 ºC (Figure 6.12); this thermal treatment temperature was chosen to guarantee monophasic films. All the peaks were indexed to the perovskite-type rhombohedral structure according to JCPDS 01-075-6667, indicating practically a pure phase for both nanopatterned porous and dense $BiFeO_3$[73],[140] thin films. The nanopatterned porous films display a very small peak around 27.7 ° 2θ, which can be attributed to the $Bi_2Fe_4O_9$ secondary phase with orthorhombic structure (JCPDS 01-081-9285). In fact, porosity enhances the contact with surrounding atmospheric and may facilitate the formation of the rich oxygen secondary phases. Despite the existence of the small impurity of the pyrochlore phase

($Bi_2Fe_4O_9$) in our films, the FE property of $BiFeO_3$ are not expected to be affected due to the inversion symmetry structure of $Bi_2Fe_4O_9$ and its high resistivity (>108 Ω cm^{-1}).[268,269] The splitting of the peaks around 39 and 57 ° is indicative of the rhombohedral distortion of $BiFeO_3$. Comparing nanopatterned porous and dense films, one can observe that the last ones present a more intense XRD pattern profile, what can be explained by the relative higher amount of material present in these films when compared with the nanopatterned porous ones (only *ca*. 43.5% of material comparing with dense film).

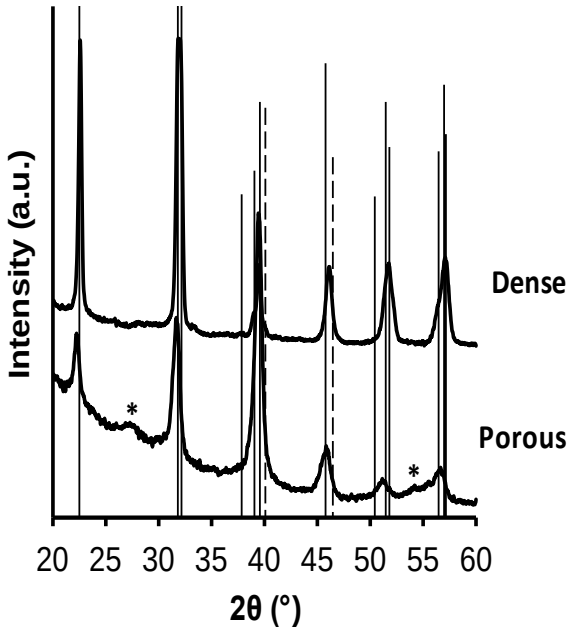

Figure 6.12: X-ray diffraction patterns of nanopatterned and dense $BiFeO_3$ thin films thermally treated at 600 ºC. Solid black vertical lines correspond to the rhombohedral phase of $BiFeO_3$ (JCPDS 01-075-6667) and dashed vertical lines correspond to the platinum layer of the substrate. The asterisk corresponds to the secondary phase, $Bi_2Fe_4O_9$ (JCPDS no 01-074-1098). The crystalline oxygen-rich secondary phase, $Bi_2Fe_4O_9$, only appears in nanopatterned thin films probably as a consequence of the porosity, which increases the contact area with the atmospheric gases. This secondary phase is present in very low concentration.

Figure 6.13 represents the topography evaluated through AFM in tapping mode of nanopatterned porous and dense $BiFeO_3$ thin films thermally treated at 600 ºC. The ordered hexagonal array of pores in the nanopatterned porous thin films (Figure 6.13a and 6.13b), and well-defined grains in dense ones (Figure 6.13d and 6.13e) are easily

seen from the AFM images, supporting the previous SEM observations. The line profiles (Figure 6.13c and 6.13f) confirm the periodicity of pores in the nanopatterned films and the presence of grains with different sizes and heights in the dense films. Root-mean-square (RMS) roughness values are 7.3 nm and 4.3 nm for nanopatterned porous and dense films, respectively, indicating the relatively flat surfaces of dense ones when compared to the nanopatterned porous films. Moreover, as the thin films have the same thickness, the difference in roughness supports the open porosity structure of the thin film and the availability of the pores for further functionalization.

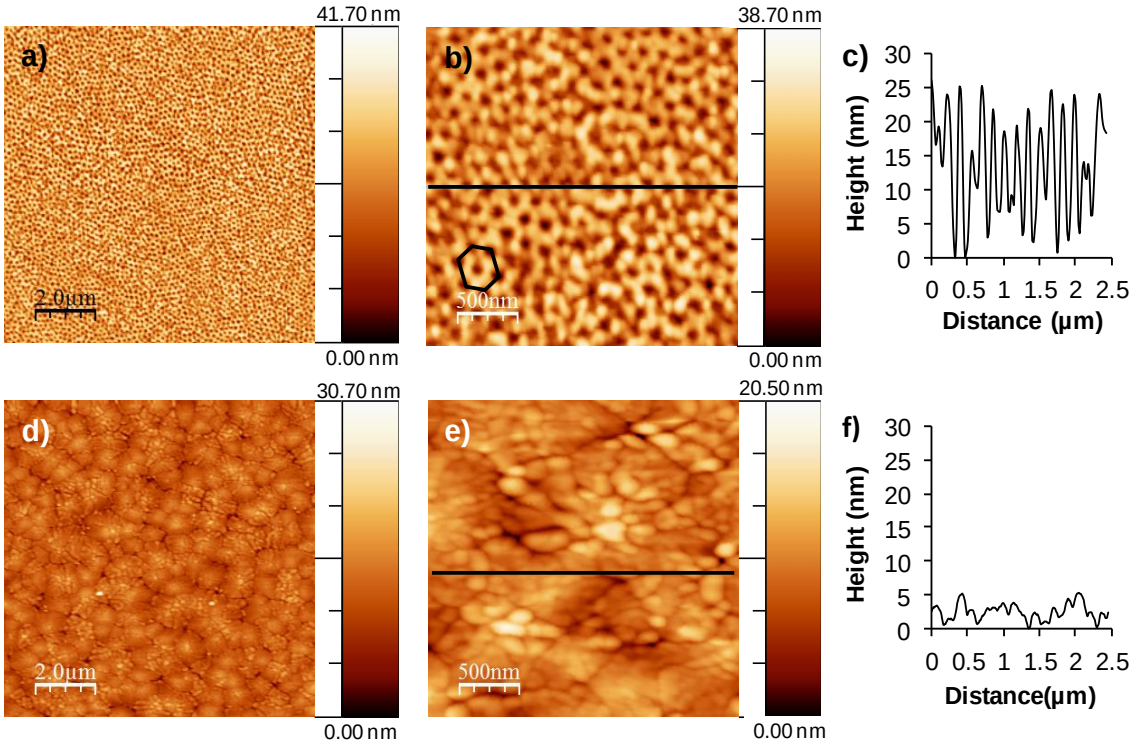

Figure 6.13: AFM topography images (5 µm x 5 µm and 2.5 µm x 2.5 µm) of nanopatterned porous (6.13a and 6.13b) and dense (6.13d and 6.13e) $BiFeO_3$ thin films thermally treated at 600 ºC. 6.13c) and 6.13f) are the line profiles along the black line represented in 6.13b) and 6.13e). The images reveal the well-defined porous and grain structures of the nanopatterned and dense thin films, respectively.

In order to probe the piezo and FE nature at room temperature of the nanopatterned porous and dense thin films treated at 600 ºC, the VPFM and PFS were carried out (Figure 6.14 and Figure 6.15). Despite the topography images have been taken simultaneously with the mixed signal in contact mode and under the convolution

effect of the tip, the porous and grain structures are clearly evident in the nanopatterned porous and dense films images (Figure 6.14a and 6.14c), respectively. These results are in agreement with the microstructure observed from SEM and AFM (Figure 6.11 and 6.13). The application of 2 V in the samples during the scan allowed observing the piezoelectric domains in both thin films (Figure 6.14b and 6.14d). The images show the mixed signal *i.e.*, the piezoresponse and the well-defined domain structure indicating the pronounced piezoelectric properties of both thin films. As these thin films present a low thickness, polycrystalline structure and random grain distribution as a result of the sol-gel process, the mixed signal images (Figure 6.14b and 6.14d) do not display the characteristic stripe-like domains as observed for epitaxial $BiFeO_3$ thin films with a thickness of few hundreds nanometers.[74,270] On the contrary, the thin films present a mosaic-like structure which is similar to the results reported by Ramesh *et al.*[271] for epitaxial $BiFeO_3$ thin films with very low thickness (below 15 nm) and by Coondoo *et al.*[272] for $BiFeO_3$ thin films prepared by sol-gel method. As the polarization in rhombohedral $BiFeO_3$ lies along the body diagonals (111), it has three polarization directions: 71º, 109º and 180º by application of an external electrical field[271] and, consequently its out-of-plane polarization possess different contrasts. In polycrystalline films with multidomain grains and random orientation, the combination of the three orientation can be observed.[273] Bright and dark contrasts correspond to anti-parallel domains with polarization oriented towards the free surface of the films (phase = 180°) and towards the substrate (phase = -180°), respectively. Intermediate contrast corresponds to the other polarization directions. Comparing the mixed signal images of both films, one can observe that the nanopatterned porous ones have two distinct piezoelectric behaviors, corresponding to areas with strong piezoelectric response and areas where the response is almost absent. This latest observation can be associated to areas with reduced degree of crystallization, to the presence of the secondary phase or even to size effects. We have tried to maximize the areas with strong piezoelectric behavior through the thermal treatments but further optimization has to be launched to tackle losing porosity order. The representative PFS results obtained from the strong piezoresponse domains are depicted in Figure 6.15a. The piezoelectric hysteresis loops are obtained by keeping the PFM tip fixed on $BiFeO_3$ domains and applying a bias between the conductive substrate (bottom electrode) coated with the film and the

conductive AFM tip (top electrode). The obtained piezoelectric hysteresis loops provide information about the switching behavior of the polarization domains. Figure 6.15a shows the remanent d_{33} hysteresis loop of both thin films with bias from - 45 to + 45 V.

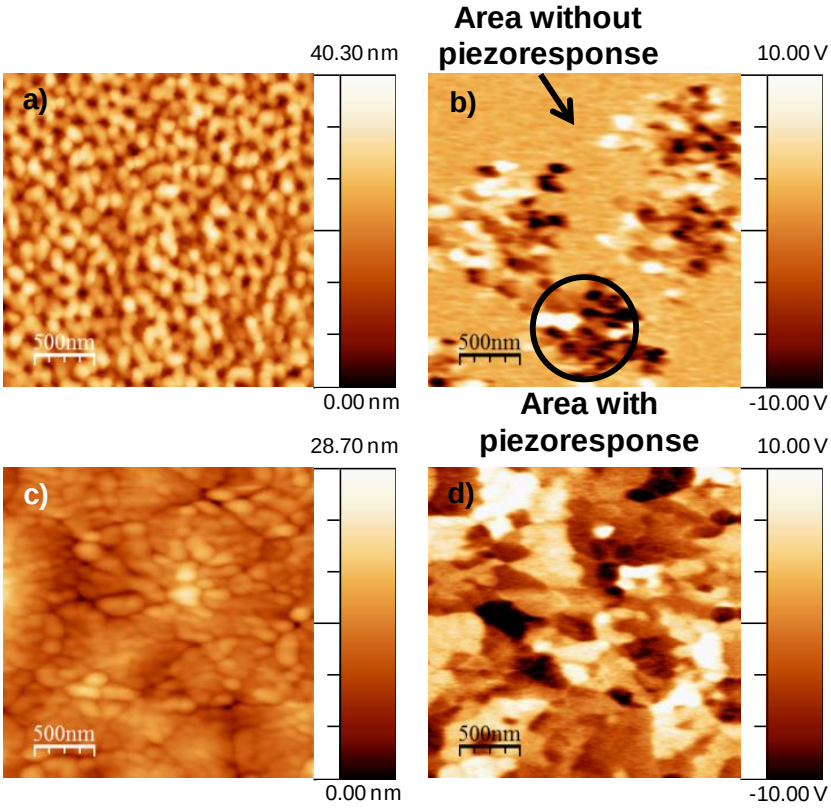

Figure 6.14: Topography and VPFM mixed signal images for nanopatterned porous (6.14a and 6.14b) and dense (6.14c and 6.14d) $BiFeO_3$ thin films thermally treated at 600 ºC, respectively. The data scale for VPFM mixed signal image ranges from -10 to 10 V. This 20 V scale corresponds to 360º, thus opposite domains oscillate 180º out of phase, as expected.

Both nanopatterned porous and dense films, display well-defined hysteresis loops which are an evidence of their FE behavior. However and importantly these films display different values of imprint, saturated piezoresponse and coercivity (here meaning the coercive field), Figure 6.15b. The imprint effect is usually caused by the preference of a certain polarization state over the other. The dense films present a higher imprint effect when compared with the porous ones (Figure 6.15b), which can be attributed to the presence of defects in the film, including oxygen vacancies and surface/interface defects (lattice distortion due to the difference of the thermal expansion coefficient between the film and the substrate) generating a layer of negative

charge.[274,238,196] The coercivity is the required electric field strength to flip the direction of the polarization. From a statistical study of at least ten hysteresis loops for each of these thin films, the coercivity and the effective piezoelectric coefficient $(d_{33})_{eff}$ are estimated to be respectively around 5.5 ± 0.4 V and 69.8 ± 2.5 pm/V for nanopatterned porous thin films, and 6.3 ± 0.9 V and 28.9 ± 1.8 pm/V for dense ones (Figure 6.15b). The analysis of these values shows a lower coercivity in the nanopatterned porous films, meaning that it is easier to switch the polarization in these films than in the dense ones. On the other hand, the $(d_{33})_{eff}$ value is higher for nanopatterned porous than for dense films.

a)

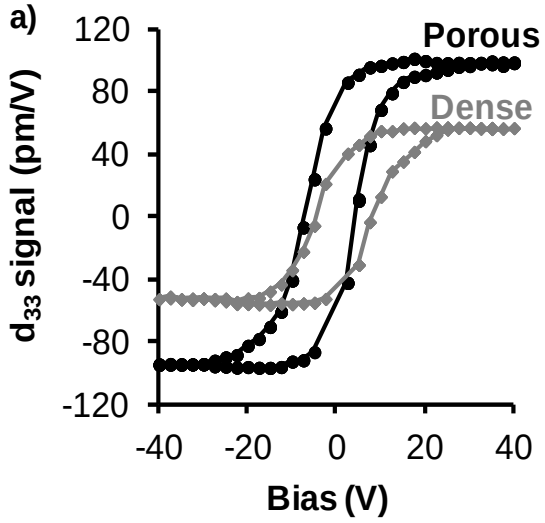

b)

	Imprint (v)	Coercivity (V)	$(d_{33})_{eff}$ (pm/V)
Porous	0.6±0.1	5.5±0.4	69.8±2.5
Dense	0.9±0.1	6.3±0.9	28.9±1.8

Figure 6.15: The representative remanent local hysteresis loops obtained for both thin films are presented in 6.15a). Average values of imprint, coercivity and $(d_{33})_{eff}$ piezoelectric coefficient calculated from several mixed hysteresis loops of the nanopatterned porous and dense thin films are presented in 6.15b). The nanopatterned porous thin films present enhanced FE properties as a consequence of its porous structure.

These results clearly point to the enhancement of the nanoscale electrical properties of the nanopatterned porous films and to the role of nano organized porosity. Comparing with the values reported in the literature, the $(d_{33})_{eff}$ value obtained for the nanopatterned porous thin film is in good agreement with the $(d_{33})_{eff}$ values reported by Ramesh *et al.*[275] for epitaxial $BiFeO_3$ thin films with tetragonal phase (~ 70 pm/V) and for heteroepitaxially constrained $BiFeO_3$ thin films (60 pm/V).[73,271] Furthermore, this value discloses the possibility of obtaining good piezo and FE behavior with rhombohedral structure for which the spontaneous polarization value should be significantly smaller than the expected value for a FE with such a high T_C. Beyond the positive effect of the porosity on local FE properties, other possible explanations can be based on the MF character of $BiFeO_3$, the magnetoelectric coupling at the domain walls,[270,276] the symmetry breaking and the lack of homogeneity in domain walls induced by the presence of the pore.

The porosity can thus lead to a reduction of the energy necessary to reorient the dipoles in the FE structures and induce instability in the dipole-dipole interaction producing a significant increase in the spontaneous polarization. In fact, this positive effect of the porosity in $BiFeO_3$ films corroborates our previous results for nanoporous $PbTiO_3$ thin films, in which we predicted and verified for the first time that nanoporosity has a positive effect on the overall piezoelectric response by facilitating the domain switching.[144] In addition the better local electric properties of the nanopatterned thin films can also be related with the reduced constraining effect of the substrate when compared with equivalent dense ones. The obtained $(d_{33})_{eff}$ value for dense thin films is comparable to the values previously reported for dense $BiFeO_3$ thin films prepared by soft chemical deposition.[272,61] Thus, the strong piezoelectric behavior of nanopatterned porous $BiFeO_3$ thin film opens an avenue of opportunities towards lead-free piezoelectrics for different application such as sensors, actuators and memory devices, whereas these thin films can be operated at lower power to obtain distinct magnitude of polarization.

The temperature dependence of the in-plane magnetization was studied by SQUID magnetometry for both nanopatterned porous and dense $BiFeO_3$ thin films thermally treated at 600 ºC (Figure 6.16).

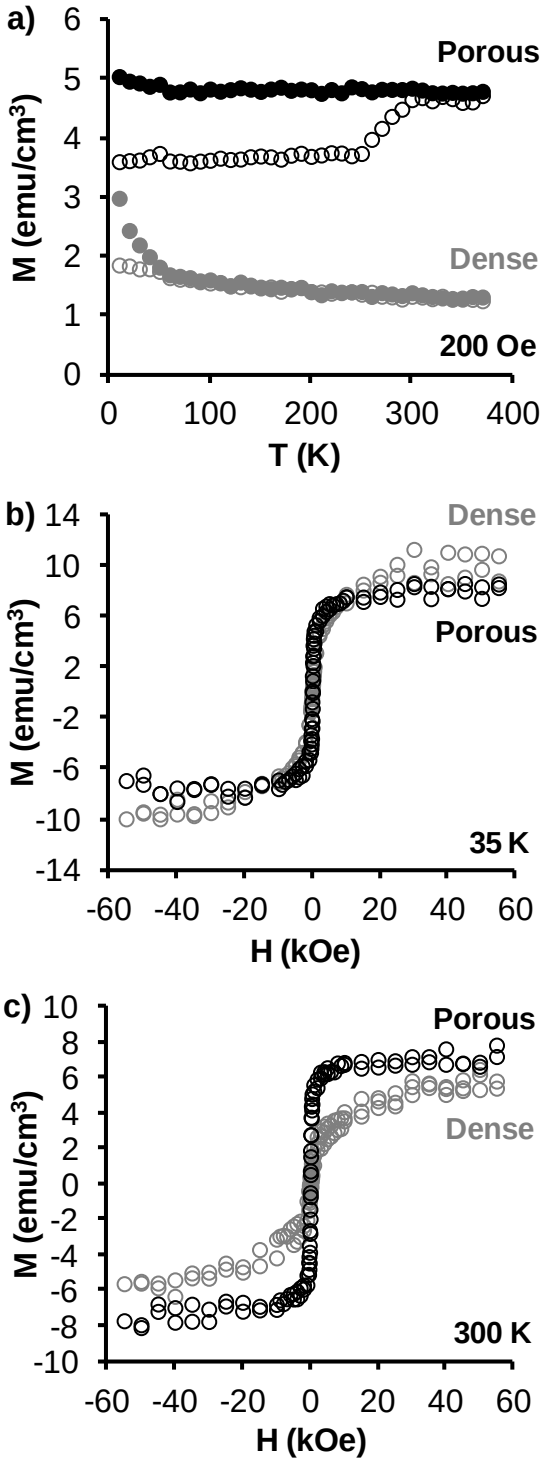

Figure 6.16: In-plane magnetic properties of the nanopatterned porous and dense $BiFeO_3$ thin films thermally treated at 600 ºC. a - ZFC (○) and FC (●) curves measured under an applied field of 200 Oe. b - and c - Magnetic hysteresis loops at 35 and 300 K. The porous structure seems to inhibit the anti-FM coupling leading to a stronger FM component and a higher remnant magnetization than in the dense films.

In these measurements the samples were cooled under zero magnetic field (Zero Field Cooling – ZFC curve) and the magnetization is recorded as a function of the increasing temperature under the applied field (20 mT in this case) or the samples were cooled under the measuring field (Field Cooled – FC curve) and the magnetization is measured again as temperature increases (Figure 6.16a). The ZFC-FC curves obtained for the dense thin films are compatible with the anti-FM behavior indicated by the magnetization versus field curves (Figure 6.16b and 6.16c), for a Neel transition temperature well above room temperature. Below 50 K the increase of the FC curve of the dense films can be associated with a spurious residual phase not detected by XRD.

The thermal variation of the magnetization for the nanopatterned porous films, displaying a ZFC magnetization value that remains almost constant up to 250 K, indicates a highly anisotropic material where the magnetic domains remain blocked up to this temperature. Figures 6.16b and 6.16c represent the magnetic hysteresis loops for both thin films obtained at 35 and 300 K. After subtraction of the substrate diamagnetic signal, the magnetic hysteresis curves of dense films clearly indicate the anti-FM behavior expected for $BiFeO_3$, with a weak FM component due to uncompensated moments. This FM component, determined by subtraction of the linear component at high fields, is represented in Figures 6.16b and 6.16c. For the nanopatterned porous films, the magnetic hysteresis loops shown in the same Figure (Figure 6.16b and 6.16c) were obtained directly by subtracting the substrate diamagnetic signal. Therefore, the field variation of the magnetization of the nanopatterned porous films points to the inhibition of antiferromagnetism by the porosity, leading to a FM signal around 50% stronger than the FM component obtained for dense counterparts (Table 6.5). For both temperatures (Figure 6.16b and 6.16c), the remnant magnetization and the saturation magnetization of the FM component is higher for the nanopatterned porous films while the coercive field is larger for the dense ones at 300 K (Table 6.5).

Brezesinski *et al.*[145,146] reported a preferential orientation of the magnetization as a consequence of the shape anisotropy within the pore walls for $CoFe_2O_4$ and $Ho_3Fe_5O_{12}$[146] mesoporous thin films.

Table 6.5: Saturation magnetization (M_{ferro}), remanent magnetization (M_r) and coercive field (H_C) for nanopatterned porous and dense $BiFeO_3$ thin films treated at 600 ºC.

	M_{ferro} (emu/cm^3)		M_r (emu/cm^3)		H_C (Oe)	
	35 K	**300 K**	**35 K**	**300 K**	**35 K**	**300 K**
Nanopatterned	10.4±0.5	8.5± 0.5	1.7±0.1	1.0±0.1	55.0±4.0	29.0±1.0
Dense	8.5±1.1	5.0±0.9	0.13±0.01	0.5± 0.1	35.0±0.5	65.0±5.0

In our case opposite to epitaxial thin films, the magnetization orientation effect is less dependent of the substrate as the "mechanical stress" does not result as much from a lattice or thermal expansion mismatch between the substrate and the film, but mainly from the strain on the solution-processed material imposed by the porous structure itself.[146] Moreover, the nanopatterned porous films have a continuous structure of large pores making them attractive structures for the development of novel and original MF materials where the magnetic behavior can be enhanced by functionalization of the pores with other magnetic material.

$BiFeO_3$ is in fact a multifunctional material and can be used in several applications. Thus, optical properties were evaluated.

Figure 6.17 shows the UV-Vis reflectance spectra for nanopatterned and dense $BiFeO_3$ thin films on $Pt(111)/TiO_2/SiO_2/Si(100)$ substrate thermally treated at 600 ºC. The absorption of $Pt(111)/TiO_2/SiO_2/Si(100)$ substrate was subtracted from that of $BiFeO_3$-$Pt(111)/TiO_2/SiO_2/Si(100)$. To determine the direct and indirect band gap, the relationship between the absorption coefficient and the incident photon energy which satisfies the Tauc representations[277] were taken into account. Thus, the $(\alpha h\nu)^{1/2}$ versus $(h\nu)$ and $(\alpha h\nu)^2$ versus $(h\nu)$ for both $BiFeO_3$ thin films were plotted and represented in Figure 6.17a and Figure 6.17b, where α and $(h\nu)$ are the absorption coefficient and the incident photon energy, respectively. From a linear extrapolation of $(\alpha h\nu)^{1/2}$ versus $(h\nu)$ and $(\alpha h\nu)^2$ versus $(h\nu)$ plots, the indirect and direct band gap were figured out, respectively. The indirect band gaps for nanopatterned porous and dense $BiFeO_3$ thin films are 2.25 eV and 2.23 eV, respectively, (Figure 6.17a), while the direct band gaps for nanopatterned porous and dense $BiFeO_3$ thin films are 2.58 eV and 2.39 eV,

respectively (Figure 6.17b). Both band gaps are located in the range of visible light and are in good agreement with those reported by other researchers[140,278,279,280] and are lower than the obtained values for other FE materials such as $BaTiO_3$, and $Pb(Zr,Ti)O_3$.

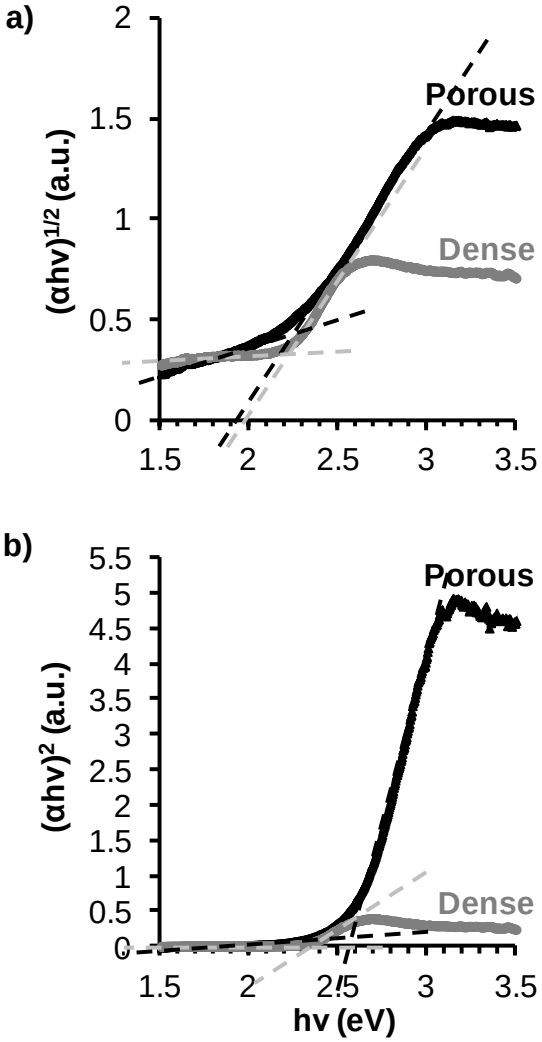

Figure 6.17: Plots for: 6.17a) indirect and 6.17b) direct optical transitions of nanopatterned porous and dense $BiFeO_3$ thin films thermally treated at 600 ºC. Extrapolation of the linear part of the curve to zero reveals that the nanopatterned and dense thin films present a similar indirect and slightly different direct optical band gaps supporting the dependence of this property with the porosity.

Most FEs present band gaps in ultraviolet region.[262,281] Nanopatterned porous thin films present slightly higher direct band gap values when compared to those obtained for dense thin films. This suggests that the porosity presents in thin films with

so low thickness induces variations in the density of states and band gap, which can be related to quantum-confinement properties of nanocrystals.[282] As reported in the literature, for thick films, around 1.5 μm of thickness, the direct band gap value is comparable to the values obtained for dense ones.[280] Comparing indirect and direct band gap values, one can observe that the indirect band gap occurs at lower energies when compared to the direct band gap previously reported.[278,279] Furthermore, the porosity (*ca*. 57 %) significantly increases the specific surface area leading to an increase of the available active sites in the catalyst. Thus, these nanopatterned $BiFeO_3$ thin films can be used as an effective visible-light photocatalyts,[283] in photovoltaic devices[262] and as an interesting alternative material class for the study of energy-related applications. Another interesting application involving the optical properties is the use of these nanopatterned porous thin films as a host of optoelectronic devices[284] taking advantage of the unique optical and MF properties of this material.

6.5 Conclusions

In Chapter 6, it was demonstrated the preparation of functional nanopatterned porous thin films, namely:

1. Well-ordered nanopatterned porous $PbTiO_3$ thin films were prepared using an easy and low-cost block-copolymer sol-gel solution. Despite being 20 nm thick the nanopatterned $PbTiO_3$ films present a tetragonal crystallographic phase, clearly exhibiting PFM domains contrast and a well-defined hysteresis loops as proof of their piezoelectric and ferroelectric behaviour, respectively. As reported in the Chapter 3, even for films with 20 nm of thickness and low tetragonality degree, the nanoporosity can be a way to enhance the local ferroelectric properties. Film and wall thicknesses and pore diameter can be tuned by tailoring the withdrawal speed and inorganic solution dilution.

2. Very homogeneous and ordered nanopatterned porous $CoFe_2O_4$ thin films with different thickness and average pore diameters between 60 to 80 nm were prepared through the same approach that nanopatterned porous $PbTiO_3$ thin films. The MFM

measurements performed perpendicularly to the substrate prevent the detection of in-plane magnetization domains. However, the analysis of the out-of-plane magnetization indicates an in-plane orientation of the magnetization differing from other $CoFe_2O_4$ films prepared by sol-gel methods and with low thickness (≈ 65 nm). Comparing nanopatterned and dense thin films, the nanopatterned porous films display at 300 K saturation magnetization values much lower than dense films with similar thicknesses and almost no remanence or coercivity properties. These features can be understood as an effect of porosity. Nevertheless, as the porosity is completely open and directed to the substrate, these nanopatterned porous thin films can also be functionalize to create a new generation of multiferroic devices, memories or even in potential applications where specific substrate and films surface properties are simultaneously required. A high saturation magnetization typical from the presence of a ferromagnetic impurity was mesasured. This impurity may be related with the formation of a platinum-rich alloy. It is proposed, in similarity with other reported works, the potential of this mixed oxide to behave as a catalyst on the oxidation of the organic moieties by providing oxygen of the lattice with consequent reduction of the lattice metal ions following a Mars-Van-Krevelen mechanism.[230,231] The metals are then available to react with platinum at low temperature. From the view point of application the alloy formation is quite interesting, as the alloy possesses strong ferromagnetic response necessary for the new generation of magnetic recording technology. This phase together with the $CoFe_2O_4$ phase can be an interesting combination in the same material for the next generation data storage media. Moreover, the formation of the alloy demonstrates the high potential of these films to be used as catalysts with large specific surface area in energy impact process, as the combustion of biogas at low temperature, avoiding the use of the cost prohibitive noble metal catalysts.

3. Very homogeneous nanopatterned porous $BiFeO_3$ thin films with ca. 66 nm of thickness and average pore size of 100 nm were prepared using the evaporation-induced self-assembly approach. Due to the porous structure, the nanopatterned porous thin films present better local electrical and macroscopic magnetic properties when compared to dense counterparts films. From analogy to the FEM and experimental results obtained in nanoporous $PbTiO_3$ thin films (Chapter 3), the results obtained for

the nanopatterned $BiFeO_3$ thin films allows to conclude that the porosity can be a way to reduce the energy necessary to reorient the dipoles in the ferroelectric structures and induce instability in the dipole-dipole interaction, thus producing a significant increase in the spontaneous polarization. In addition, the porous structure seems to inhibit the anti-ferromagnetic coupling leading to a stronger ferromagnetic component and a higher remnant magnetization than in the dense films. The nanopatterned porous $BiFeO_3$ thin films can be a unique material for the microelectronic industry as a lead-free ferroelectric material with tunable improved properties; or as a single phase multiferroic with enhanced properties. Furthermore, these thin films present a small band gap comparable with other semiconductor materials. The direct band gap value is slightly higher for the nanopatterned porous thin films suggesting that this property is dependent on the porosity.

Furthermore, as the porosity in all these nanopatterned porous thin films is completely open and directed to the substrate, these nanopatterned porous thin films can be also used to functionalize and create a new generation of the multiferroic composites if the pores are carefully functionalized with a strong room temperature magnetic material, aiming a strong magnetoelectric coupling, memories or even in potential applications where the substrate and films surface properties are simultaneously required.

CHAPTER 7

MF nanostructured thin films: a proof of concept

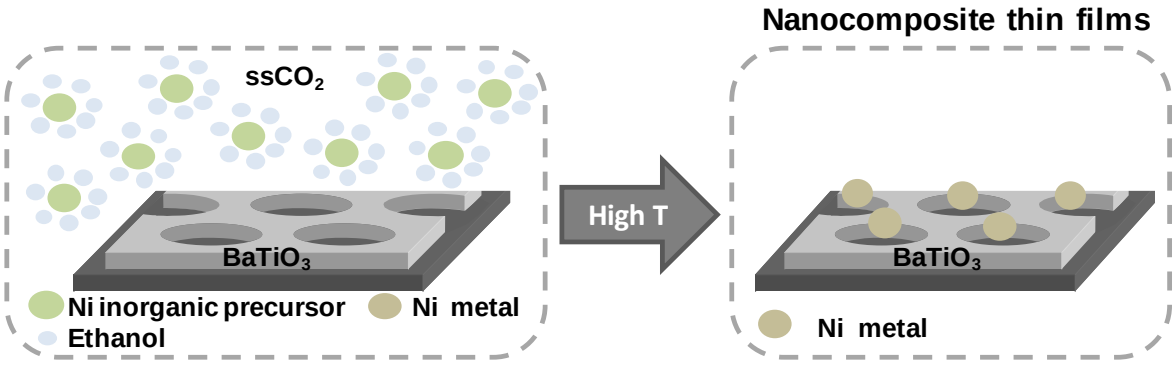

Graphical abstract: Schematic representation of the functionalization of nanopatterned porous $BaTiO_3$ with nickel nanoparticles by a supercritical CO_2 depostion process.

Abstract

A new concept to prepare multiferroic nanocomposite thin films is explored. This consists on using two chemical-based bottom-up steps, including: *i)* the formation of a porous ferroic matrix by a sol gel type process; and *ii)* the accomodation in the pores of nanoparticles from a different ferroic phase by a supercritical CO_2 deposition process. Porous nanopatterned $BaTiO_3$ thin films with *ca*. 17 nm of thickness are prepared using a cost-effective sol-gel solution containing a block-copolymer and evaporation-induced self-assembly methodology. The pores of the thin film matrix are then infiltrated with nickel nanoparticles with around 21 nm of average diameter. Hydrated nickel nitrate in a supercritical CO_2-ethanol mixture at 250 ºC is reduced and deposited in the *ca.* of 95 nm diameter pores of the porous matrix. Structural and magnetic properties prove the coexistence of both phases.

Index

7.1 Introduction

As well-ordered porous structures are excellent matrices to create multifunctional materials, we wish now to exploit the potential of these porous platforms, with vertical aligned pores perpendicularly to the substrate, to achieve MFs, by depositing a magnetic material inside the pores of the FE patterned films. The vertical architectures of the composites should lead to enhanced properties compared to the layered structure as consequence of the increase of interfacial area between the two ferroic phases and of the reduction substrate clamping effect.[5]

The deposition of the second magnetic phase in the small pores of the FE matrix is challenging because of the difficulties of filling nanosized pores without covering the all surface to achieve good interfaces between both ferroic phases. To overcome these limitations, we proposed to use supercritical CO_2 as a solvent.

The use of supercritical fluids (SCFs) in Materials Science started in the beginning of the 90s as a mean to produce nanomaterials.[285,286,287,288] Among all nanomaterials, nanoparticles and nanostructured materials are the most explored areas.[286] The interest in using SCFs relies on their unique properties, high solvating power and excellent transport properties.[285] Indeed, within the supercritical region, there is no phase boundary between the gas and liquid phases, meaning that there is continuity in the physical properties of the fluid between the gas and liquid states.[285]

The most frequently used supercritical fluid is carbon dioxide (CO_2). CO_2 is cheap, non-flammable, chemically inert, not toxic and has a relatively low critical

temperature and pressure (T_C = 31 ºC, P_C = 7.38 MPa).[289] Supercritical CO_2 can dissolve a broad range of organometallic compounds.[290,291,292] Although pure CO_2 is not a good solvent for inorganic metal salts, hydrated metal nitrates and chlorides can be dissolved in supercritical CO_2 by adding a small amount of a polar solvent such as ethanol in CO_2-ethanol solutions.[293] These precursors are less toxic, cheaper and easier to handle than the nickel organometallic compounds.

Watkins *et al.* developed a SCF based approach that consists in the deposition of metals and metal oxide by chemical reaction of suitable precursors in an SCF within a high-pressure reactor.[294,295] The reaction was generally initiated upon the addition of hydrogen (H_2) or another reducing agent such as an alcohol. The Supercritical Fluid Deposition Technique (SCFD) was used to deposit nickel films onto planar and patterned silicon wafers using supercritical CO_2[294,296,297] to achieve conformal films with high quality. The same approach was extended to deposit nickel nanoparticles into porous supports such as mesoporous silica and mesoporous carbon xerogels.[298,299,300,301] The low surface tension, high diffusivity and low viscosities of CO_2 solutions allow to deposit or incorporate metallic nanoparticles into a wide variety of inorganic and organic substrates for microelectronics, optical and catalytic applications. Although the SCFD is a solution based approach, the transport properties of SCFs, which are more like to those of a gas, afford the infiltration in the complex geometry and avoid the mass transfer limitations common to liquid phase reductions. The high solubility of the decomposition products in CO_2 enhances purity of the material deposited at low temperature by facilitating desorption of potential contaminants from its surface.[5] Furthermore, the metal loading is easy to control by adjusting concentration, deposition time and pressure.

To the best of our knowledge, SCFD has never been used to prepare MF materials. In this Chapter, the preparation of the nanopatterned $BaTiO_3$ thin films by EISA onto platinized silicon wafer, the deposition of nickel within the pores using SCFD, and the structural and physical characterization of the materials are described. As we wish only to prove a new concept for MF nanocomposite preparation using a full chemical scalable approach, nanopatterned $BaTiO_3$ thin films will be used as amorphous platforms since as mentioned before the preparation of crystalline $BaTiO_3$ thin films keeping the porous order is a very difficult task.

7.2 Experimental part

7.2.1 Nanopatterned thin films preparation

Nanopatterned $BaTiO_3$ thin films were prepared using a sol-gel method and evaporation induced self-assembly methodology. PB51-*b*-PEO62 amphiphilic block-copolymer with MW_{PB} = 51 000 $gmol^{-1}$ and MW_{PEO} = 62 000 $gmol^{-1}$, from Polymer Source, was used as a structure-directing agent.

Three solutions were prepared. In solution A, PB51-*b*-PEO62 block-copolymer (30 mg, Polymer Source) was dissolved in a mixture of absolute ethanol (119.86 mmol, Riedel-de Haën) at 70 ºC. Solution B was prepared by the dissolution of barium hydroxide octahydrate (0.20 mmol, Merck, purity ≥ 98.0% w/w) in glacial acetic acid (8.93 mmol, Merck) at room temperature. Solution C was prepared from mixing 2,4-pentanedione (0.11 mmol, Fluka, purity 99.3% w/w) with titanium (IV) *n*-butoxide (0.20 mmol, Merck, 98.0% w/w) under stirring at room temperature. Afterwards, solutions B and C were added to solution A, forming the final solution. Nanopatterned $BaTiO_3$ thin films were deposited by dip-coating onto platinized silicon ($Pt(111)/TiO_2/SiO_2/Si(100)$) (Radiant Inc.) at 1.6 mm/s. All films were thermally treated in air at 350 °C during 5 min in order to complete the inorganic condensation (mesostructuration) of the matrix and to partially decompose the organic content. The films were also thermal treated at 600 and 700 ºC during 2 min.

7.2.2 Functionalization using $scCO_2$

The experiments were conducted in a *ca*. 100 mL stirred high-pressure reactor (Autoclave Eng. Inc.) in the batch mode. Several pieces of 1 cm x 1 cm of the nanopatterned $BaTiO_3$ thin films were placed vertically inside the high-pressure reactor and in contact with the wall. The nickel (II) nitrate hexahydrate precursor, (0.069 mmol, Sigma-Aldrich, 98.5% w/w) was previously dissolved in ethanol (68.50 mmol, Riedel-de Haën, PA) and placed in a vial allocated at the bottom of the reactor without contacting the substrates.

The reactor was then heated by a heating jacket connected to a PDI controller to 60 ºC and was then filled with CO_2 (Air Liquide, purity >99.99 %) using a high-pressure

syringe pump (Isco, Inc. Model 260D) thermostated at the same temperature up to 10.0 MPa. The temperature was measured using a K-type thermocouple. The pressure was measured using a pressure gauge. The mixture of the inorganic precursor with ethanol was dissolved in $scCO_2$ and impregnated into the nanopatterned material at 60 ºC and 100 bar for 1 hour. At these conditions, the percentage of ethanol in CO_2 in the mixture was 4 %. Then, the reactor was heated at 250 ºC for 2 hours for its decomposition. During these experiments the pressure was kept below 30 MPa (which is the pressure maximum limit of the equipment) by venting a small amount of the CO_2 solution from 100 ºC. Then, the heater was turned off and the reactor was depressurized through a needle valve for the period of 1 hour.

Basically, the SCFD approach involved the dissolution of the $Ni(NO_3)_2$ salt in the CO_2-EtOH mixture at low temperature, in our case 60 ºC and 10 MPa, and the exposure of the substrate to the solution. After incorporation of the precursor on the substrate surface, the metallic precursor was reduced to its metal form by heating at 250 ºC. Ethanol acted as co-solvent favouring precursor dissolution and as reducing agent at high temperature promoting the chemical reduction of the salt.

7.2.3 Characterization

The film microstructure was investigated by high-resolution SEM using a SU-70 Hitachi microscope. The AFM and MFM measurements were carried out on Nanoscope III, using Tap300 cantilevers with Al-coated tips (Budget Sensors, resonant frequency of 200−400 kHz, force constant of 20−75 N/m) and MESP cantilevers with CoCr-coated tips (Bruker, resonant frequency of 75−100 kHz, force constant of 2.8−5.0 N/m), respectively. The AFM images were collected in contact mode. In the MFM measurements, the topography signals of the film surface were taken simultaneously with the deflection and phase signals and were collected in non-contact mode. Since the results were obtained with the same type of cantilevers and under identical scanning and acquisition conditions, comparison between both films can be made. Magnetization measurements as a function of temperature and applied magnetic field were performed using a SQUID magnetometer (QD-MPMS). The thermal variation was measured at 200 Oe, increasing the temperature from 10 to 370 K after cooling the sample down to

10 K in zero applied field (zero field cooled - ZFC) or under the measurement field (field cooled - FC). The isothermal hysteresis loops were obtained at 35 K and 300 K for magnetic fields up to 5.5 T, parallel and perpendicular to the film surface. The diamagnetic components due to the substrate and to the porous $BaTiO_3$ film were subtracted from the measured magnetic moment.

7.3 Results and discussion

Figure 7.1 shows top view SEM micrographs of nanopatterned $BaTiO_3$ thin films before (a-c) and after (e-g) functionalization with nickel and thermally treated at different temperatures. These micrographs are representative of the entire covered surfaces and exhibit good quality hexagonal ordered porous structure. This pore order and periodicity result from the self-assembly of micelles of the amphiphilic block-copolymer, followed by condensation of the inorganic species around the micelle arrays. Figures 7.1a reveals an amorphous character of the structure after thermal treatment at 350 °C for 5 min. At this temperature all pores are already open due to the complete decomposition of the block-copolymer and to the very thin deposited layer of the nanopatterned $BaTiO_3$ thin films. During the thermal decomposition of the block-copolymer, void motifs are thus created. The platinum grain structure of the Pt(111)/TiO2/SiO2/Si(100) substrate can be already observed and demonstrates that vertical pores are open. Upon thermal treatment at 600 °C, the well-ordered porous structure remained without coalescence of the pores as seen in Figure 7.1b. Otherwise, at 700 ºC some walls between the pores start to collapse and the coalescence of some pores takes place (Figure 7.1c). However, at this temperature the well-ordered array is practically kept at large scale. The amorphous character seems to prevail. XRD measurement (not shown) also confirms the amorphous character of the film. Potential explanations for the absence of XRD signals may be: *i)* the non-formation of crystalline phase due to inadequate inorganic/organic ratio;[207,241,220,112] or too low temperature for the crystallization; and *ii)* the crystallites are too small to be detected with the XRD diffractometer. It has been reported the preparation by molecular beam epitaxy of crystalline $BaTiO_3$ thin films with thickness below 2 nm.[49]

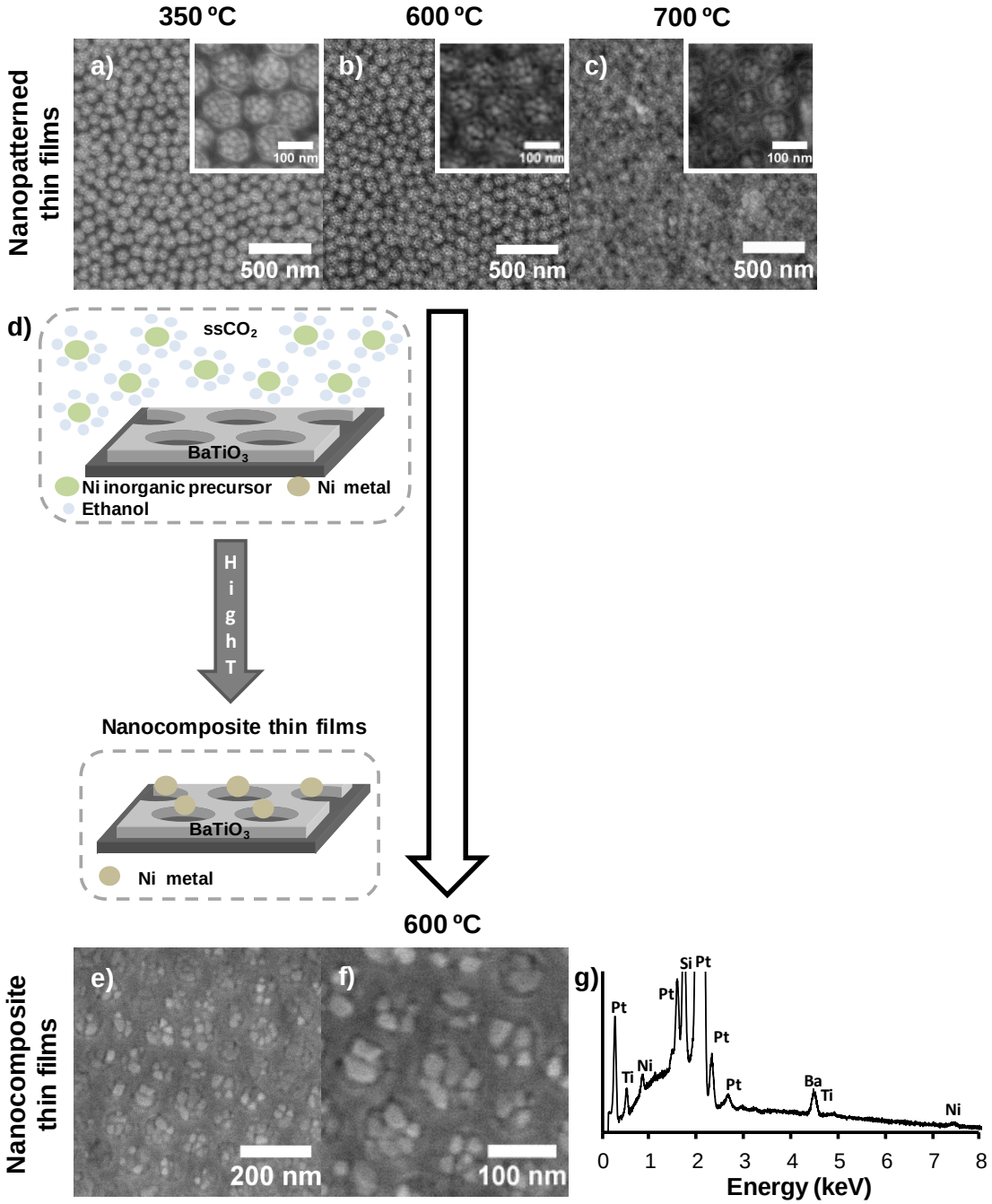

Figure 7.1: SEM of nanopatterned $BaTiO_3$ thin films before (a-c) and after (e-f) functionalization with nickel nanoparticles through SCFD. The insets present in Figures a-c zoom the respective SEM micrographs illustrating the well-ordered porous structure. The pore size is around 95 nm and nickel nanoparticles are less than 21 nm. EDX patterns of the nanopatterned thin films after functionalization with nickel nanoparticles are presented in Figure g). Figure d) schematically illustrates the approach used to functionalize the nanopatterned thin films with nickel nanoparticles.

In our case the preparation methodology would not only lead to polycrystalline structure but also would contribute to a high degree of defects, conditioning the crystallization.

The analysis of the nanoscale FE properties was dismissed due to the lack of evidence of crystalline structure.

Despite the unclear crystallographic structure of the nanopatterned $BaTiO_3$ thin films thermal treated at 600 ºC, the prepared nanopatterned thin films were used as matrices for studying the functionalization with nickel nanoparticles through the SCFD approach (Figure 7.1d) in order to prepare a MF material (Figure 7.1e-f).

From the SEM micrographs, Figure 7.1e-f, no solvent residue or big nanoparticle clusters on the surface of the nanopatterned thin films were found. The presence of distinct nanoparticles only within the pores and more than one in the same pore can be also observed, suggesting that the particles coalescence was limited by the relatively low reduction temperature (250 ºC) (Figure 7.1e-f). Nanoparticles are only placed inside the pores as an effect of the grained structure of the exposed platinum substrate which may catalyze the reduction.[302] The pore diameter and nanoparticles sizes determined from the SEM micrograph analysis are 95 ± 11 nm and 21 ± 5 nm, respectively. The chemical composition of the nanoparticles was evaluated by EDX, confirming that nanoparticles are composed by nickel (Figure 7.1h).

Figure 7.2 shows the AFM measurements performed in the nanopatterned $BaTiO_3$ thin films thermally treated at 600 ºC before (a) and after (b) functionalization with nickel. AFM images are representative of the entire covered surfaces and exhibit good quality arrays of hexagonally-like ordered porous structure (Figure 7.2a). Figure 7.2b shows that more than 70 % of the pores of nanopatterned thin films are occupied by nanoparticles with *ca*. 21 nm in diameter. Several nanoparticles were deposited per pore, suggesting that the functionalization was successful in addressing the nanoparticles into the pores. The pore size is in good agreement with that measured in the SEM micrographs. The wall thickness between pores was found to be 43 ± 10 nm. The percentage of porosity was calculated as 69 ± 2 %.

As the AFM measurements were performed in contact mode with high resolution tips with tip height of 17 µm and tip radius < 10 nm, the depth pore can be related with film thickness. Thus, the thickness of the nanopatterned $BaTiO_3$ thin films

is around 17 ± 2 nm. From the acquisition conditions and the relation between the depth pore and thickness it is possible to observe that the pores reach down to the substrate and the porosity is completely open and directed to the substrate as it was observed in the SEM micrographs. The RMS (root mean square) surface roughness for the nanopatterned thin films (Figure 2a) is 5.1 nm. However, the AFM images for nickel functionalized nanopatterned $BaTiO_3$ thin films (Figure 7.2b), present a RMS surface roughness of 3.0 nm. The decrease of the surface roughness proves that the pores are filled with nanoparticles, with consequent flattening of the surface. As for crystalline $BaTiO_3$, the nickel nanoparticles could not be identified by XRD. Again, due to the low film thickness, the nickel content may be below the resolution limit of the equipment.

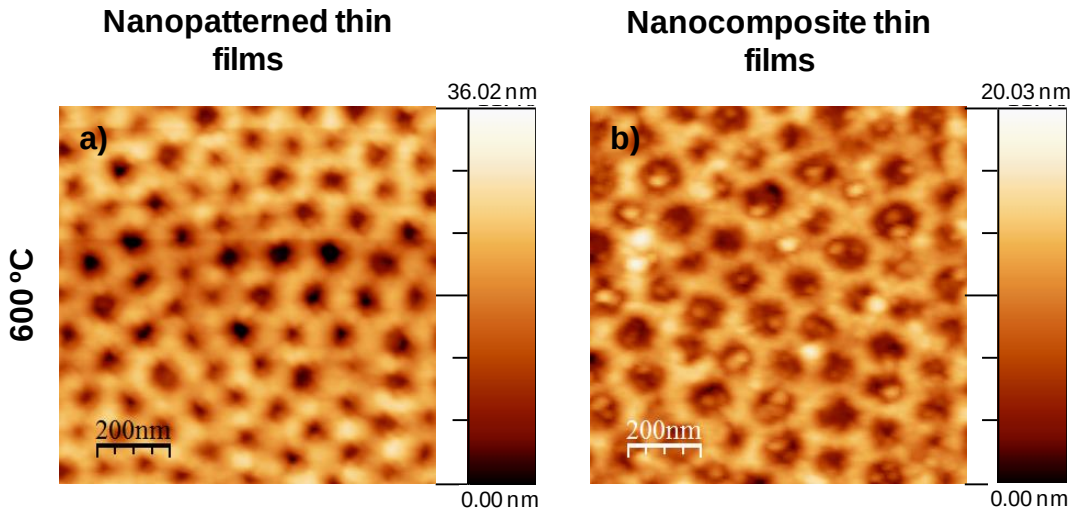

Figure 7.2: AFM topography images (1µm x 1 µm) of nanopatterned $BaTiO_3$ thin films: a) before and b) after functionalization with nickel nanoparticles through SCFD. The images show a well-ordered porous array and the nanoparticles are only within the pores. No big particles can be observed.

To evaluate the magnetic behavior, MFM measurements were performed in nickel functionalized nanopatterned $BaTiO_3$ thin films (Figure 7.3). The topography and phase are shown in Figure 7.3a and b, respectively. The topography is very similar to the one obtained by SEM (Figure 7.1) and by AFM (Figure 7.2) showing the well-ordered porous structure filled with nickel nanoparticles. However, no contrast coming from the magnetic nanoparticles can be observed in the phase image even at 5 nm from the surface (Figure 7.3b). These observations suggesting that the domains are oriented

parallel to the surface and cannot be detected by our system that only operate in out of plane.

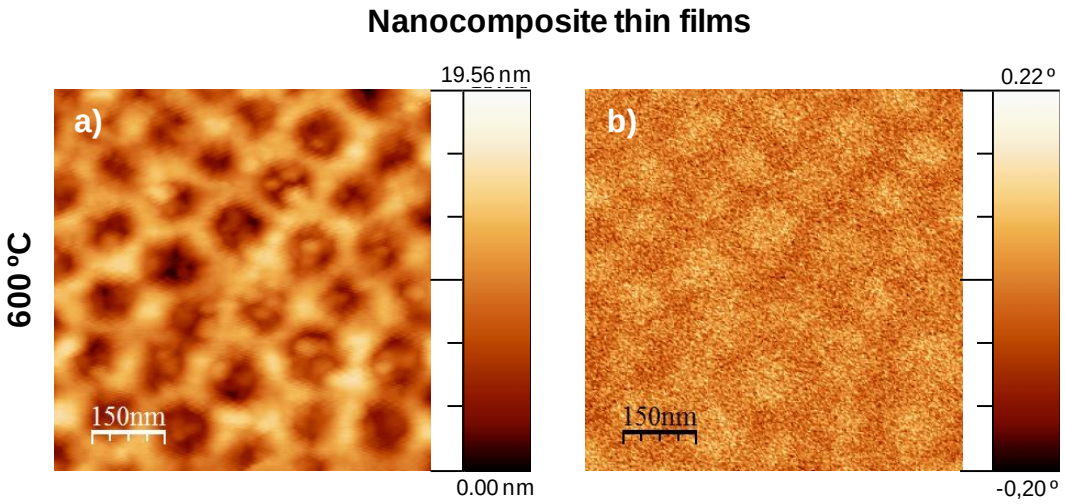

Figure 7.3: a-Topography AFM (750 nm x 750 nm) and b-MFM phase images of nanopatterned $BaTiO_3$ thin films deposited after functionalization with nickel by SCFD. The nanocomposite thin films do not present any contrast even at 5 nm from the surface suggesting the parallel orientation of the domains in relation to the surface. The slight contrast observed is a topographic effect due to the small distance between the tip and surface.

Figure 7.4 shows the magnetization measurements as a function of temperature and applied magnetic field. The diamagnetic components due to the substrate and to $BaTiO_3$ films were subtracted. The data are normalized to the nickel volume considering the mean values of film thickness (17 nm), film porosity (68%), pores diameters (95 nm) and the percentage of pores occupation by nickel nanoparticles (70%). Figures 7.4-a) and b) are consistent with a FM behavior of nickel nanoparticles (Curie temperature above room temperature) with a wide size distribution. The maximum magnetization attained at 300 K (Figure 7.4-b)) is 300 emu/cm^3, and the coercive fields are around 150 Oe and 25 Oe at 35 K and 300 K, respectively. These values which are lower than the bulk values for nickel (~485 emu/cm^3, and 100 Oe,[303] for saturation magnetization and coercive field, respectively, at 300 K) are attributed to the quite low size of the nanoparticles. Similar values have been published elsewhere for nickel nanoparticles.[304]

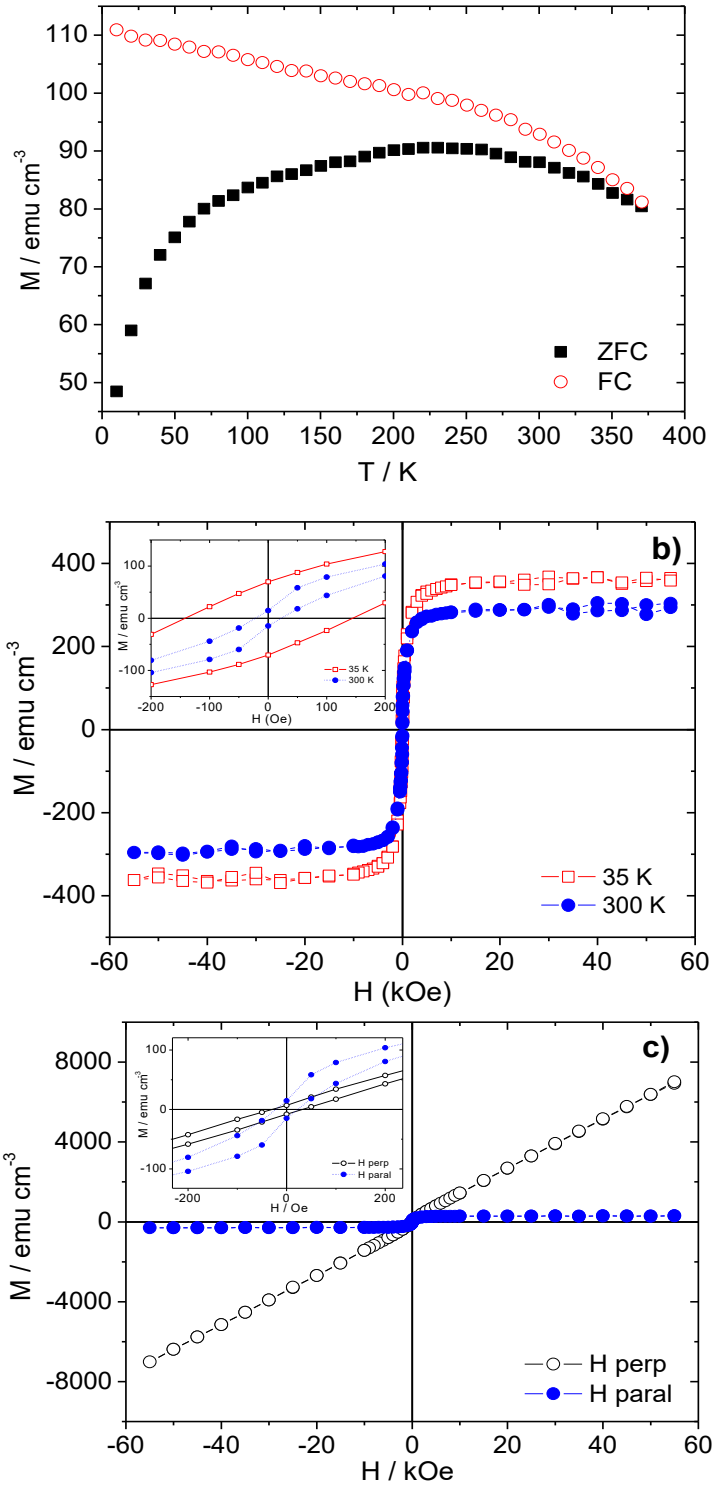

Figure 7.4: Magnetization normalized to the volume of nickel nanoparticles estimated from SEM and AFM measurements, after subtraction of the diamagnetic components: a - ZFC-FC curves measured under an applied field of 200 Oe; b - Hysteresis loops obtained at 35 and 300 K in parallel configuration; c - Hysteresis curves obtained at 300 K, with the magnetic field applied parallel and perpendicular to the film surface.

The field variation of the magnetization was also measured at 300 K with the magnetic field perpendicular to the film surface (figure 7.4-c). In this case, in contrast with the parallel field configuration, a high susceptibility remains up to the highest measured fields, indicating that there is a progressive alignment with the field of the nickel nanoparticles. This result is consistent with the fact that from MFM measurements the domains seem to be oriented parallel to the surface of the film as an out-of-plane magnetic contribution was not detected within the pores.

Although, the main aim of the functionalization was to prepare MF materials, we believe that nanocomposite thin films with small nanoparticles can be also used as a solution to avoid the magnetostatic interactions between neighboring magnetic domains in patterned magnetic media by the presence of the walls between the pores.[69,297,68] Despite further improvements are required, the proposed strategy is simple, sustainable, versatile, and proved that is possible to functionalize nanopatterned thin films by an adaptable approach and, consequently to prepare magnetic nanocomposite films or even MF materials if the preparation conditions of the nanopatterned thin films are well adjusted.

7.4 Conclusions

A well-patterned multiferroic composite thin film was fabricated by an easy, chemical-based and scalable method, avoiding costly high-resolution lithography techniques and harmful etching processes. The composites are achieved in two steps encompassing the design of a nanopatterned $BaTiO_3$ porous matrix followed by the filling of the pores with nickel nanoparticles through a supercritical CO_2 fluid. The nanopatterned thin films present a pore diameter size of *ca.* 95 nm and a thickness of *ca.* 17 nm. SEM, EDX and AFM proved the presence of nickel particles with *ca*. 21 nm of diameter within the pores. Although through the MFM measurements it was impossible to confirm the magnetic behavior due to the parallel orientation of the domains, SQUID measurements undoubtedly prove that a magnetic material was successfully deposited in the porous film of $BaTiO_3$.

Based on the physical and chemical characteristics of SCFD approach, this methodology seems more promising, low-cost, easy and effective in the nanofabrication

of composite thin films than the electrochemical deposition reported in Chapter 5. With the SCFD approach the amount of nanoparticles and subsequent growth can be tuned by controlling the dissolution and reduction time, respectively. The chemical composition of the nanoparticles can be modified by the use of different inorganic precursors. Thus, this novel strategy of functionalization based in supercritical fluid deposition allows to create nanocomposite materials and can open perspectives for the application of these materials as nanopatterned media (magnetic data storage devices) as well as multiferroic materials.

CHAPTER 8

General conclusions

The present Thesis intends to be a contribution for the conception of alternative multifunctional thin films for electronic applications exploiting nanosized porosity.

In the last decade functional oxides community has been concerned in developing new methods to afford efficient multiferroic oxide-based nanocomposites through the direct chemical-based bottom-up of functional oxides over extensive substrate areas. Within this context the present work proposes through a chemical-based bottom-up methodology using evaporation-induced self-assembly of sol-gel solutions containing amphiphilic block-copolymer the formation of nanoporous and nanopatterned thin films with tunable thickness and ordered porosity.

The introduction of porosity at the nanoscale in functional materials (such as ferromagnetic, ferroelectric or multiferroic) might be thus a way, in particular if pores can be functionalized, creating opportunities to achieve new functionalities and devices. A primary example is a multifunctional composite structure, in which a porous matrix with a narrow pore size distribution is available for further incorporation of a material with a different functional property than the matrix.

Nanoporous ferroelectric thin films with different compositions, such as: $PbTiO_3$ and $BaTiO_3$ were prepared. $PbTiO_3$ was selected to start this study due to its high polarizability, strong spontaneous polarization, high Curie temperature (around 490 °C) and high pyroelectric coefficient. $BaTiO_3$ was chosen as a prototype of a lead-free ferroelectric material.

In Chapter 3, the role of nanoporosity on the crystallization of tetragonal phase and consequently on the local ferroelectric properties was theoretically and experimentally studied through Finite Element Model and Piezoresponse Force Microscopy, respectively. Although the porous structure and arrangement is very dependent on the heat treatment; the nanoporosity has a remarkable effect on the structural and local electric properties. In the others words, the nanoporosity allows an earlier crystallization of the tetragonal perovskite phase when compared with the dense counterparts. This enhancement of the tetragonality of the nanoporous films is reflected on the enhancement of the local ferroelectric properties such as: high local piezoelectric response and low local coercive field. The earlier crystallization of the tetragonal perovskite phase leads to a reduction of the energy necessary to reorient the dipoles in the ferroelectric structures and, consequently a reduction of coercivity when compared

to dense films. On the other hand, as the porosity induces instability in the dipole-dipole interactions, the reverse polarization can be favoured at low bias values. All the PFM results were according to the theoretical predictions using Finite Element Model. Both theoretical and experimental studies clearly show that nanoporosity can be used as a tool to tailor the coercive field of ferroelectric nanostructures.

As the preparation of porous oxide thin films at the nanoscale is not trivial, we have extended the used procedure to other compositions namely to $BaTiO_3$. It has been previously reported in the literature the degradation of the organization of pores on $BaTiO_3$ nanoporous thin films upon thermal treatment above 625 °C due to the induced crystallization.[142] Thus in Chapter 4, two studies were conducted to optimize the preparation conditions of nanporous films. Several parameters such as: heating the solution, addition of inorganic precursors / organic solvent and aging time of solution, on the micellization process were addressed. Furthermore, the effect of the block size of the block-copolymer on the structural and local piezoelectric properties of the films were investigated. From the study of the initial solution parameters on the structural properties and local electric properties of $BaTiO_3$, it was possible to conclude that the solutions without inorganic precursors and with addition of the inorganic precursors/organic solvents have a narrow micelle size distribution suggesting that the micellization process obeys the closed association mechanism. When the inorganic precursors / organic solvents are added, the micellization process seems to occur in two steps. Furthermore it was observed that nanoporous $BaTiO_3$ should be prepared from a fresh prepared deposition solution not thermally treated. From the second study, effect of the block size of the block-copolymer on the structural and local piezoelectric properties of the films, it was verified that the porous structure is very dependent on the structure-directing agent. The 59-72 block-copolymer seems to allow an easier accommodation of the grains around the micelles, which permits their crystallization into a very ordered porous structure. An earlier crystallization of the tetragonal perovskite phase was verified to occur in nanoporous films prepared with the 59-72 block-copolymer.

In the Chapter 5, nanoporous $BaTiO_3$ thin films prepared with the 40-53 block-copolymer were functionalized with cobalt nanoparticles using electrochemical deposition. SEM successfully proved the filling of the pores with the cobalt

nanoparticles. However, the smallest pores were not filled and some nanoparticles were found on the film surface. The nanoparticles seem to be very aggregated being the typical size of the particles below 50 nm. The local ferroelectric characterization shows piezoelectric behavior of the composite film, however the local ferroelectric hysteresis loops were not obtained. This can be explained by the ferroelectric behavior dependence on the grain size or on the crystallinity of the film. The ferroelectricity can be completely vanished below a critical size, which is very dependent on defect level and hence on the synthesis method. Furthermore, the weak out-of-plane piezoelectric coefficient of the $BaTiO_3$ turned difficult the acquisition of the hysteresis loops. The magnetic properties were observed by Magnetic Force Microscopy and by macroscopic measurements using a SQUID magnetometer. The cobalt functionalized $BaTiO_3$ films are multiferroic films presenting both piezoelectric/ferroelectric and ferromagnetic behaviors.

As the reduction of the film thickness can facilitate the functionalization of the pores, different compositions ($PbTiO_3$, $CoFe_2O_4$ and $BiFeO_3$) of well-ordered nanopatterned porous thin films were successfully prepared using a cost-effective evaporation-induced self-assembly method (Chapter 6). Despite the 20 nm thickness, the nanopatterned $PbTiO_3$ thin films present tetragonal crystallographic phase, showing clearly Piezoresponse Force Microscopy domain contrasts and well-defined hysteresis loops as an evidence of their piezoelectric and ferroelectric behaviors. Like to the reported in the Chapter 3, even for films with 20 nm of thickness and low tetragonality degree, the nanoporosity can be a way to enhance the local ferroelectric properties. Film wall thicknesses and pore diameter can be tuned by playing with the withdrawal speed and inorganic solution dilution.

Comparing the nanopatterned $PbTiO_3$ thin films with the nanoporous $PbTiO_3$ ones it is clearly visible the reduced vertical imprint effect in the thinnest nanopatterned films. We hypothesized that this observation is related with the fact that the nanopatterned films have large pore diameters (*ca.* 82 nm) being the underneath platinum electrode almost 50% accessible. The strains of the substrate are probably of minor importance in nanopatterned than in nanoporous films.

Ordered nanopatterned porous $CoFe_2O_4$ thin films with average pore size between 60 to 80 nm were prepared with similar thicknesses and below the critical

thickness. Macroscopic magnetic measurements prove that the magnetic properties of thin films are not isotropic, indicating a preferential in-plane orientation. Comparing nanopatterned and dense thin films, the nanopatterned porous films display at 300 K saturation magnetization values much lower than dense films with similar thicknesses and almost no remanence or coercivity properties. These features can be understood as negative effect of porosity. Nevertheless, it was measured a high saturation magnetization typical from the presence of a ferromagnetic impurity. This impurity may be related with the formation of a platinum-rich alloy. It is proposed, in similarity with other reported works, the potential of this mixed oxide to behave as a catalyst of the oxidation of the organic moieties by reduction of the lattice metal ions following a Mars-Van-Krevelen mechanism.[230,231] The metals are then available to react with platinum at high temperature. From the view point of application the alloy formation is extremely interesting, as the alloy possesses strong ferromagnetic response necessary for the new generation of magnetic recording technology. This phase together with the $CoFe_2O_4$ phase can be a very interesting combination in the same material for the next generation data storage media.

Due to the porous structure, the nanopatterned porous $BiFeO_3$ thin films present better local electrical and macroscopic magnetic properties when compared to dense counterparts films. In addition, the porosity leads to a reduction of the energy necessary to reorient the dipoles in the ferroelectric structures and, consequently a reduction of coercivity when compared with dense films. Similar results were obtained for nanoporous and nanopatterned $PbTiO_3$ thin films, as described before. The porous structure seems also to inhibit the anti-ferromagnetic coupling leading to a stronger ferromagnetic component and a higher remnant magnetization than in the dense films. Moreover, these $BiFeO_3$ thin films present a small band gap compared with other semiconductor materials and the direct band gap value is slightly higher for the nanopatterned porous thin films suggesting that this property is dependent on the porosity.

Using these nanopatterned porous thin films, well-patterned multiferroic composite thin films were fabricated by an easy, chemical-based and scalable method (Chapter 7). The composites are achieved in two steps encompassing the design of nanopatterned $BaTiO_3$ porous matrix followed by the filling of the pores with nickel

metal nanoparticles. Although through the Magnetic Force Microscopy measurements it was impossible to confirm the magnetic behavior due to the parallel orientation of the domains, SQUID measurements undoubtedly prove that a magnetic material was successfully deposited in the porous film of $BaTiO_3$. Due to the all physical and chemical characteristics of the Supercritical Fluid Deposition approach, this methodology seems thus more interesting, low-cost, easy to prepare and effective in the nanocomposites thin films preparation than the electrochemical deposition also reported here (Chapter 5).

Although we have proved the concept to prepare well-patterned multiferroic composites, important features of the ferroic phases are still necessary to take into account. Among them, a good crystallinity especially of the ferroelectric phase and the quality of the interfaces is need. It is also important that the integrity of each ferroic phase is preserved. In this way, the ferroic phases must be carefully selected, including cations with ionic radium sufficiently different to avoid the intermixing of the phases during the full crystallization of ferroic crystallographic phases and/or interfaces improvement. In terms of the characterization, macroscopic electrical measurements as well as magnetoelectric coupling determination methods suitable for very thin nanocomposite thin films needs to be developed.

Appendix

Appendix – Block-copolymer-assisted nanopatterning of porous lead titanate thin films for advanced electronics

To follow the complete PB-*b*-PEO decomposition, thermal gravimetric and differential thermal analyses (TGA-DTA) were carried out on dried powder of PB-*b*-PEO block polymer. A Setaram Labsys™ TGA-DSC16 system was used with a heating rate of 10 °C/min under flowing air up to 650 °C.

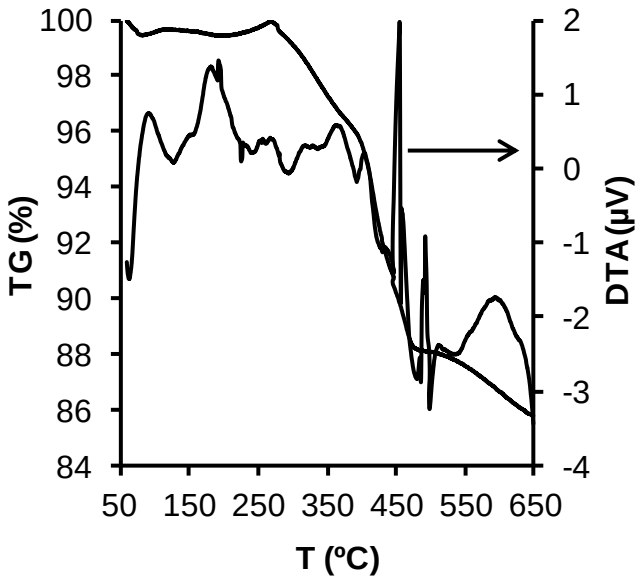

Figure A1.1: TGA-DTA of PB-*b*-PEO block-copolymer used to prepare the nanopatterned $PbTiO_3$ thin films. The TGA curve presents a significant weight loss from 250 to 450 ºC.

Figure A1.1 presents TGA-DTA analyses of PB-*b*-PEO block polymer. The TGA curve clearly show a significant weight loss (from 250 to 450 ºC) which is assigned to the decomposition of organics. From 450 to 650 ºC the weight loss reaches a value of 3% attributed to the decomposition of residual species. DTA is characterized by several thermal effects. However, these thermal effects can be attributed to the decomposition of PEO (poly(ethylene oxide)) from 150 to 250 ºC and to the decomposition of PB (Poly(butadiene)) from 250 to 450 ºC which corresponds to the higher weight loss, around 10 %.

The Figure A1.2 shows in more detail the microstructure of the nanopatterned $PbTiO_3$ thin film deposited with High C and 1.6 mm/s withdrawal rate and thermally treated at 650 ºC.

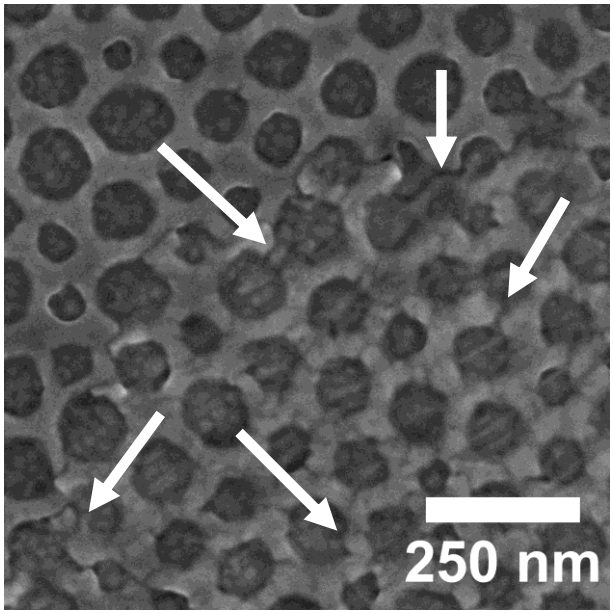

Figure A1.2: SEM micrograph of a thin film deposited with High C and 1.6 mm/s withdrawal rate and treated at 650 °C. The arrows indicate zones where the porous structure starts to collapse.

References

1 G. E. Moore, *Electronics*, 1965, **38**, 114.

2 S. Thompson and S. Parthasarathy, *Mater. Today*, 2006, **9**, 20–25.

3 *Int. Technol. RoadMap Semicond. 2015 (ITRS 2015) - http//www.itrs2.net/*.

4 *Intel Moore's Law - https//technologicallyinsane.wordpress.com/category/intel-moores-law/*.

5 L. W. Martin, S. P. Crane, Y.-H. Chu, M. B. Holcomb, M. Gajek, M. Huijben, C.-H. Yang, N. Balke and R. Ramesh, *J. Phys. Condens. Matter*, 2008, **20**, 434220–13.

6 M. Gajek, M. Bibes, S. Fusil, K. Bouzehouane, J. Fontcuberta, A. Barthélémy and A. Fert, *Nat. Mater.*, 2007, **6**, 296–302.

7 J. F. Scott, *Nat. Mater.*, 2007, **6**, 256–258.

8 S. Valencia, A. Crassous, L. Bocher, V. Garcia, X. Moya, R. O. Cherifi, C. Deranlot, K. Bouzehouane, S. Fusil, A. Zobelli, A. Gloter, N. D. Mathur, A. Gaupp, R. Abrudan, F. Radu, A. Barthélémy and M. Bibes, *Nat. Mater.*, 2011, **10**, 753–758.

9 V. Garcia, M. Bibes, L. Bocher, S. Valencia, F. Kronast, a Crassous, X. Moya, S. Enouz-Vedrenne, a Gloter, D. Imhoff, C. Deranlot, N. D. Mathur, S. Fusil, K. Bouzehouane and a Barthélémy, *Science*, 2010, **327**, 1106–1110.

10 J. F. Scott, *J. Mater. Chem.*, 2012, **22**, 4567–4574.

11 C. Lichtensteiger, M. Dawber and J.-M. Triscone, in *Physics of Ferroelectrics: A Modern Perspective*, eds. K. Rabe, C. H. Ahn and J.-M. Triscone, Springer-Verlag Berlin Heidelberg, 2007, pp. 305–338.

12 K. M. Rabe, M. Dawber, C. Lichtensteiger, C. H. Ahn and J.-M. Triscone, in *Physics of Ferroelectrics: A Modern Perspective*, eds. K. Rabe, C. H. Ahn and J.-M. Triscone, Springer-Verlag Berlin Heidelberg, 2007, vol. 30, pp. 1–30.

13 R. Ramesh and N. A. Spaldin, *Nat. Mater.*, 2007, **6**, 21–29.

14 Y. Wang, J. Hu, Y. Lin and C.-W. Nan, *NPG Asia Mater.*, 2010, **2**, 61–68.

15 J. Ma, J. Hu, Z. Li and C.-W. Nan, *Adv. Mater.*, 2011, **23**, 1062–87.

16 J. S. Andrew, J. D. Starr and M. a. K. Budi, *Scr. Mater.*, 2014, **74**, 38–43.

17 N. Marchack and J. P. Chang, *Annu. Rev. Chem. Biomol. Eng.*, 2012, **3**, 235–262.

18 Y. Kim, C. Pham and J. P. Chang, *J. Phys. D. Appl. Phys.*, 2015, **48**, 063001–25.

19 P. M. Vilarinho, in *Scanning Probe Microscopy: Characterization, Nanofabrication and Device Application of Functional Materials*, eds. Y. Rosenwaks and A. Kingon, Kluwer Academic Publishers, Springer Netherlands, 2005, pp. 3–33.

20 A. S. Bhalla, R. Guo and R. Roy, *Mater. Res. Innov.*, 2000, **4**, 3–26.

21 C. B. Carter and M. G. Norton, *Ceramic Materials: Science and Engineering*, Springer Science Business Media New York, 2nd Ed., 2007.

22 B. M. Wul and I. M. Goldman, *Compt. Rend. Acad. Sci. URSS*, 1945, **46**, 139–142.

23 A. von Hippel, R. G. Breckenridge, F. G. Chesley and L. Tisza, *Ind. Eng. Chem.*, 1946, **38**, 1097–1109.

24 J. Valasek, *Phys. Rev. Lett.*, 1921, **17**, 475.

25 N. A. Hill, *J. Phys. Chem. B*, 2000, **104**, 6694–6709.

26 A. J. Moulson and J. M. Herbert, *Electroceramics: Materials, Properties, Applications*, WILEY-VCH, 2nd Editio., 2003.

27 M. A. Aegerter, *J. Non. Cryst. Solids*, 1992, **151**, 195–202.

28 C. Lichtensteiger, P. Zubko, J.-M. Triscone, M. Stengel, P. Ghosez, P. Agguado-Puente and J. Junquera, in *Oxide Ultrathin Films: Science and Technology*, eds. G. Pacchioni and S. Valeri, WILEY-VCH, 2012, pp. 1–49.

29 K. M. Ok, E. O. Chi and P. S. Halasyamani, *Chem. Soc. Rev.*, 2006, **35**, 710–7.

30 R. E. Cohen, *Nature*, 1992, **358**, 136–138.

31 C. H. Ahn, K. M. Rabe and J.-M. Triscone, *Science (80-.).*, 2004, **303**, 488–491.

32 *FE hysteresis loop-http//www.noliac.com/Files/Billeder/Illustrations/PZT%20material%20characteristics/operation1.jpg*.

33 *Domain wall-http://www.gitam.edu/eresource/Engg_Phys/semester_2/magnetic/domain.htm*.

34 H. Han, Y. Kim, M. Alexe, D. Hesse and W. Lee, *Adv. Mater.*, 2011, **23**, 4599–613.

35 N. Setter, D. Damjanovic, L. Eng, G. Fox, S. Gevorgian, S. Hong, A. Kingon, H. Kohlstedt, N. Y. Park, G. B. Stephenson, I. Stolitchnov, A. K. Taganstev, D. V. Taylor, T. Yamada and S. Streiffer, *J. Appl. Phys.*, 2006, **100**, 0516061–46.

36 S. Li, J. A. Eastman, C. M. Foster, R. E. Newnham and L. E. Cross, *Phys. Lett. A*, 1996, 6–11.

37 J. Junquera and P. Ghosez, *Nature*, 2003, **422**, 506–509.

38 B. Meyer and D. Vanderbilt, *Phys. Rev. B*, 2001, **63**, 205426.

39 P. Ghosez and K. M. Rabe, *Appl. Phys. Lett.*, 2000, **76**, 2767–2769.

40 R. Kretschmer and K. Binder, *Phys. Rev. B*, 1979, **20**, 1065–1076.

41 D. R. Tilleya and B. Žekšb, *Solid State Commun.*, 1984, **49**, 823–828.

42 S. Li, J. A. Eastman, Z. Li, C. M. Foster, R. E. Newnham and L. E. Cross, *Phys. Lett. A*, 1996, **212**, 341–346.

43 D. D. Fong, G. B. Stephenson, S. K. Streiffer, J. A. Eastman, O. Auciello, P. H. Fuoss and C. Thompson, *Science (80-.).*, 2004, **304**, 1650–1653.

44 D. D. Fong, A. M. Kolpak, J. A. Eastman, S. K. Streiffer, P. H. Fuoss, G. B. Stephenson, C. Thompson, D. M. Kim, K. J. Choi, C. B. Eom, I. Grinberg and a. M. Rappe, *Phys. Rev. Lett.*, 2006, **96**, 3–6.

45 C. Lichtensteiger, J.-M. Triscone, J. Junquera and P. Ghosez, *Phys. Rev. Lett.*, 2005, **94**, 047603–4.

46 J. M. Gregg, *Phys. Status Solidi*, 2009, **206**, 577–587.

47 Y. S. Kim, D. H. Kim, J. D. Kim, Y. J. Chang, T. W. Noh, J. H. Kong, K. Char, Y. D. Park, S. D. Bu, J.-G. Yoon and J.-S. Chung, *Appl. Phys. Lett.*, 2005, **86**, 102907.

48 D. Tenne, P. Turner, J. Schmidt, M. Biegalski, Y. Li, L. Chen, a. Soukiassian, S. Trolier-McKinstry, D. Schlom, X. Xi, D. Fong, P. Fuoss, J. Eastman, G. Stephenson, C. Thompson and S. Streiffer, *Phys. Rev. Lett.*, 2009, **103**, 177601.

49 C. Dubourdieu, J. Bruley, T. M. Arruda, A. Posadas, J. Jordan-Sweet, M. M. Frank, E. Cartier, D. J. Frank, S. V Kalinin, A. A. Demkov and V. Narayanan, *Nat. Nanotechnol.*, 2013, **8**, 748–54.

50 R. Ahluwalia and D. Srolovitz, *Phys. Rev. B*, 2007, **76**, 174121.

51 A. E. Feuersanger and P. Lublin, *J. Electrochem. Soc.*, 1963, **110**, C192.

52 A. E. Feuersanger, A. K. Hagenlocher and A. L. Solomon, *J. Electrochem. Soc.*, 1964, **111**, 1387–1391.

53 J. R. Slack and J. C. Burfoot, *J. Phys. C Solid State Phys.*, 1971, **4**, 898–909.

54 O. Auciello, J. F. Scott and R. Ramesh, *Phys. Today*, 1998, **51**, 22.

55 N. Setter, D. Damjanovic, L. Eng, G. Fox, S. Gevorgian, S. Hong, A. Kingon, H. Kohlstedt, N. Y. Park, G. B. Stephenson, I. Stolitchnov, A. K. Taganstev, D. V. Taylor, T. Yamada and S. Streiffer, *J. Appl. Phys.*, 2006, **100**, 0516061–46.

56 M. Alexe, C. Harnagea, D. Hesse and U. Gösele, *Appl. Phys. Lett.*, 1999, **75**, 1793–1795.

57 J. F. Scott1, F. D. Morrison, M. Miyake, P. Zubko, X. Lou, V. M. Kugler, S. Rios, M. Zhang, T. Tatsuta, O. Tsuji and T. J. Leedham, *J. Am. Ceram. Soc.*, 2005, **88**, 1691–1701.

58 N. Setter, D. Damjanovic, L. Eng, G. Fox, S. Gevorgian, S. Hong, A. Kingon, H. Kohlstedt, N. Y. Park, G. B. Stephenson, I. Stolitchnov, A. K. Taganstev, D. V. Taylor, T. Yamada and S. Streiffer, *J. Appl. Phys.*, 2006, **100**, 1–46.

59 *ITRS 2015-http//www.itrs.net/Links/2015ITRS/Home2015.htm.*

60 N. A. Spaldin, *Magnetic Materials Fundamentals and Applications*, Cambridge University Press, United States of America, 2ª ed., 2010.

61 A. H. M. Gonzalez, A. Z. Simões, L. S. Cavalcante, E. Longo, J. A. Varela and C. S. Riccardi, *Appl. Phys. Lett.*, 2007, **90**, 052906.

62 *Descr. ordering spins ferroic Mater. - https//www.britannica.com/science/paramagnetism.*

63 D. Grosso, C. Boissière, B. Smarsly, T. Brezesinski, N. Pinna, P. a Albouy, H. Amenitsch, M. Antonietti and C. Sanchez, *Nat. Mater.*, 2004, **3**, 787–792.

64 K. Liu, J. L. Vicent, I. K. Schuller, J. I. Mart and J. Nogu, *J. Magn. Magn. Mater.*, 2003, **256**, 449–501.

65 S. Y. Chou, *Proc. IEEE*, 1997, **85**, 652–671.

66 S. Y. Chou and P. R. Krauss, *J. Magn. Magn. Mater.*, 1996, **155**, 151–153.

67 C. Haginoya, K. Koike, Y. Hirayama, J. Yamamoto, M. Ishibashi, O. Kitakami and Y. Shimada, *Appl. Phys. Lett.*, 1999, **75**, 3159–3161.

68 C. A. Ross, *Annu. Rev. Mater. Res. 2001.*, 2001, **2**, 203–35.

69 C. A. Ross, H. I. Smith and M. Walsh, *J. Vac. Sci. Technol. B*, 1999, **17**, 3168–3176.

70 W. Eerenstein, N. D. Mathur and J. F. Scott, *Nature*, 2006, **442**, 759–65.

71 L. W. Martin and D. G. Schlom, *Curr. Opin. Solid State Mater. Sci.*, 2012, **16**, 199–215.

72 C. Ederer and N. A. Spaldin, *Phys. Rev. B*, 2005, **71**, 060401–4.

73 J. Wang, J. B. Neaton, H. Zheng, V. Nagarajan, S. B. Ogale, B. Liu, D. Viehland, V. Vaithyanathan, D. G. Schlom, U. V Waghmare, N. A. Spaldin, K. M. Rabe, M. Wuttig and R. Ramesh, *Science (80-.).*, 2003, **299**, 1719–1722.

74 G. Catalan and J. F. Scott, *Adv. Mater.*, 2009, **21**, 2463–2485.

75 T. Zhao, A. Scholl, F. Zavaliche, K. Lee, M. Barry, A. Doran, M. P. Cruz, Y. H. Chu, C. Ederer, N. A. Spaldin, R. R. Das, D. M. Kim, S. H. Baek, C. B. Eom and R. Ramesh, *Nat. Mater.*, 2006, **5**, 823–9.

76 X. Gao, B. J. Rodriguez, L. Liu, B. Birajdar, D. Pantel, M. Ziese, M. Alexe and D. Hesse, *ACSNano*, 2010, **4**, 1099–1107.

77 J. L. MacManus-Driscoll, P. Zerrer, H. Wang, H. Yang, J. Yoon, A. Fouchet, R. Yu, M. G. Blamire and Q. Jia, *Nat. Mater.*, 2008, **7**, 314–320.

78 Q. He, E. Arenholz, A. Scholl, Y.-H. Chu and R. Ramesh, *Curr. Opin. Solid State Mater. Sci.*, 2012, **16**, 216–226.

79 C.-W. Nan, G. Liu, Y. Lin and H. Chen, *Phys. Rev. Lett.*, 2005, **94**, 197203.

80 H. Zheng, Q. Zhan, F. Zavaliche, M. Sherburne, F. Straub, M. P. Cruz, L. Chen, U. Dahmen and R. Ramesh, *Nano Lett.*, 2006, **6**, 1401–1407.

81 F. Zavaliche, H. Zheng, S. Y. Yang and Q. Zhan, *Nano Lett.*, 2005, **4**, 2–5.

82 L. Yan, Z. Wang, Z. Xing, J. Li and D. Viehland, *J. Appl. Phys.*, 2010, **107**, 064106.

83 N. M. Aimon, D. H. Kim, X. Sun and C. A. Ross, *ACS Appl. Mater. Interfaces*, 2015, **7**, 2263–2268.

84 I. Levin, J. Li, J. Slutsker and A. L. Roytburd, *Adv. Mater.*, 2006, **18**, 2044–2047.

85 H. Zheng, J. Wang, S. E. Lofland, Z. Ma, T. Zhao, S. R. Shinde, S. B. Ogale, F. Bai, D. Viehland, Y. Jia, D. G. Schlom, M. Wuttig, A. Roytburd and R. Ramesh, *Science (80-.).*, 2004, **303**, 661–663.

86 M. Bibes and A. Barthélémy, *Nat. Mater.*, 2008, **7**, 425–426.

87 H. Han, Y. Kim, M. Alexe, D. Hesse and W. Lee, *Adv. Mater.*, 2011, **23**, 4599–613.

88 S. Bühlmann, B. Dwir, J. Baborowski and P. Muralt, *Appl. Phys. Lett.*, 2002, **80**, 3195–3197.

89 D. Li and D. A. Bonnell, *Annu. Rev. Mater. Res.*, 2008, **38**, 351–368.

90 E. J. Ozimek, *J. Appl. Phys.*, 1985, **57**, 5406–5408.

91 H. Zhang, S. Chung and C. A. Mirkin, *Nano Lett.*, 2003, **25**, 1–3.

92 L. Francioso and P. Siciliano, *Nanotechnology*, 2006, **17**, 3761–3767.

93 Y. Liu, T. Cui, P. J. Coane, M. J. Vasile and J. Goettert, *Microsyst. Technol.*, 2003, **9**, 171–175.

94 A. J. Haes, C. L. Haynes, A. D. Mcfarland and G. C. Schatz, *MRS Bull.*, 2005, **30**, 368–375.

95 F. Zhu, G. Chern, O. Tchernyshyov, X. Zhu, J. Zhu and C. Chien, *Phys. Rev. Lett.*, 2006, **96**, 027205–4.

96 J. a. Rogers, K. E. Paul, R. J. Jackman and G. M. Whitesides, *Appl. Phys. Lett.*, 1997, **70**, 2658–2660.

97 J. Aizenberg, J. A. Rogers, K. E. Paul and G. M. Whitesides, *Appl. Phys. Lett.*, 1997, **71**, 3773–3775.

98 D. Makarov, P. Krone, D. Lantiat, C. Schulze, A. Liebig, C. Brombacher, M. Hietschold, S. Hermann, C. Laberty, D. Grosso and M. Albrecht, *IEEE Trans. Magn.*, 2009, **45**, 3515–3518.

99 M. M. Alkaisi, R. J. Blaikie, S. J. Mcnab, N. E. Science and N. Zealand, *Microelectron. Eng.*, 2000, **53**, 237–240.

100 J. I. Martín, Y. Jaccard, A. Hoffmann, J. Nogués, J. M. George, J. L. Vicent and I. K. Schuller, *J. Appl. Phys.*, 1998, **84**, 411–415.

101 D. J. Smith, R. E. Dunin-Borkowski, M. R. McCartney, B. Kardynal and M. R. Scheinfein, *J. Appl. Phys.*, 2000, **87**, 7400–7403.

102 R. P. Cowburn, *J. Phys. D Appl. Phys.*, 2000, **33**, 1–16.

103 Y. Yokoyama, Y. Suzuki, S. Yuasa, K. Ando, K. Shigeto, T. Shinjo, P. Gogol, J. Miltat, A. Thiaville, T. Ono and T. Kawagoe, *J. Appl. Phys.*, 2000, **87**, 5618–5620.

104 P. Vavassori, V. Metlushko and M. Grimsditch, *Phys. Rev. B*, 2000, **61**, 5895–5898.

105 N. M. Aimon, H. K. Choi, X. Y. Sun, D. H. Kim and C. A. Ross, *Adv. Mater.*, 2014, **26**, 3063–3067.

106 H. K. Choi, N. M. Aimon, D. H. Kim, X. Y. Sun, J. Gwyther, I. Manners and C. A. Ross, *ACS Nano*, 2014, **8**, 9248–9254.

107 R. Comes, H. Liu, M. Khokhlov, R. Kasica, J. Lu and S. A. Wolf, *Nano Lett.*, 2012, **12**, 2367–2373.

108 T. Sun, Z. Pan, V. P. Dravid, Z. Wang, M.-F. Yu and J. Wang, *Appl. Phys. Lett.*, 2006, **89**, 163117–3.

109 L. Piraux, J. M. George, J. F. Despres, C. Leroy, E. Ferain, R. Legras, K. Ounadjela and a. Fert, *Appl. Phys. Lett.*, 1994, **65**, 2484.

110 J.-G. Lee, J. Y. Park, Y.-J. Oh and C. S. Kim, *J. Appl. Phys.*, 1998, **84**, 2801–2804.

111 J. R. Morber, Y. Ding, M. S. Haluska, Y. Li, J. P. Liu, Z. L. Wang and R. L. Snyder, *J. Phys. Chem. B*, 2006, **110**, 21672–21679.

112 D. Grosso, F. Cagnol, G. J. de A. A. Soler-Illia, E. L. Crepaldi, H. Amenitsch, a. Brunet-Bruneau, a. Bourgeois and C. Sanchez, *Adv. Funct. Mater.*, 2004, **14**, 309–322.

113 D. J. C. Herr, *J. Mater. Res.*, 2011, **26**, 122–139.

114 W. Lee, H. Han, A. Lotnyk, M. A. Schubert, S. Senz, M. Alexe, D. Hesse, S. Baik and U. Gösele, *Nat. Nanotechnol.*, 2008, **3**, 402–7.

115 C. Sanchez, L. Rozes, F. Ribot, C. Laberty-Robert, D. Grosso, C. Sassoye, C. Boissiere and L. Nicole, *Comptes Rendus Chim.*, 2010, **13**, 3–39.

116 Y. L. Cheng, Y. Wang, H. L. W. Chan and C. L. Choy, *Microelectron. Eng.*, 2003, **66**, 872.

117 M. Nayak, S. Y. Lee and T. Tseng, *Mater. Chem. Phys.*, 2002, **77**, 34–42.

118 Y. H. Deng, J. Wei, Z. K. Sun and D. Y. Zhao, *Chem. Soc. Rev.*, 2013, **42**, 4054–4070.

119 C. Sanchez, B. Julián, P. Belleville and M. Popall, *J. Mater. Chem.*, 2005, **15**, 3559.

120 C. Sanchez, C. Boissière, D. Grosso, C. Laberty and L. Nicole, *Chem. Mater.*, 2008, **20**, 682–737.

121 G. J. de A. A. Soler-Illia, P. C. Angelomé, M. C. Fuertes, D. Grosso and C. Boissiere, *Nanoscale*, 2012, **4**, 2549–66.

122 R. W. Schwartz, T. Schneller and R. Waser, *Comptes Rendus Chim.*, 2004, **7**, 433–461.

123 C. T. Kresge, M. E. Leonowicz, W. J. Roth, J. C. Vartuli and J. S. Beck, *Nature*, 1992, **359**, 710–712.

124 J. S. Beck, J. C. Vartuli, W. J. Roth, M. E. Leonowicz, C. T. Kresge, K. D. Schmitt, C. T. W. Chu, D. H. Olson and E. W. Sheppard, *J. Am. Chem. Soc.*, 1992, **114**, 10834–10843.

125 L. Mahoney and R. Koodali, *Materials (Basel).*, 2014, **7**, 2697–2746.

126 *IUPAC-http://iupac.org/*.

127 F. Hoffmann, M. Cornelius, J. Morell and M. Fröba, *Angew. Chem. Int. Ed. Engl.*, 2006, **45**, 3216–51.

128 X. He and D. Antonelli, *Angew. Chemie Int. Ed.*, 2002, **41**, 214.

129 P. Yang, D. Zhao, D. I. Margolese, B. F. Chmelka and G. D. Stucky, *Nature*, 1998, **396**, 152–155.

130 P. V. Braun, P. Osenar and S. I. Stupp, *Nature*, 1996, **380**, 325–328.

131 U. Ciesla, S. Schacht, G. D. Stucky, K. K. Unger and F. Schiith, *Angew. Chemie Int. Ed. English*, 1996, **35**, 541–543.

132 G. S. Attard, P. N. Bartlett, J. M. Coleman, Nicholas R. B. Elliott, J. R. Owen and J. H. Wang, *Science (80-.).*, 1997, **278**, 838–840.

133 L. Zhao, H. Qin, R. Wu and H. Zou, *J. Chromatogr. A*, 2012, **1228**, 193–204.

134 D. M. Antonelli and J. Y. Ying, *Angew. Chemie Int. Ed. English*, 1995, **34**, 2014–2017.

135 D. Grosso, G. J. de A. A. Soler-Illia, F. Babonneau, C. Sanchez, P.-A. Albouy, A. Brunet-Bruneau and A. R. Balkenende, *Adv. Mater.*, 2001, **13**, 1085–1090.

136 B. C. J. Brinker, Y. Lu, A. Sellinger and H. Fan, *Adv. Mater.*, 1999, **11**, 579–585.

137 E. L. Crepaldi and D. Grosso, 2003, **8**, 109–126.

138 C. Boissie, C. Bourgaux, E. Prouzet and C. A. Bunton, *Chem. Mater.*, 2001, **13**, 3580–3586.

139 D. Grosso, C. Boissière, L. Nicole and C. Sanchez, *J. Sol-Gel Sci. Technol.*, 2006, **40**, 141–154.

140 C. Reitz, C. Suchomski, C. Weidmann and T. Brezesinski, *Nano Res.*, 2011, **4**, 414–424.

141 C. Reitz, K. Brezesinski, J. Haetge, J. Perlich and T. Brezesinski, *RSC Adv.*, 2012, **2**, 5130.

142 P. Ferreira, R. Z. Hou, A. Wu, M.-G. Willinger, P. M. Vilarinho, J. Mosa, C. Laberty-Robert, C. Boissière, D. Grosso and C. Sanchez, *Langmuir*, 2012, **28**, 2944–2949.

143 C. Reitz, P. M. Leufke, H. Hahn and T. Brezesinski, *Chem. Mater.*, 2014, **26**, 2195–2202.

144 A. Castro, P. Ferreira, B. Rodriguez and P. M. Vilarinho, *J. Mater. Chem. C*, 2015, **3**, 1035–1043.

145 T. E. Quickel, V. H. Le, T. Brezesinski and S. H. Tolbert, *Nano Lett.*, 2010, **10**, 2982–2988.

146 C. Suchomski, C. Reitz, D. Pajic, Z. Jaglicic, I. Djerdj and T. Brezesinski, *Chem. Mater.*, 2014, **26**, 2337–2343.

147 C. Reitz, C. Suchomski, J. Haetge, T. Leichtweiss, Z. Jagličić, I. Djerdj and T. Brezesinski, *Chem. Commun.*, 2012, **48**, 4471–4473.

148 J. Haetge, C. Suchomski and T. Brezesinski, *Inorg. Chem.*, 2010, **49**, 11619–11626.

149 J. Haetge, C. Suchomski and T. Brezesinski, *Small*, 2013, **9**, 2541–4.

150 J. Haetge, I. Djerdj and T. Brezesinski, *Chem. Commun.*, 2012, **48**, 6726–6728.

151 K. Brezesinski, J. Haetge, J. Wang, S. Mascotto, C. Reitz, A. Rein, S. H. Tolbert, J. Perlich, B. Dunn and T. Brezesinski, *Small*, 2011, **7**, 407–14.

152 M. Kuemmel, J.-H. Smått, C. Boissière, L. Nicole, C. Sanchez, M. Lindén and D. Grosso, *J. Mater. Chem.*, 2009, **19**, 3638.

153 M. Kuemmel, C. Boissière, L. Nicole, C. Laberty-Robert, C. Sanchez and D. Grosso, *J. Sol-Gel Sci. Technol.*, 2008, **48**, 102–112.

154 C. Sanchez, G. J. de A. A. Soler-Illia, F. Ribot and D. Grosso, *Comptes Rendus Chim.*, 2003, **6**, 1131–1151.

155 G. J. D. a a Soler-Illia, C. Sanchez, B. Lebeau and J. Patarin, *Chem. Rev.*, 2002, **102**, 4093–138.

156 M. Faustini, B. Louis, P. A. Albouy, M. Kuemmel, D. Grosso and M. Curie, *J. Phys. Chem. C*, 2010, **114**, 7637–7645.

157 G. Riess, *Prog. Polym. Sci.*, 2003, **28**, 1107–1170.

158 *DLS Tech. - http//www.horiba.com/*.

159 A. K. Tyagi, M. Roy, S. K. Kulshreshtha and S. Banerjee, in *Advanced Techniques for Materials Characterization*, eds. A. K. Tyagi, M. Roy, S. K. Kulshreshtha and S. Banerjee, Trans Tech Publications, Softcover., 2009, p. 433.

160 P. Gill, T. T. Moghadam and B. Ranjbar, *J. Biomol. Tech.*, 2010, **21**, 167–193.

161 D. B. Williams and C. B. Carter, *Transmission Electron Microscopy: A Textbook for Materials Science*, Springer Science+Business Media New York, Second edi., 2009, vol. V1-V4.

162 C. R. Brundle, C. A. Evans and S. Wilson, *Encyclopedia of Materials Characterization: Surface, Interfaces, Thin films*, Butterworth-Heinemann, 1992.

163 N. Yao and Z. L. Wang, Eds., *Handbook of microscopy for nanotechnology*, Kluwer Academic, 2005.

164 A. R. Clarke and C. N. Eberhardt, *Microscopy techniques for materials science*, Woodhead Publishing Limited and CRC Press LLC, 2002.

165 G. Cao, *Nanostructures and nanomaterials: synthesis, properties and applications*, Imperial College Press, 2004.

166 P. J. Goodhew, J. Humphreys and R. Beanland, *Electron Microscopy and analysis*, Taylor and Francis, 2001.

167 S. Ohara, T. Adschiri, T. Ida, M. Yashima, T. Mikayama, H. Abe, Y. Setsuhara, K. Nogi, M. Miyahara, K. Kaneko and A. Ohtomo, in *Nanoparticle technology handbook*, eds. M. HosoKawa, K. Nogi, M. Naito and T. Yokoyma, Elsevier, 2007.

168 *XRD-http://www.eag.com/mc/x-ray-diffraction.html*.

169 *Raman Spectrosc. - http//www.microspectra.com/support/technical-support/raman-science/35-technical-support/126-science-of-micro-raman-spectroscopy*.

170 *Raman spectrometers-http://www.horiba.com/us/en/scientific/products/raman-spectroscopy/raman-spectrometers/*.

171 *Raman-http://www.surfgroup.be/raman*.

172 G. Binnig and C. F. Quate, *Phys. Rev. Lett.*, 1985, 56, 930–934.

173 R. García and R. Perez, *Surf. Sci. Rep.*, 2002, **47**, 197–301.

174 *Asylum Res. - www.AsylumResearch.com*.

175 B. J. Rodriguez, R. Proksch, P. Maksymovych and S. V Kalinin, in *Handbook of Nanoscopy*, eds. G. Van Tendeloo and D. Van Dyck, WILEY-VCH, first edit., 2012, pp. 539–614.

176 *Bruker AFM-http://www.brukerafmprobes.com/*.

177 C. Harnagea, A. Pignolet, M. Alexe and D. Hesse, *Integr. Ferroelectr.*, 2002, **44**, 113–124.

178 *AFM-http://www.parkafm.com/*.

179 *Agilent-http://www.agilent.com/home*.

180 R. Proksch and S. Kalinin, *Asylum Res. app note 10*.

181 B. J. Rodriguez, North Carolina State University, 2003.

182 *EMRL-http://www.emrl.de/r_m_2.html*.

183 A. Gruverman and S. V. Kalinin, *J. Mater. Res.*, 2006, **41**, 107–116.

184 S. Jesse, A. P. Baddorf and S. V. Kalinin, *Appl. Phys. Lett.*, 2006, **88**, 062908.

185 *Asylum Res. - https//www.asylumresearch.com/Applications/PFMAppNote/PFM-ANLR.pdf*.

186 *SQUID-http://spa-mxpweb.spa.umn.edu/s09/Projects/S09_SQUID/theory.htm*.

187 J. Liu, W. Chen, B. Wang and Y. Zheng, *Materials (Basel).*, 2014, **7**, 6502–6568.

188 C. E. Ciomaga, S. Olariu, L. Padurariu, A. V. Sandu, C. Galassi and L. Mitoseriu, 2012, **094103**, 1–8.

189 A. Seifert, P. Muralt and N. Setter, *Appl. Phys. Lett.*, 1998, **72**, 2409.

190 J. Harjuoja, A. Kosola, M. Putkonen and L. Niinistö, *Thin Solid Films*, 2006, **496**, 346–352.

191 D. G. Wang, C. Z. Chen, J. Ma and T. H. Liu, *Appl. Surf. Sci.*, 2008, **255**, 1637–1645.

192 I. Taguchi, A. Pignolet, L. Wang, M. Proctor, F. Lévy and P. E. Schmid, *J. Appl. Phys.*, 1993, **74**, 6625–6631.

193 I. Taguchi, A. Pignolet, L. Wang, M. Proctor, F. Lévy and P. E. Schmid, *J. Appl. Phys.*, 1993, **73**, 394–399.

194 Z. C. Feng, B. S. Kwak, A. Erbil and L. A. Boatner, *Appl. Phys. Lett.*, 1994, **64**, 2350.

195 R. A. Frey and E. Silberman, *Helv. Phys. Acta*, 1976, **49**, 1–11.

196 M. Alexe, C. Harnagea, D. Hesse and U. Gösele, *Appl. Phys. Lett.*, 2001, **79**, 242–244.

197 A. L. Kholkin, K. G. Brooks, D. V. Taylor, S. Hiboux and N. Setter, *Integr. Ferroelectr.*, 1998, **22**, 525–533.

198 J. Frey, F. Schlenkrich and A. Schönecker, *Integr. Ferroelectr.*, 2001, **35**, 105–113.

199 A. Wu, P. M. Vilarinho, V. V Shvartsman, G. Suchaneck and a L. Kholkin, *Nanotechnology*, 2005, **16**, 2587–2595.

200 A. Seifert, 1999, **20**, 13–20.

201 J. Li, B. Nagaraj, H. Liang, W. Cao, C. H. Lee and R. Ramesh, *Appl. Phys. Lett.*, 2004, **84**, 1174.

202 J. R. Quintana, M. D. Jafiez, I. Katime, G. D. N. Materiales, D. D. O. Fisica and F. De Ciencias, 1998, **39**, 2111–2117.

203 R. Quintana and D. Ja, 1996, **7463**, 2196–2199.

204 N. Nuraje and K. Su, *Nanoscale*, 2013, **5**, 8752–80.

205 O. Harizanov, a Harizanova and T. Ivanova, *Mater. Sci. Eng. B*, 2004, **106**, 191–195.

206 I. Vukovic, G. Ten Brinke and K. Loos, *Polymer (Guildf).*, 2013, **54**, 2591–2605.

207 M. Kuemmel, J. Allouche, L. Nicole, C. Boissière, C. Laberty, H. Amenitsch, C. Sanchez and D. Grosso, *Chem. Mater.*, 2007, **19**, 3717–3725.

208 M. Villacampa and I. A. Katime, 1993, **26**, 601–605.

209 J. Quintana, M. D. Jáñez and I. Katime, *Polymer (Guildf).*, 1996, **37**, 3531–3535.

210 J. R. Quintana, M. D. Jbnez, M. Villacampa and I. Katime, 1995, **28**, 4139–4143.

211 J. N. Phillips, *Trans. Faraday Soc.*, 1955, **51**, 561.

212 J. R. Quintana, M. Villacampa, M. Muijoz, A. Andrio and I. A. Katime, 1992, **25**, 3125–3128.

213 J. R. Quintana, M. Villacampa and I. A. Katime, *Macromolecules*, 1993, **26**, 606–611.

214 Z. Li and E. E. Dormidontova, *Macromolecules*, 2010, **43**, 3521–3531.

215 C. Honda, Y. Hasegawa, R. Hirunuma and T. Nose, *Macromolecules*, 1994, **27**, 7660–7668.

216 P. Bahadur and N. V. Sastry, *Eur. Polym. J.*, 1988, **24**, 285–288.

217 S. Forster and T. Plantenberg, *Angew. Chem. Int. Ed. Engl.*, 2002, **41**, 688.

218 C. J. Brinker, *Curr. Opin. Colloid Interface Sci.*, 1998, **3**, 166–173.

219 H. Yang, N. Coombs, I. Sokolov and G. A. Ozin, *Nature*, 1996, **381**, 589–592.

220 E. L. Crepaldi, G. J. D. a a Soler-Illia, D. Grosso, F. Cagnol, F. Ribot and C. Sanchez, *J. Am. Chem. Soc.*, 2003, **125**, 9770–86.

221 K. Liu, M. Zhang, K. Shi and H. Fu, *Mater. Lett.*, 2005, **59**, 3308–3310.

222 A. Thomas, H. Schlaad, B. Smarsly and M. Antonietti, *Langmuir*, 2003, **19**, 4455–4459.

223 R. Asiaie, W. D. Zhu, S. a Akbar and P. K. Dutta, *Chem. Mater.*, 1996, **8**, 226–234.

224 P. Allongue, L. Cagnon, C. Gomes, a. Gündel and V. Costa, *Surf. Sci.*, 2004, **557**, 41–56.

225 a. Azizi, a. Sahari, M. L. Felloussia, G. Schmerber, C. Mény and a. Dinia, *Appl. Surf. Sci.*, 2004, **228**, 320–325.

226 J. A. Koza, M. Uhlemann, A. Gebert and L. Schultz, *J. Electroanal. Chem.*, 2008, **617**, 194–202.

227 C. Qiang, J. Xu, S. Xiao, Y. Jiao, Z. Zhang, Y. Liu, L. Tian and Z. Zhou, *Appl. Surf. Sci.*, 2010, **257**, 1371–1376.

228 A. L. Patterson, *Phys. Rev.*, 1939, **56**, 978.

229 J. Lee, H. Min and C. Sung, *J. Magn. Magn. Mater.*, 1998, **181**, 900–902.

230 R. Dumitru, F. Papa, I. Balint, D. C. Culita, C. Munteanu, N. Stanica, A. Ianculescu, L. Diamandescu and O. Carp, *Appl. Catal. A Gen.*, 2013, **467**, 178–186.

231 S. Royer, H. Alamdari, D. Duprez and S. Kaliaguine, *Appl. Catal. B-Environmental*, 2005, **58**, 273–288.

232 M. Alexe, C. Harnagea and D. Hesse, *J. electroceramics*, 2004, 69–88.

233 B.-H. Wu, L.-W. Zhu, Y. Ou, W. Tang, L.-S. Wan and Z.-K. Xu, *J. Phys. Chem. C*, 2015, **119**, 1971−1979.

234 T. H. Nguyen, M. Vayer, D. Grosso, H. Amenitsch and C. Sinturel, *J. Phys. Chem. C*, 2012, **116**, 5295–5302.

235 M. A. Morris, *Microelectron. Eng.*, 2015, **132**, 207–217.

236 C. Kresge, M. Leonowicz and W. Roth, *Nature*, 1992, **359**, 710–712.

237 Y. Yang, X. Wang, C. Zhong, C. Sun and L. Li, *Appl. Phys. Lett.*, 2008, **92**, 122907–3.

238 A. Gruverman and A. Kholkin, *Reports Prog. Phys.*, 2006, **69**, 2443–2474.

239 H. Jun, B. Im, K. H. Lee, I. K. Yang, Y. H. Jeong and J. S. Lee, *Nanotechnology*, 2012, **23**, 135602–8.

240 A. Fischer, A. Fisher, M. Kuemmel, M. Järn, M. Linden, C. Boissière, L. Nicole, C. Sanchez and D. Grosso, *Small*, 2006, **2**, 569–74.

241 M. Järn, F. J. Brieler, M. Kuemmel, D. Grosso and M. Lindén, *Chem. Mater.*, 2008, 1476–1483.

242 A. V Bune, V. M. Fridkin and S. Ducharme, *Nature*, 1998, **391**, 874–877.

243 T. Tybell, C. H. Ahn and J. Triscone, 1999, **75**, 1999–2001.

244 Y. Kim, H. Han, Y. Kim, W. Lee, M. Alexe, S. Baik and J. K. Kim, *Nano Lett.*, 2010, **10**, 2141–6.

245 J. M. Macak, C. Zollfrank, B. J. Rodriguez, H. Tsuchiya, M. Alexe, P. Greil and P. Schmuki, *Adv. Mater.*, 2009, **21**, 3121–3125.

246 S. Ha, T. Walther, R. Ko, S. G. Ebbinghaus and M. Tiemann, *J. Phys. Chem. C*, 2013, **117**, 24471–24478.

247 A. Moser, K. Takano, D. T. Margulies, M. Albrecht, Y. Sonobe, Y. Ikeda, S. Sun and E. E. Fullerton, *J. Phys. D. Appl. Phys.*, 2002, **35**, R157–R167.

248 X. S. Gao, D. H. Bao, B. Birajdar, T. Habisreuther, R. Mattheis, M. a Schubert, M. Alexe and D. Hesse, *J. Phys. D. Appl. Phys.*, 2009, **42**, 175006.

249 A. Lisfi, C. Williams, L. Nguyen, J. Lodder, A. Coleman, H. Corcoran, A. Johnson, P. Chang, A. Kumar and W. Morgan, *Phys. Rev. B*, 2007, **76**, 054405.

250 A. Lisfi and C. M. Williams, *J. Appl. Phys.*, 2003, **93**, 8143.

251 O. F. Cobalt and S. Ferrites, *Solid State Commun.*, 1998, **107**, 471–476.

252 C. A. Schneider, W. S. Rasband and K. W. Eliceiri, 2012, 671–675.

253 C. Thompson, *Interface Sci.*, 1998, **93**, 85–93.

254 X. W. Wang, Y. Q. Zhang, H. Meng, Z. J. Wang and Z. D. Zhang, *J. Alloys Compd.*, 2011, **509**, 7803–7807.

255 A. Lisfi and C. M. Williams, *J. Appl. Phys.*, 2003, **93**, 8143–8145.

256 R. E. Vandenberghe, V. R., E. De Grave and G. Robbrecht, *J. Magn. Magn. Mater.*, 1980, **15-18**, 1117–1118.

257 D. J. Craik, *Magnetic Oxides: Part II*, John Wiley., 1975.

258 D. C. Lee, A. Ghezelbash, C. A. Stowell and B. A. Korgel, *J. Phys. Chem. B*, 2006, **110**, 20906–20911.

259 M. Chen and D. E. Nikles, *Nano Lett.*, 2002, **2**, 211–214.

260 A. Wu, P. M. Vilarinho, I. M. M. Salvado, J. L. Baptista, Z. Zhou, I. M. Reaney, A. R. Ramos and M. F. Silva, *J. Am. Ceram. Soc.*, 2004, **85**, 641–646.

261 L. Han, U. Wiedwald, J. Biskupek, K. Fauth, U. Kaiser and P. Ziemann, *Beilstein J. Nanotechnol.*, 2011, **2**, 473–85.

262 S. Y. Yang, L. W. Martin, S. J. Byrnes, T. E. Conry, S. R. Basu, D. Paran, L. Reichertz, J. Ihlefeld, C. Adamo, A. Melville, Y.-H. Chu, C.-H. Yang, J. L. Musfeldt, D. G. Schlom, J. W. Ager and R. Ramesh, *Appl. Phys. Lett.*, 2009, **95**, 062909–3.

263 F. Gao, X. Y. Chen, K. B. Yin, S. Dong, Z. F. Ren, F. Yuan, T. Yu, Z. G. Zou and J.-M. Liu, *Adv. Mater.*, 2007, **19**, 2889–2892.

264 H. Yang, H. M. Luo, H. Wang, I. O. Usov, N. A. Suvorova, M. Jain, D. M. Feldmann, P. C. Dowden, R. F. DePaula and Q. X. Jia, *Appl. Phys. Lett.*, 2008, **92**, 102113–3.

265 A. Lahmar, K. Zhao, S. Habouti, M. Dietze, C.-H. Solterbeck and M. Es-Souni, *Solid State Ionics*, 2011, **202**, 1–5.

266 N. Bassiri-Gharb, Y. Bastani and A. Bernal, *Chem. Soc. Rev.*, 2014, **43**, 2125–2140.

267 S. M. Selbach, M. Einarsrud and T. Grande, *Chem. Mater.*, 2009, **21**, 169–173.

268 D. H. Wang and C. K. Ong, *J. Appl. Phys.*, 2006, **100**, 044111.

269 H. Naganuma, T. Okubo, K. Kamishima, K. Kakizaki, N. Hiratsuka and S. Okamura, *IEEE Trans. Ultrason. Ferroelectr. Freq. Control*, 2008, **55**, 1051–5.

270 G. Catalan, H. Béa, S. Fusil, M. Bibes, P. Paruch, a. Barthélémy and J. Scott, *Phys. Rev. Lett.*, 2008, **100**, 027602.

271 Y. H. Chu, T. Zhao, M. P. Cruz, Q. Zhan, P. L. Yang, L. W. Martin, M. Huijben, C. H. Yang, F. Zavaliche, H. Zheng and R. Ramesh, *Appl. Phys. Lett.*, 2007, **90**, 252906.

272 I. Coondoo, N. Panwar, A. Tomar, I. Bdikin, a. L. Kholkin, V. S. Puli and R. S. Katiyar, *Thin Solid Films*, 2012, **520**, 6493–6498.

273 S. H. Baek and C. B. Eom, *Philos. Trans. A. Math. Phys. Eng. Sci.*, 2012, **370**, 4872–89.

274 S. Jesse, H. N. Lee and S. V. Kalinin, *Rev. Sci. Instrum.*, 2006, **77**, 073702.

275 S. Y. Yang, F. Zavaliche, L. Mohaddes-Ardabili, V. Vaithyanathan, D. G. Schlom, Y. J. Lee, Y. H. Chu, M. P. Cruz, Q. Zhan, T. Zhao and R. Ramesh, *Appl. Phys. Lett.*, 2005, **87**, 102903.

276 M. Daraktchiev, G. Catalan and J. F. Scott, *Ferroelectrics*, 2008, **375**, 122–131.

277 J. Tauc, R. Grigorovici and A. Vancu, *Phys. Status Solidi*, 1966, **15**, 627–637.

278 J. F. Ihlefeld, N. J. Podraza, Z. K. Liu, R. C. Rai, X. Xu, T. Heeg, Y. B. Chen, J. Li, R. W. Collins, J. L. Musfeldt, X. Q. Pan, J. Schubert, R. Ramesh and D. G. Schlom, *Appl. Phys. Lett.*, 2008, **92**, 142908.

279 T. P. Gujar, V. R. Shinde and C. D. Lokhande, *Mater. Chem. Phys.*, 2007, **103**, 142–146.

280 D. Tiwari, D. J. Fermin, T. K. Chaudhuri and A. Ray, *J. Phys. Chem. C*, 2015, **119**, 5872–5877.

281 P. Brody and F. Crowne, *J. Electron. Mater.*, 1975, **4**, 955–971.

282 B. On, T. Carrier and T. Mechanisms, 2007, **25**, 1143–1148.

283 S. J. Clark and J. Robertson, *Appl. Phys. Lett.*, 2007, **90**, 132903.

284 S. R. Basu, L. W. Martin, Y. H. Chu, M. Gajek, R. Ramesh, R. C. Rai, X. Xu and J. L. Musfeldt, *Appl. Phys. Lett.*, 2008, **92**, 091905.

285 F. Cansell and C. Aymonier, *J. Supercrit. Fluids*, 2009, **47**, 508–516.

286 E. Reverchon and R. Adami, *J. Supercrit. Fluids*, 2006, **37**, 1–22.

287 J. D. Holmes, D. M. Lyons and K. J. Ziegler, *Chem. Eur. J.*, 2003, **9**, 2145–51.

288 C. Aymonier, A. Loppinet-Serani, H. Reverón, Y. Garrabos and F. Cansell, *J. Supercrit. Fluids*, 2006, **38**, 242–251.

289 M. J. Tenorio, C. Pando, J. A. R. Renuncio, J. G. Stevens, R. A. Bourne, M. Poliakoff and A. Cabañas, *J. Supercrit. Fluids*, 2012, **69**, 21–28.

290 M. Škerget, Z. Knez and M. Knez-Hrncic, *J. Chem. Eng. Data*, 2011, **56**, 694–719.

291 N. G. Smart, T. Carleson and T. Kast, 1997, **44**, 137–150.

292 O. Aschenbrenner, S. Kemper, N. Dahmen, K. Schaber and E. Dinjus, *J. Supercrit. Fluids*, 2007, **41**, 179–186.

293 J. Ming, C. Wu, H. Cheng, Y. Yu and F. Zhao, *J. Supercrit. Fluids*, 2011, **57**, 137–142.

294 J. J. Watkins, J. M. Blackburn and T. J. McCarthy, *Chem. Mater.*, 1999, **11**, 213–215.

295 J. J. Watkins and T. J. McCarthy, *Chem. Mater.*, 1995, **7**, 1991–1994.

296 J. M. Blackburn, D. P. Long, A. Cabanas and J. J. Watkins, *Science*, 2001, **294**, 141–5.

297 E. T. Hunde and J. J. Watkins, *Chem. Mater.*, 2004, 498–503.

298 S. E. Bozbag, D. Sanli and C. Erkey, *J. Mater. Sci.*, 2011, **47**, 3469–3492.

299 C. Erkey, *J. Supercrit. Fluids*, 2009, **47**, 517–522.

300 S. E. Bozbag, L. C. Zhang, M. Aindow and C. Erkey, *J. Supercrit. Fluids*, 2012, **66**, 265–273.

301 J. Morère, S. Royuela, G. Asensio, P. Palomino, E. Enciso, C. Pando and A. Cabañas, *Philos. Trans. A*, 2015, accepted.

302 L. Suresh and J. Y. Walz, *J. Colloid Interface Sci.*, 1996, **183**, 199–213.

303 B. D. Cullity and C. D. Graham, *Introduction to Magnetic Materials*, Hoboken, New Jersey, 2nd edn., 2009.

304 X. He, W. Zhong, C.-T. Au and Y. Du, *Nanoscale Res. Lett.*, 2013, **8**, 446.